Characterization of Carbon-Nanotube-Reinforced-Polymer-Composite Material based on Multiscale Finite Element Model and Probabilistic Approach

Jorge Alberto Palacios Moreno

A Thesis
In the Department
of
Mechanical, Industrial and Aerospace Engineering

Presented in Partial Fulfillment of the Requirements
For the Degree of
Doctor of Philosophy (Mechanical Engineering) at
Concordia University
Montreal, Quebec, Canada

November 2019

CONCORDIA UNIVERSITY

SCHOOL OF GRADUATE STUDIES

This is to certify that the thesis prepared

By: Jorge Alberto Palacios

Entitled: Characterization of Carbon-Nanotube-Reinforced-Polymer-Composite Material based on Multiscale Finite Element Model and Probabilistic Approach

and submitted in partial fulfillment of the requirements for the degree of

Doctor Of Philosophy (Mechanical Engineering)

complies with the regulations of the University and meets the accepted standards with respect to originality and quality.

Signed by the final examining committee:

_____ Chair
Dr. Willam Lynch

_____ External Examiner
Dr. Farid Taheri

_____ External to Program
Dr. Yousef R. Shayan

_____ Examiner
Dr. Suong Van Hoa

_____ Examiner
Dr. Mingyuan Chen

_____ Thesis Supervisor
Dr. Rajamohan Ganesan

Approved by _____
Dr. Ivan Contreras, Graduate Program Director

February 19, 2020 _____
Dr. Amir Asif, Dean
Gina Cody School of Engineering & Computer Science

Abstract

Characterization of Carbon-Nanotube-Reinforced-Polymer-Composite Material based on Multiscale Finite Element Model and Probabilistic Approach

Jorge Alberto Palacios Moreno, Ph.D.

Concordia University, 2019

Carbon-Nanotube-Reinforced-Polymer-Composite (CNRPC) materials have generated widespread interest over the last several years in practical engineering applications, such as aeronautical and aerospace engineering structures. However, studies still need to be carried out to characterize their mechanical properties, especially the dynamic properties, and the effects of defects on the mechanical properties. Experimental investigations intended for this purpose have limitations and, in most cases, reliable cost-effective experimental work could not be carried out. Computational modelling and simulation encompassing multiscale material behavior provide an alternate approach in this regard to characterize the material behavior. A probabilistic approach serves as a suitable approach to characterize the effects of material and structural defects. The present thesis reports the development of a computational framework of the Representative Volume Element (RVE) of a CNRPC material model to determine its static and dynamic responses, and also for the evaluation of its static and dynamic reliabilities based on a probabilistic characterization approach. A 3D multiscale finite element model of the RVE of the nanocomposite material consisting of a polymer matrix, a Single-Walled-Carbon-Nanotube (SWCN) and an interface region has been constructed for this purpose. The multiscale modeling is performed in terms of using different theories and corresponding strain energies to model the individual parts of the RVE of the CNRPC material. The macroscale continuum mechanics is used for the polymer matrix, the mesoscale mechanics is used for the interface region, and the nanoscale-level atomistic

mechanics is used for the SWCN. The polymer matrix is modeled using the Mooney-Rivlin strain energy function to calculate its non-linear response, while the interface region is modeled via the van der Waals links. The SWCN is first modeled as a space frame structure by using the Morse potential, and then as a thin shell based on a suitable shell theory. For this purpose, the suitability and the accuracy of popular shell theories for use in the multiscale model of the RVE are assessed.

Acknowledgments

Montreal. . . There are not enough words in my mind to express the bliss in my heart when I think of my days in this glorious city. I am thankful to God, for the blessing of my time in Montreal.

I would like to express my sincere gratitude to my supervisor Professor Rajamohan Ganesan for the continuous support during my PhD study and related research, for his patience, motivation, and immense knowledge. His guidance helped me in all the time of research and writing of this thesis.

Besides my supervisor, I would like to thank my committee: Professor Ashok Kaushal, Professor Suong Van Hoa and Professor Yousef R. Shayan for their insightful comments during my examinations, and also for the hard questions which incented me to widen my research from various perspectives.

I would also like to take this opportunity to acknowledge the support provided by Concordia University, Fonds de recherche du Quebec - Nature et technologies, and Consejo Nacional de Ciencia y Tecnologia (CONACYT), Mexico, for providing scholarships and financial support for my research.

Last, I would like to express my appreciation to all my family, friends and colleagues; whose unwavering encouragement, support, and patience allowed me to complete this work.

Contributions of Authors in Publications

Authors:

Jorge Alberto Palacios Moreno

Contributions: Conceptualization, Methodology, Software, Validation, Formal Analysis, Investigation, Data Curation, Writing – Original Draft, Visualization.

Rajamohan Ganesan

Contributions: Conceptualization, Methodology, Resources, Investigation, Writing – Review & Editing, Supervision, Research Project Formulation and Administration.

Table of Contents

List of Tables

List of Figures

Nomenclature

Symbol	Definition
r_n	Radius of the nanotube
t_n	Thickness of the nanotube
L_n	Polymer matrix and nanotube length
$\mathbb{C}_{\boldsymbol{h}}$	Chiral vector
a_1	Lattice vector of the graphene monolayer
a_2	Lattice vector of the graphene monolayer
C_h	Magnitude of chiral vector
T	Translational vector of nanotube
$U_{stretch}$	Energy of Morse potential
$F_{stretch}$	Force stretching of C-C covalent bonds
D_e	Force stretching parameter
β	Force stretching parameter
Δr	Covalent bond length variation
ρ_b	Covalent bond density
m_c	Carbon atom mass
v_n	Poisson's ratio of carbon nanotube

ρ_n	Density of carbon nanotube
d_n	Diameter of carbon nanotube
x, θ, z	Coordinate system of thin shell model
u, v, w	Components of the deformation of the shell
E_n	Young's modulus of carbon nanotube
k	Non-dimensional thickness parameter
$[L_D]$	Differential operator for Donnell's Shell Theory
λ_m	Axial wavenumber
A_{mn}, B_{mn}, C_{mn}	Wave amplitudes in the z, θ, x directions
$[\Delta_D]$	Eigenvalue problem operator
$\widetilde{\Omega}$	Frequency parameter of eigenvalue problem
ω_n	Natural frequency
K_i	Coefficients of bicubic characteristic equation
$[L_{MOD1}]$	Differential operator for Flugge's Shell Theory
$[\Delta_F]$	Eigenvalue problem operator
ΔK_i	Coefficients of characteristic equation
$[L_{MOD2}]$	Differential operator for Sanders's Shell Theory
V_n	Volume fraction of carbon nanotube
W	Mooney-Rivlin strain energy function

I_i	Invariants of the strain tensor
v_m	Poisson's ratio of polymer matrix
c_{im}	Mooney-Rivlin material parameters
k_m	Bulk modulus of the polymer matrix
ρ_m	Density of polymer matrix
E_m	Young's modulus of polymer matrix
U	Lennard-Jones potential
$\tilde{\varepsilon}, \tilde{\sigma}$	Lennard-Jones potential parameters
F_{vdW}	Van der Waals forces
τ	Shear stress
τ_{cr}	Critical shear stress
ΔL_n	Change in the length of the composite
ΔL_{Cn}	Change in the length of carbon nanotube
η	Loss factor
U_{diss}	Total dissipation energy
ΔU	Dissipation energy
ε_0	Strain of matrix material due to loading
τ_2	Bonding stress related to longitudinal shear stress
ε_2	Strain between nanotube and polymer matrix

G_0	Shear modulus of polymer matrix
E^{eq}	Equivalent modulus of nanotube
A	Contact area between nanotube and matrix
V	Volume of polymer matrix
Q	Factor Q
ζ	Damping ratio
ω	Excitation frequency of harmonic analysis
r	Frequency ratio
ω_d	Damped natural frequency
M	Magnification factor
ζ	Viscous damping ratio
λ	Structural damping coefficient
SE	Entropy
λ_i	Lagrange multipliers
x	Random variable
H_{ij}	Hessian matrix
m_i	Statistical moments
S	Strength
s	applied stress

R	Reliability function
Q	Unreliability function
H	Static hazard function
δ	Interference random variable
β	Weibull scale-parameter
α	Weibull shape-parameter
μ_δ	Mean value of variable δ
σ_δ	Standard deviation of variable δ
μ_S	Mean value of the strength
σ_S	Standard deviation of the strength
μ_s	Mean value of the stress
σ_s	Standard deviation of the stress
S_f	Fixed stress point
SFc	Safety factor
R_D	Dynamic reliability
Q_D	Dynamic unreliability
H_D	Dynamic hazard function
Ω	Excitation frequency for reliability of natural frequencies
δ_f	Frequency interference random variable

μ_{δ_f}	Mean value of the variable δ_f
σ_{δ_f}	Standard deviation of the variable δ_f
μ_{ω_n}	Mean value of ω_n
σ_{ω_n}	Standard deviation of ω_n
μ_{Ω}	Mean value of Ω
σ_{Ω}	Standard deviation of Ω
f_{ω_n}	Density function of ω_n
f_{Ω}	Density function of Ω
ω_{b_i}	Bending mode frequencies
ω_{a_i}	Axial mode frequencies

Acronym	**Definition**
CNRPC	Carbon-Nanotube-Reinforced-Polymer-Composite
CNRP	Carbon-Nanotube-Reinforced-Polymer
CN	Carbon Nanotube
MD	Molecular Dynamics
SWCN	Single-Walled-Carbon-Nanotube
RVE	Representative Volume Element
MCS	Monte Carlo Simulation

MEM	Maximum Entropy Method
pdf	probability density function
MM	Molecular Mechanics
FEM	Finite Element Method
vdW	van der Waals
C-C	Carbon-Carbon
DWCN	Double-Walled-Carbon-Nanotube
MWCN	Multi-Walled-Carbon-Nanotube
DST	Donnell's Shell Theory
FST	Flugge's Shell Theory
SST	Sanders' Shell Theory
RMSE	Root Mean Square Error
CF	Clamped-Free
CC	Clamped-Clamped
PAI	Polyamide-imide
PEEK	Polyetheretherketone
ME4	Maximum-Entropy distribution with four-moments
ME5	Maximum-Entropy distribution with five-moments
cdf	cumulative distribution function

EFLEM cdf	Empirical Frequency cdf of Longitudinal Elastic Modulus
EFULS cdf	Empirical Frequency cdf of Ultimate Longitudinal Strength
EFAS cdf	Empirical Frequency cdf of Applied Stress
MSTF	Mean-Stress-To-Failure
MRS	Mean-Residual-Strength
EFIRV cdf	Empirical Frequency cdf of Interference Random Variable
EFOS	Empirical Frequency of Operational Stress
EFFB cdf	Empirical Frequency cdf of First Bending mode frequency
EFFIRV cdf – bending mode	Empirical Frequency cdf of Frequency Interference Random Variable in bending mode
EFOF – bending mode	Empirical Frequency of Operational Frequency in bending mode

Chapter 1. Introduction

1.1 Carbon-Nanotube-Reinforced-Polymer-Composites

A considerable amount of opportunities and challenges exist in the development and characterization of engineering materials. Polymers are increasingly becoming an attractive option for a wide variety of industries. There is an increase in the use of polymer materials in engineering applications due to their ease of manufacture and processing, low cost, low weight, and excellent chemical properties. After the introduction of structural adhesives, numerous recent technological achievements, especially those associated with particular applications, have become possible. However, there has always been an essential need to apply novel polymer materials with enhanced properties in industry, such as in aeronautical and aerospace industries. Such materials, known as polymer-based nanocomposites, are preferred over conventional polymer materials because of their superior mechanical properties. There are different techniques to enhance the material properties of this type of nanocomposites, such as reinforcements [1, 2], material coating [3], and thermal treatment [4]. One option to enhance their mechanical properties is by using Carbon Nanotubes (CNs) [5] as reinforcement. CNs have attracted significant research attention from various disciplines of engineering and science due to their outstanding chemical and physical characteristics such as high stiffness, high strength but very low density [6-11]. These hollow cylinder-shaped nanostructures are created by hexagonal unit cells, which were discovered by Iijima in 1991 [5]. Many studies have been conducted in order to estimate and to develop the characteristics of CNs in their stiffness and dynamic responses. These studies mainly focus on modal analysis, considering zigzag and armchair nanotubes, and sometimes, varying chirality by using Molecular Dynamics (MD) [12-15].

Hence, a Carbon-Nanotube-Reinforced-Polymer-Composite (CNRPC) material consists of a polymer material in which carbon nanotubes are used as reinforcement material to enhance its physical and mechanical properties and material behavior. Due to their multifunctional properties, CNRPCs are currently used in a wide range of industries, including but not limited to electronics, aerospace, aeronautical and biomedical/bioengineering. CNRPCs have great potential in

structural/non-structural and other specialized applications such as electromagnetic interference shielding and electrostatic discharge, improving the performance of topcoat on airplanes and high-performance adhesives for repair patches, and aircraft components in the aerospace industry [16]. The CNRPC soft coating has also been successfully applied to replace the heavy metal mesh used for EMI shielding [17-21]. Researches have also shown that CNRPCs are promising candidates for interior panels and brake pads of aircraft [22, 23]. Other noteworthy areas of application of CNRPCs include thermal management [24-29] and the introduction of combined electrical/thermal multifunctionality in spacecrafts and airplanes [30-33]. There are many engineering applications in which CNRPCs exhibit a better performance than other types of materials, such as plain polymers and epoxies. To understand and to develop the modeling of carbon nanotubes, a description of their atomic structures is required, as well as information about graphene sheets. CNs are obtained from graphene sheets. Hence, in the next sub-section, the atomic structure of carbon nanotubes is explained in detail.

1.1.1 Atomic Structure of Carbon Nanotubes

The hexagonal arrangement of atoms in carbon nanotubes and graphene sheets can be described in terms of the tube's chirality or helicity, using the chiral vector, $\mathbb{C}_h$ or the chiral angle φ. The chiral vector, $\mathbb{C}_h$, also known as the roll-up vector, is defined by the following equation:

$$\mathbb{C}_h = n\,\boldsymbol{a_1} + m\,\boldsymbol{a_2} \tag{1.1}$$

where the integers n and m are the numbers of steps along the lattice vectors (unit vector) $\boldsymbol{a_1}$ and $\boldsymbol{a_2}$, as defined in Figure 1.1. The lattice vectors can be expressed as follows:

$$\boldsymbol{a_1} = \left(\frac{\sqrt{3}}{2}a, \frac{3}{2}a\right) \text{ and } \boldsymbol{a_2} = \left(\frac{\sqrt{3}}{2}a, -\frac{3}{2}a\right) \tag{1.2}$$

where a is the length of each unit vector and is defined as $a = \sqrt{3}a_{c-c}$, where a_{c-c} is the covalent bond length. In carbon nanotubes, the covalent bond length is $a_{c-c} = 1.42$ Angstroms, and thus, $a = 2.46$ Angstroms [34, 35]. The chiral angle φ determines the amount of twist of the carbon nanotube. Hence, the carbon nanotubes are fundamentally classified into three main categories according to their chiral vector, $\mathbb{C}_h$. A chiral (n, m) nanotube has unequal, non-zero n and m integers, i.e. $n \neq m \neq 0$ and the chiral angle φ is between its two limits ($0^\circ < \varphi < 30^\circ$), whereas

for the two limiting cases, i.e. zigzag nanotube with a chiral angle equal to zero ($\varphi = 0^{\circ}$) and armchair nanotube with $\varphi = 30^{\circ}$, the integers are represented as $(n, 0)$ and (n, n), respectively. These last two cases are generally known as symmetric carbon nanotubes [34]. The chiral, armchair and zigzag carbon nanotubes sometimes exhibit different properties. For instance, chiral and zigzag nanotubes show semiconducting behavior, whereas armchair carbon nanotubes are categorized as metal and are considered conducting materials [36]. In addition to chirality, the number of layers is also another factor that is considered for categorizing carbon nanotubes. Hence, they are classified as Single-Walled-Carbon-Nanotube (SWCN) and Multi-Walled-Carbon-Nanotube (MWCN).

A SWCN can be described as a graphene sheet that has been rolled into a tube or cylinder. The thickness of the cylinder's wall is considered equal to that of a graphene sheet, which is about 0.34 nm [33, 37, 38]. For a given (n, m) SWCN, the diameter d_n of the cylinder can be calculated using chiral vector integers, n and m, as follows:

$$d_n = \frac{a}{\pi}\sqrt{n^2 + nm + m^2} \tag{1.3}$$

Moreover, the translational vector **T** can be defined as:

$$\mathbf{T} = \frac{n + 2m}{gcd}\,\boldsymbol{a_1} + \frac{2n + m}{gcd}\,\boldsymbol{a_2} \tag{1.4}$$

where gcd is the greatest common divisor of $n + 2m$ and $2n + m$. Note that vector **T** is perpendicular to the vector $\mathbb{C}_h$ and decides the size of the unit cell of the nanotube together with $\mathbb{C}_h$. The CNRPCs are not perfect, so that their structures possess defects. In the next section, structural defects in CNRPCs are introduced and explained in detail.

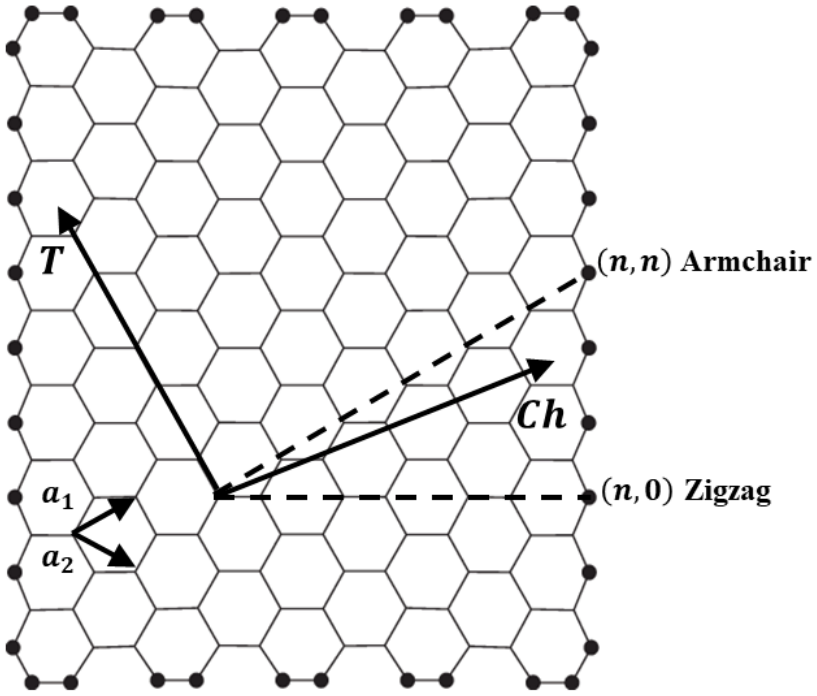

Figure 1.1. Description of carbon nanotube

1.2 Defects in Carbon-Nanotube-Reinforced-Polymer-Composites

Carbon-Nanotube-Reinforced-Polymer-Composite (CNRPC) materials are not perfect in practical engineering applications, so that their structures possess imperfections. In CNRPCs, the effects of the random arrangement and orientation of carbon nanotubes in a polymer matrix, the entanglement of fillers and kinking, are probably dominant. However, to the extent that the mechanical properties of the nanotube reinforcement influence the properties of the nanocomposite, there would be a corresponding sensitivity of the nanocomposite property to the variations in the properties of the nanotube reinforcement and interface properties. This source of randomness can be compared to the other sources mentioned before. Hence, considering the randomness due to defects in a carbon nanotube or interphase, while assuming that the carbon nanotubes are correctly aligned is duly justified in the references from the literature. Moreover, the use of stochastic modeling to analyze the effects of structural vacancies in the Single-Walled-Carbon-Nanotube (SWCN) is also of interest in manufacturing, due to the fact that vacancies are randomly distributed in the SWCN and are unavoidable in engineering applications [39-42]. In the

next sub-section, the random distribution and orientation of SWCNs inside a polymer matrix material, the entanglement of fillers, and kinking are explained, as well as structural defects in the structure of the nanocomposite material.

1.2.1 Single-Walled-Carbon-Nanotube distribution in a polymer matrix material, entanglement of fillers, and kinking

Fiber orientation and concentration play important roles on the properties of composites. At nanoscale however, analytical investigation on the influence of defects in the arrangement of Carbon Nanotubes (CNs) inside the matrix material would be very difficult. On the other hand, experimental studies would be also very expensive. Hence, modeling and simulation of nanocomposite behavior under various situations are very likely to be employed for predicting the influence of imperfect dispersion of fibers into matrix. In some investigations, innovative techniques for simulating non-homogenous dispersion of CNs, inside the polymer material matrix, as schematically illustrated in Figure 1.2(a) for orientation of CNs and in Figure 1.2(b) for orientation and distribution density of CNs, have been achieved.

In terms of orientation, the fibers can be parallel or randomly distributed with respect to each other. Different approaches have been employed to predict the elastic behavior of CN-based composites with aligned short fibers. However, relatively less attention has been paid to study randomly distributed short fiber composites. In initial investigations on the topic, simple two-dimensional [43] and three-dimensional [44] random arrangements of CN have been investigated. The general orientation distribution [45] was also studied briefly in 1989. Though, in more recent investigations for simulating various CN orientations, introducing CN-Matrix islands with various CN degrees was suggested in Ref. [46] and randomness, in terms of distribution density, was also studied in Ref. [47].

Regarding the entanglement of fillers and kinking, this defect is also important because it can cause that the structure of the nanocomposite is weak and fragile. For instance, if a repeated stress or strain is constantly applied on the nanocomposite material, it can suffer several damages, such as a crack or fracture in its structure [48].

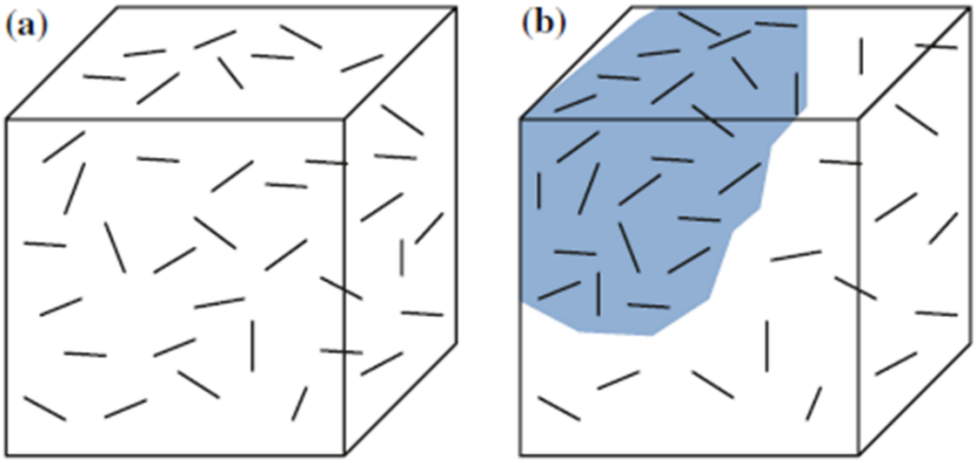

Figure 1.2. Random distribution of CN fibers inside a polymeric matrix, in terms of (a) orientation and (b) orientation and distribution density proposed in Ref. [48].

1.2.1 Structural vacancy defects in the nanocomposite material

A vacancy defect is a point defect that occurs naturally in the ideal hexagonal lattice of Carbon Nanotubes (CNs), as shown in Figure 1.3(a), in which one or several atoms are missing from the structure [48]. Vacancies, as illustrated in Figure 1.3(b) through Figure 1.3(d), may be formed during solidification process, as a result of the vibrations of atoms, or they may happen due to local rearrangement of atoms after plastic deformation, or by heavy ion bombarding and irradiation of high-energy beams [49, 50]. Once the atom is knocked out its lattice site, the dangling bonds in the vacant site rehybridize to create some new bonds [50] and the atom returns back to the surface of the structure to participate in a new bonding arrangement. Initial reconstruction of the three dangling bonds is in a way that two of the three free bonds, in a mono vacancy defect, bridge to form a strained 5-membered pentagonal ring, leaving a single dangling bond, shown in Figure 1.3(e). Finally, in Figure 1.3(f), a Stone-Wales (SW) defect is shown. In a SW defect [48], four adjacent hexagons are converted into two pentagons and two heptagons with a 90° rotation of the horizontal bond of the hexagonal structure. In the present thesis, different structural vacancies (i.e. missing carbon atoms and covalent bonds) in the Single-Walled-Carbon-Nanotube (SWCN) will be modeled and discussed to obtain the reliability of the nanocomposite material. Hence, in the next section, modeling and simulation of Carbon-Nanotube-Reinforced-Polymer-Composite materials are explained in detail.

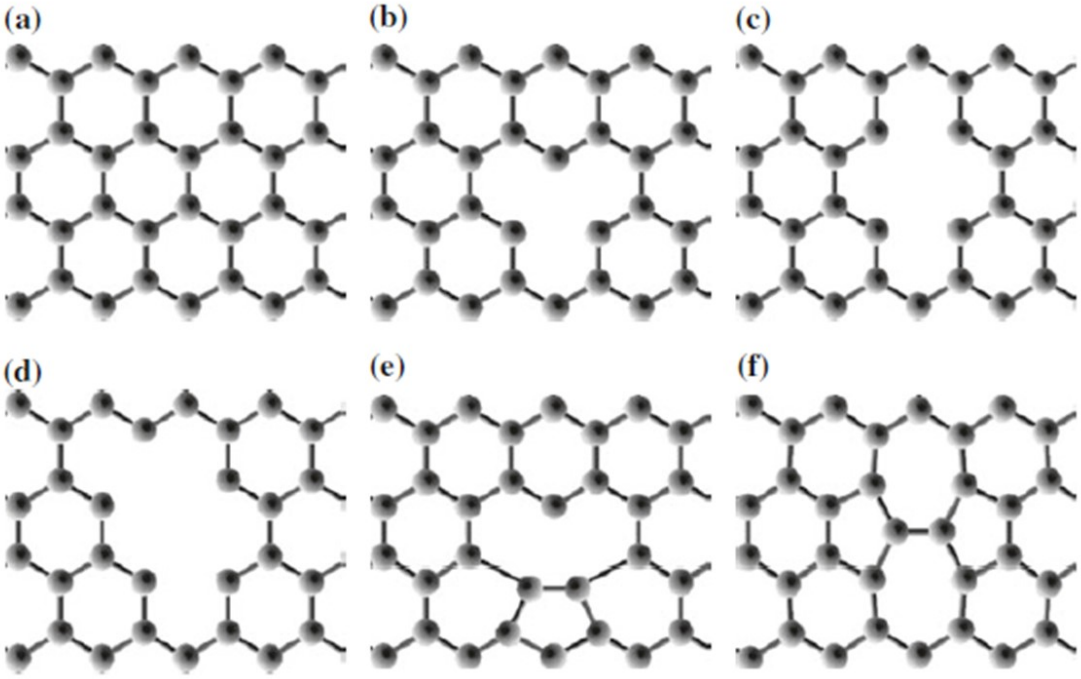

Figure 1.3. (a) Ideal structure, (b) monovacancy, (c) double-vacancy, (d) triple-vacancy, (e) reconstructed monovacancy and (f) Stone-Wales defect proposed in Ref. [48].

1.3 Modeling and simulation of Carbon-Nanotube-Reinforced-Polymer-Composites

During the last decades, the application of Carbon-Nanotube-Reinforced-Polymer-Composite (CNRPC) materials in engineering applications has become increasingly popular, mainly in the aerospace and aeronautical industries [51]. Molecular Dynamics (MD) and Molecular Mechanics (MM) computational methods are atomistic-based methods which are the most common tools used for simulation of such materials. However, fully atomistic methods are limited in length and time scales and are not capable of simulating coarse-scale systems. Recently, some authors have proposed different research lines concerned with the modeling of nanocomposite materials using a Representative Volume Element (RVE) of the material model and multiscale modeling [52]. The concept of RVE is important in the study of the mechanical response of heterogeneous materials. Mathematically, a RVE is the length scale limit relative to the microscale (or the length scale of a single heterogeneity), where the material appears uniform, and therefore, the continuum concepts are applicable. A RVE is useful for modeling the effect of

nano and mesoscale heterogeneities on the overall mechanical response of the macro-size components of the material [53]. On the other hand, multiscale modeling refers to a technique of modeling in which multiple models at different scales are used simultaneously to describe a material or mechanical system. The different models regularly focus on different scales of resolution. They sometimes consider physical laws of varying nature, for example, one from continuum mechanics and one from MD. Therefore, the need for multiscale modeling comes from the fact that the available macroscale models are not accurate enough. Moreover, the microscale models are sometimes felt to be not efficient enough and/or offer too much information to process [54].

By combining both points of view, it is possible to arrive at a reasonable compromise between accuracy and efficiency. Hence, the RVE modeling and multiscale modeling are alternative methods to model CNRPC materials as well as their large-scale response to the small-scale behavior using the features of both atomistic and continuum-based computational calculations [51, 52, 55, 56]. In such methods, atomistic modeling could be applied in localized regions where the atomistic-scale dynamics are essential, while continuum simulation could be used in the rest of the material [57-59]. The main difficulties of these types of approaches are related to boundary conditions between the models and the selection of suitable parameters for the multiscale operations [54, 56, 57]. Currently, there are multiscale approaches developed to study the mechanical behavior of different types of composite materials by defining a RVE of the composite model, such as polymers reinforced with single-walled carbon nanotubes, in problems related to elasticity [60-65], molecular dynamics [66-70], and vibration analysis [55, 71-75]. Most multiscale modeling techniques implement either coupled or atomistic-based continuum approaches to model the reinforcement of nanocomposites with carbon nanotubes. In the following, some general features of each multiscale method are explained.

1.3.1 Coupled methods

In the coupled methods, it is common to employ Molecular Dynamics (MD) for atomistic scales and Finite Element Method (FEM) for continuum scales. The coupled MD-FEM approaches can be further subdivided into hierarchical and concurrent coupling methods.

1.3.1.1 Hierarchical methods

Hierarchical multiscale methods fall under the category of coarse-graining methods where simulation results of lower spatial scales are used as input to the next level simulation step (Figure 1.4) [52]. The underlying assumption for the hierarchical multiscale methods is that the problem considered can be easily separated into processes that are ruled by different length and time scales [54, 58]. Hierarchical multiscale methods have two significant limitations [52, 54, 56]: (1) the nature of dependence of physical laws governing different length scales must be known a priori. In other words, the information received from the lower length scale simulations must be utilized in determining the parameters that govern the process at coarser length scale. Hence, the accuracy of coarse-scale parameters depends on the accuracy and reliability of lower length scale simulations, and (2) if the governing laws for different spatial scales show a strong dependence on each other, one-time exchange of information from lower length scale to higher length scale may not be enough and may require an iterative approach.

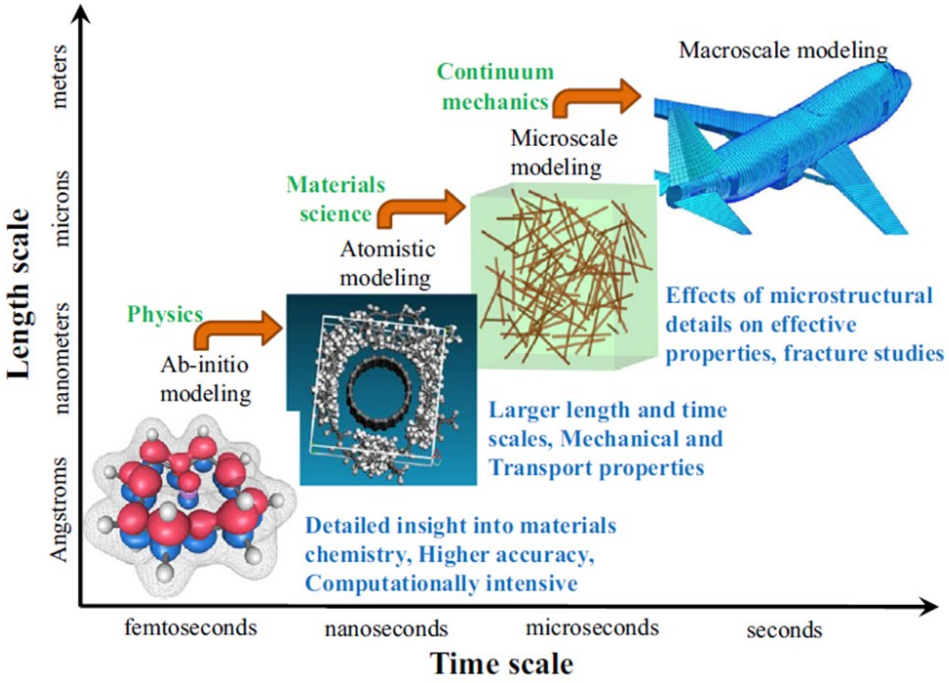

Figure 1.4. Schematic diagram of the information flow in hierarchical multiscale modeling proposed in Ref. [52].

1.3.1.2 Concurrent methods

In the concurrent multiscale methods, the information is continuously exchanged between different spatial levels and the entire simulation, involving multiple scales, is performed simultaneously (Figure 1.5) [52]. The modeling scheme does not demand any assumption about the physical phenomenon under consideration. The process evolves under the constitutive laws of each length scale and the coupling among them and a priori information about scale inter-dependence are not required. In these methods, the entire simulation is performed in one step. Therefore, a reliable and accurate handshake coupling zone is necessary to facilitate smooth exchange of data between regions representing the different spatial scales involved [54, 58]. Most concurrent multiscale techniques suffer from one or more of the following significant limitations [52, 54, 56]: (1) the FEM regions down to the atomic scale induces physical inconsistencies and numerical difficulties, (2) contamination of the solution resulting from the improper description of the transition zone, (3) the combination of different energy levels (FEM/MD) produces erroneous nonphysical effects in the transition region.

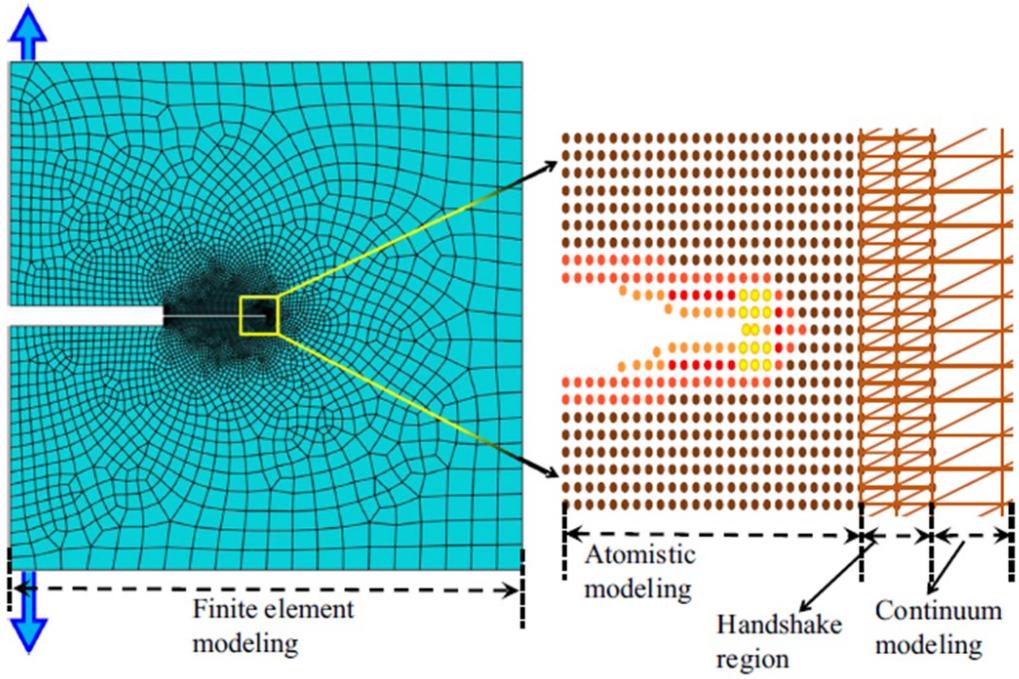

Figure 1.5. Schematic diagram for information embedment in concurrent multiscale modeling proposed in Ref. [52].

1.3.2 Atomistic-level based continuum methods

The atomistic-level based continuum technique has the advantage of describing atomic positions, their interactions, and their governing interatomic potentials in a continuum framework (Figure 1.6). The interatomic potentials (deformation measures) considered in the model capture the atomistic structure of the different phases considered. Thus, the influence of the nanophase is considered via appropriate atomistic constitutive formulations [76]. Consequently, these measures are fundamentally different from those in the classical continuum theory. The strength of atomistic-level based continuum methods lies in their ability to avoid a large number of degrees of freedom found in the discrete modeling techniques while allowing for the description of the nonlinear behavior of the components of the system [54, 58, 76]. Hence, in the next section an atomistic- level based continuum approach to model Carbon-Nanotube-Reinforced-Polymer-Composite materials is explained.

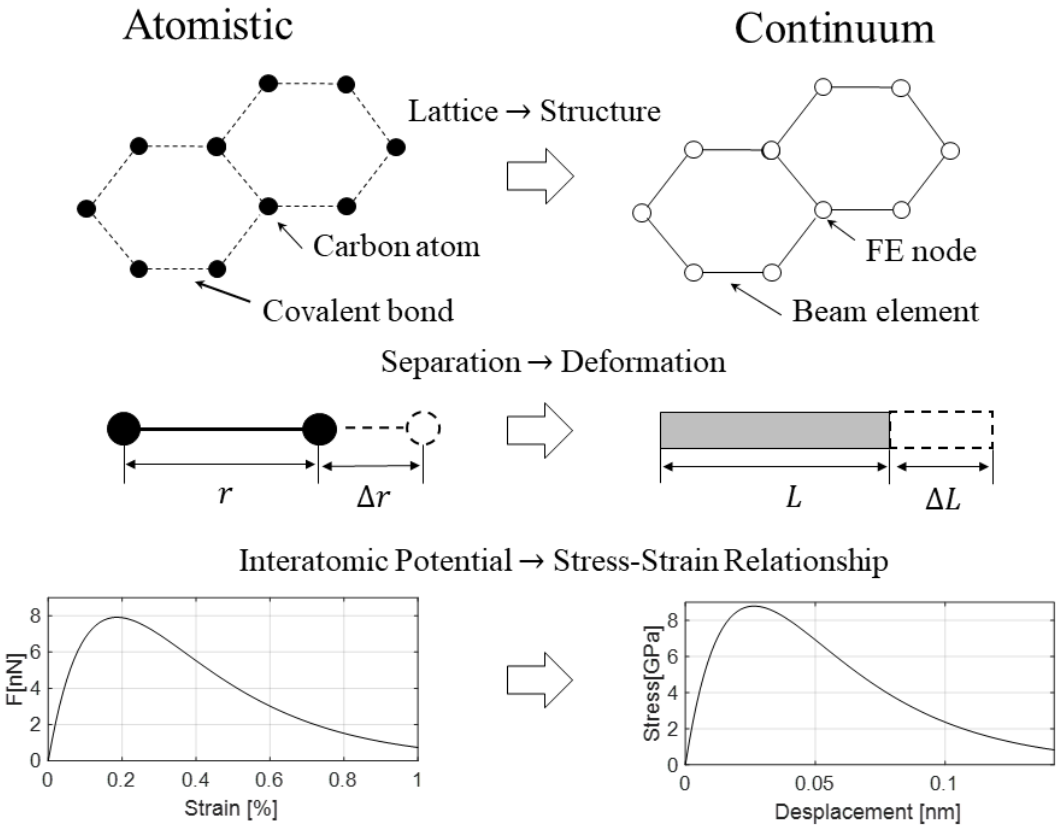

Figure 1.6. Schematic of the atomistic-based continuum modeling technique as it relates to simulating SWCN structures presented in Ref. [76].

1.4 Atomistic-level based continuum method for Carbon-Nanotube-Reinforced-Polymer Composite materials

In the development of a Representative Volume Element (RVE) for the study of nano-reinforced polymer systems, it is essential to define an atomistic-level based continuum method to consider the coupling of atomistic and continuum scales, and the nonlinearity of the atomic interactions. Hence, the description of the interatomic potentials must be included during the analysis because they provide the constitutive relations for these types of nanocomposites at the atomistic scale. The interatomic potentials also describe how the atomic interactions act under different loading conditions. The general form of an interatomic potential is expressed as follows:

$$E_{total} = E_{bonded} + E_{nonbonded} \tag{1.1}$$

where the bonded interactions E_{bonded} can be subdivided as:

$$E_{bonded} = E_s + E_b + E_I + E_t \tag{1.2}$$

where E_s corresponds to the bond stretching potential, E_b corresponds to the bond-angle bending potential, E_I corresponds to the inversion potential and E_t corresponds to the torsion potential. In the case of the nonbonded interactions $E_{nonbonded}$, these interactions are represented as follows:

$$E_{nonbonded} = E_{vdW} \tag{1.3}$$

where E_{vdW} corresponds to the van der Waals (vdW) forces based on the Lennard-Jones potential. The atomic interaction deformations can be appreciated from Figure 1.7. The interatomic potentials are nonlinear so that their nonlinearity must be taken into account in any analysis. The approaches to develop a RVE of a nano-reinforced polymer system have mostly been linear [32, 38, 77, 78]. Thus, these formulations become unable to predict the appropriate nonlinear response of the nanocomposite material.

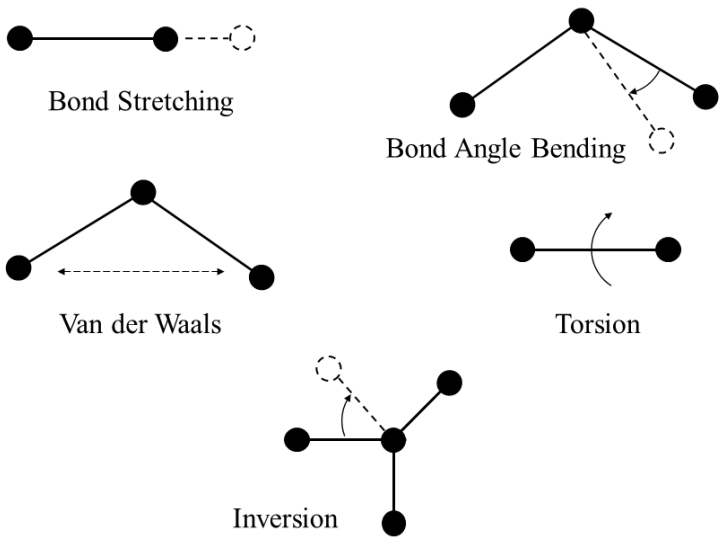

Figure 1.7. Atomic bond interactions.

In this thesis, a nonlinear atomistic-level based RVE for the study of the mechanical behavior of a Carbon-Nanotube-Reinforced-Polymer-Composite (CNRPC) material is developed. The RVE of the CNRPC material consists of a Single-Walled-Carbon-Nanotube (SWCN), a surrounding polymer matrix, and a SWCN–polymer interface region, as depicted in Figure 1.7. Due to the nanoscale involved in simulating SWCN structures, a continuum-atomistic description is incorporated. The Carbon-Carbon (C-C) covalent bonds in the SWCN structure are described using the Morse potential [79]. The nanostructure of the SWCN is also modeled using a suitable shell theory [80, 81]. In the case of the polymer matrix material, solid finite elements are used to describe its mechanical behavior in a continuum domain. The nonlinear response of the polymer matrix is modeled using the Mooney-Rivlin strain energy [82]. In the interface region, the atomic van der Waals (vdW) interactions between the atoms in the SWCN and the atoms in the inner surface of the polymer matrix are described using the Lennard-Jones potential [83]. This description implies the assumption of a nonbonded interfacial region. All the components used in the development of the RVE of the nanocomposite material are represented in Figure 1.8(a) and 1.8(b). As it was mentioned in section 1.2, Carbon-Nanotube-Reinforced-Polymer-Composite (CNRPC) materials are not perfect. Hence, it is important to obtain the reliability and hazard associated with their material properties. In the next section, a reliability-based probabilistic approach is explained to quantify the risk and safety of CNRPC materials in practical applications.

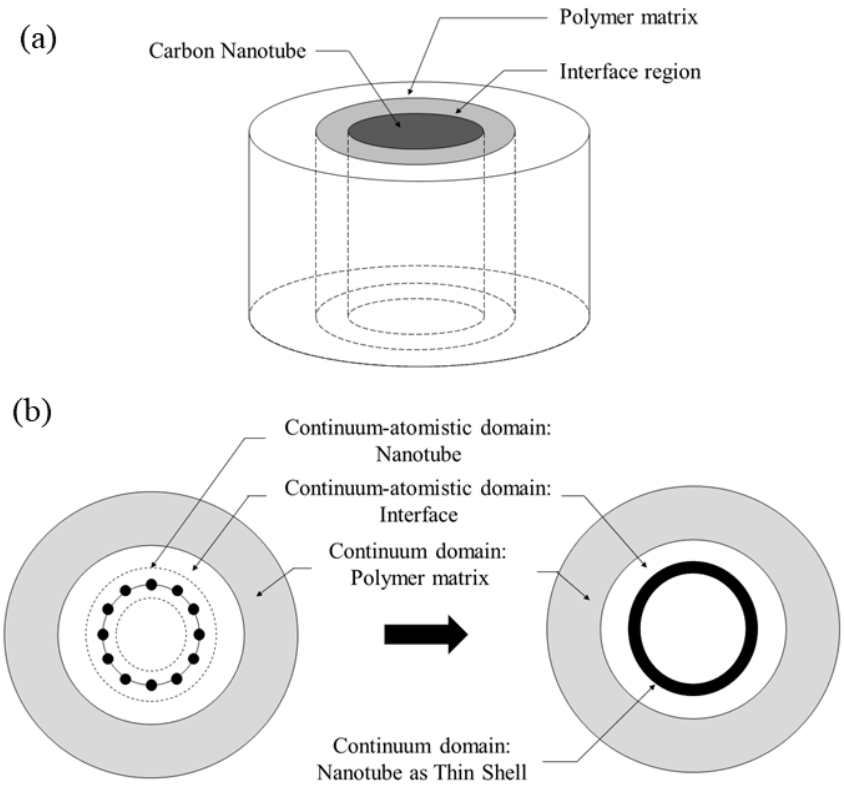

Figure 1.8. (a) Representative Volume Element (RVE) of the Carbon-Nanotube-Reinforced-Polymer-Composite (CNRPC) material and (b) Components used in the development of the RVE.

1.5 Reliability-based probabilistic approach

Reliability is a time-dependent characteristic, which provides the probability that a product or service will operate properly for a specified period of time (design life) under the design operating conditions without failure [84]. Hence, reliability can be defined as the probability that a unit performs its expected mission over an intended time under some specified conditions of use. The concept of reliability usually consists of four basic parts [85]: probability, adequate performance, time and operating conditions. Probability provides the numerical input for the assessment of the reliability of a component or system, and also the first index of system adequacy. On the other hand, adequate performance, time and operating conditions provide information about all engineering parameters. In engineering applications, the concept of reliability is applied to components and structures to determine the probability of a component or a system performing its

function (purpose) adequately for the period of time intended under the operating conditions encountered. In this thesis, the reliability concept is applied to the Representative Volume Element (RVE) of the nanocomposite model at the nano-level through the stress-strength model and prediction approach to determine if the nanocomposite material has the capacity to tolerate damage. The strength is considered as the capacity of the nanocomposite material to tolerate damage, while the stress is regarded as the challenge that the nanocomposite material must tolerate. The stress-strength model and prediction approach is based on the challenge-capacity model, which describes that a mechanical system fails when the capacity of the system is less than the challenge that the system must face, where both capacity and challenge are random variables [53]. The reliability of the nanocomposite material is determined as a function of the mechanical properties of the RVE of the nanocomposite material instead of a certain period of time. In this thesis, the concept of hazard is also applied because it provides more inside information about the material system than the reliability analysis and quantifies the risk associated with the material system [86]. In practical applications, the nanocomposite material is not perfect, and it possesses structural defects. Hence, to perform the reliability analysis, it is necessary to apply the Monte Carlo Simulation (MCS) technique to simulate and model the structural defects in the nanocomposite material [84]. MCS technique is a computerized mathematical technique that can be used to account for risk in quantitative analysis and decision making.

The results of the probabilistic analysis using the MCS technique provide information about different material properties of the nanocomposite material, which are considered as random variables. The probability distributions of the random variables can be calculated using the assumptions of Weibull and Gaussian distributions [87]. However, a more accurate and efficient approach such as the Maximum Entropy Method [88] should be used for estimating the probability density function (pdf) of each random variable. The Maximum Entropy Method (MEM) was suggested in Ref. [89], as a rational approach for estimating the pdf of a random variable under specified moment constraints when little information is available on the data. The approach results in the least biased probability distribution among all possible distributions that are consistent with available data. The MEM is widely recognized as an efficient stochastic modeling tool especially when a small number of samples are available, which has been successfully applied to many problems and in a wide variety of fields. Therefore, in the next sub-section, a brief description about the MCS technique and the MEM are provided.

1.5.1 Monte Carlo Simulation technique

Monte Carlo Simulation (MCS) technique is a computational approach that relies on repeated random sampling to obtain numerical results [84]. The underlying concept is to use randomness to solve problems that might be deterministic in principle. Hence, the MCS technique has six essential elements [84]: (1) defining the problem in terms of all the random variables; (2) quantifying the probabilistic characteristics of all the random variables in terms of their probability density functions (pdfs) and the corresponding parameters; (3) generating the values of these random variables; (4) evaluating the problem deterministically for each set of realizations of all the random variables, that is, numerical experimentation; (5) extracting probabilistic information from N such realizations; and (6) determining the accuracy and efficiency of the simulation. This technique is mainly used in three types of problems: optimization, numerical integration, and generating random data from a probability distribution [85].

In this thesis, the MCS technique will be utilized to determine the probability distributions of the material properties of the nanocomposite material, considering different structural problems in the material model. A general procedure of the MCS technique is provided as follows [85]:

1. Determine the function relating the independent random variables s to the dependent random variable Y, or relating the inputs to the output as

$$Y = f(s_1, s_2 \cdots s_n) \tag{1.4}$$

2. Determine the distribution of each independent variable, or input, or

$$f(s_1), f(s_2) \cdots f(s_n) \tag{1.5}$$

or the pdfs of each component.

3. Determine the cumulative distribution function (cdf) of each variable, or input, or $F(s_i)$, where $i = 1, 2, \cdots n$.

4. Generate a random number u, uniformly distributed between zero and one, for each random variable. The uniform distribution function is given by

$$f(u) = \begin{cases} 1 & 0 \leq u \leq 1 \\ 0 & elsewhere \end{cases} \tag{1.6}$$

5. Obtain a set of randomly chosen values for each random variable from

$$u_i = \int_{-\infty}^{s_i} f(s_i) ds \tag{1.7}$$

where s_i represents the random variable involved.

6. Repeat many times, for instance, 10000 or more, preferably.

7. Substitute the values of each set; i.e., $s_{1,1};\ s_{2,1}\ \cdots s_{n,1}$ into the output function, and determine a random value of the output, or

$$\begin{aligned} Y_1 &= f\left(s_{1,1};\ s_{2,1} \cdots s_{n,1}\right) \\ &\vdots \\ Y_N &= f\left(s_{1,N};\ s_{2,1} \cdots s_{n,N}\right) \end{aligned} \tag{1.8}$$

8. Arrange Y, or s, values in ascending value or order, or as $Y_1 \leq Y_2 \leq Y_N$, where $N = 10000$ or more preferably.

9. Calculate the four moments from the Monte Carlo values of the output, or of s, if it is necessary.

In the next sub-section, the Maximum Entropy Method is explained that seeks and obtains a more realistic distribution of each material property of the nanocomposite material.

1.5.2 Maximum Entropy Method

The principle of Maximum Entropy (ME) [88] can represent stochastic information in data using a probability density function (pdf) that depends on its moment constraints. For a random variable x, whereby its realization x takes on all values over an integral of real numbers with unique pdf $f(x)$, the Entropy SE can be defined as [86]:

$$SE(x) = -\int_{\mathbb{R}} f(x) \ln f(x) dx \tag{1.9}$$

In the moment-based ME method, the Entropy SE is maximized subject to:

$$\int_{\mathbb{R}} x^i f(x)\, dx = m_i \tag{1.10}$$

where m_i are the constrained moments, $(i = 0, \dots, n)$ and n is the number of moments. Using the method of Lagrange multipliers [90], the optimization problem with n+1 constraints is then reduced to the optimization of the unconstrained function:

$$\mathcal{L}(\boldsymbol{\lambda}) = \int_{\mathbb{R}} exp\left(\sum_{i=0}^{n} \lambda_i x^i\right) dx - \sum_{i=0}^{n} \lambda_i x^i \tag{1.11}$$

where $\boldsymbol{\lambda} = \{\lambda_i\}$ for $i = \{0, \dots, n\}$ are the Lagrange multipliers for its corresponding $\boldsymbol{x} = \{x^i\}$. Equation (1.11) has a solution for $f(x)$ as follows [88]:

$$f(x) = exp\left(\sum_{i=0}^{n} \lambda_i x^i\right) \tag{1.12}$$

All the ME distributions are achieved when $\partial\mathcal{L}/\partial\boldsymbol{\lambda} = 0$, which satisfies the moment constraints in Equation (1.10) and takes the general form of $f(x)$ in Equation (1.12). Note that since $x^0 = 1$ (for $i = 0$) in Equation (1.12), λ_0 can be determined by using the following expression:

$$\lambda_0 = -ln \int_{\mathbb{R}} exp\left(\sum_{i=0}^{n} \lambda_i x^i\right) dx \tag{1.13}$$

In the next section, a literature review on Carbon-Nanotube-Reinforced-Polymer-Composite materials is provided, including references about RVE modeling in static and dynamic responses, and considering defects in the nanocomposite material.

1.6 Literature review on Carbon-Nanotube-Reinforced-Polymer-Composites

Both coupled and atomistic-level based continuum multiscale methods have been applied to simulate Carbon-Nanotube-Reinforced-Polymer-Composite (CNRPC) materials [51, 52]. Generally, the atomistic modeling is incorporated at lower length scales as the first step in these multiscale schemes to study the primary response fields (displacement, vibrational frequency, etc.) and energetics (potential and kinetic energies), while the continuum modeling is incorporated at higher length scales [51, 52, 76]. A suitable selection of boundary conditions and design parameters would make multiscale modeling an efficient technique to solve complex problems in elasticity, molecular dynamics, and vibration analysis.

It is a standard practice to use a Representative Volume Element (RVE) in the simulation and modeling of any type of composites (that are metal-based, ceramic-based and polymer-based) [53]. For studying the static response of polymer matrices with Single-Walled-Carbon-Nanotubes (SWCNs) as reinforcement, Liu and Chen [77] evaluated the effective properties of SWCN-based composites through the development of a RVE based entirely on continuum mechanics. However, their RVE did not include a model for the interface region, nor did it include an atomistic description. Hu et al. [32] developed a RVE that included the SWCN–polymer interface region. However, the interface was simulated using solid FE elements with linear material properties. Tserpes et al. [30] constructed their RVE by representing the SWCN as a hollow beam element embedded in a solid polymer matrix. However, their work did not include an interface region in their RVE. Li and Chou [38, 91] constructed their RVE using a space frame structure for the SWCN, solid elements for the polymer matrix, and truss rods to represent the interface region. The SWCN and the polymer matrix presented a linear behavior, while the interface surface presented a nonlinear response. Shokrieh and Rafiee [78] extended the model of Li and Chou [38, 91] to incorporate a nonlinear interface region based on the Lennard–Jones potential. However, their model did not include a nonlinear description of the SWCN and the surrounding polymer. Georgantzinos et al. [92] proposed a modification of the rule of mixtures that can consider the interfacial effects between the reinforcement consisting from a SWCN and the polymer matrix, to predict the effective Young's modulus of the nanocomposite simulated as a RVE. They used two-noded interfacial joint elements of variable stiffness for modeling the interface region. However, its interface region had a linear behavior as well as the SWCN.

Later, Georgantzinos et al. [79] included the nonlinear behavior of the SWCN modeled by using the Morse potential, but the interface region still had a linear behavior. Recently, Spanos et al. [93] extended the work conducted in Ref. [79] considering a nonlinear response in the interfacial elements for the interface region, but the SWCN was modeled with linear material properties. Mohammadpour et al. [94] presented a RVE of a polymer matrix reinforced with a SWCN, replacing the SWCN with a solid model constructed from nonlinear elements in the shape of a hollow cylinder and integrating the mechanical properties into solid elements. Despite modeling the interface region with contact elements saving computing efforts, this model cannot study other types of mechanical behavior as bending, buckling and torsion. Later, Wernik and Meguid [76] proposed a nonlinear RVE to investigate the useful mechanical properties of a nano-reinforced polymer, including nonlinear effects on the SWCN and the interface region.

Later, Ionita [95] conducted atomistic and mesoscale simulations to estimate the effects of the diameter and weight fraction of SWCNs on the mechanical behavior and glass transition temperature of SWCN-reinforced epoxy resin composites. Spanos et al. [43] extended the work of Ref. [79] to study the stress transfer between the SWCN and the polymer matrix. The interfacial effects between the two materials were simulated by stiffness variations defining a heterogeneous region. Other works, such as that of Ghorbanpour et al. [96], conducted the static stress analysis of the RVE under non-axisymmetric thermo-mechanical loads and uniform electromagnetic fields. Their results showed that the fatigue life of the composite material was dependent on magnetic intensity, angle orientation and volume fraction of SWCN.

On the other hand, Ghasemi et al. [97] studied the effects of carbon nanofibers on thermo-mechanical properties of a RVE and their impact on residual stress. Jia et al. [98] proposed to analyze the stress transfer properties of a RVE with a SWCN and a Double-Walled-Carbon-Nanotube (DWCN) at low temperatures environments. The results were obtained for both reinforcements (SWCN and DWCN). However, a perfect bonding was assumed between the polymer matrix and the SWCN and the DWCN. Later, Kyu et al. [99] determined the mechanical behavior of a RVE made with aluminum and a SWCN. In this work, the interface region between both the materials was modeled using van del Waals interactions.

Recently, Garcia-Macias et al. [100] developed a RVE to study its effective elastic moduli, including an atomistic-based computational model and a micromechanics approach at the nano and micro-scales, respectively. The covalent bonds of the SWCN were modeled as Timoshenko

beams. Later, Papadopoulos and Impraimakis [101] proposed a hierarchical multiscale approach in order to evaluate the nonlinear constitutive behavior of concrete reinforced with SWCNs. Other authors, such as Sun et al. [102], presented a multiscale computational analysis based on RVE modeling and molecular dynamics simulations to investigate the microscopic failure mechanisms of unidirectional carbon fiber reinforced polymer composites, while Chevalier et al. [103] proposed a multiscale approach to characterize and to model the transverse compression response of a unidirectional carbon fiber reinforced epoxy.

Despite most of the works done on polymer matrices with SWCNs as reinforcement are on static response, there are very few works that study the dynamic response of this type of nanocomposite material. Latibari et al. [104] extended the model of [38, 91], including a nonlinear interfacial region based on the Lennard–Jones potential to calculate the damping ratio of the nanocomposite material by evaluating its dissipation energy. However, their model did not incorporate a nonlinear description of the SWCN. Later, Jamal-Omidi et al. [105] analyzed a SWCN embedded in volume element using 3D finite element and analytical methods to compute its natural frequencies with different aspect ratios. Shokrieh et al. [106] predicted the viscoelastic properties for an embedded SWCN in a polymer matrix by using a time-dependent formulation of the interface region. The SWCN was modeled using space frame beam, the interface region was modeled using non-linear springs based on van der Waals interactions and the polymer matrix using solid continuum elements. Later, Gajbhiye and Singh [107] proposed a RVE for a polypropylene matrix along with different percentages of SWCNs to evaluate its natural frequencies, rate-dependent characteristics and damping properties. The covalent bond of the nanotube was modeled using Tersoff–Brenner potential, and the interaction between the nanotube and the polymer matrix was modeled using Lennard–Jones potential represented by nonlinear spring elements.

In the case of nano-reinforced polymer systems with structural imperfections, such as vacancy defects, Shokrieh and Rafiee [41] developed a stochastic multiscale modeling technique to estimate the mechanical properties of carbon nanotube-reinforced polymers considering valid parameters at nano, micro, meso, and macro-scales. Later, Davoudabadi and Farahani [108] investigated the influence of different vacancy defects on Young's modulus of a SWCN - reinforcement polymer composite in the axial direction by using a structural model in commercial software ANSYS®. In another work, Ghasemi et al. [39] studied the uncertainties propagation and

their effects on the reliability of polymeric nanocomposite continuum structures considering material, structural, and modeling uncertainties. They considered the length, waviness, agglomeration, orientation, and dispersion of the SWCNs as random variables. Yuan and Lu [109] proposed a geometric generation algorithm to produce a 3D finite element model of a polymeric composite with randomly dispersed and wavy SWCNs to analyze its elastic-plastic properties, as well as Joshi et al. [110], who proposed a multiscale 3D RVE approach for modeling the elastic behavior of carbon nanotube reinforced composites with vacancy defects. Other authors, such as Ju et al. [42], investigated the interfacial strengths between polypropylene-carbon fiber composites through experimental observation as well as using molecular dynamics simulation to determine its optimal chemical functionalization groups, while Rafiee and Mahdavi [40] presented a theoretical characterization of the interaction between a SWCN and a surrounding polymer using molecular dynamics simulation. They conducted a stochastic analysis treating numbers of established covalent bonds between the SWCN and the polymer material, and their positions as random parameters.

Later, Chawla et al. [111] explored the effect of vacancy defects on SWCN reinforced polypropylene composites using molecular dynamics simulation and comparing the influence of a perfect and an imperfect SWCN as reinforcement. Ozden-Yenigun et al. [112] studied the crosslinking route and interfacial interactions for achieving superior properties in a SWCN-reinforced epoxy by using multiscale modeling. Other authors, such as Zhu et al. [113], presented a probabilistic multiscale approach to model the random spatial distribution of local elastic properties arising from the different waviness and orientation of SWCN fillers within a 3D microscale continuum RVE of a SWCN-reinforced polymer matrix. Recently, Jeong et al. [114] proposed a 3D stochastic computational homogenization model for SWCN-epoxy matrix composites. They found that stochastic waviness, agglomeration, and orientation of SWCN fillers caused random spatial variations of the elasticity tensor of the SWCN-epoxy matrix within a microscale RVE, resulting in probabilistic changes of the homogenized stiffness of the RVE. In the next section, the research motivation of this thesis that focuses on Carbon-Nanotube-Reinforced-Polymer-Composite materials will be explained in detail.

1.7 Research Motivation

During the last few decades the application of Carbon-Nanotube-Reinforced-Polymer-Composite (CNRPC) materials, in engineering applications, has become increasingly popular, particularly in the aerospace and aeronautical industries. However, further and more comprehensive studies are still required to be carried out, especially on their dynamic response and on the reliability and hazard (related to risk) corresponding to their static and dynamic responses. Experimental investigations for this purpose have limitations and, in most cases, appropriate experimental work could not be carried out. Therefore, the computational modeling of a Representative Volume Element (RVE) of the CNRPC material and simulation encompassing multiscale material behavior provide an alternate approach to study the material behavior of this type of nanocomposite material. The RVE modeling of the CNRPC material allows to study the mechanical behavior of the nanocomposite material by considering the following features: (1) the microstructure, global mechanical properties such as elastic modulus, and micro-mechanical response of the RVE are statistically similar to those of a macro-size specimen of the same nanocomposite material, and (2) the micro-mechanical response of the RVE is unique for a given loading direction, although different loading directions may yield different micro-mechanical responses due to non-uniform nature of the micro-structure. Nevertheless, in practical applications, CNRPC materials are not perfect and their structures possess defects.

Hence, the primary motivation is to characterize the mechanical behavior of an imperfect CNRPC material through probabilistic modeling and to calculate its reliability and hazard so as to quantify the risk and safety conditions in practical applications. For this purpose, a reliability-based probabilistic approach should be used to be able to characterize the structural defects of the CNRPC material by using the Monte Carlo Simulation (MCS) technique, and to obtain a more realistic distributions of the reliability and hazard functions by using the Maximum Entropy Method (MEM). Hence, in the next section, the problem statement of this thesis is presented.

1.8 Problem Statement

Experimental investigations to study the material behavior of Carbon-Nanotube-Reinforced-Polymer-Composite (CNRPC) materials have limitations. Hence, the computational modeling of the Representative Volume Element (RVE) of the nanocomposite material and simulation

encompassing multiscale material behavior provide an alternate approach to study the mechanical properties of such materials. The material properties of CNRPC materials have been studied and analyzed in many works in the literature. In these works, the rule of mixtures provides an approach to predict the material properties of a CNRPC material made up of continuous and unidirectional fibers, based on the weighted contributions from the fiber filler and the matrix. According to the rule of mixtures, the properties of composite materials that can be calculated are density, Young's modulus, coefficient of thermal expansion, shear modulus and Poisson's ratio. However, material properties such as ultimate strength, loss factor, dissipation energy, structural damping coefficient, and viscous damping ratio can not be calculated following this approach.

Moreover, there are a few studies that analyzed and characterized the dynamic material properties of CNRPC materials. However, there has been a lack of research on the reliability and hazard evaluation of the mechanical properties of CNRPC materials, considering imperfections in their structure. Therefore, a CNRPC material model is developed in this thesis to study and to characterize the mechanical behavior of this type of nanocomposite materials, by using a 3D multiscale finite element model of the RVE of the nanocomposite material. Moreover, the reliability and hazard evaluation of the CNRPC material is proposed and used as a characterization approach for nanocomposite materials. The RVE represents the smallest material volume element of the CNRPC material with discontinuous carbon nanotubes (as is shown in Figure 1.9). The RVE of the CNRPC material is considered and analyzed in this thesis work. Figure 1.10 shows the methodology to build the computational model of the RVE of the CNRPC material. As it was mentioned in section 1.7, the Single-Walled-Carbon-Nanotube (SWCN) is first modeled as a space frame by using the Morse potential and then as a thin shell based on a suitable shell theory. The polymer matrix material is simulated by using the Mooney-Rivlin strain energy to calculate its non-linear response, while the interface region between the SWCN and the polymer matrix is modeled via van der Waals (vdW) links. In the next section, the scope and objectives of this thesis are presented and explained in detail.

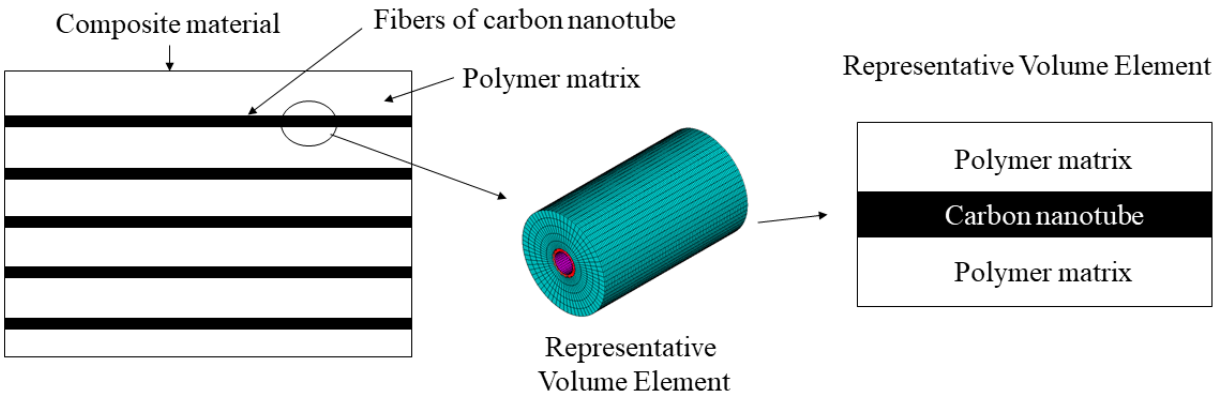

Figure 1.9. Representative Volume Element (RVE) of the nanocomposite material.

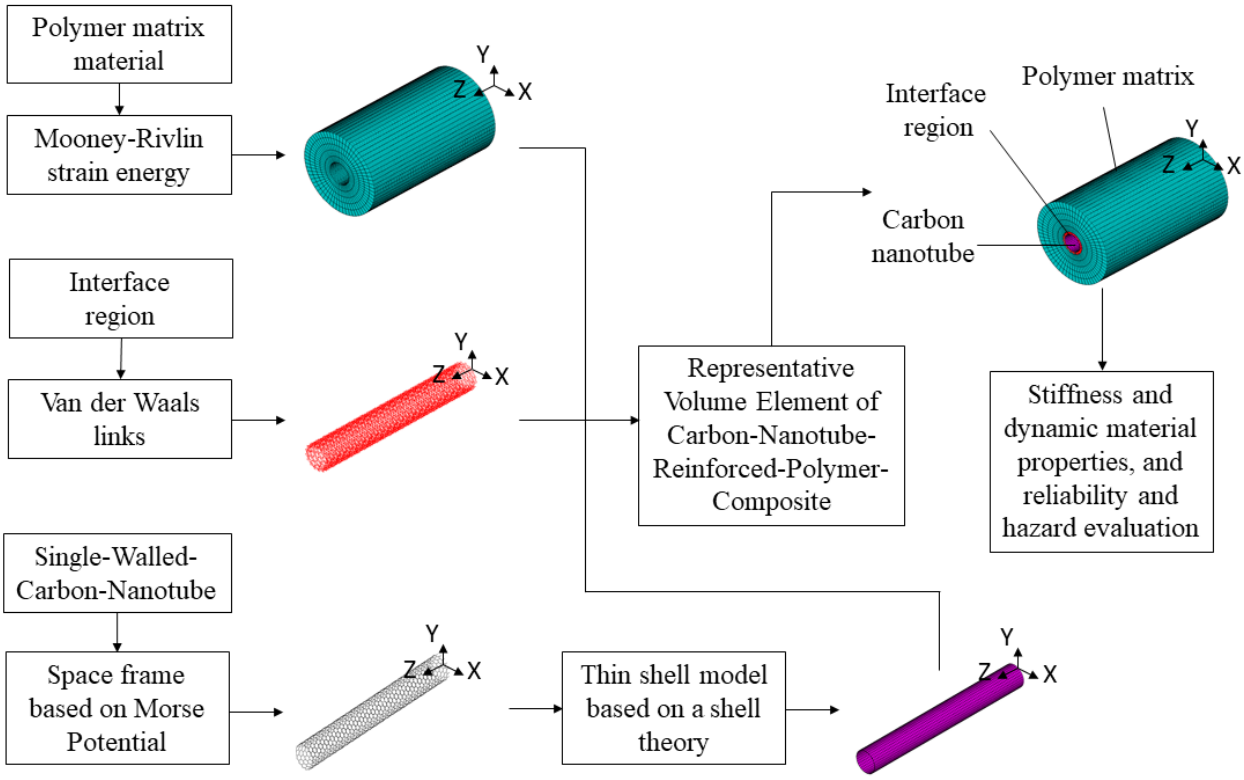

Figure 1.10. Methodology used to develop the CNRPC material model.

1.9 Scope and objectives of the thesis

1.9.1 Scope of the thesis

There are techniques based on multiscale modeling to solve different types of engineering problems in nanocomposite materials. However, further studies still need to be carried out to study and to characterize their mechanical properties. Therefore, the scope of this thesis is to study the stiffness and dynamic responses of a Carbon-Nanotube-Reinforced-Polymer-Composite (CNRPC) material by developing and using a 3D multiscale finite element model of the Representative Volume Element (RVE) of the nanocomposite material. The stiffness response is studied in terms of its stress-strain behavior, while the dynamic response in terms of its natural frequencies, steady-state response and damping properties. The reliability and hazard of the CNRPC material are also determined based on its stiffness response and natural frequencies as a characterization approach by using the challenge-capacity model. Hence, a computational model consisting of a Single-Walled-Carbon-Nanotube (SWCN), an interface region and the polymer matrix material has been constructed for this purpose. The multiscale modeling is performed in terms of using different theories and corresponding strain energies to model the individual parts of the RVE of the CNRPC material. The macroscale continuum mechanics is used for the polymer matrix, the mesoscale mechanics is used for the interface region, and the nanoscale-level atomistic mechanics is used for the SWCN. The SWCN is modeled as a space frame structure by using the Morse potential and also as a thin shell based on a suitable shell theory. The polymer matrix is modeled with the Mooney-Rivlin strain energy to calculate its non-linear response and the interface region is modeled via van der Waals links based on the Lennard-Jones potential. The CNRPC material is also called as Carbon-Nanotube-Reinforced-Polymer (CNRP) material in certain chapters because some journals preferred that kind of wording. In the next section, a breakdown of the objectives of this thesis is provided.

1.9.2 Objectives of the research work

The objectives of this research work are listed below:

1. To develop a 3D multiscale finite element model of the Representative Volume Element (RVE) of the Carbon-Nanotube-Reinforced-Polymer-Composite (CNRPC) material to conduct a parametric study to determine its static and dynamic responses. The static analysis is carried out

in terms of its stiffness response, while the dynamic analysis is carried out in terms of its modal and steady-state responses and damping properties. The RVE of the CNRPC material considers different volume fractions of SWCNs and a perfect structure for the Single-Walled-Carbon-Nanotube (SWCN) and van der Waals (vdW) links. Moreover, the results of its viscous and structural damping mechanisms are compared with the experimental data available from the literature.

2. To develop an advanced probabilistic analysis to determine the static and dynamic reliabilities of the CNRPC material for achieving reliable and safe design, considering structural defects in the nanocomposite material that are unavoidable in practical engineering applications. The longitudinal modulus and ultimate longitudinal strength of the CNRPC material are used to quantify the risk in terms of the static reliability and static hazard. Moreover, the characterization of dynamic reliability and dynamic hazard is based on the modal parameters of the CNRPC material. For this purpose, the frequency sweep of the excitation and the nearness to resonance of the material system are considered as a viable characterization approach.

The content of this thesis can be appreciated from Figure 1.11. A flowchart is used to show the process of developing the CNRPC material model and each study performed on it to determine its static and dynamic responses, considering a perfect SWCN and a perfect interface region, and then an imperfect SWCN and an imperfect interface region.

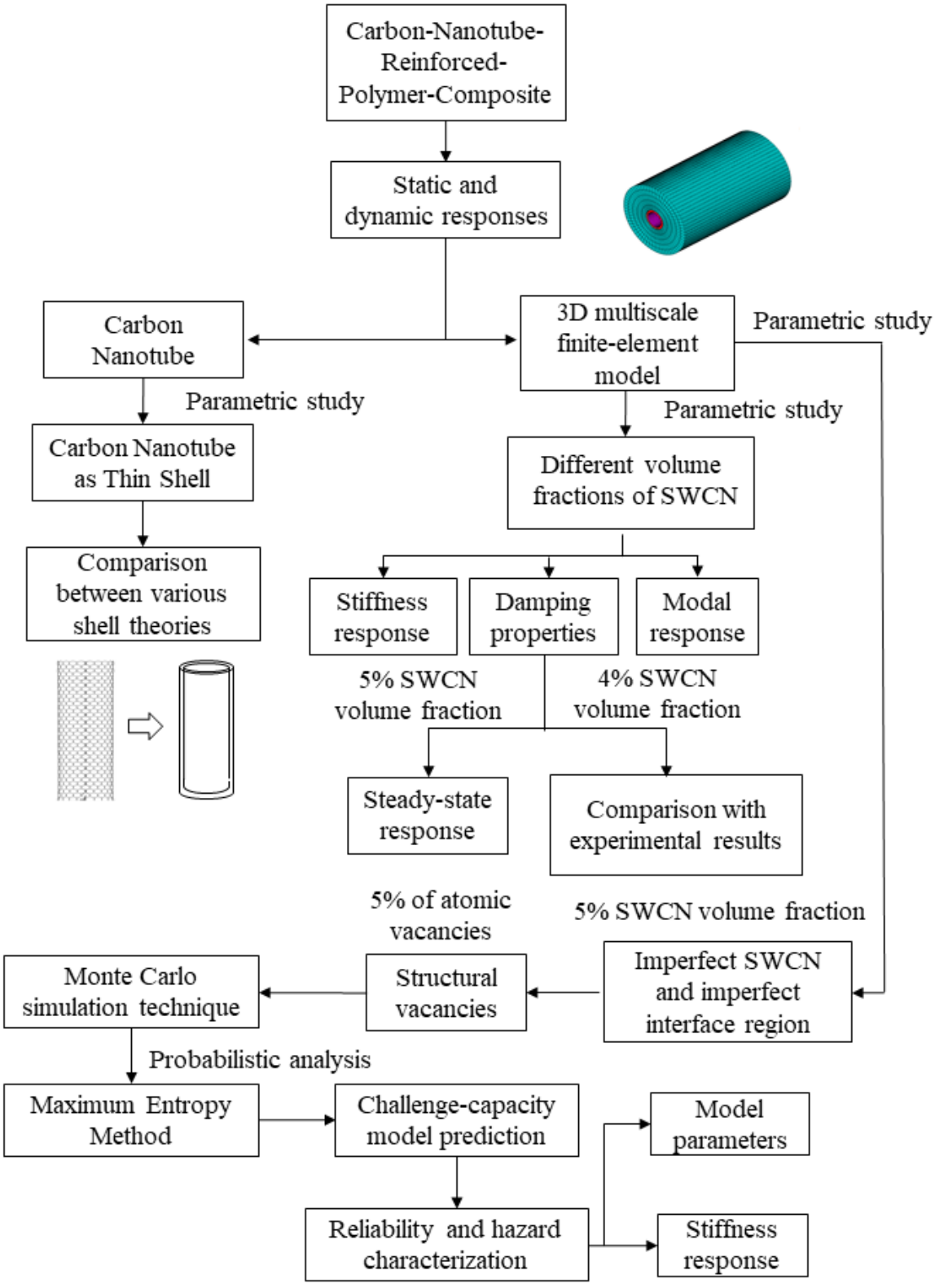

Figure 1.11. Flowchart of the contents of the thesis.

1.10 Overview of the Thesis

This thesis is a manuscript-based thesis that is organized into seven chapters. Moreover, there are forewords that provide expository transitions between the different journal papers. The chapters of this thesis are organized as in the following:

Chapter 1 provides a brief introduction to Carbon-Nanotube-Reinforced-Polymer-Composite (CNRPC) materials and their applications. This chapter also presents a brief overview of the different modeling and simulation techniques introduced in the literature to model CNRPC materials, and the overview of the atomistic-level based continuum multiscale technique chosen as the simulation tool of the Representative Volume Element (RVE) of the Carbon-Nanotube-Reinforced-Polymer-Composite (CNRPC) material. This chapters also provides a brief description of reliability-based probabilistic approach. It also includes a literature review on CNRPC material considering the definition of a RVE of the nanocomposite material. It also covers the research motivation, scope and objectives, and an overview of the thesis.

Chapter 2 focuses on the first step of the thesis: modeling the Single-Walled-Carbon-Nanotube (SWCN) as a space frame structure and as a thin shell. The SWCN is modeled as a space frame structure by using the Morse potential and as a thin circular shell by using a shell theory. A comparison between various shell theories is also provided to determine which theory is more suitable to model the SWCN based on its aspect ratio and chirality. Stress-strain behavior and modal and steady-state responses of different types of SWCNs are analyzed in this chapter.

Chapter 3 describes the development of a 3D multiscale finite element model of the Representative Volume Element (RVE) of the Carbon-Nanotube-Reinforced-Polymer-Composite (CNRPC) material to determine its stiffness response, in terms of its stress-strain behavior, and its dynamic response, in terms of its modal and steady-state responses and damping properties. A computational model consisting of a polymer matrix, an SWCN and interface region between the SWCN and the polymer matrix is constructed for this purpose.

Chapter 4 describes a parametric study of the RVE of CNRPC with 4% volume fraction of SWCN, to compare its viscous and structural damping mechanisms with the experimental data available from the literature.

Chapter 5 presents a parametric study to determine the static reliability and static hazard of the CNRPC material, considering a RVE with an imperfect SWCN and imperfect interface region. The imperfect SWCN possesses structural vacancies, which are characterized by using the Monte Carlo Simulation (MCS) technique. The static reliability and static hazard functions of the CNRPC material are obtained using the Maximum Entropy Method (MEM) along with Gaussian and Weibull distributions based on stress-strength (challenge-capacity) modeling and prediction. The ultimate longitudinal strength of CNRPC is considered as the capacity of the system and an applied stress as the challenge that the CNRPC material must tolerate.

Chapter 6 presents a parametric study to determine the dynamic reliability and dynamic hazard of the CNRPC material, considering a RVE with an imperfect SWCN and imperfect interface region. The imperfect SWCN possesses structural vacancies, which are characterized by using the MCS technique. The dynamic reliability and dynamic hazard characterization are performed by using the challenge-capacity modeling and prediction based on the modal parameters of the CNRPC material. The consideration of the frequency sweep of the excitation and the nearness to resonance of the material system is used as a basis for the characterization of dynamic reliability and dynamic hazard. The dynamic reliability and dynamic hazard functions are obtained using the MEM.

Chapter 7 provides conclusions and contributions of this thesis and makes recommendations for future studies on the CNRPC material.

Chapter 2. Dynamic response of Single-Walled-Carbon-Nanotubes based on various shell theories

Foreword

This chapter contains the journal paper: J. A. Palacios and R. Ganesan, "Dynamic response of single-walled carbon nanotubes based on various shell theories," Journal of Reinforced Plastics and Composites, vol. 38, no. 9, pp. 413-425, 2019.

In this chapter, different studies are performed, in terms of the stiffness response, modal analysis and steady-state response of Single-Walled Carbon Nanotubes (SWCNs) by using a 3D finite-element model of the SWCN, under different types of boundary conditions, to provide more results in this field. The SWCN is modeled as a space frame structure by using the Morse potential and as a thin shell model based on various shell theories. A parametric study on chirality effects and aspect ratio is also conducted to determine which shell theory is more suitable to model the mechanical behavior of SWCNs.

2. Dynamic response of Single-Walled-Carbon-Nanotubes based on various shell theories

2.1 Abstract

Carbon nanotubes are used in several engineering applications because of their superior mechanical properties. Scientific works still need to be carried out, especially on their dynamic response. These studies mainly focus on modal analysis, considering zigzag and armchair nanotubes, and sometimes, varying chirality. However, these works do not present any results on the steady-state responses. Therefore, the objective of this chapter is to perform different studies, in terms of the stiffness response, modal analysis and steady-state response of Single-Walled Carbon Nanotubes (SWCNs) by using a 3D finite-element model of the SWCN, under different types of boundary conditions, to provide more results in this field. The SWCN is modeled as a space frame structure by using the Morse potential and as a thin shell model based on various shell theories. Static analysis is performed to compare the stress-strain behavior between the Morse potential and the thin shell model. A parametric study on chirality effects and aspect ratio is also conducted to determine which shell theory is more suitable to model the mechanical behavior of SWCNs. Finally, the analysis of the harmonic response is conducted to describe the steady-state response between both models.

2.2. Introduction

The discovery of carbon nanotubes [5] established a new era in the field of materials science. The exceptional mechanical properties of nanotubes have shown great promise for a wide variety of applications, such as nano-transistors, semiconductors, hydrogen storage devices, structural materials, and molecular sensors [115]. Their exceptional and multipurpose properties have stimulated many researchers to incorporate them into polymers as a reinforcing agent for a new generation of composite materials. During the last few decades, the application of carbon nanotubes as an option of reinforcing element in nanocomposites has become considerably popular, particularly in a wide variety of structural applications in automotive, aerospace, aeronautical, mass transit, and nuclear industries. However, nanotube properties do not necessarily translate into the same properties for the nanocomposite. Several issues about the alignment, dispersion, length, size, chirality, orientation, and load transfer need to be considered and

optimized to obtain the best properties of the composite. Since experimentation at the nanoscale is still a developing field, the most effective way of quantifying the effects of such parameters is predominantly through computational modeling techniques [52].

In the analysis of Single-Walled Carbon Nanotubes (SWCNs), there are in the literature three-dimensional finite element models [116-118] for armchair, zigzag and chiral SWCNs, wherein the bonds between carbon atoms are considered as connecting load-carrying members, while the carbon atoms as joints of the members. To create the Finite Element (FE) models, nodes are placed at the locations of carbon atoms, and the bonds between them are modeled using three-dimensional elastic beam elements. In other approaches [31, 119], the finite element method is used to analyze the structure, and the modified Morse interatomic potential is used to simulate the non-linear force field of the C–C bonds. In these studies, just the bond stretching potential is considered since the bond stretching dominates nanotube strength, and the effect of angle-bending potential is small. In order to represent the stretching bond interactions between carbon atoms, non-linear beam elements are utilized. Recent works study the behavior of a SWCN as a thin cylindrical shell [120-122] by using the mechanical behavior of the SWCN obtained from molecular dynamics and different shell theories, such as Donnell's Shell Theory [80], combined with other approaches [123].

Despite the scientific work done on carbon nanotubes, further and more comprehensive studies are still required to be carried out especially on their dynamic response. Scientific works done on the dynamic response of carbon nanotubes are mainly focus on modal analysis, considering zigzag and armchair nanotubes, and sometimes, varying chirality. However, these works do not present any results on the steady-state responses. Therefore, the contribution of this chapter is to model and to conduct different studies, in terms of the stiffness response, natural frequencies and steady-state response of Single-Walled-Carbon-Nanotubes by using a 3D finite-element model of the SWCN, under different types of boundary conditions, to provide more results in this field. The SWCN is modeled as a space frame structure by using the Morse potential [79] and as a thin shell based on various shell theories, including Donnell's Shell Theory [80]. A parametric study on chirality effects is conducted to compare and to analyze the stress-strain behavior obtained from the thin shell model with results obtained from Morse potential. A parametric study on aspect ratio and chirality effects on natural frequencies is also conducted to determine which shell theory is more suitable, considering different values of aspect ratio and

chirality, to model the mechanical behavior of SWCNs. Harmonic analysis is performed to analyze and compared the steady-state response between both models. The novel aspects of this chapter are the following: (1) the stress-strain non-linear behavior of the nanotube is utilized into the shell model along with its density to perform vibration analysis, such as modal and harmonic analyses, through the Finite-Element analysis; (2) the numerical values of the shell thickness of 0.066 nm [120] instead of the common value of nanotube thickness of 0.34 nm [52]; (3) the comparison between different shell models for SWCNs is provided in terms of their aspect ratios; and (4) the steady-state response of two types of SWCNs, zigzag and armchair, is compared between the Morse potential and a shell model.

2.3 Non-linear analysis of SWCN

Non-linear mechanical behavior of a SWCN is based on its atomistic nanostructure with radius r_n. The nanotube is considered as a space frame structure wherein carbon atoms are represented by nodes and their positions in three-dimensional space are defined with the following algorithm. The concept of the algorithm for the generation of the atomic coordinates of nanotubes is simply to roll a graphene sheet to make a cylinder. Therefore, the nanotube can be generated according to its classification by a chiral vector $\mathbb{C}_h = (n, m)$ given with respect to the Bravais lattice vector a_1 and a_2 of the graphene monolayer. Then, it is possible to obtain the mean radius $r_n = C_h/2\pi$, where C_h is the magnitude of $\mathbb{C}_h$. The translational vector $\mathbf{T} = (n + 2m, 2n + m)/gcd$, where gcd is the greatest common divisor of $n + 2m$ and $2n + m$. Note that vector **T**, given in the Bravais lattice vector and perpendicular to the vector $\mathbb{C}_h$, decides the size of the unit cell of the nanotube together with $\mathbb{C}_h$. For simplicity, the original coordinate system of the graphene sheet is transformed into a new system such that **T** is along the *z*-axis. Finally, the graphene atomic coordinates (x', y') are converted to (x, y, z) with the following transformation equation [124]:

$$(x, y, z) = \left(r_n cos\left(\frac{x'}{r_n}\right), r_n sin\left(\frac{x'}{r_n}\right), y'\right) \tag{2.1}$$

The nodes that arise by using the Equation (2.1) are connected with non-linear beam elements in order to represent the potential energy of the interatomic interactions, which is expressed by the

Morse potential. The effect of angle-bending potential is negligible so that the bond stretching potential describes the nanotube behavior and can be calculated as follows [79]:

$$U_{stretch} = D_e \left(\left[1 - e^{-\beta \Delta r} \right]^2 - 1 \right) \tag{2.2}$$

where $U_{stretch}$ represents the energy corresponding to bond stretching, $\Delta r = r - r_0$ is the bond length variation, and D_e and β are the force parameters in the potential energy. The stretching force $F_{stretch}$ of the non-linear behavior of these beams can be obtained by differentiating U_{streth} potential as follows:

$$F_{stretch}(\Delta r) = 2\beta D_e \left(1 - e^{-\beta \Delta r} \right) e^{-\beta \Delta r} \tag{2.3}$$

C-C bond is assumed to break at 19% bond strain, according to [79], where the force parameters are: D_e = 6.03105 x 10^{-19} Nm, β = 2.625 x 10^{10} m^{-1} and r_0 = 1.421 x 10^{-10} m. The non-linear beam elements have six degrees of freedom at each node, which include translations in the x, y, and z directions and rotations about the x, y, and z directions. Although the Morse potential can be used to predict the stress-strain behavior of nanotube and to obtain its Young's modulus E_n, this potential can be also used to perform a free vibration and harmonic analysis by adding the numerical values for the density ρ_b = 2.3 x 10^3 kg/m^3 for the beams and the mass of the carbon atom m_c= 2.0 x 10^{-26} kg [125].

2.4 Thin shell model for carbon nanotubes

Due to the similarity of the geometry of a SWCN to a cylinder, the SWCN structure can be modeled as a cylindrical shell. Therefore, instead of performing MD simulations, it is possible to replace the molecular model with a thin shell model based on a shell theory constructed from nonlinear elements in the shape of a circular hollow cylinder [94], as depicted in Figures 2.1 and 2.2. The nanostructure can be modeled using Finite Element Method (FEM) by assuming the Poisson's ratio of nanotube v_n = 0.19, its thickness t_n = 0.066 nm and its radius r_n (depending on its chirality), as given in [120], in which these parameters were estimated by equating the axial rigidity and bending rigidity of SWCNs calculated from MD simulation with the axial rigidity and

bending rigidity expressions obtained using thin shell theory. These simulations can include nonlinear effects from the stress-strain curve of the nanotube and its density ρ_n, calculated as in [126]. The effective transversal area for the thin shell is calculated with the diameter d_n of the nanotube and the new thickness, which is expressed by $\pi d_n t_n/(1-v_n^2)$. Elements of 8 nodes, with six degrees of freedom (three translations and three rotations corresponding to the 3D coordinate system) per node, are employed for this purpose. These elements can offer good accuracy in vibration analysis and include the effects of transverse shear deformation. Regarding the shell theory used to predict the mechanical behavior of the nanotube, the thin shell model can be based on different shell theories, such as Donnell's Shell Theory [80], Flugge's Shell Theory [81] and Sanders' Shell Theory [81]. These shell theories are explained in the following sub-sections for performing a free vibration analysis.

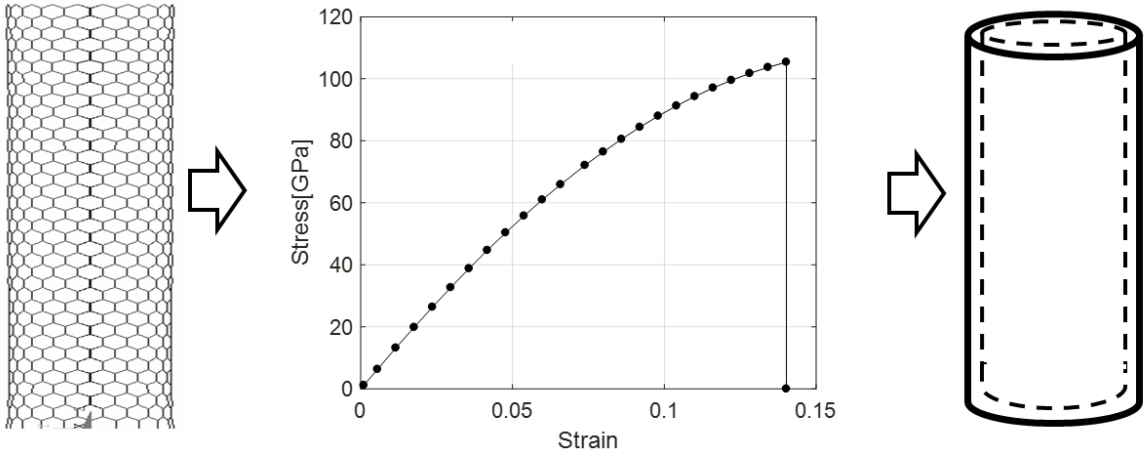

Figure 2.1. Procedure for incorporating SWCN's properties into a thin shell: (a) SWCN modeled with the modified Morse potential, (b) Stress-strain behavior of the SWCN and (c) SWCN modeled as a thin shell model.

2.4.1 Donnell's Shell Theory

Figure 2.2 shows a thin cylindrical shell model, where L_n is the length of the cylinder. An orthogonal coordinate system (x, θ, z) is fixed on the middle surface of the cylindrical shell. u, v, w denote the components of the deformation of the cylindrical shell with reference to the coordinate

system in x, θ, and z directions, respectively, as shown in Figure 2.2. For Donnell's Shell Theory (DST), the equations of motion of a thin cylindrical shell are given by the following expressions:

$$r_n{}^2\frac{\partial^2 u}{\partial z^2}+\frac{1-v_n}{2}\frac{\partial^2 u}{\partial \theta^2}+r_n\frac{1+v_n}{2}\frac{\partial^2 v}{\partial z\partial\theta}-v_n r_n\frac{\partial w}{\partial z}=\rho_n\frac{1-v_n^2}{E_n}r_n{}^2\frac{\partial^2 u}{\partial t^2} \tag{2.4a}$$

$$\frac{\partial^2 v}{\partial \theta^2}+r_n{}^2\frac{1-v_n}{2}\frac{\partial^2 v}{\partial z^2}+r_n\frac{1+v_n}{2}\frac{\partial^2 u}{\partial z\partial\theta}-\frac{\partial w}{\partial \theta}=\rho_n\frac{1-v_n^2}{E_n}r_n{}^2\frac{\partial^2 v}{\partial t^2} \tag{2.4b}$$

$$v_n r_n\frac{\partial u}{\partial z}+\frac{\partial v}{\partial \theta}-w-k\left(r_n{}^2\frac{\partial^4 w}{\partial z^4}+2r_n{}^2\frac{\partial^4 w}{\partial z^2\partial\theta^2}+\frac{\partial^4 w}{\partial \theta^4}\right)=\rho_n\frac{1-v_n^2}{E_n}r_n{}^2\frac{\partial^2 w}{\partial t^2} \tag{2.4c}$$

where $k=(1/12)(t_n/r_n)$ is the non-dimensional thickness parameter, ρ_n is the density of the shell (representing the nanotube density) and E_n its Young's modulus (carbon nanotube).

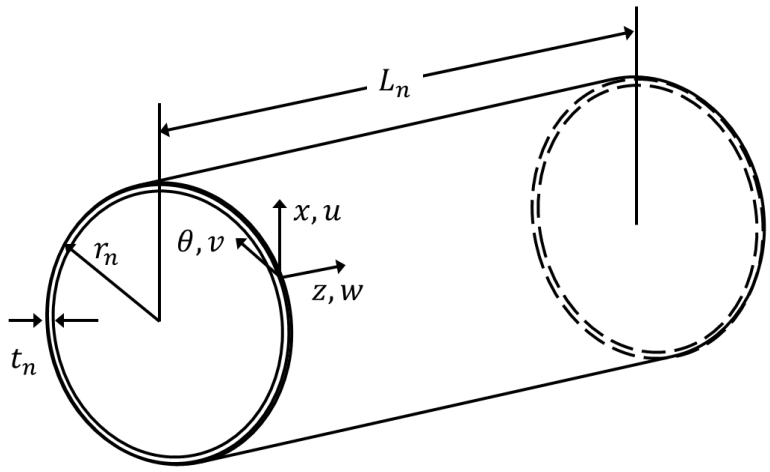

Figure 2.2. Sketch of a thin cylindrical shell.

Equations (2.4a-c) can be rewritten in a matrix form as follows:

$$[L_D]\begin{Bmatrix}u\\v\\w\end{Bmatrix}=\rho_n\frac{1-v_n^2}{E_n}r_n{}^2\frac{\partial^2}{\partial t^2}\begin{Bmatrix}u\\v\\w\end{Bmatrix} \tag{2.5}$$

where the differential operator $[L_D]$ is defined in Appendix 2.1. The solution of equations (2.4a-c), satisfying all the specific boundary conditions, is given in the form of wave propagation, associated with an axial wavenumber λ_m and circumferential wavenumber n, by [127]:

$$u = A_{mn} e^{-i(\lambda_m z + n\theta - \omega t)} \tag{2.6a}$$

$$v = B_{mn} e^{-i(\lambda_m z + n\theta - \omega t)} \tag{2.6b}$$

$$w = C_{mn} e^{-i(\lambda_m z + n\theta - \omega t + \pi/2)} \tag{2.6c}$$

where A_{mn}, $B_{mn}$and C_{mn} are, respectively, the wave amplitudes in the z, θ, x directions, and ω is the angular frequency. By substituting expressions (2.6a-c) into Equations (2.5), a matrix equation defining an eigenvalue problem can be obtained as follows:

$$[\Delta_D] \begin{Bmatrix} A_{mn} \\ B_{mn} \\ C_{mn} \end{Bmatrix} = \{0\} \tag{2.7}$$

where $[\Delta_D]$ is defined in Appendix 2.1. By imposing the non-trivial solution condition, and setting the determinant of the characteristic matrix equal to zero, the eigenvalue Equation (2.7) can be solved to obtain the following bicubic characteristic equation:

$$\widetilde{\Omega}^6 - K_2 \widetilde{\Omega}^4 + K_1 \widetilde{\Omega}^2 - K_0 = 0 \tag{2.8}$$

where $\widetilde{\Omega} = (1 - v_n^2)\rho_n \omega_n r_n / E_n$ is a frequency parameter, ω_n is the natural frequency and the coefficients K_i are given as follows:

$$K_2 = 1 + \frac{3 - v_n}{2}(n^2 + \lambda_m^2 {r_n}^2) + k(n^2 + \lambda_m^2 {r_n}^2)^2 \tag{2.9a}$$

$$K_1 = \frac{1 - v_n}{2}\left[(3 + 2v_n)\lambda_m^2 {r_n}^2 + n^2 + (n^2 + \lambda_m^2 {r_n}^2)^2 + \frac{3 - v_n}{1 - v_n} k(n^2 + \lambda_m^2 {r_n}^2)^3\right] \tag{2.9b}$$

$$K_0 = \frac{1 - v_n}{2}[(1 - v_n^2)\lambda_m^4 {r_n}^4 + k(n^2 + \lambda_m^2 {r_n}^2)^4] \tag{2.9c}$$

The Equation (2.8) gives three-real roots for any couple of *m* and *n* values. The corresponding eigenvectors are three different natural modes, one associated with a radial, one with a longitudinal and one with a circumferential prevalent displacement, each one having its distinct natural frequency. The lowest natural frequency is usually associated with a mode with predominant radial displacement.

It is possible to obtain the frequencies corresponding to forward wave and backward wave using the polynomial Equation in (2.8), once the axial wavenumber λ_m is determined for a cylindrical shell with specific boundary conditions. However, an exact value of the axial wavenumber is difficult to calculate, so that in flexural vibration, mode shapes of a cylindrical shell in the axial direction are assumed to have the same form as mode shapes of a transversely vibrating beam as in [128, 129]. Thus, λ_m can be determined by using the wavenumber of an equivalent beam with similar boundary conditions as the cylindrical shell. For example, the characteristic equation of a beam with both ends simply supported is: $\sin(\lambda_m L_n) = 0$, so that the axial wavenumber can be calculated by the expression $\lambda_m = m\pi/L_n$. For other types of boundary conditions, expressions for wavenumbers were proposed in [130] and are: $\lambda_m = (2m-1)\pi/2L_n$ for Clamped-Free and $\lambda_m = (2m+1)\pi/2L_n$ for Clamped-Clamped .

2.4.2 Flugge-Lu'e-Byrne's Shell Theory

According to the Flugge-Lu'e-Byrne's Shell Theory, the equations of motion of a thin cylindrical shell are given by:

$$([L_D] + k[L_{MOD1}]) \begin{Bmatrix} u \\ v \\ w \end{Bmatrix} = \rho_n \frac{1-\nu_n^2}{E_n} {r_n}^2 \frac{\partial^2}{\partial t^2} \begin{Bmatrix} u \\ v \\ w \end{Bmatrix} \tag{2.10}$$

where $[L_D]$ is defined in Appendix 2.1, $k = (1/12)(t_n/r_n)$ is the non-dimensional thickness parameter and $[L_{MOD1}]$ in Appendix 2.2. Substituting equations (2.6a-c) into (2.10), the eigenvalue problem can be written as:

$$([\Delta_D] + k[\Delta_F]) \begin{Bmatrix} A_{mn} \\ B_{mn} \\ C_{mn} \end{Bmatrix} = \{0\} \tag{2.11}$$

where Δ_D is defined in Appendix 2.1 and Δ_F in Appendix 2.2. The eigenvalues can be calculated as follows:

$$\widetilde{\Omega}^6 - (K_2 + k\Delta K_2)\widetilde{\Omega}^4 + (K_1 + k\Delta K_1)\widetilde{\Omega}^2 - (K_0 + k\Delta K_0) = 0 \tag{2.12}$$

where $\widetilde{\Omega} = (1 - v_n^2)\rho_n \omega_n r_n / E_n$ is a frequency parameter, ω_n is the natural frequency and the coefficients K_i are given by equations (2.9a-c) and ΔK_i by:

$$\Delta K_2 = \Delta K_1 = 0 \tag{2.13a}$$

$$\Delta K_0 = \frac{1 - v_n}{2}[2(2 - v_n)\lambda_m^2 {r_n}^2 n^2 + n^4 - 2v_n \lambda_m^6 {r_n}^6 \\ -6\lambda_m^4 {r_n}^4 n^6 2(4 - v_n)\lambda_m^2 {r_n}^2 n^4 - 2n^6] \tag{2.13c}$$

The eigenvalues are obtained and used, as explained in the case of Donnell's Shell Theory.

2.4.3 Sanders's Shell Theory

Following a similar methodology as in Flugge's Shell Theory, the equations of motion of a thin cylindrical shell for Sander's Shell Theory are given by:

$$([L_D] + k[L_{MOD2}]) \begin{Bmatrix} u \\ v \\ w \end{Bmatrix} = \rho_n \frac{1 - v_n^2}{E_n} {r_n}^2 \frac{\partial^2}{\partial t^2} \begin{Bmatrix} u \\ v \\ w \end{Bmatrix} \tag{2.14}$$

where $[L_D]$ is defined in Appendix 2.1, $k = (1/12)(t_n/r_n)$ is the non-dimensional thickness parameter and $[L_{MOD2}]$ in Appendix 2.3. Substituting equations (2.6a-c) into (2.14), the eigenvalue problem can be solved, and the eigenvalues can be obtained as follows:

$$\widetilde{\Omega}^6 - (K_2 + k\Delta K_2)\widetilde{\Omega}^4 + (K_1 + k\Delta K_1)\widetilde{\Omega}^2 - (K_0 + k\Delta K_0) = 0 \tag{2.15}$$

where $\widetilde{\Omega} = (1 - v_n^2)\rho_n \omega_n r_n / E_n$ is a frequency parameter, ω_n is the natural frequency and the coefficients K_i are given by equations (2.9a-c) and ΔK_i by:

$$\Delta K_2 = \frac{9(1-v_n)}{8}\lambda_m^2 + \frac{9-v_n}{8}n^2 \tag{2.16a}$$

$$\Delta K_1 = \frac{9(1-v_n)}{8}\lambda_m^2 + \frac{9-v_n}{8}n^2 + \frac{9(1-v_n)}{8}\lambda_m^4 - \frac{1}{4}(4-3v_n+3v_n^2)\lambda_m^2 n^2 - \frac{11-5v_n}{8}n^4 \tag{2.16b}$$

$$\Delta K_0 = \frac{1-v_n}{2}\left[\frac{9(1-v_n^2)}{8}\lambda_m^4 + 4\lambda_m^2 n^2 + n^4 - 6\lambda_m^4 n^2 - 8\lambda_m^2 n^4 - 2n^6\right] \tag{2.16c}$$

The eigenvalues are obtained and used, as explained in the case of Donnell's Shell Theory.

2.5 Results and discussion

2.5.1 Stress-strain behavior of SWCN

Static analysis is performed on SWCNs with different chiralities in order to compare their stress-strain behavior obtained in the literature, using the Morse potential and the stress-strain behavior obtained here by using a thin shell model based on Donnell's Shell Theory. To investigate the stress-strain behavior of SWCNs, a tensile displacement is applied to one side of the SWCN, and the other side is clamped. In the literature, a thickness t_n = 0.34 nm is used to predict the mechanical behavior of SWCNs with the Morse potential, while for a thin shell the thickness is 0.066 nm. Figure 2.3 shows the stress-strain curves for different types of SWCNs obtained from the literature with length L_n = 7.96-10 nm compared with stress-strain curves obtained here by using a thin shell model with the same numerical values for length, that is, L_n = 7.96-10 nm.

Table 2.1 shows the Root Mean Square Error (RMSE) and the Chi-square error for the comparison between the stress-strain curves obtained using the Morse potential and the thin shell model. For the case of (5,5) SWCN [131], the RMSE and the Chi-square are 0.5319 and 0.5179 respectively, while for (8,0) SWCN [132] and (9,0) SWCN [131] the RMSE and the Chi-square error are 0.3739 and 0.4977, and 0.2840, respectively. In the case for SWCNs with similar diameters, such as (20,0) [79], (12,12) [119] and (16,8) SWCNs [119], the RMSE and the Chi-square error present a range between 0.3172-0.4931 and 0.3313-0.6006, respectively. For SWCNs with similar diameters, such as (16,0) [76] and (9,9) SWCNs [76] the RMSE and the Chi-square

error present a range between 0.1431-0.2478 and 0.3083-0.3894, respectively. These ranges of the RMSE and the Chi-square error indicate a high degree of correlation between the compared stress-strain curves. The results in Figure 2.4 and Table 2.1 show that a thin shell model is a good option for predicting the mechanical behavior of carbon nanotubes. However, it is necessary to select a shell theory with its appropriate parameters to model the SWCNs with better accuracy. In the next section, a parametric study is conducted to determine which shell theory is the best option to perform a vibration analysis in nanotubes.

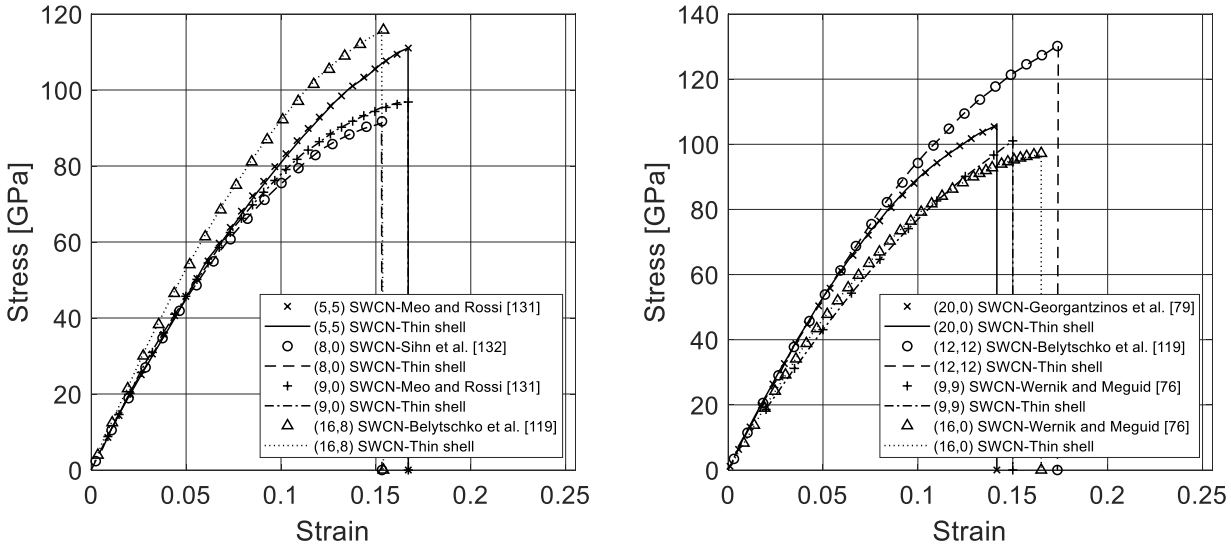

Figure 2.3. Comparison of stress-strain curves obtained using the Morse potential and the thin shell model based on Donnell's Shell Theory.

Table 2. 1. RMSE and Chi-square error for SWCNs.

Nanotube (Chirality)	RMSE	Chi-square error
(5,5)	0.5319	0.5179
(8,0)	0.3739	0.4977
(9,0)	0.2471	0.2840
(16,8)	0.4931	0.6006
(20,0)	0.3811	0.4783

(12,12)	0.3172	0.3313
(16,0)	0.1431	0.3083
(9,9)	0.2478	0.3894

2.5.2 Natural frequencies of SWCN

Free vibration analysis is carried out for a (16, 0) SWCN, with $L_n = 10$ nm and $t_n = 0.34$ nm, to compare its natural frequencies obtained using the Morse potential as described in section 2.3 with frequencies calculated using the proposed thin shell model using Finite Element Method (FEM) as described in section 2.4, with $t_n = 0.066$ nm and $L_n = 10$ nm, for two types of boundary conditions: Clamped-Free (CF), Clamped-Clamped (CC). There are two numerical values for thickness t_n: one for the Morse potential and another for the thin shell as in [120]. The values of first mode frequencies in bending and axial deformations are studied and are reported in Table 2.2. The mode shapes obtained using both models are depicted in Figure 2.4, which shows a good agreement between the results obtained using the Morse potential and the thin shell model, as described in section 2.4. The percentage errors in the frequencies with respect to thin shell model between the results of both models for CF boundary conditions are in the range of 1.41-4.39%, while for CC boundary conditions are in a range of 1.97-4.69%. It can also be appreciated that the thin shell model presents lower natural frequencies than the Morse potential model. Analyzing the first bending mode frequency for CF boundary condition, this frequency for the thin shell model is 0.74 GHz, while for Morse potential is 0.774 GHz. In the case of first axial mode frequency, the thin shell presents a natural frequency of 7.890 GHz, while for the Morse potential is 8.017 GHz. Regarding CC boundary condition, the first bending mode frequency for the thin shell shows a natural frequency of 3.98 GHz, while for the Morse potential the first bending mode is 4.176 GHz. In the case of first axial mode frequency, the thin shell presents a natural frequency of 9.665 GHz, while for the Morse potential is 9.895 GHz.

Table 2.2. Natural frequencies (GHz) of a (16, 0) SWCN with different boundary conditions

Mode	Clamped – Free			Clamped – Clamped		
	(16,0) SWCN	Thin Shell - FEM	Error (%)	(16,0) SWCN	Thin Shell - FEM	Error (%)
1 (First bending)	0.771	0.74	4.39	4.176	3.98	4.69
2	0.774	0.741	4.26	4.178	4.02	3.78
3	4.219	4.112	2.53	9.542	9.352	1.99
4	4.221	4.118	2.44	9.543	9.355	1.97
5 (First axial)	8.017	7.890	1.62	9.895	9.665	2.32
6	10.144	9.981	1.60	15.140	14.821	2.10
7	10.146	9.982	1.61	15.141	14.823	2.10
8	14.178	13.978	1.41	15.938	15.542	2.48
9	15.013	14.721	1.94	15.939	15.545	2.49
10	15.014	14.720	1.95	15.988	15.621	2.29

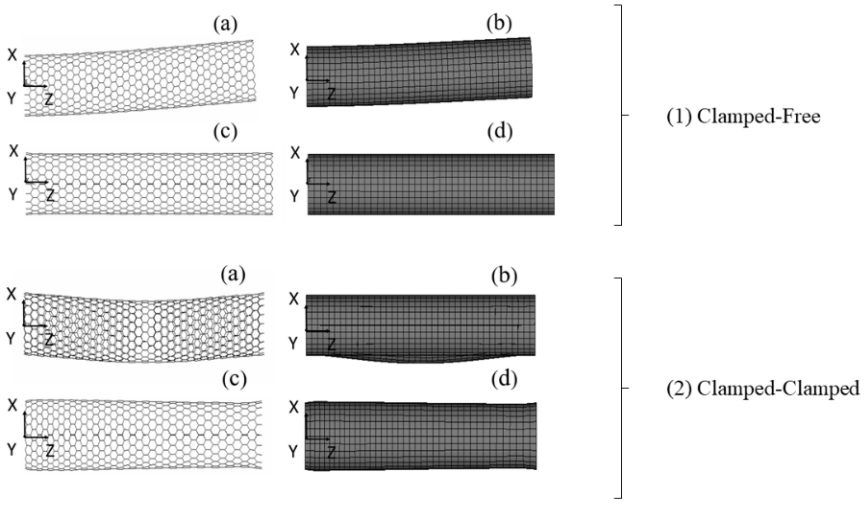

Figure 2.4. Mode shapes, first bending and first axial, of a (16, 0) SWCN with different boundaries conditions: (1) Clamped-Free and (2) Clamped-Clamped. Mode shapes based on Morse potential are located on the left side, and that for the thin shell model are on the right side.

In order to validate the results for the thin shell model, Table 2.3 and Table 2.4 show the comparison for the first bending mode natural frequencies of different types of SWCNs with different chiralities obtained from the Morse potential model and the thin shell model with various shell theories, for CF and CC boundary conditions, respectively. The shell theories used in the present chapter, as described in section 2.4 are: Donnell's Shell Theory (DST), Flugge's Shell Theory (FST) and Sanders' Shell Theory (SST). Regarding the error percentages between the frequencies obtained from the thin shell model using FEM and the above shell theories, Table 2.3 also shows that DST presents a percent error in a range of 2.64-18.22%; while FST presents an error of 6.94-27.09% and SST presents an error of 6.42-27.03%, for CF boundary conditions. Table 2.4 also shows the error percentages for CC boundary conditions between the thin shell model using FEM and the shell theories, where DST presents a percentage error in a range of 5.14-19.50%, FST presents a range of 0.8-21.21%, and SST presents a range of 1.31-21.38%. It should be noted that DST shows a range of error four times lower than the range of error from FST and SST for CF boundary conditions; while for CC boundary conditions, percent error from DST are approximately two times higher than percentage error from FST and SST.

Table 2.3. Comparison of natural frequencies in GHz obtained using different shell theories for the first bending mode (CF).

Nanotube (Chilarity)	Morse Potential	Thin Shell - FEM	Donnell	Error (%)	Flugge	Error (%)	Sanders	Error (%)
(20,0)	1.504	1.546	1.664	7.69	1.127	27.09	1.128	27.03
(8,0)	0.629	0.574	0.652	13.58	0.502	12.54	0.503	12.36
(14,0)	1.08	1.006	1.123	11.63	0.894	11.13	0.896	10.93
(5,5)	0.692	0.576	0.681	18.22	0.536	6.94	0.539	6.42
(9,9)	0.771	0.756	0.821	8.59	0.625	17.37	0.624	17.26
(16,0)	0.774	0.7	0.751	7.28	0.641	8.42	0.642	8.28
(12,12)	1.563	1.519	1.57	3.39	1.125	25.87	1.126	25.82
(16,8)	1.497	1.442	1.59	2.64	1.145	24.55	1.146	24.5

Table 2.4. Comparison of natural frequencies in GHz obtained using different shell theories for the first bending mode (CC).

Nanotube (Chirality)	Morse Potential	Thin Shell - FEM	Donnell	Error (%)	Flugge	Error (%)	Sanders	Error (%)
(20,0)	6.726	6.924	7.57	9.33	7.468	7.76	7.473	7.85
(8,0)	3.724	3.574	3.916	9.58	3.602	0.8	3.62	1.31
(14,0)	5.602	5.504	6.48	17.74	5.992	8.86	6.001	9.04
(5,5)	4.019	3.538	3.356	5.14	3.656	3.35	3.672	3.79
(8,8)	4.079	3.464	4.102	18.4	4.125	19.08	4.126	19.11
(16,0)	4.176	3.46	4.135	19.5	4.194	21.21	4.200	21.38
(12,12)	6.928	6.994	7.764	11.01	7.67	9.67	7.676	9.75
(16,8)	6.985	7.06	7.67	8.76	7.593	7.55	7.596	7.62

In order to validate the results obtained based on the three shell theories, a study is performed on SWCNs to compare and to discuss the natural frequencies obtained based on DST, FST and SST with the frequencies obtained in reference [133], which were calculated from Molecular Dynamics (MD) simulations based on Timoshenko beam model. The material parameters of SWCNs used in these simulations are: rigidity $E_n t_n$ = 278.25 GPa·nm, the ratio of Young's modulus and mass density, E_n/ρ_{mass} = 3.6481 x 10^8 m^2/s^2, Poisson's ratio v_n= 0.2 and diameter d = 6.86645 x 10^{-10} m. for CC and CF boundary conditions. Tables 2.5 and 2.6 show the natural frequency (THz) as a function of L_n/d (length-to-diameter ratio) for nanotubes with CC and CF boundary conditions, respectively, for the first vibration mode (m, n) = (1, 1). For CF-SWCNs (see Table 2.5), the calculations are performed with 12 different values of L_n/d (4.68, 6.47, 7.55, 8.28, 10.07, 13.69, 17.30, 20.89, 24.50, 28.07, 31.64 and 35.34), where the results show a good agreement for the whole length-to-diameter ratio range. DST presents a percent error between 0.86-24.21%, FST between 0.72-12.86% and SST between 0.3-12.50%. For CC-SWCNs (see Table 2.6), the calculations are performed with 11 different values of L_n/d (4.86, 6.67, 8.47, 10.26, 13.89, 17.49, 21.06, 24.66, 28.31, 31.85 and 35.53), where the results show a good accuracy for the whole length-to-diameter ratio range. DST presents a percent error between 5.18-31.91%, FST between 1.02-17.6% and SST between 0.6-17.21%.

Table 2.5: Comparison of frequencies in GHz of CF-SWCNs for the first vibration mode (*m, n*) = (1, 1).

L_n/d	MD [133]	Donnell	Error (%)	Flugge	Error (%)	Sanders	Error (%)
4.67	231.93	229.93	0.86	206.70	10.87	207.56	10.50
6.47	128.72	149.52	5.21	115.86	9.98	116.34	9.61
7.55	97.66	117.33	7.14	87.12	10.78	87.49	10.41
8.28	79.35	84.51	6.53	73.27	7.65	73.58	7.26
10.07	54.93	67.60	24.21	50.49	8.07	50.70	7.68
13.69	30.52	37.74	23.65	27.84	8.74	27.96	8.36
17.30	18.31	22.32	21.9	17.59	3.91	17.66	3.51
20.89	12.21	13.41	9.8	12.12	0.72	12.17	0.3
24.50	9.16	10.92	10.21	8.83	3.51	8.87	3.11
28.07	6.90	7.93	10.49	6.74	2.25	6.77	1.83
31.64	6.10	7.21	8.19	5.31	12.86	5.33	12.50
35.34	4.58	5.21	9.75	4.26	6.89	4.28	6.50

Table 2.6: Comparison of frequencies in GHz of CC-SWCNs for the first vibration mode (*m,n*) = (1, 1).

L_n/d	MD [133]	Donnell	Error (%)	Flugge	Error (%)	Sanders	Error (%)
4.86	1068.12	898.41	10.88	880.05	17.60	884.22	17.21
6.67	646.97	596.78	7.75	580.43	10.28	582.98	9.88
8.47	433.35	425.68	1.76	408.70	5.68	410.43	5.28
10.26	305.18	304.01	0.51	302.06	1.02	303.33	0.60
13.89	183.11	182.41	0.32	181.21	1.03	181.96	0.62
17.49	115.97	152.97	31.91	120.08	3.54	120.58	3.97
21.06	76.29	95.97	6.47	85.23	11.72	85.58	12.18
24.66	57.98	71.35	23.05	63.30	9.19	63.57	9.64

28.31	45.78	51.09	10.96	48.63	6.22	48.83	6.67
31.85	36.62	39.39	8.02	38.74	5.79	38.90	6.24
35.53	30.52	32.40	5.98	31.32	2.65	31.46	3.08

It should be noted that, in CF boundary conditions, if L_n/d ratio value increases, the natural frequencies decrease considerably from 229.32 to 5.21 GHz for DST, from 206.70 to 4.26 GHz for FST and from 207.56 to 4.28 GHz for SST. In the case of CC-SWCNs, the natural frequencies present a similar behavior, the frequencies decrease from 898.41 to 35.40 GHz for DST, from 880.05 to 31.32 GHz for FST and from 884.22 to 31.46 GHz for SST. The computed results of the present chapter are in good agreement, in most of the given cases, with that obtained using MD simulations [133] in the literature with present numerical values generally under predicting the natural frequencies. However, there a few discrepancies in the calculations in CF boundary conditions, such as in DST with L_n/d = 10.07, 13.69 and 17.30 with a percentage error of 24.21%, 23.65% and 21.90%, respectively. For FST and SST, there is a discrepancy in L_n/d = 31.64 with a percentage error of 12.86% and 12.50%, respectively. Regarding CC boundary conditions, there are a few discrepancies for DST in L_n/d = 17.49 and 24.66 with a percentage error of 31.91% and 23.05%, respectively. In the case of FST and SST, there is a discrepancy in L_n/d = 4.86 with a percentage error of 17.6% and 17.21%, respectively. These discrepancies can occur because of the selection of the appropriate parameters for each shell theory, such as the non-linearity of the stiffness response of carbon nanotubes or its density. For values of L_n/d > 10.07 for CF-SWCNs, FST and SST are more suitable than DST, except for a value of L_n/d = 31.64. However, for values of L_n/d < 8.28, DST is more suitable than FST and SST. For CC-SWCNs, for values of L_n/d > 17.49 FST and SST are more suitable, except for a value of L_n/d = 21.06. For values of L_n/d < 13.89 DST is more suitable than FST and SST.

In the present chapter, a (16, 0) SWCN, with d = 1.253 nm, L_n = 10 nm and L_n/d = 7.98, and a (9, 9), with d = 1.221 nm, L_n = 10 nm and L_n/d = 8.19, are utilized to study the steady-state response of SWCNs. In this way, it can be noticed from Tables 2.3 and 2.4 that for these types of SWCNs, DST presents a percent error of 7.28-8.59% in CF boundary condition and 18.40-19.50% in CC boundary condition; while FST presents a percent error of 8.42-17.37% in CF and 19.19-21.21% in CC, and SST presents a percent error of 8.28-17.26% in CF and 19.11-21.38%

in CC. In Table 2.5, for a L_n/d value = 8.28, which is the closest value related to L_n/d = 7.98 for the (16, 0) SWCN and L_n/d = 8.19 for the (9, 9) SWCN, DST presents a percentage error of 6.53% that is lower than the percentage error of 7.65% for FST and 7.26% for SST. Regarding the calculations related to MD simulations [39] in Table 2.6, a L_n/d value = 8.47 shows a percent error of 1.76% for DST, 5.68% for FST and 5.28% for SST. Thus, a thin shell model based on Donnell's Shell Theory is selected, from the analysis results of the parametric study, to model the mechanical behavior of a (16, 0) SWCN and a (9, 9) SWCN. In the next section, the steady-state response of a (16, 0) SWCN and a (9, 9) SWCN are studied to verify that a thin shell model based on Donnell's Shell Theory can be used to represent the mechanical behavior of SWCNs.

2.5.3 Steady-state harmonic response of SWCNs

Regarding the computation of the steady-state harmonic response, the boundary conditions of the SWCNs are applied as a cantilever for an axial and a transversal sinusoidal force, which are applied in the free end of the SWCN, with amplitude $F_0 = 1x10^{11}N$ and an excitation frequency ω in the range of 0 - 60 GHz. Figures 2.5(a) and 2.5(b) show the results of a harmonic analysis applying an axial and a transversal sinusoidal force at the free end of both nanotubes, respectively, on the (16, 0) SWCN modeled with the Morse potential and by using a thin shell model based on Donnell's Shell Theory. The sinusoidal forces are applied at one side of the SWCN, and the other side is clamped. It can be appreciated that both steady-state responses in Figure 2.5 have similar behavior with good accuracy for excitation frequencies no higher than 25 GHz in axial loading case and no higher than 23 GHz in transversal loading case. However, in the Figure 2.5(a) for the axial sinusoidal force, the amplitude of the shell model is higher than that of the Morse potential model for excitation frequencies higher than 25 GHz, while for the transversal sinusoidal force, in Figure 2.5(b), for excitation frequencies higher than 23 GHz, there is a phase-shifting in the amplitudes of both models.

In the case for the (9, 9) SWCN, Figures 2.6(a) and 2.6(b) show the results of a harmonic analysis applying an axial and a transversal sinusoidal force, respectively. For (9, 9) SWCN, the results show discrepancies for the axial loading case for frequencies higher than 30 GHz, while in the transversal loading case, the amplitude is higher in the Morse potential than the shell model for excitation frequencies higher than 13 GHz. There is also a phase-shifting for frequencies higher than 40 GHz, while for the axial loading case for frequencies higher than 30 GHz, the results show

a light phase shifting. Regarding the predictivity of the shell model, in the axial loading case for the (16, 0) SWCN, the shell model is less predictive in the amplitude of the steady-state response, but the axial frequencies agree in the Morse potential and shell models. This can be due to the non-linearity of the stiffness response of the nanotube used in the shell model. In the case of transversal loading case of (9, 9) SWCN, the shell model is also less predictive due to the non-linearity of the nanotube used in the shell model, which has an effect on the phase shifting for frequencies higher than 40 GHz and a lower amplitude than that of the Morse potential model.

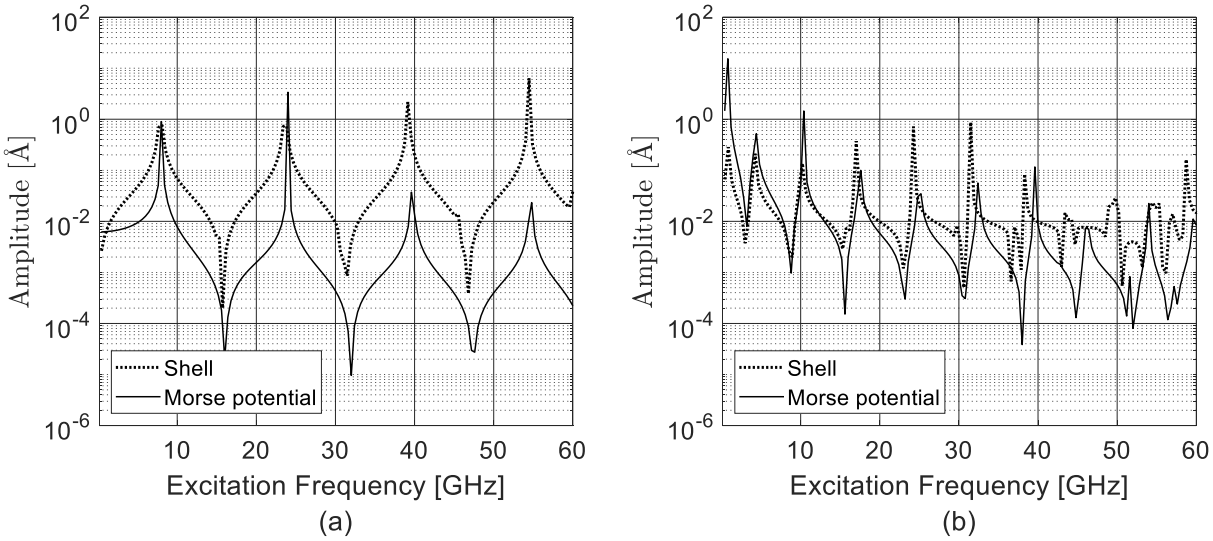

Figure 2.5. The steady-state harmonic response of a (16, 0) SWCN with an (a) axial and (b) transversal sinusoidal force with amplitude $F_0 = 1x10^{11}N$ and an excitation frequency ω in the range of 0 – 60 GHz.

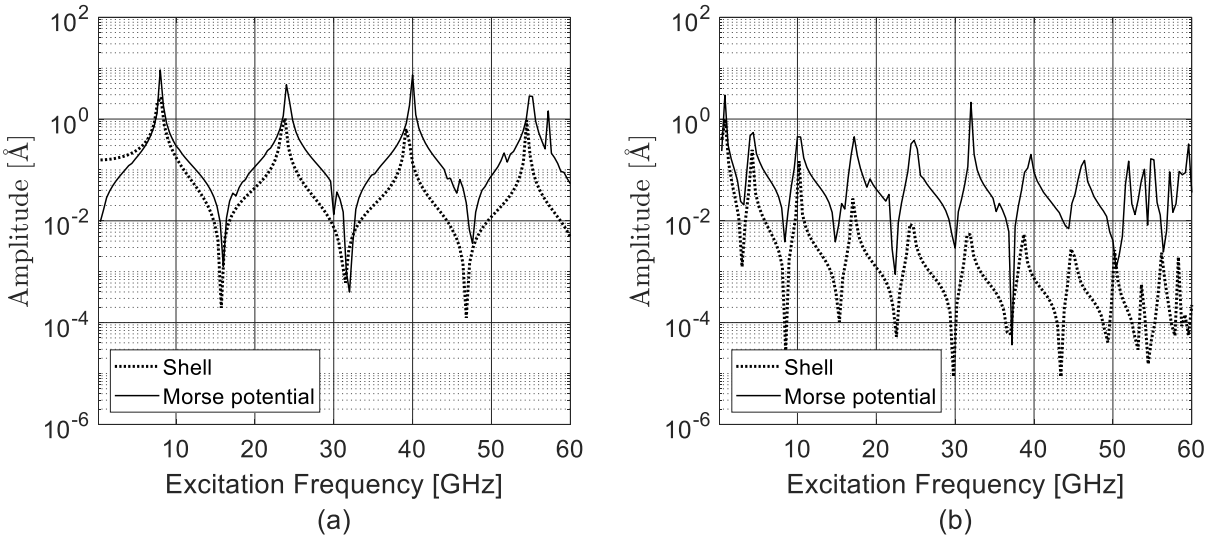

Figure 2.6. The steady-state harmonic response of a (9, 9) SWCN with an (a) axial and (b) transversal sinusoidal force with amplitude $F_0 = 1x10^{11}N$ and an excitation frequency ω in the range of 0 – 60 GHz.

2.6 Conclusion

The main objective of the present chapter was to study the mechanical behavior of SWCNs by using the Morse potential and various shell theories, such as Donnell's Shell Theory (DST), Flugge's Shell Theory (FST) and Sanders' Shell Theory (SST). Static, modal analysis and harmonic analyses were carried out to determine the stress-strain behavior, natural frequencies, and harmonic response of the SWCNs.

In the analysis, the stress-strain behavior of different types of SWCNs modeled with the Morse potential and as a thin shell using the Finite-Element Method was analyzed to calculate the accuracy to predict the mechanical behavior of nanotubes by using a thin shell. The RMSE and Chi-error were used to determine the accuracy of these simulations between the results obtained from the thin shell and results from the literature. Regarding the natural frequencies of SWCNs with different chirality, a parametric study was performed to compare the results obtained for the thin shell model and Morse potential with different shell theories that are DST, FST, and SST in Clamped-Free and Clamped-Clamped boundary conditions. Another parametric study that considers the aspect ratio of SWCNs was also performed to compare the results obtained for

different shell theories with results obtained from the literature. The results of these parametric studies show that a thin shell model based on Donnell's Shell Theory is suitable for the physical properties of SWCNs for aspect ratios lower than 8.28 for Clamped-Free boundary conditions and 13.89 for Clamped-Clamped boundary conditions. For aspect ratios higher than the previous ones, Flugge's and Sanders' Shell Theories are more suitable, except for an aspect ratio of 31.64 in CF boundary conditions and an aspect ratio of 21.06 in CC boundary conditions. The thin shell model presents enough accuracy of SWCN modeling and allows to study other mechanical properties, such as bending, buckling, and torsion response.

In the harmonic response of SWCNs, the amplitudes of both models show a good agreement for the (16, 0) SWCN with an axial sinusoidal force for excitation frequencies no higher than 25 GHz and no higher than 23 GHz in transversal loading case. On the other hand, in the axial loading case, the amplitude of the shell model is higher than that of the Morse potential model for excitation frequencies higher than 25 GHz, while for the transversal sinusoidal force for excitation frequencies higher than 23 GHz, there is a phase-shifting in the amplitudes of both models. In the case of the transversal sinusoidal force for the (9, 9) SWCN, the amplitudes of Morse potential model show a considerable increase with respect to the amplitudes of the thin shell model for excitation frequencies higher than 13 GHz. There is also a phase-shifting for frequencies higher than 40 GHz, while for the axial loading case for frequencies higher than 30 GHz, the results show a light phase shifting. This behavior can occur due to the non-linearity of the stress-strain behavior obtained using the Morse potential model for both nanotubes, (16, 0) SWCN and (9, 9) SWCN, and which is utilized in the thin shell model.

Appendix 2.1

Differential operator $[L_D]$ for Donnell's Shell Theory is given by:

$$[L_D] = \begin{bmatrix} r_n{}^2 \dfrac{\partial^2}{\partial z^2} + \dfrac{1-v_n}{2}\dfrac{\partial^2}{\partial \theta^2} & r_n \dfrac{1+v_n}{2}\dfrac{\partial^2}{\partial z \partial \theta} & -v_n r_n \dfrac{\partial}{\partial z} \\ r_n \dfrac{1+v_n}{2}\dfrac{\partial^2}{\partial z \partial \theta} & \dfrac{\partial^2}{\partial \theta^2} + r_n{}^2 \dfrac{1-v_n}{2}\dfrac{\partial^2}{\partial z^2} & \dfrac{\partial}{\partial \theta} \\ v_n r_n \dfrac{\partial}{\partial z} & \dfrac{\partial}{\partial \theta} & -1 - k\left(r_n{}^2 \dfrac{\partial^4}{\partial z^4} + 2 r_n{}^2 \dfrac{\partial^4}{\partial z^2 \partial \theta^2} + \dfrac{\partial^4}{\partial \theta^4}\right) \end{bmatrix} \tag{2.17}$$

where the differential operator $[L_D]$ becomes symmetric by changing the sign of the third column which is equivalent to taking w positive outward. Operator $[\Delta_D]$ for eigenvalue problem is defined as:

$$[\Delta_D] = \begin{bmatrix} M_{11} & M_{12} & M_{13} \\ & M_{22} & M_{23} \\ sym. & & M_{33} \end{bmatrix} \tag{2.18}$$

where

$$M_{11} = \lambda_m^2 r_n{}^2 + \frac{1-v_n}{2} n^2 - \Omega^2, \;\; M_{12} = \lambda_m r_n \frac{1+v_n}{2} n, \;\; M_{13} = -v_n \lambda_m r_n \tag{2.19a}$$

$$M_{22} = \frac{1-v_n}{2} \lambda_m^2 r_n{}^2 + n^2 - \Omega^2, \;\; M_{23} = n, \;\; M_{33} = 1 + k(\lambda_m^2 r_n{}^2 + n^2)^2 - \Omega^2 \tag{2.19b}$$

$$\widetilde{\Omega}^2 = (\rho_n / E_n)(1 - v_n^2)\omega^2 r_n{}^2 \tag{2.19c}$$

Appendix 2.2

Operator $[L_{MOD1}]$ for the equations of motion of a thin cylindrical shell for Flugge-Lu'e-Byrne's Shell Theory is defined as follows:

$$[L_{MOD1}] = \begin{bmatrix} \frac{1-v_n}{2}\frac{\partial^2}{\partial\theta^2} & 0 & {r_n}^3\frac{\partial^3}{\partial z^3} - \frac{1-v_n}{2}r_n\frac{\partial^3}{\partial z\partial\theta^2} \\ 0 & \frac{3(1-v_n)}{2}{r_n}^2\frac{\partial^2}{\partial z^2} & \frac{3-v_n}{2}{r_n}^2\frac{\partial^3}{\partial z^2\partial\theta} \\ -{r_n}^3\frac{\partial^3}{\partial z^3} + \frac{1-v_n}{2}r_n\frac{\partial^3}{\partial z\partial\theta^2} & -\frac{3-v_n}{2}{r_n}^2\frac{\partial^3}{\partial z^2\partial\theta} & -1-2\frac{\partial^2}{\partial\theta^2} \end{bmatrix} \tag{2.20}$$

Operator $[\Delta_F]$ for eigenvalue problem is defined as:

$$[\Delta_F] = \begin{bmatrix} -\frac{1-v_n}{2}n^2 & 0 & \lambda_m^2{r_n}^2\left(-\lambda_m^2{r_n}^2 + \frac{1-v_n}{2}n^2\right) \\ 0 & -3\frac{1-v_n}{2}\lambda_m^2{r_n}^2 & \frac{3-v_n}{2}n\lambda_m^2{r_n}^2 \\ \lambda_m^2{r_n}^2\left(-\lambda_m^2{r_n}^2 + \frac{1-v_n}{2}n^2\right) & \frac{3-v_n}{2}n\lambda_m^2{r_n}^2 & -(1-2n^2) \end{bmatrix} \tag{2.21}$$

Appendix 2.3

Operator $[L_{MOD2}]$ for the equations of motion of a thin cylindrical shell for Sander's Shell Theory is defined as follows:

$$[L_{MOD2}] = \begin{bmatrix} \frac{1-v_n}{8}\frac{\partial^2}{\partial\theta^2} & -\frac{3(1-v_n)}{8}\frac{\partial^2}{\partial z\partial\theta^2} & \frac{1-v_n}{2}r_n\frac{\partial^3}{\partial z\partial\theta^2} \\ -\frac{3(1-v_n)}{8}\frac{\partial^2}{\partial z\partial\theta^2} & \frac{9(1-v_n)}{8}\frac{\partial^2}{\partial z^2} + \frac{\partial^2}{\partial\theta^2} & \frac{3-v_n}{2}\frac{\partial^3}{\partial z^2\partial\theta} - \frac{\partial^3}{\partial\theta^3} \\ \frac{1-v_n}{2}r_n\frac{\partial^3}{\partial z\partial\theta^2} & \frac{3-v_n}{2}\frac{\partial^3}{\partial z^2\partial\theta} - \frac{\partial^3}{\partial\theta^3} & 0 \end{bmatrix} \tag{2.22}$$

Chapter 3. Dynamic response of Carbon-Nanotube-Reinforced-Polymer materials based on multiscale finite element analysis

Foreword

This chapter contains the journal paper: J. A. Palacios and R. Ganesan, "Dynamic response of Carbon-Nanotube-Reinforced-Polymer materials based on multiscale finite element analysis," Composites Part B: Engineering, vol. 16, pp. 497-508, 2019.

In this chapter, a 3D multiscale finite element of the Representative Volume Element of Carbon-Nanotube-Reinforced-Polymer-Composite material is developed to conduct a parametric study to determine its dynamic response, in terms of its modal and steady-state responses and damping properties, for different volume fractions of SWCNs. A model consisting of an SWCN, an interface region, and the polymer matrix has been constructed for this purpose.

3. Dynamic response of Carbon-Nanotube-Reinforced-Polymer materials based on multiscale finite element analysis

3.1 Abstract

Nanocomposites are preferred over conventional materials because of their superior mechanical properties. Studies need to be carried out, especially on the dynamic response of the composite material. The objective of the present chapter is to study the dynamic response of Carbon-Nanotube-Reinforced-Polymer (CNRP) material by developing a 3D multiscale finite-element model of the Representative Volume Element (RVE) of the composite material to determine its dynamic properties, in terms of its natural frequencies and damping properties. A computational model consisting of a Single-Walled Carbon Nanotube (SWCN), an interface region and the polymer matrix is constructed for this purpose. The SWCN is modeled as a space frame structure by using the Morse potential and as a thin shell model based on Donnell's Shell Theory. The polymer matrix is modeled with the Mooney-Rivlin strain energy to calculate its non-linear response and the interface region is modeled via van der Waals links based on the Lennard-Jones Potential. The natural frequencies of CNRP are compared with the natural frequencies of the polymer matrix. A relation between damping ratio and natural frequencies is then obtained. Finally, the analysis of harmonic response is conducted to characterize the effects of the SWCN reinforcement in the polymer material.

3.2 Introduction

The exceptional and multipurpose properties of Carbon Nanotubes (CNs) have stimulated many researchers to incorporate them into polymers as a reinforcing agent for a new generation of composite materials [115]. The models that have been developed to reveal the reinforcement mechanism in nanocomposite materials have predominantly been based upon either traditional continuum mechanics or purely atomistic methods. However, traditional continuum mechanical models are incapable of accurately describing the influence of the dispersion of nanofillers into composites upon their mechanical properties because they lack the appropriate constitutive relations that govern the behavior of these composites at this scale [134]. For this reason, a

multiscale approach is the best option to analyze the mechanical behavior of a nanocomposite because it is a technique involving the analysis at different scales, which means problem analysis can connect different levels of modeling from diverse models (such as molecular dynamics or continuum mechanics). Currently, there are several multiscale methods in the literature used to solve problems related to elasticity, molecular dynamics, and vibration analysis. Most multiscale modeling techniques adopt either coupled, or atomistic-based continuum approaches to treat the reinforcement of nanocomposites with CNs. In the coupled approach, it is common to employ Molecular Dynamics (MD) for atomistic scales and Finite Element Method (FEM) for continuum scales. The coupled MD-FEM methods can be further subdivided into sequential and concurrent coupling methods. The sequential approach assumes that the problem considered can be easily separated into processes that are governed by different lengths and time scales. On the other hand, concurrent methods perform the entire multiscale simulation simultaneously and continually feed information from one length scale to the other in a dynamic way. Regarding the atomistic-based continuum technique, this approach has the advantage of describing atomic positions, their interactions, and their governing interatomic potentials in a continuum framework.

One of the most common techniques to simulate and to model a nanocomposite is the definition of Representative Volume Element (RVE) of the material [53]. For studying the static response of polymer matrices with CNs as a reinforcement, Liu and Chen [77] evaluated the effective properties of CN-based composites through the development of a RVE based entirely on continuum mechanics. However, their RVE did not include a representation of the interface, nor did it include an atomistic description. Li and Chou [38, 91] constructed their RVE using a space-frame structure for the CN, solid elements for the polymer, and truss rods to represent the interfacial region. Constant material properties were used throughout the model and nonlinear behavior for the interface surface. Shokrieh and Rafiee [78] extended the model of Li and Chou [38, 91] to incorporate a nonlinear interfacial region based on the Lennard–Jones potential. However, their model did not attempt to incorporate a nonlinear description of the CN and the surrounding polymer. Georgantzinos et al. [92] proposed a modification of the rule of mixtures that can consider the interfacial effects between the reinforcement consisting from a single-walled carbon nanotube and the polymer matrix, to predict the effective Young's modulus of the nanocomposite simulated as RVE. They used two-noded interfacial joint elements of variable stiffness for modeling the interface region. However, its interface region had a linear behavior as

well as the SWCN. Later, Georgantzinos et al. [79] included the nonlinear behavior of a SWCN modeled by using the Morse potential, but the interface region still had a linear behavior. Mohammadpour et al. [94] presented a RVE of a polymer matrix reinforced with a SWCN, replacing the SWCN with a solid model constructed from nonlinear elements in the shape of a hollow cylinder and integrating the mechanical properties into solid elements. Despite modeling the interface region with contact elements saving computing efforts, this model cannot study other types of mechanical behavior as bending, buckling, and torsion. Later, Wernik and Meguid [76] proposed a nonlinear RVE to investigate the effective mechanical properties of a nano-reinforced polymer, including nonlinear effects on the SWCN and the interface region. Ionita [95] conducted atomistic and mesoscale simulations to estimate the effects of the diameter and weight fraction of SWCNs on the mechanical behavior and glass transition temperature of SWCN-reinforced epoxy resin composites. Spanos et al. [93] extended the work of Ref. [79] to study the stress transfer between the SWCN and the polymer matrix. Stiffness variations defining a heterogeneous region simulated the interfacial effects between the two materials. Other works such as that of Ghorbanpour et al. [96] conducted the static stress analysis of the RVE under non-axisymmetric thermo-mechanical loads and uniform electro-magnetic fields. Their results showed that the fatigue life of the composite material was dependent on magnetic intensity, angle orientation, and volume fraction of SWCN. On the other hand, Ghasemi et al. [97] studied the effects of carbon nanofibers on thermo-mechanical properties of a RVE and their effect on residual stress. Jia et al. [98] proposed to analyze the stress transfer properties of a RVE with a SWCN and a Double-Walled-Carbon-Nanotube (DWCN) at low temperatures environments. The results were obtained for both reinforcements (SWCN and DWCN). However, a perfect bonding was assumed between the polymer matrix and the SWCN and the DWCN. Later, Kyu et al. [99] determined the mechanical behavior of the RVE made with aluminum and a SWCN. In this work, the interface region between both the materials was modeled using van del Waals interactions. Recently, Garcia-Macias et al. [100] developed a RVE to study its effective elastic moduli, including an atomistic-based computational model and a micromechanics approach at the nano and micro-scales, respectively. The covalent bonds of the SWCN were modeled as Timoshenko beams.

Most of the existing works on polymer matrices with SWCNs as reinforcement are on the static response; there are very few models that study the dynamic response of this type of nanocomposite. Latibari et al. [104] extended the model of [38, 91], including a nonlinear

interfacial region based on the Lennard–Jones potential to calculate damping ratio of nanocomposite by evaluating its dissipation energy. However, their model does not incorporate a nonlinear description of the SWCN. Jamal-Omidi et al. [105] analyzed a SWCN embedded in volume element using 3D finite element and analytical methods to compute its natural frequencies with different aspect ratios. They studied two models with Lennard-Jones potential and one with perfect bonding between the SWCN and the surrounding polymer. Gajbhiye and Singh [107] proposed a RVE for a polypropylene matrix along with different percentages of single-walled carbon nanotubes to evaluate its natural frequencies, rate-dependent characteristics, and damping properties. The covalent bond of the nanotube is modeled using Tersoff–Brenner potential, and the interaction between nanotube and polymer matrix is modeled using Lennard–Jones potential represented by nonlinear spring elements. Recently, Xu et al. [135] developed a method that can extract elastic modulus over a range of strain rates and temperatures from the dynamic mechanical analysis data for nanocomposites. The steady-state harmonic response of CNs and nanocomposites have not so far been studied in existing works in the literature.

Despite the scientific work done on nanocomposites, further and more comprehensive studies are still required to be carried out especially on their dynamic response, in terms of their free vibration and steady-state harmonic response. Experimental investigations for this purpose have limitations and, in most cases, appropriate experimental work could not be carried out. Computational modeling and simulation encompassing multiscale material behavior, especially by using an atomistic-behavior-based continuum technique, provides an alternate approach to study the material behavior. Therefore, the purpose of the present chapter is to model and to analyze and to conduct a study on the dynamic and harmonic response of Carbon-Nanotube-Reinforced-Polymer (CNRP) material by developing and using a 3D multiscale finite-element model of the Representative Volume Element (RVE) of the composite. The RVE investigated in this chapter consists of a single-walled carbon nanotube embedded in a polymer matrix and an interface region between the SWCN and the polymer material. The SWCN is modeled as a space frame structure by using the Morse potential [79] and as a thin shell based on Donnell's Shell Theory [80]. The polymer matrix is modeled using the Mooney-Rivlin strain energy [82] to calculate its non-linear response, and the interface region is modeled via van der Waals links based on the Lennard-Jones Potential [83]. Polyamide-imide (PAI) is considered as matrix material due to their applications in

the aeronautical and aerospace industries. This material exhibits high mechanical performance and thermal properties, including creep resistance and low flammability.

3.3 Multiscale Finite Element Modeling of the Representative Volume Element

The Representative Volume Element (RVE) investigated in the present chapter consists of a Single-Walled Carbon Nanotube (SWCN) embedded in a polymer matrix and an interface region between the SWCN and the polymer material (Figure 3.1). The interactions between the SWCN and the polymer matrix are treated as nonbonded van der Waals interactions. The volume fraction of the SWCN in the composite material denoted as V_n, with respect to the RVE can be calculated as follows [79]:

$$V_n = \frac{8 r_n t_n}{4 r_m^2 - (2 r_n - t_n)^2} \tag{3.1}$$

where r_n is the mean radius of the nanotube, r_m is the radius of the matrix material and t_n is the thickness of the nanotube. The matrix is regarded as a continuum medium since the matrix volume is far higher than that of the SWCN for the volume fractions considered. The RVE length is the same as that of the matrix length and nanotube length L_n (Figure 3.1).

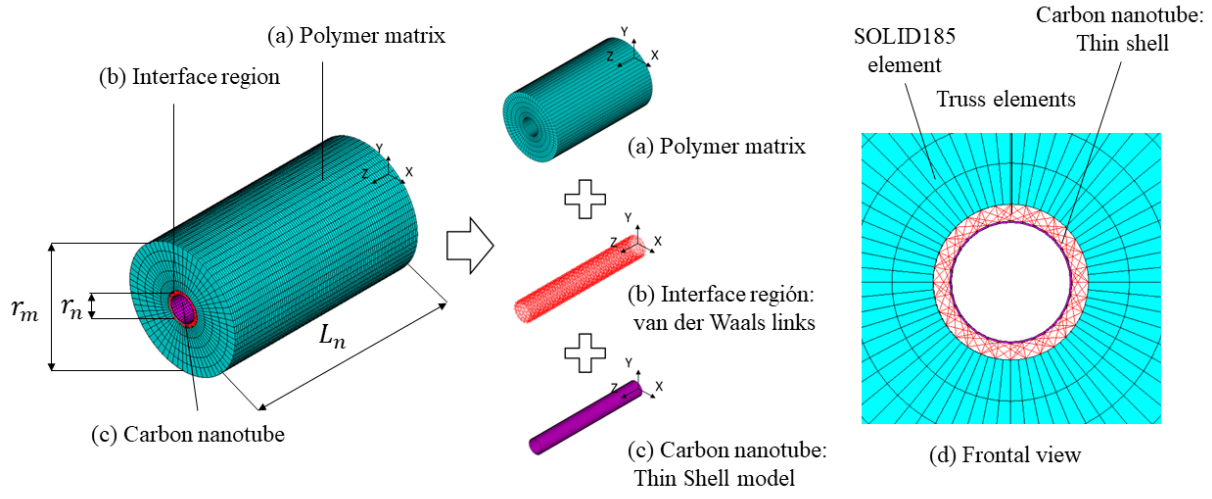

Figure 3.1. Finite element modeling of the representative volume element: (a) Polymer matrix, (b) Interface region: van der Waals links, and (c) Carbon nanotube: Thin Shell model, (d) frontal view of the region surrounding the nanotube.

3.3.1 Space frame model of SWCN

The mechanical behavior of a SWCN depends on its atomistic nanostructure. For computational modeling, the SWCN is modeled as a space frame structure wherein the carbon atoms are represented by the so-called nodes of the frame finite-element and their positions in three-dimensional space are defined with the following algorithm. The concept of the algorithm for the generation of the coordinates of the carbon atoms in the nanotube is to obtain the nanotube by rolling a graphene sheet into a cylinder. Therefore, the nanotube geometry can be generated by a chiral vector $\mathbb{C}_h = (n, m)$ given with respect to the Bravais lattice vector a_1 and a_2 of the graphene monolayer, in which a_1 and a_2 are the unit vectors of the graphene. The two integer indices (n, m) define the nanotube diameter and their chirality, respectively. In terms of this notation, the armchair nanotubes are indicated by (n, n) and the zig-zag nanotubes are denoted as $(n, 0)$. Then, it is possible to obtain the mean radius $r_n = C_h/2\pi$, where C_h is the magnitude of $\mathbb{C}_h$, given by $C_h = \|(n, m)\|$. The translational vector $\mathbf{T} = (n + 2m, 2n + m)/GCD$, where GCD is the greatest common divisor of both the quantities $n + 2m$ and $2n + m$. Note that the vector **T** is given in the Bravais lattice vector and perpendicular to the vector $\mathbb{C}_h$. It decides the size of the unit cell, which consists of two carbon atoms of the nanotube together with $\mathbb{C}_h$. For simplicity, the original coordinate system of the graphene sheet is transformed into a new system such that **T** is along the *z*-axis, where the *z*-axis is, as shown in Figure 3.1, the longitudinal axis of the nanotube as well as the RVE. Hence, the graphene sheet atomic coordinates (x', y') are converted to nanotube cylindrical coordinates (x, y, z) using the following transformation equation [124]:

$$(x, y, z) = \left(r_n cos\left(\frac{x'}{r_n}\right), r_n sin\left(\frac{x'}{r_n}\right), y'\right) \tag{3.2}$$

The nodes, the coordinates of which are defined by the equation (3.2), are connected by non-linear frame finite elements in order to represent the potential energy of the interatomic interactions. This potential energy is expressed by using the Morse potential. The effect of angle-bending potential is negligible, so that the bond stretching potential, denoted by $U_{stretch}$, alone can adequately describe the nanotube behavior. $U_{stretch}$ can be calculated as follows [79]:

$$U_{stretch} = D_e\left(\left[1 - e^{-\beta\Delta r}\right]^2 - 1\right) \tag{3.3}$$

where $U_{stretch}$ represents the potential energy corresponding to bond stretching, $\Delta r = (r - r_0\ )$ is the bond length variation, and D_e and β are the force parameters in the potential energy. The stretching force $F_{stretch}$ of the non-linear behavior of the frame finite element can be obtained by differentiating $U_{strecth}$ potential with respect to Δr. Hence, $F_{stretch}$ is obtained to be:

$$F_{stretch} = 2\beta D_e\left(1 - e^{-\beta\Delta r}\right)e^{-\beta\Delta r} \tag{3.4}$$

It is considered that the C-C bond breaks at 19% bond strain, according to Ref. [79], and correspondingly the force parameters are: D_e = 6.03105 x 10^{-19} Nm, β = 2.625 x 10^{10} m^{-1} and r_0 = 1.421 x 10^{-10} m. BEAM188 element, which is available in commercial software ANSYS®, is used to model the non-linear frame finite element. This element, which is shown in Figure 3.2(a), is capable of uniaxial tension or compression along with torsional and bending deformations and it has six degrees of freedom at each of its end nodes, which include the translations in the x, y, and z directions and rotations about the x, y, and z axes. The density ρ_b = 2.3 x 10^3 kg/m^3 is used for the frame element, in accordance with Ref. [125], and the mass of carbon atom m_c= 2.0 x 10^{-26} kg [125]. The mass m_c is used at the nodes, representing the mass of the carbon atoms. The number of elements of the SWCN is 4512.

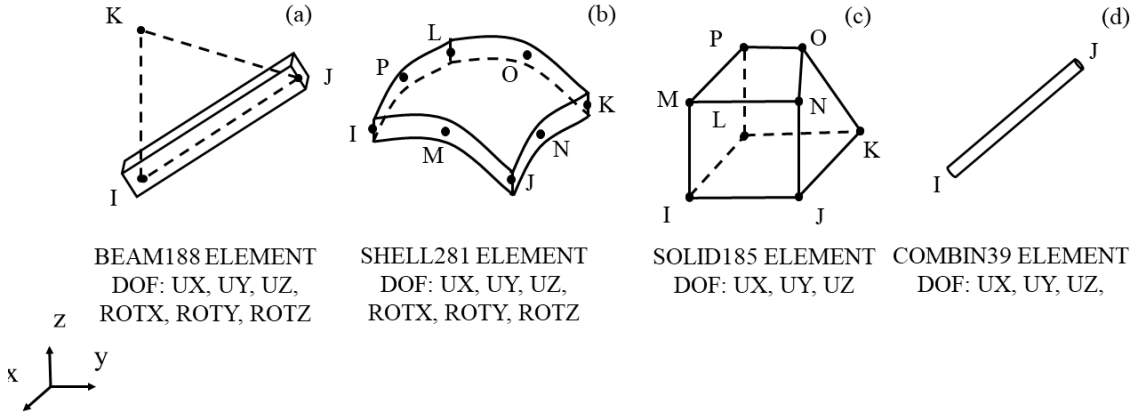

Figure 3.2. Elements used in the finite element modeling of the representative volume element: (a) BEAM188 element, (b) SHELL281 element, and (c) SOLID185 element, (d) COMBIN39 element.

3.3.2 Thin shell model of SWCN

Due to the similarity of carbon nanotube's geometry to a cylinder, nanotube structure can be modeled as an equivalent cylindrical shell. It is possible to replace the molecular structure of SWCN with a thin shell model based on a shell theory of continuum mechanics in the shape of a circular hollow cylinder [94], as depicted in Figure 3.3. The thin shell structural model can then be modeled using Finite Element Method (FEM) by assuming the Poisson's ratio of nanotube v_n (= 0.19), its thickness t_n (= 0.066 nm) and its radius r_n (value depending on its chirality). As given in Ref. [120], these parameters were estimated by equating the axial rigidity and bending rigidity of SWCN that are calculated from Molecular Dynamics (MD) simulations with the axial rigidity and bending rigidity expressions obtained using thin shell theory. Regarding the shell theory used to predict the mechanical behavior of the nanotube, Donnell's thin shell theory can be used [80]. These simulations can include nonlinear effects from the stress-strain curve of the nanotube and its density ρ_n, that were calculated as in Ref. [126]. The effective transversal area for the thin shell is calculated using the diameter d_n of the nanotube and the equivalent thickness, which is expressed by $\pi d_n t_n/(1-v_n^2)$. SHELL281 element, which is available in commercial software ANSYS®, is used to model the thin shell. This element is suitable for analyzing thin to moderately-thick shell structures and in large strain nonlinear applications. This element, which is shown in Figure 3.2(b), also consists of 8 nodes, with six degrees of freedom (three translations

and three rotations corresponding to a 3D coordinate system) per node. The number of elements of the shell model is 3040.

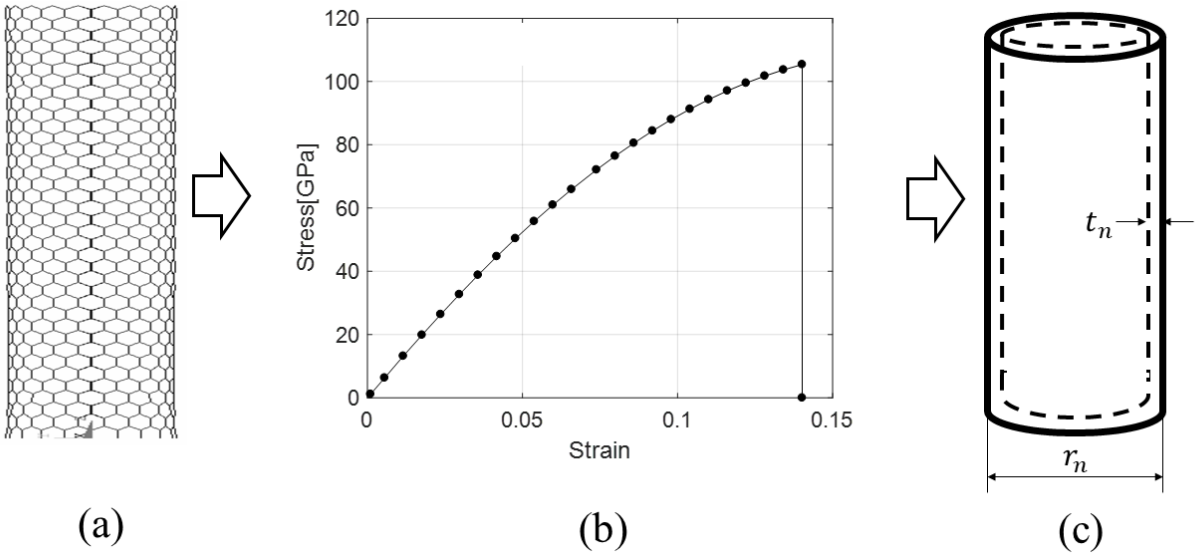

Figure 3.3. Procedure for incorporating SWCN's properties into a thin shell: (a) SWCN modeled with the Morse potential, (b) Stress-strain behavior of the SWCN and (c) SWCN modeled as a thin shell.

3.3.3 Polymer matrix

The polymer matrix is modeled by using linear three-dimensional hexahedral isoparametric finite element SOLID185 available in commercial software ANSYS®, which is capable of simulating both material and geometrical nonlinearities of hyperelastic material. This element, which is shown in Figure 3.2(c), is defined by eight nodes having three degrees of freedom at each node: translations in the nodal x, y, and z directions. Although a 20-node solid element would be more compatible with SHELL218 element to perform the simulations, SOLID185 element (with eight nodes) is suitable for modeling general 3-D solid structures. It allows for prism, tetrahedral, and pyramid degenerations when used in an irregular region. In order to describe the mechanical behavior of the polymer matrix, the following Mooney–Rivlin strain energy density function is utilized in conjunction with the SOLID185 element [82]:

$$W(I_1, I_2, I_3, v_m) = \tag{3.5}$$

$$c_{1m}(I_1 - 3) + c_{2m}(I_2 - 3) + c_{3m}(I_1 - 3)(I_2 - 3) + \frac{1}{2}k_m(I_3 - 3)^2$$

where I_1, I_2, and I_3 define the invariants of the strain tensor, v_m is the Poisson's ratio, c_{1m}, c_{2m} and c_{3m} are material parameters and k_m is the bulk modulus of the material. Polyamide-imide (PAI) is considered as the polymer matrix material. Tension experiments were carried out by Richeton et al. [136] to determine the mechanical properties of PAI. The fitting of the experimental stress-strain behavior of this material with the specific Mooney-Rivlin parameters is made in the present chapter by using the method of least squares, which is a standard approach in regression analysis to the approximate solution of the overdetermined system. The stress-strain curve thus determined is depicted in Figure 3.4 with the Mooney-Rivlin parameters c_{1m}= -1.052 GPa, c_{2m}= 1.443 GPa, c_{3m}= 0.231 GPa and k_m= 2.041 GPa.

The model parameters for the polymer material consist of internal radius, and external radius and 10.0 nm length. The Young's modulus E_m of the polymer material is obtained from the stress-strain curve in order to perform the vibration analysis. Hence, the mechanical properties of PAI used in the vibration analysis are as follows: E_m= 2.45 x 10^9 Pa, density ρ_m = 1.4 x 10^3 kg/m^3 and Poisson's ratio v_m= 0.3. The number of elements of the polymer matrix material is 36480.

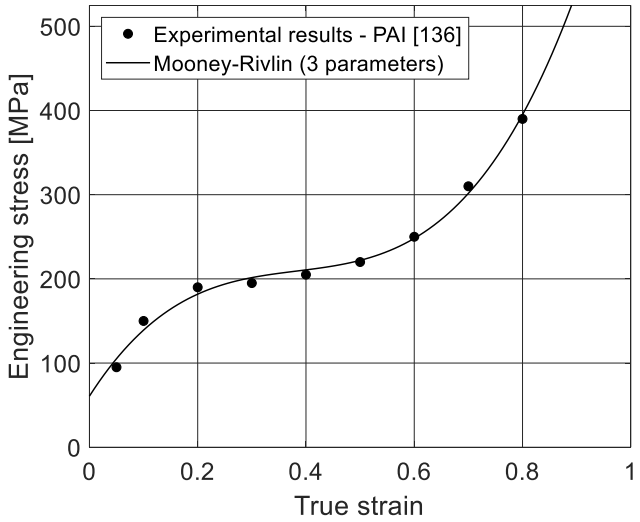

Figure 3.4. Stress-strain behavior of PAI under uniaxial loading.

3.3.4 Interface modeling

The most important factor determining the advantage of SWCNs in improving the properties of polymers at the nanoscale level is the efficiency of the transfer of loads from the matrix to nanotubes, which occurs through the interface region between the nanostructure and the polymer matrix. From the atomistic point of view, the governing interactions between the SWCN and the surrounding polymer are weakly nonbonded van der Waals (vdW) interactions in the absence of chemical functionalization [137]. If the covalent cross-links between the carbon atoms of the nanotube and the molecules of the polymer are introduced, the functionalization process can enhance the load transferring ability [138]. However, for convenience in the calculations, just the vdW interactions between the nanotube and the inner surface of the polymer matrix are considered. Therefore, the interface region is treated as that providing the nonbonded interactions and is modeled using vdW interactions. From the structural point of view, the interface can be simulated either as a continuum or as a discrete region. However, in this chapter the interface region is represented with the use of truss finite elements, also called LINK elements in commercial software ANSYS®, connecting carbon atoms of the discrete structure of the SWCN to nodes of the internal surface of matrix elements. COMBIN39 element, which is shown in Figure 3.2(d), is used to model trusses, links, and springs and it is a uniaxial tension-compression element with three degrees of freedom at each node: translations in the nodal x, y, and z directions. For simulations of van der Waals interactions at the nanotube-polymer interface, a truss element model, which was introduced in Ref. [76], is adopted. The properties of the LINK elements, shown in Figure 3.5, are obtained by using the corresponding van der Waals forces based on the Lennard-Jones potential, which is expressed as [83]:

$$U(r) = 4\tilde{\varepsilon}\left[\left(\frac{\tilde{\sigma}}{r}\right)^{12} - \left(\frac{\tilde{\sigma}}{r}\right)^{6}\right] \tag{3.6}$$

where r is the distance between interacting atoms of the nanotube and the polymer, $\tilde{\varepsilon}$ and $\tilde{\sigma}$ are the Lennard–Jones parameters. For carbon atoms, the Lennard–Jones parameters are $\tilde{\varepsilon}$ = 0.0556 kcal/mole and $\tilde{\sigma}$ = 3.4 Angstroms. Based on the Lennard-Jones potential, the van der Waals force F_{vdW} between interacting atoms is determined as follows:

$$F_{vdW}(r) = -\frac{dU(r)}{dr} = 24\frac{\tilde{\varepsilon}}{\tilde{\sigma}}\left[2\left(\frac{\tilde{\sigma}}{r}\right)^{13} - \left(\frac{\tilde{\sigma}}{r}\right)^{7}\right] \tag{3.7}$$

The activation of the truss element in the computational simulation is determined by the distance between an atom (a node) in the nanotube and a node in the internal surface of the polymer matrix, such that if this distance is less than $2.5\tilde{\sigma}$ (0.85 nm), the truss element is activated. A macro file is written using Python language to create the interface, which can be appreciated in Figure 3.1(d), in the finite element modeling. The number of elements of the interface region is 7560.

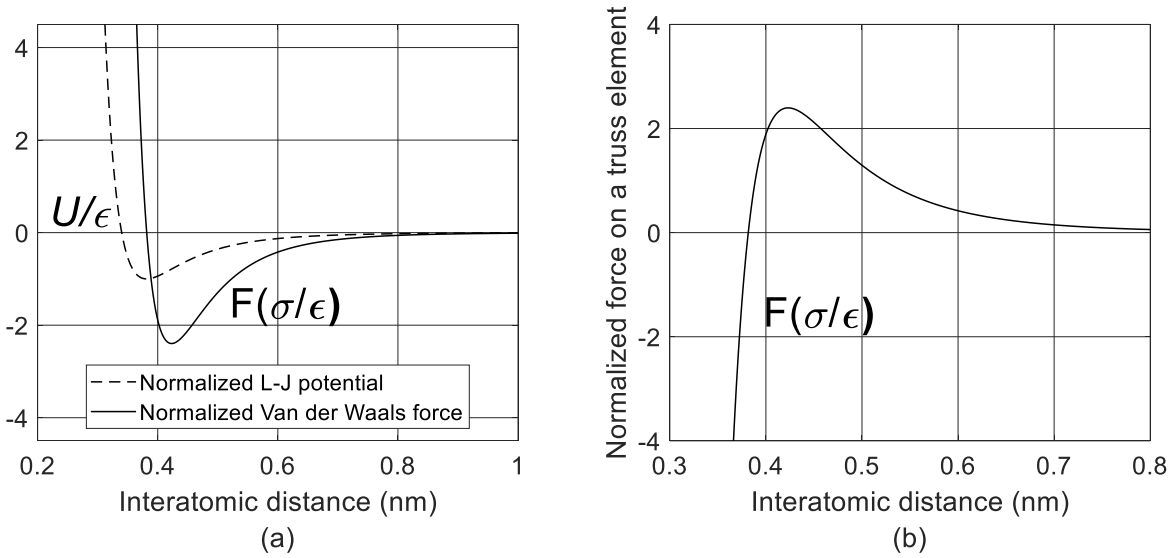

Figure 3.5. (a) Lennard–Jones potential and van der Waals force versus interatomic distance, (b) Load-displacement curve of the nonlinear truss element.

3.4 Damping properties of CNRP

3.4.1. Concept of ‘‘stick-slip’’ behavior

The “stick-slip” mechanism in a nanocomposite is shown in Figure 3.6. When normal tensile stress is applied to a composite, this mechanism starts elongating (showing an increase in its length denoted as ΔL_n). Because of this applied stress, the polymer matrix, in turn, applies shear stress,

τ, on the nanotube, thus causing the load transfer to the nanotube. Consequently, a normal strain develops in the nanotube, which elongates accordingly. When the applied stress is small, the nanotube remains fully bonded to the polymer matrix. Both the polymer matrix and the nanotube move together during this phase, and the strains are equal in both elements. As the applied stress is increased, the shear stress on the nanotube increases. At a certain value of shear stress (called the critical shear stress, τ_{cr}), the nanotube debonds from the polymer matrix. When the shear stress on the nanotube increases beyond this value (because of increased applied stress), the polymer matrix starts flowing over the surface of the nanotube (thereby causing a change in its length denoted as ΔL_{Cn}). The strain in the nanotube remains constant at its maximum level, while the strain in the polymer matrix increases (slipping phase). In this phase, there is no load transfer between the nanotube and the polymer matrix, but there is energy dissipation due to the slippage. Because of this energy dissipation, the so-called structural damping develops in the nanocomposite.

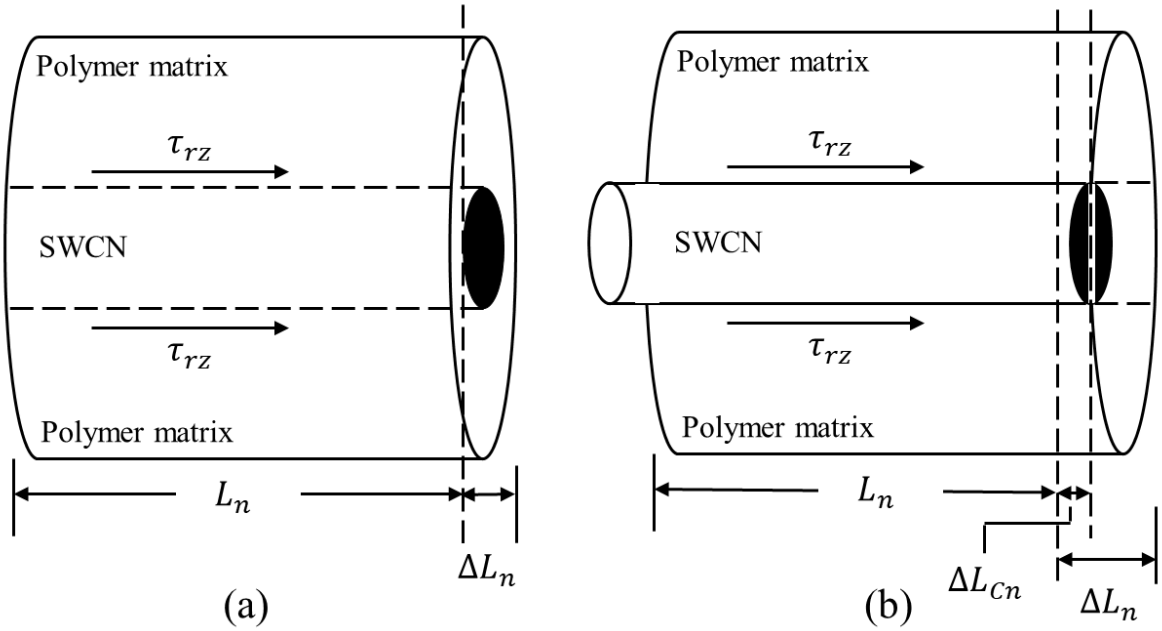

Figure 3.6. Stick-slip behavior of SWCN-based composite: (a) when $\tau_{rz} <$ critical shear stress τ_{cr} and (b) when $\tau_{rz} >$ critical shear stress τ_{cr}.

3.4.2 Loss factor and damping ratio

As described in the sub-section 3.4.1, one of the important causes of damping in the nanotube-reinforced composite is the friction between the nanotube and matrix. Dissipated energy via interfacial movement of nanotube and matrix is equivalent to the shear force and the differential displacement between the nanotube and matrix. To determine the loss factor η, the total dissipation energy (U_{diss}), and dissipation energy (ΔU), the following equations can be used [139]:

$$\eta = sin^{-1}\left(\frac{\Delta U}{2\pi U_{diss}}\right) \tag{3.8}$$

$$U_{diss} = \int_V \frac{\sigma_{ij}\varepsilon_{ij}}{2} dV \tag{3.9}$$

$$\Delta U = 2\tau_{cr}(2r_n L_n^2)(\varepsilon_0 - \varepsilon_2) \tag{3.10}$$

where r_n is the radius of the nanotube, L_n is the length of the nanotube, ε_0 is the strain of matrix material due to loading, ε_2 is the strain between the nanotube and polymer matrix and τ_{cr} is the maximum value of bonding stress (shear stress) τ_{rz} associated with the longitudinal shear stress between nanotube and matrix material, which is obtained when the maximum normal stress and strain are reached due to loading. Hence, τ_{cr} can be calculated as a function of ε_2 as follows [139]:

$$\tau_{cr} = E^{eq} \cdot \varepsilon_2 \int_0^{L_n/2} \frac{sinh\big(\beta(L_n/2 - z)\big)}{cosh(\beta\, L_n/2)} dz \sqrt{\frac{G_0}{E^{eq}} \frac{1}{2ln(r_m/r_n)}} \tag{3.11}$$

where r_m is the radius of the polymer matrix; G_0 is the shear modulus of matrix material (G_0 = 0.2 *GPa* for polymers) and E^{eq} is the equivalent modulus of nanotube which can be calculated as: $E^{eq} = 2t_n E_n/r_n$, where t_n is the thickness of carbon nanotube, E_n is Young's modulus of the nanotube. Parameter β can be obtained from the following equation [140]:

$$\beta = \left(\frac{G_0 2\pi}{E^{eq} A ln(r_m/r_n)}\right)^{1/2} \tag{3.12}$$

where $A = (2V_n/r_n)V$ is the contact area between the nanotube and polymer matrix and V is the volume of the polymer matrix and V_n is the volume fraction of nanotube. τ_{cr} can also be determined if a tensile displacement is applied to one side of the RVE when the other side is clamped. The displacement is applied until the nanotube strain, and polymer matrix's strain become different. At that strain, the maximum shear stress τ_{cr} occurs. Hence, the strain ε_2, between the nanotube and the polymer matrix, is obtained as follows:

$$\varepsilon_2 = \frac{\tau_{cr}(L_n/2)}{E^{eq}\int_0^{L_n/2}\frac{sinh\left(\beta(L_n/2-z)\right)}{cosh(\beta\, L_n/2)}dz\sqrt{\frac{G_0}{E^{eq}}\frac{1}{2ln(r_m/r_n)}}} \tag{3.13}$$

The total dissipation energy U_{diss} and dissipation energy ΔU are calculated from equations (3.9) and (3.10), respectively, with the numerical values of τ_{cr}, ε_2 and tensile stress at each strain level of the applied tensile displacement. The loss factor η is then determined from equation (3.8) with the values of U_{diss} and ΔU. Using the numerical values of the loss factor η, it is possible to determine the quality factor Q^{-1}, which is used for estimating the interfacial damping ratio ζ, as follows [141]:

$$Q^{-1} = \sqrt{1+\eta} - \sqrt{1-\eta} \tag{3.14}$$

Here, η represents the loss factor. Using the numerical value of the quality factor Q^{-1}, the interfacial damping ratio ζ is then determined by the relation [142]:

$$\zeta = Q^{-1}/2 \tag{3.15}$$

3.5 Dynamic analysis

3.5.1 Free vibration response

The generalized equation of motion for the CNRP system is given as follows [142]:

$$[M]\{\ddot{u}\} + [C]\{\dot{u}\} + [K]\{u\} = \{F\} \tag{3.16}$$

where $[M]$ is the mass matrix, $\{\ddot{u}\}$ is the acceleration vector, $[C]$ is the damping matrix, $\{\dot{u}\}$ is the velocity vector, $[K]$ is the stiffness matrix, $\{u\}$ is the displacement vector, and $\{F\}$ is the force vector. Modal analysis is used for the determination of the natural frequencies and mode shapes while the damping is ignored. The equation of motion for an undamped system under free motion is given by:

$$[M]\{\ddot{u}\} + [K]\{u\} = \{0\} \tag{3.17}$$

For a linear system, free vibrations can be harmonic with the following form:

$$\{u\} = \{\varphi\}_i cos(\omega_{n_i} t) \tag{3.18}$$

where $\{\varphi\}_i$ is the vector of the mode shape for the *i*th natural frequency ω_{n_i} and t is the time. Thus, Equation (3.17) can be expressed as:

$$\left(-\omega_{n_i}^2[M] + [K]\right)\{\varphi\}_i = \{0\} \tag{3.19}$$

This equality is satisfied if $\left|[K] - \omega_{n_i}^2[M]\right| = 0$. Hence, this matrix equation represents an eigenvalue problem which can be solved for *n* values of ω_n^2 and *n* eigenvectors which satisfy the Equation (3.17), where *n* is the number of degrees of freedom. Block Lanczos method [143] is used for the extraction of the eigenvalues and eigenvectors, and the normalization of each eigenvector is performed concerning the mass matrix according to:

$$\{\varphi\}_i^T [M]\{\varphi\}_i = 1 \tag{3.20}$$

3.5.2 Steady-state harmonic response

Regarding the steady-state harmonic response [144], harmonic analysis is used to determine the steady-state response of a mechanical system under loads that vary sinusoidally (harmonically) as a function of time. The objective of this analysis is to calculate the CNRP system's response at several frequencies and to obtain a graph of a response quantity (usually displacement) versus

frequency. The steady-state harmonic response is obtained from the equation of motion, given by Equation (3.16), where the force vector $\{F\}$ can have three components F_j (j = 1,2,3), which are expressed as follows:

$$F_j = F_{0\mathrm{j}} sin(\omega_j t) \tag{3.21}$$

where $F_{0\mathrm{j}}$ is the amplitude of the force and ω_j denotes the excitation frequency. $F_{0\mathrm{j}}$ can be calculated by performing an eigenvalue buckling analysis in the undamped CNRP system to obtain the critical compressive loads that induce the different ways in which the structural system can be deformed. The harmonic analysis used to calculate the steady-state harmonic response utilizes the full system matrices so that no mass matrix approximation is involved [144]. The particular solution for a 1D equation of motion is a steady-state oscillation having the same frequency ω as the exciting force and a phase angle ϕ and it can be written as follows:

$$x_p = Xcos(\omega t - \phi) \tag{3.22}$$

where

$$X = \frac{F_0}{\sqrt{(k - m\omega^2)^2 + (c\omega)^2}} \tag{3.23a}$$

$$\phi = tan^{-1}\left(\frac{c\omega}{k - m\omega^2}\right) \tag{3.23b}$$

where k is the stiffness of the system, and m is the mass of the system. Using the natural frequency ω_n of the system and the damping ratio ζ, the following expressions can be defined:

$$X_0 = \frac{F_0}{k} \tag{3.24a}$$

$$r = \frac{\omega}{\omega_n} \tag{3.24b}$$

where X_0 is the deflection under the static force F_0 and r is the frequency ratio. Thus, an equation for the magnification factor *M* can be determined as follows:

$$M = \frac{X}{X_0} = \frac{1}{\sqrt{(1-r^2)^2 + (2\zeta r)^2}} \tag{3.25}$$

and the phase angle ϕ is expressed as:

$$\phi = tan^{-1}\left(\frac{2\zeta r}{1-r^2}\right) \tag{3.26}$$

3. 6 Results and discussion

3.6.1 Stress-strain behavior of CNRP

Regarding the Carbon-Nanotube-Reinforced-Polymer (CNRP) properties, the stress-strain curve of a polymer matrix, Polyamide-imide (PAI), that is reinforced with a (16, 0) SWCN or a (9, 9) SWCN, is determined based on modeling the nanotube as a thin shell based on Donnell's Shell Theory. The RVE is loaded under, and the volume of the polymer is varied to investigate the effect of SWCN volume fraction on the mechanical properties of the CNRP material. The boundary conditions of CNRP correspond to a cantilever, where the translational and rotational movements of one end of the matrix are prevented, while the other end is free to move so that the SWCN transfers its mechanical properties onto the matrix via the vdW links. The length of the CNRP material is 10 nm. The diameter of the (16, 0) SWCN is 1.2535 nm, while the diameter of the (9, 9) SWCN is 1.2213 nm. Hence, the aspect ratio (that is defined as length of nanotube/diameter of nanotube) of the (16, 0) SWCN is 7.977 and the aspect ratio of the (9, 9) SWCN is 8.187.

The CNRP material reinforced with a (16, 0) SWCN is analyzed considering the polymer material with different volume fractions of nanotubes, and the results are given in Figure 3.7(a). It can be noticed in Figure 3.7(a) that the addition of nanotube, into the PAI matrix (CNRP-PAI) improves the load-carrying capacity of the matrix material PAI. Nanotube has better tensile properties compared to the polymer so that when the SWCN is combined with the polymer

material, it improves the overall mechanical properties of the nanocomposite material by sharing some of the applied stress. Figure 3.7(b) shows the stress-strain curves for CNRP-PAI reinforced with a (9, 9) SWCN for different volume fractions and a length of 10 nm. It can be appreciated that the stress-strain curves also confirm that the (9, 9) SWCN acts as a better reinforcing agent when compared to the (16, 0) SWCN. Regarding Young's modulus of CNRP-PAI, Young's modulus of PAI increased with a (16, 0) SWCN as a reinforcement from 2.56 GPa to 4.39 GPa for 1% of SWCN volume fraction and from 2.56 GPa to 60 GPa for 10% of SWCN volume fraction. Using a (9, 9) SWCN as a reinforcement, Young's modulus of PAI increased from 2.56 GPa to 4.99 GPa for 1% of SWCN volume fraction and from 2.59 GPa to 78.52 GPa for 10% of SWCN volume fraction. In Appendix A, a convergence study is provided regarding the element size (and the number of elements) of the finite element model of the polymer matrix that is used to discretize the RVE of the CNRP material. The convergence analysis is performed for the CNRP with 5% volume fraction of SWCN. The reinforcement used for this analysis is a (16, 0) SWCN. The convergence analysis is conducted for the non-linear analysis of the stress-strain curve and Young's modulus of the CNRP, and its first bending and first axial mode frequencies. The convergence study shows that the number of elements used to discretize the RVE of the CNRP are suitable and appropriate to study its stiffness, free vibration response, and steady-state harmonic response.

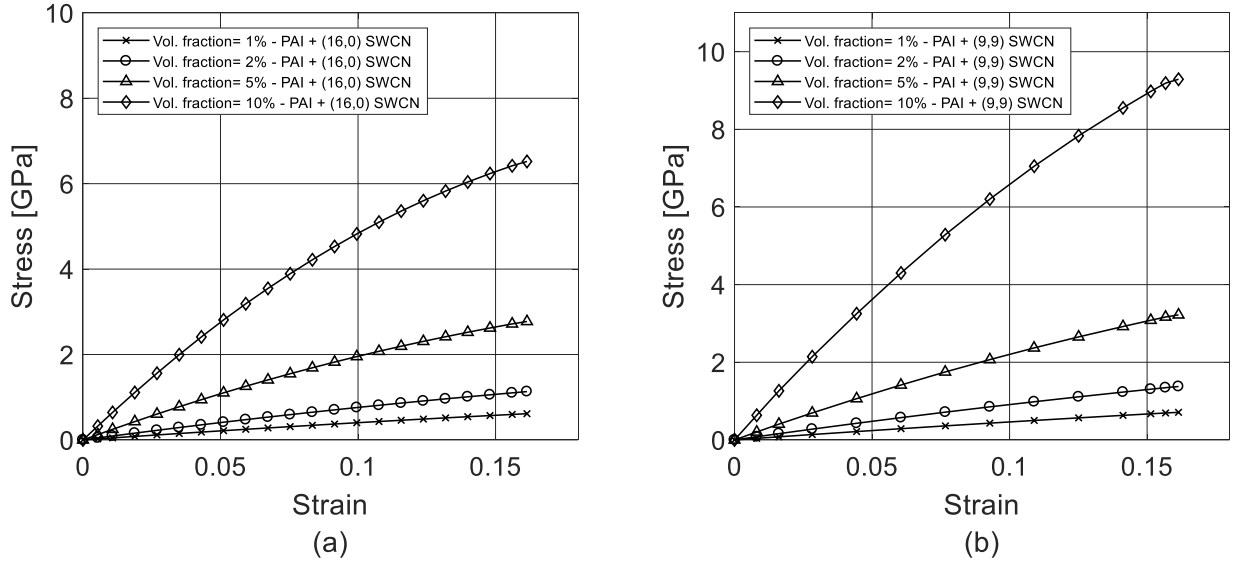

Figure 3.7. Stress-strain curves for CNRP for different (a) (16, 0) SWCN and (b) (9, 9) SWCN volume fractions.

3.6.2 Natural frequencies of CNRP

The changes in the natural frequencies of the matrix material caused by the addition of 1%, 2%, 5% and 10% volume fractions of SWCN are studied in this section. A modal analysis is performed for the RVE of the CNRP nanocomposite and the PAI material to investigate the influence of SWCN on the natural frequencies of the polymeric material. The Block Lanczos method [143], which is often utilized in analyses where high accuracy is required, is used to perform the modal analysis. Clamped-Free (CF) boundary conditions are applied to the 3D multiscale finite-element model of the RVE of the CNRP material and the polymer material. In this case, two configurations of the nanotube are also considered: armchair (9, 9) and zigzag (16, 0), as in the last section. The variations of the natural frequencies of the plain PAI material and the nanocomposite material CNRP-PAI are shown in Figure 3.8. It can be appreciated from Figure 3.8 that the natural frequencies for the first and second mode numbers of the CNRP with both reinforcements, (16, 0) SWCN and (9, 9) SWCN, present almost the same numerical values for 1%, 2%, 5% and 10% volume fractions of SWCN. However, from 3rd mode number onward, the values of the natural frequencies increase considerably due to the presence of higher volumes of SWCN.

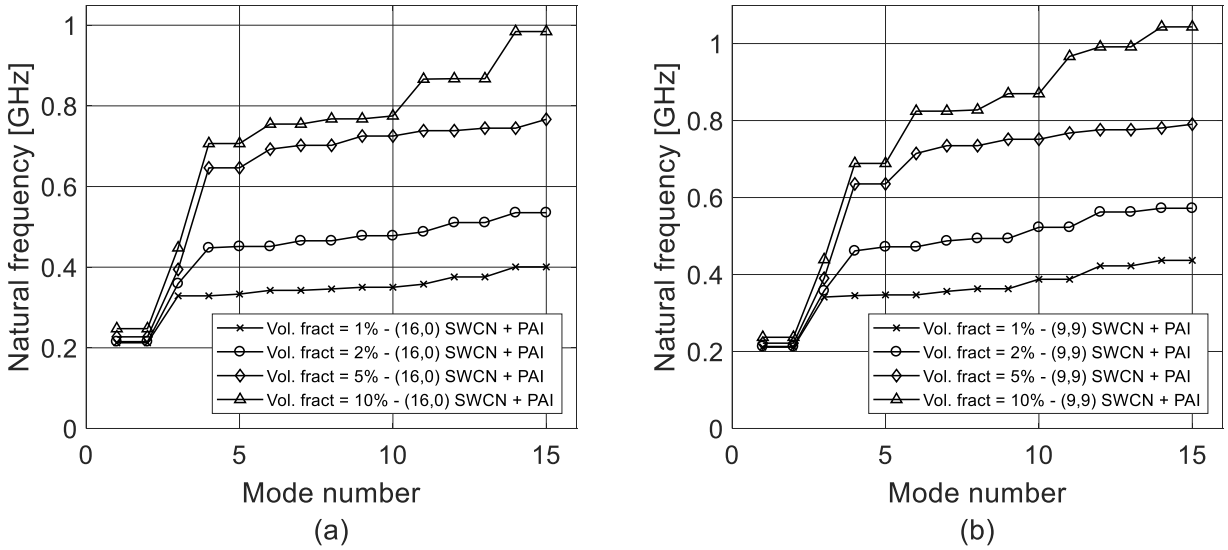

Figure 3.8. Natural frequencies for CNRP-PAI with CF boundary condition containing: (a) (16, 0) SWCN and (b) (9, 9) SWCN.

Also, the percentage increase in the natural frequencies of the first 15 modes of the polymer material with 5% of SWCN volume fraction is tabulated in Table 3.1. It is observed from Table 3.1 that the addition of nanotubes significantly improves the natural frequencies of the polymer material, especially for the first mode number, which is the first bending mode frequency. This is attributed to the high stiffness of the carbon nanotube reinforced polymer compared to that of the plain polymeric material. For CNRP-PAI the frequencies increase in a range of 52.53-140.88% with (16, 0) SWCN as reinforcement and a range of 55.85-135.0% with (9, 9) SWCN as reinforcement. If the first bending mode frequency is analyzed in detail, it can be noticed that for CNRP-PAI, the corresponding natural frequency increases by 140.88% due to reinforcement with (16, 0) SWCN, while for reinforcement with (9, 9) SWCN, the first bending mode frequency increases by 135.0%. For the first axial mode (4th mode number), the corresponding natural frequency increases by 95.43% due to reinforcement with (16,0) SWCN and by 92.11% with (9, 9) SWCN as reinforcement.

Table 3.1: Comparison of natural frequencies with 5% SWCN volume fraction of polymer matrix PAI and CNRP-PAI in GHz.

Mode	PAI	CNRP-PAI (16, 0) SWCN	(%) Increase	CNRP-PAI (9, 9) SWCN	(%) Increase
1	**0.094**	**0.227**	**140.88**	**0.222**	**135.00**
2	0.094	0.227	140.88	0.222	135.00
3	0.233	0.394	69.19	0.390	67.42
4	**0.331**	**0.646**	**95.43**	**0.635**	**92.11**
5	0.366	0.646	76.58	0.635	73.58
6	0.366	0.693	89.23	0.714	95.19
7	0.471	0.702	48.96	0.735	55.85
8	0.471	0.702	48.96	0.735	55.85
9	0.471	0.725	53.85	0.751	59.39
10	0.471	0.725	53.85	0.751	59.39
11	0.484	0.739	52.53	0.768	58.54
12	0.484	0.739	52.53	0.776	60.27

13	0.484	0.745	53.81	0.776	60.27
14	0.484	0.745	53.81	0.781	61.23
15	0.491	0.767	56.16	0.790	60.99

3.6.3 Damping properties of CNRP

Considering the stick-slip behavior, which was described in sub-section 3.4.1, that is exhibited by the SWCN and the polymer matrix, one side of the RVE is clamped, and the other side is pulled by applying a displacement in the axial direction. It can be observed that, up to a certain strain in the finite element model, the nodes of nanotube and corresponding nodes of the polymer matrix, have similar displacement, and by increasing the strain, at the interface of matrix and nanotube slip occurs. Because of this, the displacement of matrix nodes will be larger than that of the corresponding nodes of the nanotube.

Damping properties can be obtained, if the RVE behaves exactly as per the mechanism of stick-slip motion and follows the equations that govern this mechanism. From the results of finite element simulations, the critical shear stress τ_{cr} and dissipation energy U_{diss} are determined and used with the model properties of the CNRP such as radius, area, and Young's modulus to calculate the interfacial damping ratio from the equations given in sub-section 3.4.2. The dissipation energy and loss factor of the CNRP for different SWCN volume fractions of (16, 0) SWCN and (9, 9) SWCN are investigated, and the results are shown in Figures 3.9(a) and 3.9(b), respectively. It can be noticed that the dissipation energy increases due to nanocomposite's strain, where the magnitude of the increase is lower when SWCN volume fraction decreases. The loss factor decreases due to nanocomposite's strain, and the magnitude of the decrease is higher when SWCN volume fraction decreases for both types of carbon nanotubes. By increasing the volume fraction, it appears that the SWCNs influence positively in the dissipation energy and results in decreasing the loss factor, which means that by adding more SWCNs more damping capacity of CNRP is achieved.

In Figure 3.9(a), the dissipation energy presents a similar value for strains lower than 0.05 for all volume fractions of both SWCNs in the CNRP, while for strain values higher than 0.05, there is a difference in the dissipation energy values for all volume fractions of SWCNs in the CNRP, especially for 10% volume fraction. In Figure 3.9(a), the dissipation energy corresponding

to 10% volume fraction of (9, 9) SWCN is also considerably higher than the dissipation energy corresponding to 10% volume fraction of (16, 0) SWCN for strain values higher than 0.05. In Figure 3.9(b), the values of loss factor are similar for strain values higher than 0.125 for all volume fractions of both SWCNs, thus exhibiting the same volume fraction effect beyond this strain value.

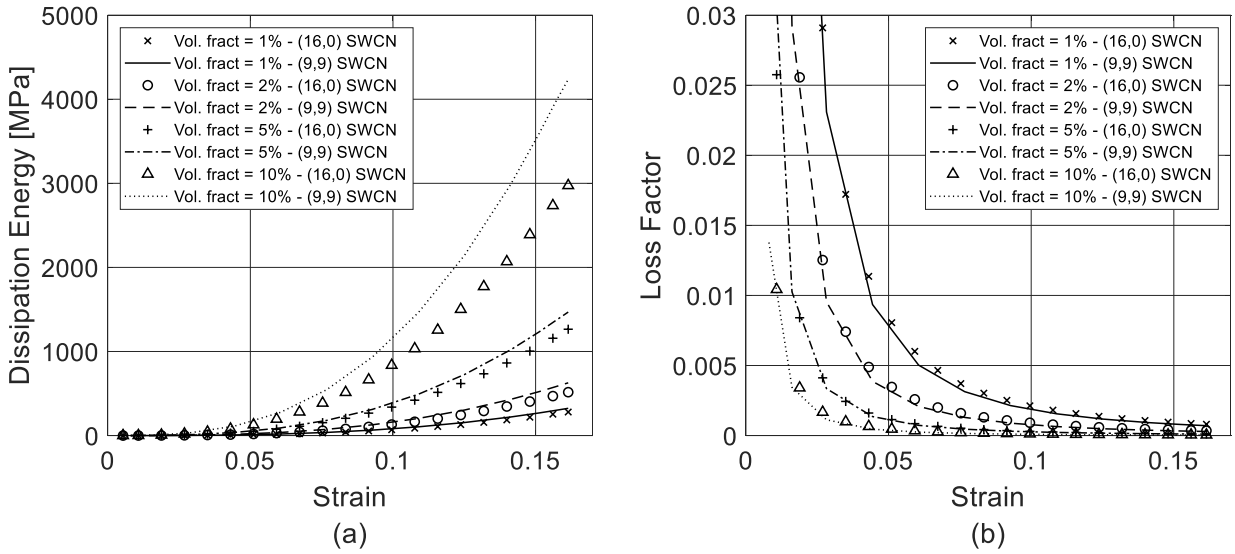

Figure 3.9. (a) Dissipation energy and (b) loss factor for CNRP-PAI for different volume fractions of (16, 0) SWCN and (9, 9) SWCN.

Regarding the damping ratio, Figure 3.10 shows the influence of SWCN volume fraction on the damping ratio for the CNRP as a function of natural frequencies. It can be noticed that there are different values for the damping ratio for different SWCN volume fractions for any natural frequency value. In the case of (16, 0) SWCN, the values for the damping ratio are within a range of 0.0021 (for 10% volume fraction) - 0.0863 (for 0.1% volume fraction). In the case of (9, 9) SWCN, the values for the damping ratio are within a range of 0.0007 (for 10% volume fraction) - 0.0436 (for 0.5% volume fraction). In Figures 3.10(a) and 3.10(b), it can be appreciated that the values of damping ratios decrease with higher values of natural frequencies for all volume fractions of CNRP. In the natural frequency range from 0.6 GHz to 0.8 GHz in Figure 3.10(a), it can also be noticed that the volume fraction effect (for 5% and 10%) is same with (16, 0) SWCN, however in Figure 3.10(b), the volume fraction effect is not same with (9, 9) SWCN. Comparing values of damping ratios for 5% volume fraction of (16, 0) SWCN and (9, 9) SWCN in Figure 3.10, it can

be observed that the reinforcement with (16, 0) SWCN presents lower values of damping ratios than the reinforcement with (9, 9) SWCN.

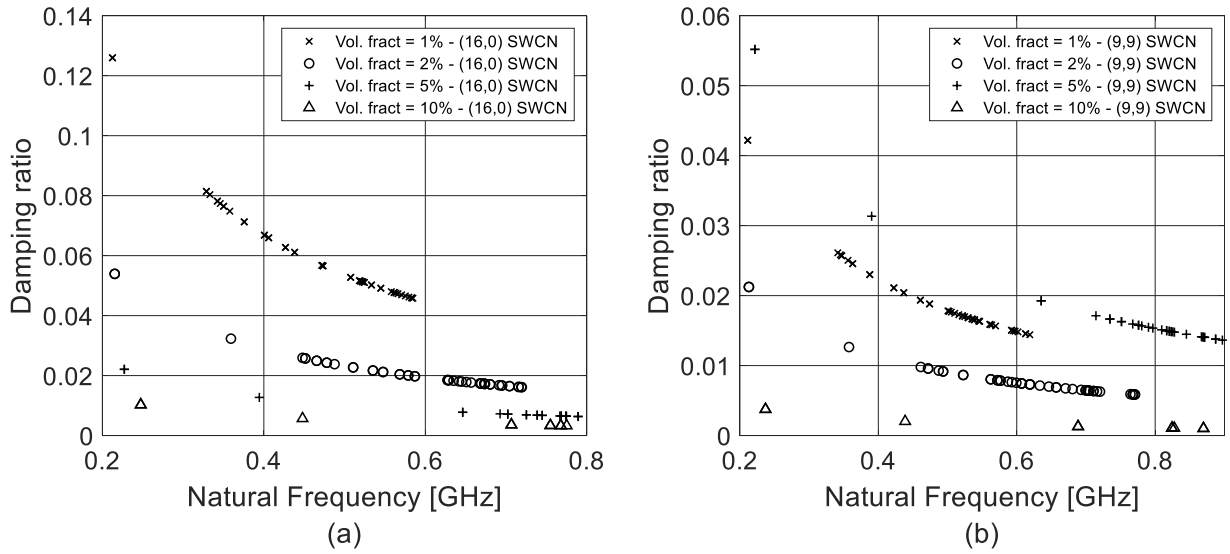

Figure 3.10. Damping ratio for CNRP-PAI with CF boundary condition containing different volume fractions of (a) (16, 0) SWCN and (b) (9, 9) SWCN.

The damping ratio of the CNRP with 5% volume fraction of (16, 0) SWCN are compared in Table 3.2 with that of the 5% volume fraction of (10, 0) SWCN-epoxy [104], which consists of a polymer matrix (Young's modulus = 3.3 GPa and Poisson's ratio = 0.3), and a (10, 0) SWCN with length of 10 nm. It can be appreciated from Table 3.2 that the CNRP shows similar natural frequencies as the natural frequencies of (10, 0) SWCN-epoxy, but different values of damping ratios. The values of natural frequencies of (10, 0) SWCN-epoxy are 0.35, 0.76 and 1.619 GHz, while for (16, 0) SWCN-PAI, the CNRP studied in the present chapter, the values are 0.271, 0.775 and 0.995 GHz.

Table 3.2. Comparison of damping ratios of CNRP-PAI with 5% volume fraction of SWCN and 5% SWCN-epoxy [104] as a function of natural frequencies (GHz).

5% (10, 0) SWCN - Epoxy [104]		CNRP-PAI - 5% (16, 0) SWCN	
Natural Frequency	Damping ratio	Natural Frequency	Damping ratio
0.35	0.0032	0.271	0.0442
0.76	0.0033	0.775	0.0157
1.619	0.0037	0.995	0.0122

3.6.4 Steady-state harmonic response of CNRP

Regarding the computation of the steady-state harmonic response, the boundary conditions for a 5% (16, 0) SWCN reinforced polymer and the polymer material are defined for an axial and a transversal sinusoidal forces with amplitude $F_0 = 1x10^8 N$ and an excitation frequency ω in the range of 0 - 4 GHz. The boundary conditions are applied as a cantilever, where at one end of the cylindrical RVE only the nodes of the polymer matrix are fully restrained; while, at the other end of the RVE a sinusoidal force is applied on the polymer matrix for axial and bending motions. Figures 3.11(a) and 3.11(b) show the results of the harmonic analysis of CNRP and PAI material RVEs applying an axial and a transversal sinusoidal forces, whereas the natural frequencies of CNRP are higher than that of PAI, the amplitudes of vibrations of CNRP are lower than that of PAI due to the reinforcement with the nanotubes.

In Figure 3.11, the axial vibration amplitude of CNRP decreased by about 69%, while the amplitude of the transversal vibration decreased by about 85% from that of PAI. Figure 3.12(a) shows the magnification factor M [144] as a function of frequency ratio ($r = \omega/\omega_n$) for each natural frequency ω_n (of first bending and first axial mode frequencies) of CNRP with (16, 0) SWCN as the reinforcement, considering their respective damping ratios, which were calculated in sub-section 3.6.3. Figure 3.12(b) shows the phase angle [144] of response for CNRP as a function of frequency ratio ($r = \omega/\omega_n$). It can be noticed that the phase angle is higher for first bending mode than for first axial mode for CNRP due to its damping, which also reduces the value of the magnification factor. Table 3.3 summarizes the information about the natural frequencies and damping ratios used for calculating the maximum value of magnification factor M and also

the damped natural frequency $\omega_d = \omega_n\sqrt{1-\zeta^2}$. It can be noticed that any amount of damping $\zeta > 0$ reduces the magnification factor M for all the values of the forcing frequency ω. For $0 < \zeta < 1/\sqrt{2}$, the maximum value of M occurs when $r = \sqrt{1-2\zeta^2}$. Furthermore, the maximum value of M (when $r = \sqrt{1-2\zeta^2}$) is given by $M = 1/2\zeta\sqrt{1-\zeta^2}$. For the CNRP, the maximum value of M for the first bending mode is 9.72, and for the first axial mode it is 230.4, while the damped natural frequency ω_d is 0.2266 GHz for the first bending mode and 0.6459 GHz for the first axial mode. It can be appreciated that the magnification factor for the first axial mode is 23 times higher than the magnification factor for the first bending mode.

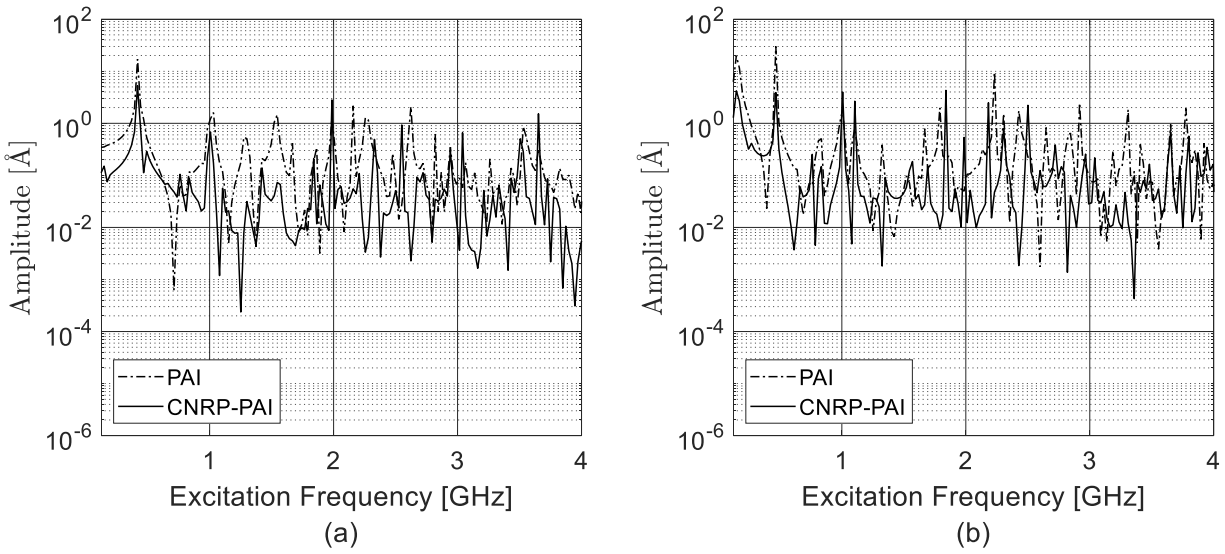

Figure 3.11. The steady-state harmonic response of the CNRP-PAI and PAI with (a) an axial and (b) a transversal sinusoidal force with amplitude $F_0 = 1x10^8N$ and excitation frequency ω in the range of 0 - 4 GHz.

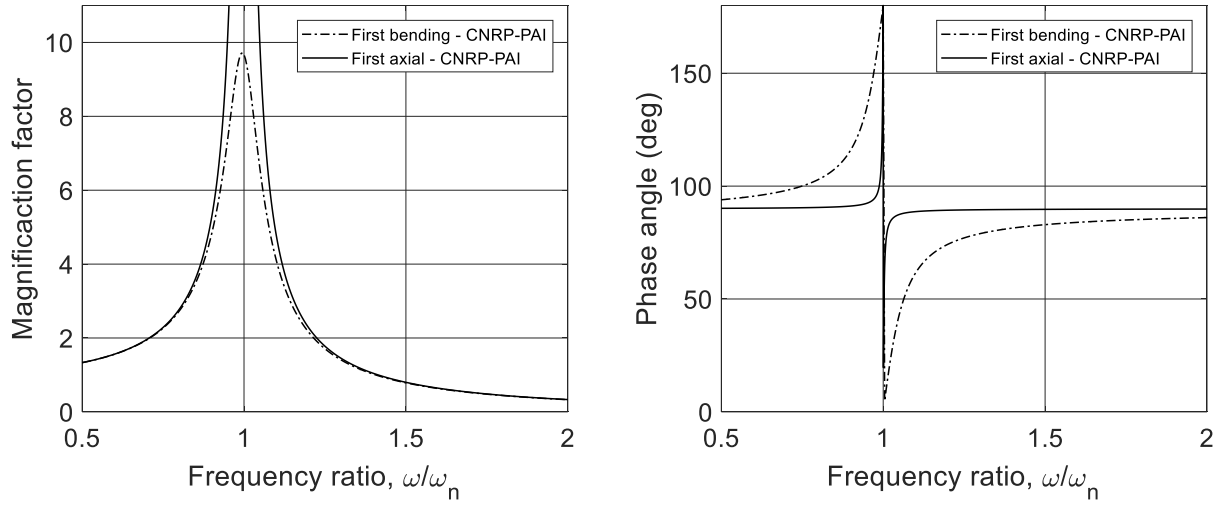

Figure 3.12. Magnification factor and phase angle as a function of natural frequencies (first bending and first axial mode) of CNRP-PAI.

Table 3.3. Natural frequencies and damping ratio used for calculating magnification factor *M*.

Mode	ω_n (GHz)	Damping ratio ζ	Maximum value of *M*	ω_d (GHz)
First bending	0.227	0.0517	9.72	0.2266
First axial	0.646	0.00217	230.41	0.6459

3.7 Conclusion

The main objective of the present chapter was to study the influence of a Single-Walled-Carbon-Nanotube (SWCN) as reinforcement in a polymer matrix. The analysis was performed on a Representative Volume Element (RVE) of the Carbon-Nanotube-Reinforced-Polymer (CNRP) material to determine its modal and harmonic response, considering different volume fractions of SWCNs. Regarding the mechanical behavior of CNRP, static analysis was performed on the CNRP material to obtain its stress-strain curve for different volume fractions of (16, 0) SWCN and (9, 9) SWCN. Cantilever boundary conditions were applied onto the CNRP material, and its first 15 vibration modes were determined and compared in free vibration analysis. The results show an increase in the natural frequencies of the CNRP for all volume fractions of SWCN, with both types

of reinforcements, that are, (16, 0) SWCN and (9, 9) SWCN. Also, the natural frequencies of CNRP with 5% volume fraction of SWCN were compared to that of polymer material PAI, and an increase in the natural frequencies of PAI is observed, especially for the first bending mode due to the reinforcement with both types of nanotubes.

Regarding the damping properties of CNRP, the concept of the stick-slip motion behavior was used to obtain the critical shear stress, dissipation energy, and loss factor in order to calculate the interfacial damping ratio of CNRP for different volume fractions of (16, 0) SWCN and (9, 9) SWCN. The dissipation energy and loss factor were analyzed for all volume fractions of both SWCNs in the CNRP material. The influence of SWCN volume fraction on the damping ratio of the CNRP as a function of the natural frequencies of CNRP was also analyzed and compared with the results available in the literature. The values of damping ratios of the CNRP material decrease with higher values of natural frequencies of the CNRP for all volume fractions of the SWCN. Comparing the values of damping ratios of the CNRP for 5% volume fraction of (16, 0) SWCN and (9, 9) SWCN, it was observed that the reinforcement with a (16, 0) SWCN presents lower values of damping ratios than the reinforcement with a (9, 9) SWCN.

In the harmonic analysis, the results expose that the amplitude of the vibration for the CNRP (PAI with a (16, 0) SWCN as reinforcement) decreased considerably due to the reinforcement with the SWCN, while for the polymer material the amplitude of the vibration was a lot higher. Regarding the magnification factor and phase angle, these parameters were determined considering the damping ratios calculated for the CNRP material. The maximum values for the magnification factor and damped natural frequency were obtained for first bending and first axial mode frequencies of CNRP, where it was also noticed that the maximum value for the magnification factor depends on the value of damping ratio. From the results for the phase angle, it can be noticed that this parameter takes on a higher value for the first bending mode frequency than the first axial mode frequency of the CNRP material due to its damping ratio, which also reduces the value of the magnification factor.

Appendix 3.1 Convergence study

A convergence study is performed on the finite element model of the RVE of the CNRP material with 5% volume fraction of SWCN to determine the most reliable and accurate size of the finite elements of the polymer matrix in the CNRP material that can be used to discretize the

RVE. The reinforcement used in this analysis is a (16, 0) SWCN. Figure 3.13 shows the element size used to discretize the RVE where the element length is denoted by L_p and element width by w_p. Considering that the shape of the element of the RVE is not rectangular but trapezoidal, the element size is determined with the coordinates of its nodes. The element length L_p is determined using a straight line that runs from the bottom surface to the top surface of the element, as shown in Figure 3.13. The element width w_p is considered to be equal to that of the bottom surface of the element, as shown in Figure 3.13.

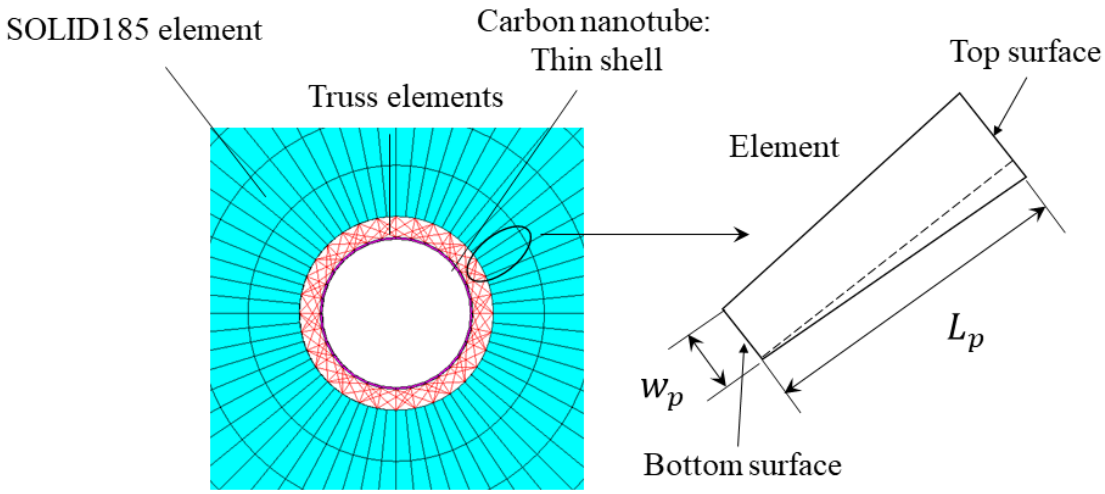

Figure 3.13. Aspect ratio of the element of the polymer matrix in the CNRP material.

The convergence analysis is performed for the non-linear analysis of the stress-strain behavior and Young's modulus of the CNRP material. The largest element size of the polymer matrix is determined in terms of the aspect ratio w_p/L_p. The numerical values of the aspect ratio w_p/L_p of the element in the mesh used in the convergence, study are: 0.125 which corresponds to 12160 elements, 0.15 which corresponds to 18240 elements, 0.175 which corresponds to 24320 elements, 0.2 which corresponds to 30400 elements, 0.375 which corresponds to 36480 elements and 0.5 which corresponds to 42560 elements. Figure 3.14 shows the convergence of the stress-strain curve and Young's modulus. It can be appreciated from Figure 3.14(a) that the stress-strain curves of the CNRP for all aspect ratios of the element are very close to each other. However, as shown in Figure 3.14(b), Young's modulus takes on different numerical values for w_p/L_p values lower than 0.375, and the same numerical value for values of w_p/L_p higher than 0.375. Therefore,

the element size used to discretize the RVE of the CNRP corresponds to 0.375, which in turn corresponds to 36480 elements, as shown in Figure 3.13.

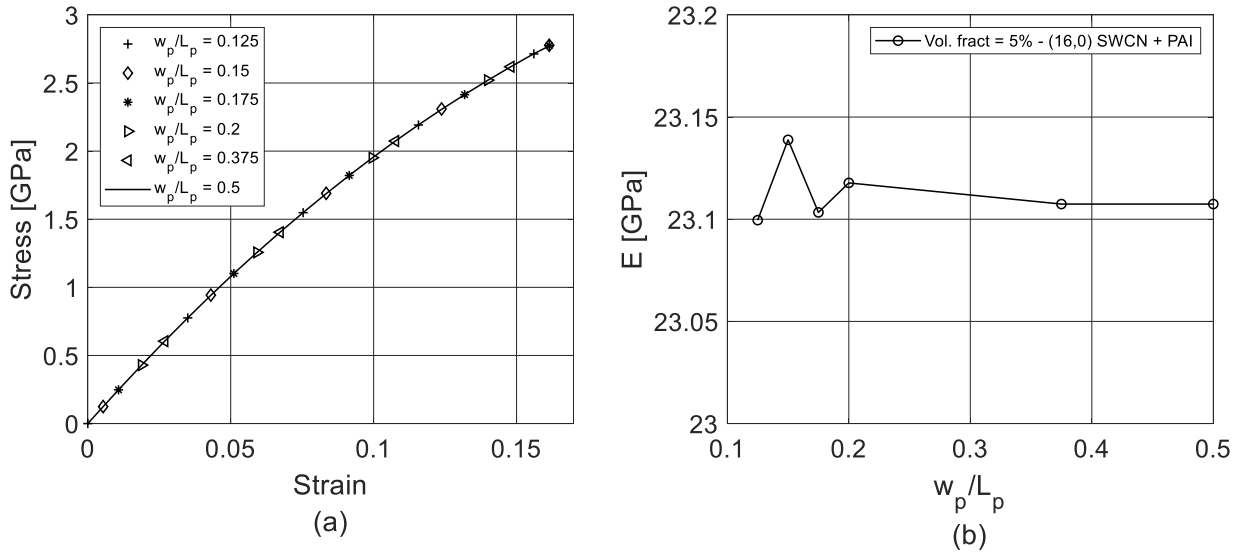

Figure 3.14. The convergence of (a) the stress-strain curve and (b) Young's modulus of the CNRP material.

A convergence study is also performed on the first bending and first axial mode frequencies with the same element sizes used in the convergence study of the stress-strain curve and Young's modulus. Figure 3.15(a) shows the convergence of the first bending mode frequency to the same numerical value for values of w_p/L_p higher than 0.375, while Figure 3.15(b) presents the convergence of the first axial mode frequency to the same numerical value for values of w_p/L_p higher than 0.375. It can also be noticed that for values of w_p/L_p lower than 0.375 the variations of the modal response of the CNRP material are more than that of the stiffness response of the CNRP material. As in the case of stiffness response, the element size used to discretize the RVE of the CNRP material corresponds to the aspect ratio of 0.375, as shown in Figure 3.13.

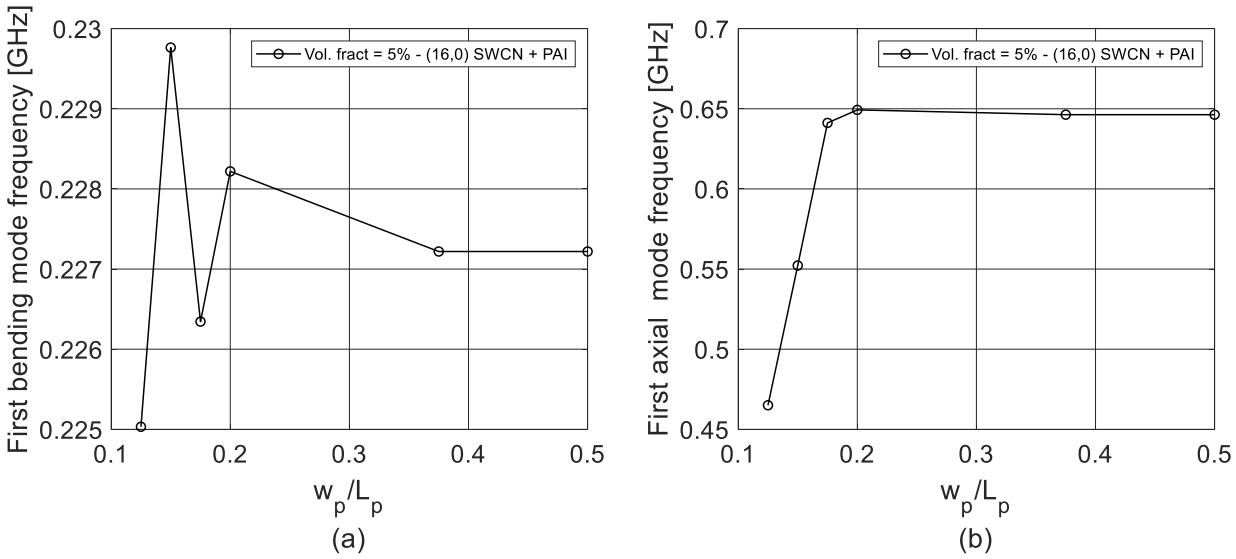

Figure 3.15. The convergence of (a) the first bending and (b) the first axial mode frequencies of the CNRP material.

Chapter 4. Enhancement of stiffness and dynamic mechanical properties of polymers using single-walled-carbon-nanotube – a multiscale finite element formulation study

Foreword

This chapter contains the journal paper: J. A. Palacios and R. Ganesan, "Enhancement of stiffness and dynamic mechanical properties of polymers using single-walled-carbon-nanotube – a multiscale finite element formulation study," Journal of Polymer Research, vol. 26, no. 124, pp. 1-15, 2019.

In this chapter, a parametric study of the RVE of CNRPC considering 4% volume fraction of SWCN is developed to compare its viscous and structural damping mechanism with the experimental data available from the literature.

4 Enhancement of stiffness and dynamic mechanical properties of polymers using single-walled-carbon-nanotube – a multiscale finite element formulation study

4.1 Abstract

The static and dynamic mechanical properties of polymeric materials can significantly be enhanced by using carbon nanotubes as reinforcement material. However, studies still need to be carried out to characterize the dynamic mechanical properties of polymer materials reinforced with carbon nanotubes. Experimental investigations for this purpose have severe limitations and, in most cases, appropriate and reliable experimental work could not be carried out. Computational modeling and simulation encompassing multiscale material behavior provide an alternate approach to study the material behavior. The objective of the present work is to study the enhancement of stiffness and dynamic mechanical properties of Carbon-Nanotube-Reinforced-Polymer (CNRP) material by using a 3D multiscale finite-element model of the representative volume element of the CNRP material. A composite material model consisting of a polymer matrix, an interface region, and a Single-Walled Carbon Nanotube (SWCN) is constructed for this purpose. The polymer matrix is modeled with the Mooney-Rivlin strain energy function to calculate its non-linear response and the interface region is modeled via van der Waals links. The SWCN is modeled as a space frame structure by using the Morse potential and as a thin shell model based on Donnell's Shell Theory. The stiffness response of the CNRP material is calculated, and the natural frequencies of the CNRP material are also determined. The viscoplastic behavior of the polymer matrix material is considered, and the rate-dependent characteristics of the CNRP material are studied. The damping properties of the CNRP material are investigated based on its viscous and structural damping mechanisms. The effectiveness of the SWCN reinforcement is quantified and characterized.

4.2 Introduction

During the last few decades, the application of polymer materials in engineering applications has become considerably popular, particularly in a wide variety of structural applications in automotive, aerospace, aeronautical, mass transit, and nuclear industries. However, in many

engineering applications, polymer properties need to be improved to present a better performance. There are different techniques to enhance their material properties such as reinforcements [1, 2], material coating [3] and thermal treatment [4]. One of the best options to improve the mechanical properties of a polymer is by using Carbon Nanotubes (CNs) [5] as a reinforcement to create a nanocomposite, but nanotube properties do not necessarily translate into the same properties for the nanocomposite [52]. One of the best techniques to simulate and to model the mechanical behavior of a nanocomposite is a multiscale approach, which is a technique involving the analysis at different scales, through the definition of the Representative Volume Element (RVE) of the composite material [53].

For studying the static response of polymer matrices with Single-Walled Carbon Nanotubes (SWCNs) as a reinforcement, Li and Chou [38, 91] constructed their RVE using a space-frame structure for the nanotube, solid elements for the polymer, and truss rods to represent the interfacial region. Constant material properties were used throughout the model and nonlinear behavior for the interface surface. Later, Georgantzinos et al. [79] included the nonlinear behavior of a SWCN modeled by using the Morse potential and two-noded interfacial joint elements of variable stiffness for modeling the interface region, but the interface region had a linear behavior. Mohammadpour et al. [94] presented a RVE of a polymer matrix reinforced with a SWCN, replacing the SWCN with a solid model constructed from nonlinear elements in the shape of a hollow cylinder and integrating the mechanical properties into solid elements. Despite modeling the interface region with contact elements saving computing efforts, this model cannot study other types of mechanical behavior as bending, buckling, and torsion. Later, Wernik and Meguid [76] proposed a nonlinear RVE to investigate the effective mechanical properties of a nano-reinforced polymer, including nonlinear effects on the SWCN and the interface region. Later, Sadek et al. [145] conducted a study on the mechanical and electrical properties of multi-walled carbon nanotubes reinforced poly (vinyl alcohol) composites. The nanocomposites were prepared by dispersion techniques. Recently, Wang et al. [2] studied the influence of carbon spheres on thermal and mechanical properties of epoxy composites. The reinforcement using carbon spheres was synthesized by hydrothermal methods, and the carbon spheres-epoxy composite was prepared using a polymerization technique.

Despite most of the works on polymer matrices with SWCNs as reinforcement, which are on the static response, there is a lack of models that study the dynamic response of this type of

nanocomposite. Latibari et al. [104] extended the model of [38, 91], including a nonlinear interfacial region based on the Lennard–Jones potential to calculate damping ratio of nanocomposite by evaluating its dissipation energy. However, their model does not incorporate a nonlinear description of the SWCN. Jamal-Omidi et al. [105] analyzed a SWCN embedded in volume element using 3D finite element and analytical methods to compute its natural frequencies with different aspect ratios. They studied two models with Lennard-Jones potential and one with perfect bonding between SWCN and the surrounding polymer. Later, Qi-lin and Xin [146] conducted a study to determine the effect of the polymer matrix and nanofiller on non-bonding interfacial properties of nanocomposites. They performed experiments using different nanofillers, such as graphene and carbon nanotube, in various polymer matrix systems including polyethylene, poly (methyl methacrylate), polytetrafluoroethylene and poly (vinylidene chloride). They simulated the interfacial properties via van der Waals forces based on Lennard-Jones potential.

Despite the scientific work done on polymers and their engineering applications, further and more comprehensive studies are still required to be carried out especially on the enhancement of their mechanical properties. Therefore, the purpose of the present research is to model and to analyze and to conduct a study on the static and dynamic material properties of a polymer matrix by using a single-walled carbon nanotube as reinforcement. Carbon-Nanotube-Reinforced-Polymer (CNRP) material is developed by using a 3D multiscale finite-element model of the Representative Volume Element (RVE) of the composite. The RVE investigated in this work consists of a single-walled carbon nanotube embedded in a polymer matrix and an interface region between the SWCN and the polymer material. The polymer matrix is modeled using the Mooney-Rivlin strain energy [82] to calculate its non-linear response. Polyetheretherketone (PEEK) is considered as matrix material due to its applications in the aeronautical and aerospace industries. This material exhibits high mechanical performance and thermal properties, including creep resistance and low flammability. The SWCN is modeled as a space frame structure by using the Morse potential [79] and as a thin shell based on Donnell's Shell Theory [80], and the interface region is modeled via van der Waals links based on the Lennard-Jones Potential [83]. The stress-strain behavior is computed for 4% volume fraction of SWCN, while the dynamic material properties of CNRP are analyzed in terms of its natural frequencies and damping properties. The viscoplastic behavior of the polymer matrix material is considered, and the rate-dependent characteristics of CNRP are studied, while the damping properties of CNRP are analyzed in terms

of its viscous and interfacial damping mechanisms. Finally, viscous and the structural damping mechanisms are compared and analyzed.

4.3 Multiscale finite element modeling procedure for the composite material

The polymer material reinforced with a Single-Walled Carbon Nanotube (SWCN) is analyzed with Representative Volume Element (RVE) of the composite material, as depicted in Figure 4.1. The RVE investigated in the present work consists of a SWCN embedded in a polymer matrix and an interface region between the SWCN and the polymer material. The interactions between the SWCN and the matrix are treated as nonbonded van der Waals interactions. The volume fraction of SWCN in the composite denoted as V_n with respect to the RVE can be calculated as follows [79]:

$$V_n = \frac{8r_n t_n}{4r_m^2 - (2r_n - t_n)^2} \tag{4.1}$$

where r_n is the mean radius of the nanotube, r_m is the radius of the matrix material and t_n is the thickness of the nanotube. The matrix is regarded as a continuum medium since the matrix volume is higher than the SWCN for the volume fractions considered. The RVE length is the same as that of the matrix length and nanotube length L_n.

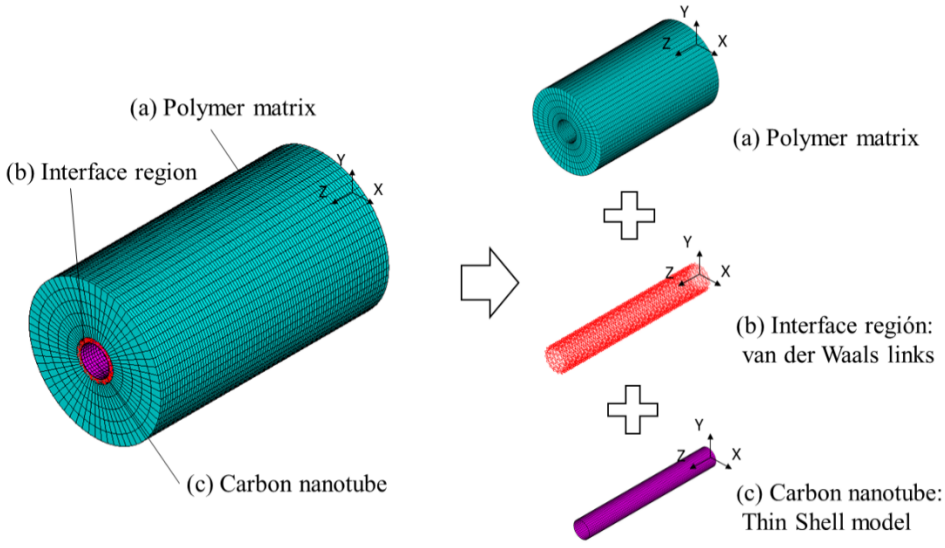

Figure 4.1. Multiscale modeling for representative volume element: (a) Polymer matrix, (b) Interface region: van der Waals links, and (c) Carbon nanotube: Thin Shell model.

4.3.1 Polymer matrix

The polymer matrix is modeled by using linear three-dimensional hexahedral isoparametric finite element SOLID185 available in commercial software ANSYS®, which is capable of simulating both material and geometrical nonlinearities of hyperelastic material. This element is defined by eight nodes having three degrees of freedom at each node: translations in the nodal x, y, and z directions. In order to describe the mechanical behavior of the polymer matrix, the following Mooney–Rivlin strain energy density function is utilized in conjunction with the SOLID185 element [82]:

$$W(I_1, I_2, I_3, v_m) = c_{1m}(I_1 - 3) + c_{2m}(I_2 - 3) + c_{3m}(I_1 - 3)(I_2 - 3) + \frac{1}{2}k_m(I_3 - 3)^2 \quad (4.2)$$

where I_1, I_2, and I_3 define the invariants of the strain tensor, v_m is the Poisson's ratio, c_{1m}, c_{2m} and c_{3m} are material parameters and k_m is the bulk modulus of the material. Polyetheretherketone (PEEK) is considered as the polymer matrix material. Tension experiments were carried out by El-Qoubaa et al. [147] to determine the mechanical properties of PEEK. The fitting of the experimental stress-strain behavior of this material with the specific Mooney-Rivlin parameters is made in the present work by using the method of least squares, which is a standard approach in regression analysis to the approximate solution of the overdetermined system. The stress-strain curve thus determined is depicted in Figure 4.2 with the Mooney-Rivlin parameters: c_{1m}= -3.75 GPa, c_{2m}= 4.82 GPa, c_{3m}= 1.5 GPa, and k_m= 4.083 GPa.

The model parameters for the polymer material consist of internal radius, and external radius and 7.96 nm length. The Young's modulus E_m of the polymer material is obtained from the stress-strain curve in order to perform the vibration analysis. Hence, the mechanical properties of PEEK used in the vibration analysis are as follows: E_m= 4.9 x 10^9 Pa, density ρ_m = 1.3 x 10^3 kg/m^3 and Poisson's ratio v_m= 0.3. The number of elements of the polymer matrix material is 36480.

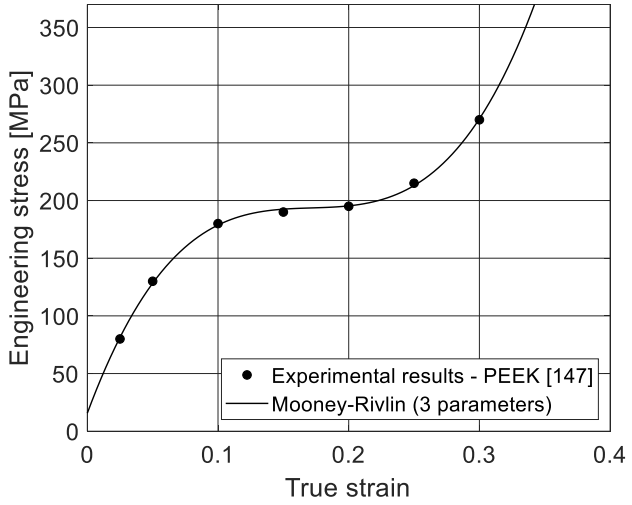

Figure 4.2. Stress-strain behavior of PEEK under uniaxial loading.

4.3.2 Non-linear analysis of SWCN

The mechanical behavior of a SWCN depends on its atomistic nanostructure. For computational modeling, the SWCN is modeled as a space frame structure wherein the carbon atoms are represented by the so-called nodes of the frame finite-element and their positions in three-dimensional space for a particular (n, m) SWCN are defined with the following transformation equation [124]:

$$(x, y, z) = \left(r_n cos\left(\frac{x'}{r_n}\right), r_n sin\left(\frac{x'}{r_n}\right), y'\right) \tag{4.3}$$

where (x', y') are the graphene atomic coordinates which are converted to the nodes in the (x, y, z) coordinates. The nodes, the coordinates of which are defined by the Equation (2), are connected by non-linear frame finite elements in order to represent the potential energy of the interatomic interactions. This potential energy is expressed by using the Morse potential. The effect of angle-bending potential is negligible, so that the bond stretching potential, denoted by $U_{stretch}$, alone can adequately describe the nanotube behavior. $U_{stretch}$ can be calculated as follows [79]:

$$U_{stretch} = D_e\left(\left[1 - e^{-\beta\Delta r}\right]^2 - 1\right) \tag{4.4}$$

where $U_{stretch}$ represents the energy corresponding to bond stretching, $\Delta r = r - r_0$ is the bond length variation, and D_e and β are the force parameters in the potential energy. The stretching force $F_{stretch}$ of the non-linear behavior of the frame finite element can be obtained by differentiating U_{streth} potential with respect to Δr. Hence, $F_{stretch}$ is obtained to be:

$$F_{stretch}(\Delta r) = 2\beta D_e\left(1 - e^{-\beta\Delta r}\right)e^{-\beta\Delta r} \tag{4.5}$$

It is considered that the C-C bond breaks at 19% bond strain, according to [79], and correspondingly the force parameters are: D_e = 6.03105 x 10^{-19} Nm, β = 2.625 x 10^{10} m^{-1} and r_0 = 1.421 x 10^{-10} m. BEAM188 element, which is available in commercial software ANSYS®, is used to model the non-linear frame finite element. This element is capable of uniaxial tension or compression along with torsional and bending deformations, and it has six degrees of freedom at each of its end nodes, which include the translations in the x, y, and z directions and rotations about the x, y, and z axes. The density ρ_b = 2.3 x 10^3 kg/m^3 is used for the frame element, in accordance with Ref. [125], and the mass of the carbon atom m_c= 2.0 x 10^{-26} kg [125]. The mass m_c is used at the nodes, representing the mass of the carbon atoms. The number of elements of the SWCN is 4512.

Due to the similarity of carbon nanotube's geometry to a cylinder, nanotube structure can be modeled as a cylindrical shell. It is possible to replace the molecular structure of SWCN with a thin shell model based on a shell theory of continuum mechanics in the shape of a circular hollow cylinder [94], as depicted in Figure 4.3. The thin shell structural model can then be modeled using Finite Element Method (FEM) by assuming the Poisson's ratio of nanotube v_n (= 0.19), its thickness t_n (= 0.066 nm) and its radius r_n (value depending on its chirality). As given in Ref. [120], these parameters were estimated by equating the axial rigidity and bending rigidity of SWCN that are calculated from Molecular Dynamics (MD) simulations with the axial rigidity and bending rigidity expressions obtained using thin shell theory. Regarding the shell theory used to predict the mechanical behavior of the nanotube, Donnell's thin shell theory can be used [80]. These simulations can include nonlinear effects from the stress-strain curve of the nanotube and

its density ρ_n, that were calculated as in Ref. [126]. The effective transversal area for the thin shell is calculated using the diameter d_n of the nanotube and the equivalent thickness, which is expressed by $\pi d_n t_n/(1-v_n^2)$. SHELL281 element, which is available in commercial software ANSYS®, is used to model the thin shell. This element is suitable for analyzing thin to moderately-thick shell structures and in large strain nonlinear applications. This element also consists of 8 nodes, with six degrees of freedom (three translations and three rotations corresponding to a 3D coordinate system) per node. The number of elements of the shell model is 3040.

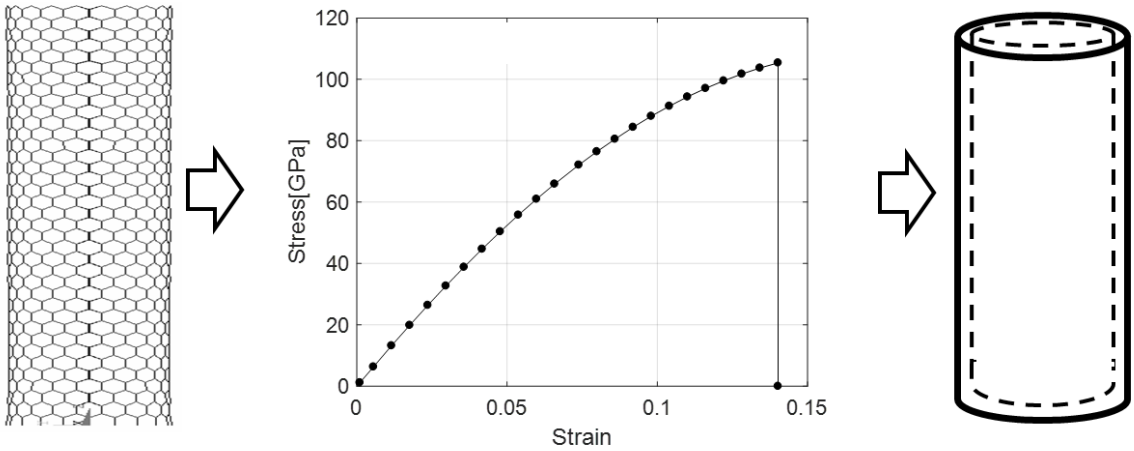

Figure 4.3. Procedure for incorporating SWCN's properties into a thin shell: (a) SWCN modeled with the modified Morse potential, (b) Stress-strain behavior of the SWCN and (c) SWCN modeled as a thin shell model.

4.3.3 Interface modeling

The interface can be simulated either as a continuum or as a discrete region. For convenience in the calculations, just the van der Waals (vdW) interactions between the nanotube and the inner surface of the polymer matrix are considered. Hence, in this work the interface region is represented with the use of truss finite elements, also called LINK element in commercial software ANSYS®, connecting carbon atoms of the discrete structure of the SWCN to nodes of the internal surface of matrix elements. COMBIN39 element is used to model trusses, links, and springs, and

it is a uniaxial tension-compression element with three degrees of freedom at each node: translations in the nodal x, y, and z directions. For simulations of van der Waals interactions at the nanotube-polymer interface, a truss element model, which was introduced in Ref. [76], is adopted. The properties of the LINK elements, shown in Figure 4.4, are obtained by using the corresponding van der Waals forces based on the Lennard-Jones potential, which is expressed as [83]:

$$U(r) = 4\tilde{\varepsilon}\left[\left(\frac{\tilde{\sigma}}{r}\right)^{12} - \left(\frac{\tilde{\sigma}}{r}\right)^{6}\right] \tag{4.6}$$

where, r is the distance between interacting atoms of the nanotube and the polymer, $\tilde{\varepsilon}$, and $\tilde{\sigma}$ are the Lennard–Jones parameters. For carbon atoms, the Lennard–Jones parameters are $\tilde{\varepsilon}$ = 0.0556 kcal/mole and $\tilde{\sigma}$ = 3.4 Angstroms. Based on the Lennard-Jones potential, the van der Waals force F_{vdW} between interacting atoms is written as follows:

$$F_{vdW}(r) = -\frac{dU(r)}{dr} = 24\frac{\tilde{\varepsilon}}{\tilde{\sigma}}\left[2\left(\frac{\tilde{\sigma}}{r}\right)^{13} - \left(\frac{\tilde{\sigma}}{r}\right)^{7}\right] \tag{4.7}$$

The activation of the truss element in the computational simulation is determined by the distance between an atom (a node) in the nanotube and a node in the internal surface of the polymer matrix, such that if this distance is less than $2.5\tilde{\sigma}$ (0.85 nm), the truss element is activated. The number of elements of the interface region is 7560.

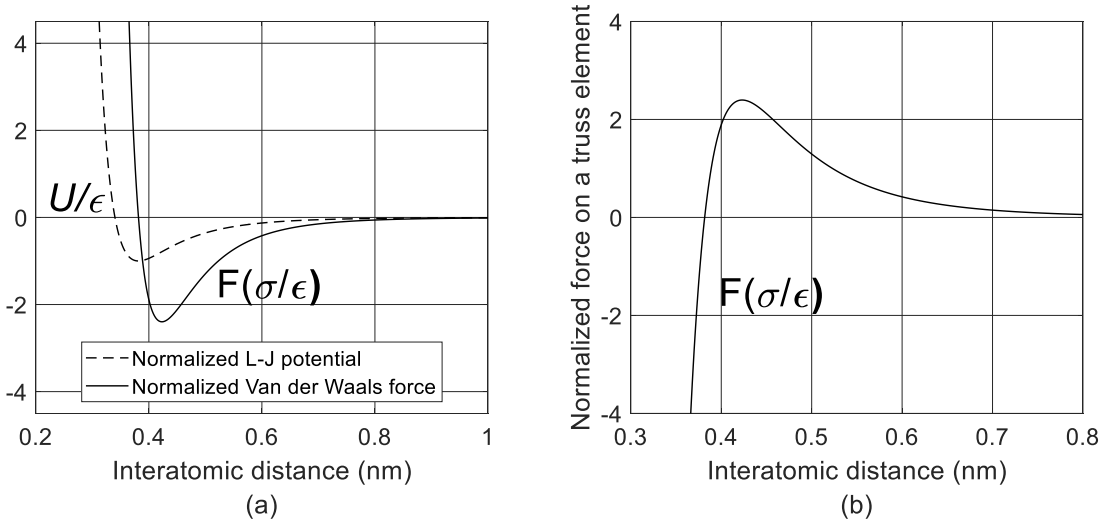

Figure 4.4. (a) Lennard–Jones potential and van der Waals force versus interatomic distance, (b) Load-displacement curve of the nonlinear truss element.

4.4 Viscous damping of CNRP

4.4.1 Rate-dependent behavior of CNRP

The rate-dependent plasticity (viscoplasticity) behavior of nanocomposite material is studied in this section. Viscoplasticity describes the flow rule of materials, that depends on time. The deformation of materials is assumed to develop as a function of strain. Arriaga et al. [148] studied the 20% mineral-filled polypropylene homopolymer under impact loading using simulation and experiments. They carried out the simulation in commercial software ANSYS® and LS-DYNA® to validate the elastoplastic strain rate sensitive constitutive models implemented in both codes, where it is possible observed that the test result from force-time and velocity-time curves are in good match with the viscoplastic strain rate sensitive Perzyna's model [149]. Galliot and Luchsinger [150] investigated the mechanical behavior of ETFE foils under uniaxial and biaxial loading using experimental work and finite element calculations, in which the foil material behavior was predicted by using Perzyna material model with different strain rates. Vasiukov et al. [151] studied the behavior of glass and fiber laminate composite plates with various stacking sequences, in which a viscoplasticity model based on modified Hoffman criterion in combination with Perzyna model was used to simulate the time dependence of the material response. Similar

strategy of analyzing the viscoplastic behavior of material is used in the present work to study the rate-dependent characteristics of nanocomposite reinforced with a SWCN. The viscoplastic behavior of polymer matrix is modeled using Perzyna model, which is available in commercial software ANSYS®, along with the nonlinear material properties of stress-strain behavior. The Perzyna model is given by the following expression [148]:

$$\sigma_{yield} = \left[1 + \left(\frac{\dot{\varepsilon}_{plastic}}{\gamma}\right)^{m}\right]\sigma_0 \tag{4.8}$$

where σ_{yield} is the rate-dependent true yield stress, σ_0 is the static true yield stress, $\dot{\varepsilon}_{plastic}$ is the true plastic strain rate, and, m and γ are the parameters that describe the material strain hardening and viscosity, respectively.

4.4.2 Loss factor and viscous damping ratio

To investigate the viscous damping of composite material, the same design and material properties of the RVE of CNRP are used, including Perzyna model [149], which was explained in sub-section 4.4.1. The loss factor η was originally introduced as a measure of intrinsic damping of viscoelastic materials. However, a definition in terms of energy concept with respect to steady-state oscillations can be used as follows:

$$\eta = \frac{\Delta U}{2\pi U_{diss}} \tag{4.9}$$

where ΔU stands for the energy dissipated per cycle of harmonic motion (or equivalently the amount of energy to be provided to maintain steady-state conditions) and U_{diss} is the total dissipation energy associated with the vibration. The loss factor can also be expressed in terms of cyclic stress and strain of harmonic strain, given by $sin[2 \times \pi \times \omega \times t]$, where ω and t are the frequency and period, respectively. Therefore, the following expression can be used to calculate the numerical value of the loss factor:

$$\eta = tan\left(\frac{2\pi \times Phase\ shift}{Time\ period}\right) \tag{4.10}$$

where the phase shift is the phase angle between cyclic stress and strain. To investigate the loss factor related to viscous damping, an axial harmonic strain is applied to one side of the RVE, while the other side is clamped. The loss factor can be obtained using the phase angle between cyclic stress and strain, and period of the axial harmonic strain. Using the numerical values of the loss factor η, it is possible to determine the quality factor Q^{-1}, which is used for estimating the damping ratio ζ, as follows [141]

$$Q^{-1} = \sqrt{1+\eta} - \sqrt{1-\eta} \tag{4.11}$$

Here η is the loss factor. The viscous damping ratio ζ can then be determined using the numerical value of the quality factor Q^{-1} by the relation [142]:

$$\zeta = Q^{-1}/2. \tag{4.12}$$

4.5 Structural Damping of CNRP

4.5.1 Concept of ''stick-slip'' behavior

The "stick-slip" mechanism in a nanocomposite material is shown in Figure 4.5. When normal tensile stress is applied to a composite, this mechanism starts elongating (showing an increase in its length denoted as ΔL_n). Because of this applied stress, the polymer matrix, in turn, applies shear stress, τ, on the nanotube, thus causing the load transfer to the nanotube. Consequently, a normal strain develops in the nanotube, which elongates accordingly. When the applied stress is small, the nanotube remains fully bonded to the polymer matrix. Both the polymer matrix and the nanotube move together during this phase, and the strains are equal in both elements. As the applied stress is increased, the shear stress on the nanotube increases. At a certain value of shear stress (called the critical shear stress, τ_{cr}), the nanotube debonds from the polymer matrix. When the shear stress on the nanotube increases beyond this value (because of increased

applied stress), the polymer matrix starts slipping over the surface of the nanotube (thereby causing a change in its length denoted as ΔL_{Cn}). The strain in the nanotube remains constant at its maximum level, while the strain in the polymer matrix increases (slipping phase). In this phase, there is no load transfer between the nanotube and the polymer matrix, but there is energy dissipation due to the slippage. Because of this energy dissipation, the so-called structural damping develops in the nanocomposite.

4.5.2 Loss factor and structural damping coefficient

As described in the sub-section 4.5.1, one of the essential causes of damping in nanotube-reinforced composites is the friction between nanotube and matrix. Dissipated energy via interfacial movement of nanotube and matrix is equivalent to the shear force and the differential displacement between tube and matrix. For investigating loss factor η, total dissipation energy (U_{diss}), and dissipation energy (ΔU) in structural damping, the following equations can be used to calculate their numerical values [139]:

$$\eta = sin^{-1}\left(\frac{\Delta U}{2\pi U_{diss}}\right) \tag{4.13}$$

$$U_{diss} = \int_V \frac{\sigma_{ij}\varepsilon_{ij}}{2} dV \tag{4.14}$$

$$\Delta U = 2\tau_2(2r_n L_n^2)(\varepsilon_0 - \varepsilon_2) \tag{4.15}$$

where r_n is the radius of the nanotube, L_n is the length of the nanotube, ε_0 is the strain of matrix material due to loading, ε_2 is the strain between the nanotube and polymer matrix and τ_{cr} is the maximum value of bonding stress (shear stress) τ_{rz} associated with the longitudinal shear stress between nanotube and matrix material, which is obtained when the maximum normal stress and strain are reached due to loading. Hence, τ_{cr} can be calculated as a function of ε_2 as follows [139]:

$$\tau_{cr} = E^{eq} \cdot \varepsilon_2 \int_0^{L_n/2} \frac{sinh\big(\beta(L_n/2 - z)\big)}{cosh(\beta\, L_n/2)} dz \sqrt{\frac{G_0}{E^{eq}} \frac{1}{2ln(r_m/r_n)}} \tag{4.16}$$

where r_m is the radius of the polymer matrix; G_0 is the shear modulus of matrix material (G_0 = 0.2 GPa for polymers) and E^{eq} is the equivalent modulus of nanotube which can be calculated as: $E^{eq} = 2t_n E_n / r_n$, where t_n is the thickness of carbon nanotube, E_n is Young's modulus of the nanotube. Parameter β can be obtained from the following equation [140]:

$$\beta = \left(\frac{G_0 2\pi}{E^{eq} A ln(r_m / r_n)} \right)^{1/2} \tag{4.17}$$

where $A = (2V_n / r_n)V$ is the contact area between the nanotube and polymer matrix and V is the volume of the polymer matrix and V_n is the volume fraction of nanotube. τ_{cr} can also be determined if a tensile displacement is applied to one side of the RVE when the other side is clamped. The displacement is applied until the nanotube strain, and polymer matrix's strain become different. At that strain, the maximum shear stress τ_{cr} occurs. Hence, the strain ε_2, between the nanotube and the polymer matrix, is obtained as follows:

$$\varepsilon_2 = \frac{\tau_{cr}(L_n/2)}{E^{eq} \int_0^{L_n/2} \frac{sinh\left(\beta (L_n/2 - z)\right)}{cosh(\beta\, L_n/2)} dz \sqrt{\frac{G_0}{E^{eq}} \frac{1}{2ln(r_m/r_n)}}} \tag{4.18}$$

The total dissipation energy U_{diss} and dissipation energy ΔU are calculated from Equations (4.14) and (4.15), respectively, with the numerical values of τ_{cr}, ε_2 and tensile stress at each strain level of the applied tensile displacement. The loss factor η is then determined from Equation (4.13) with the values of U_{diss} and ΔU. Using the numerical values of the loss factor η, it is possible to determine the quality factor Q^{-1}, which is used for estimating the structural damping coefficient λ, as follows [141]:

$$Q^{-1} = \sqrt{1 + \eta} - \sqrt{1 - \eta} \tag{4.19}$$

Here, η represents the loss factor. Using the numerical value of the quality factor Q^{-1}, the structural damping coefficient λ is then determined by the relation [142]:

$$\lambda = Q^{-1}/2 \tag{4.20}$$

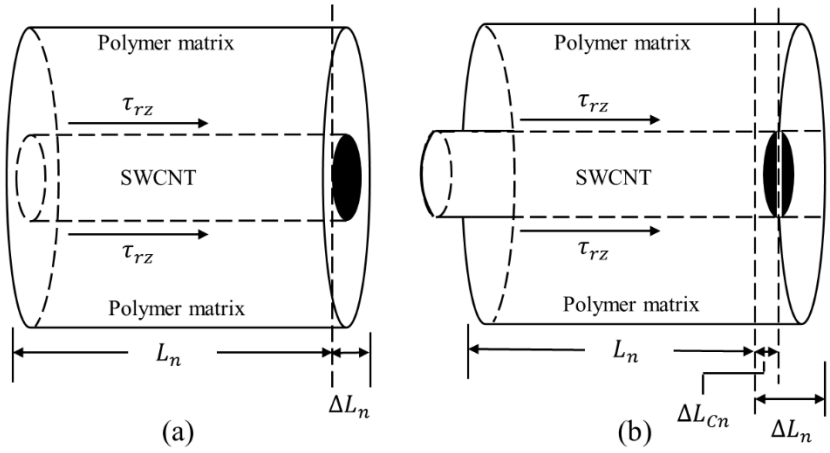

Figure 4.5. Stick-slip behavior of SWCN-based composite: (a) when $\tau_{rz} <$ critical shear stress τ_{cr} and (b) when $\tau_{rz} >$ critical shear stress τ_{cr}.

4.6 Results and discussion

4.6.1 Stiffness response of CNRP

Regarding the Carbon-Nanotube-Reinforced-Polymer (CNRP) properties, the stress-strain curve is examined for a polymer matrix, made with Polyetheretherketone (PEEK), reinforced with a (20, 0) Single-Walled-Carbon-Nanotube (SWCN), with modeling the nanotube as a thin shell based on Donnell's Shell Theory. The RVE is loaded under tension to provide the respective properties, and the volume of the surrounding polymer is defined as 4% volume fraction of SWCN on the mechanical properties. The boundary conditions of CNRP correspond to a cantilever, where the translational and rotational movements of one end of the matrix are prevented, while the other end is free to move so that the SWCN transfers its mechanical properties into the matrix via the vdW links. The length of the CNRP is 7.96 nm and the diameter of the (20, 0) SWCN is 1.569 nm. Hence, the aspect ratio of the (20, 0) SWCN is defined as length of nanotube/diameter of nanotube. The aspect ratio of the (20, 0) SWCN is then calculated as 5.070.

Figures 4.6(a) and 4.6(b) show the stress-strain curve for the CNRP with 4% volume fraction of SWCN and PEEK, respectively. It can be appreciated from Figure 4.6(a) that Young's modulus of the nanocomposite E_c is 42.78 GPa, while for PEEK, the Young's modulus $E_m$is 4.9 GPa. The

Young's modulus E_c is eight times higher than that of PEEK, which shows the SWCN's influence in the polymer. It can also be observed that the ultimate strength of the nanocomposite is higher than that of the plain polymer, where the ultimate strengths of the nanocomposite and the polymer are 4.29 GPa and 0.18 GPa, respectively. Although according to the theory, these stress levels would be possible, in practical application, it is not possible to approach these levels of strength magnitude in the CNRP material because the nanocomposite material could have different defects that affect its mechanical properties. These defects include the effects of the random arrangement of carbon nanotubes in a polymer matrix, the entanglement of fillers and kinking, and structural imperfections (vacancy defects, etc) of the nanocomposite. These defects play important roles in the properties of composites because they can cause that the structure of the nanocomposite is weak and fragile suffering several damages, such as a crack or fracture. Another important defect is that a poor interface induces the debonding of nanoscale fillers from the polymer matrix during loading, possibly weakening the polymer matrix.

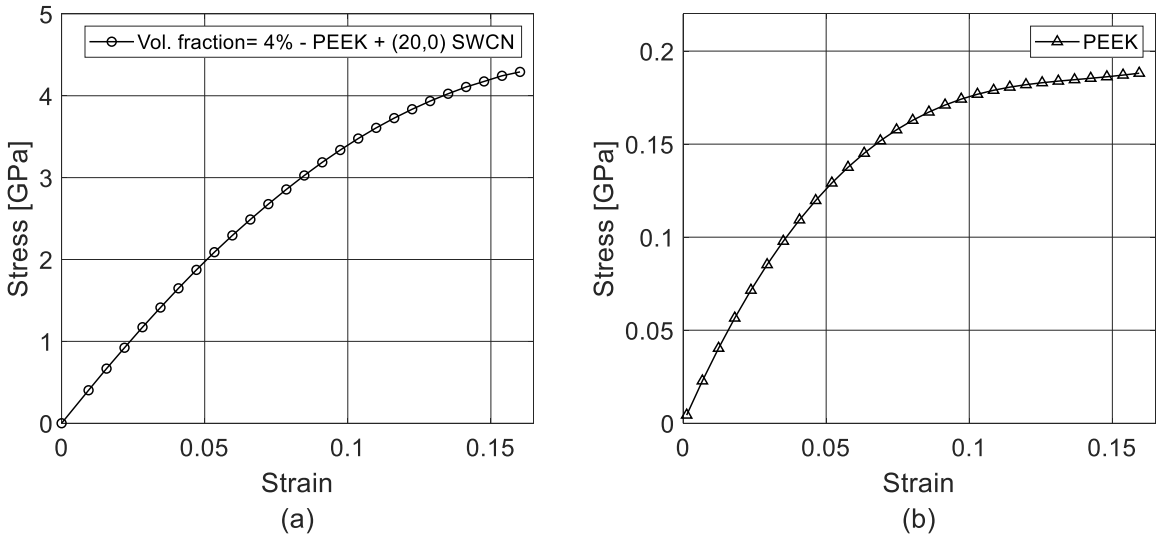

Figure 4.6. Stress-strain curves of (a) CNRP and (b) PEEK.

4.6.2 Comparison of the present CNRP simulation model with other models

In order to compare the effectiveness of the present simulation model to that of other existing models, the results obtained in the present chapter using the present Representative Volume Element (RVE) simulation model of the CNRP material are compared with the stress-strain curves

obtained using the RVE proposed by Wernik and Meguid [76]. The RVE proposed in Ref. [76] consists of a polymer matrix, which is a two-component epoxy adhesive (SikaDur330), reinforced with different volume fractions of (16, 0) SWCN and (9, 9) SWCN. The tensile stress-strain curves of both RVEs are depicted in Figure 4.7(a) and 4.7(b). It can be noticed from Figure 4.7 that the stress-strain behavior is similar for both models so that the CNRP model proposed in the present work can be used to model different types of polymer materials reinforced with SWCNs.

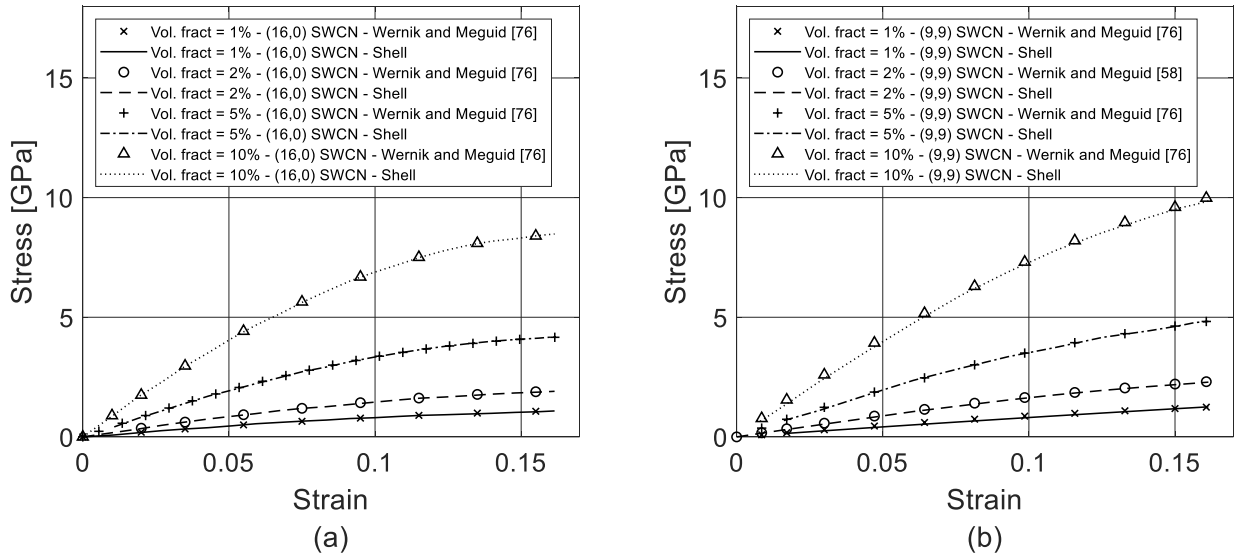

Figure 4.7. Comparison of the stress-strain curves of the RVE models proposed in Ref. [76] and in the present work, for the CNRP containing different volume fractions of, (a) (16, 0) SWCN and (b) (9, 9) SWCN.

The Root Mean Square Error (RMSE) and the Chi-square error were also calculated to determine further the effectiveness of the RVE simulation model proposed in the present work. Table 4.1 shows the Root Mean Square Error (RMSE) and the Chi-square error for the comparison between the stress-strain curves obtained using the RVE simulation model proposed in Ref. [76] and the RVE simulation model proposed in the present work. For the case of (16, 0) SWCN, the RMSE and the Chi-square error for the RVE with 1% volume fraction of (16, 0) SWCN are 0.4385 and 0.3256, respectively, while for 2% volume fraction, the RMSE and the Chi-square error are 0.3268 and 0.4287, respectively. For 5% volume fraction, the RMSE and the Chi-square error are 0.4235 and 0.3682, respectively, while for 10% volume fraction, the RMSE and the Chi-square

error are 0.2791 and 0.4395, respectively. In the case of (9, 9) SWCN, the RMSE and the Chi-square error for 1% volume fraction are 0.3521 and 0.4135, respectively, while for 2% volume fraction, the RMSE and the Chi-square error are 0.2943 and 0.3916, respectively. For 5% volume fraction, the RMSE and the Chi-square error are 0.3275 and 0.3785, respectively, while for 10% volume fraction, the RMSE and the Chi-square error are 0.3472 and 0.4861, respectively. These ranges of RMSE and Chi-square error indicate a high degree of correlation between the compared stress-strain curves. The results in Figure 4.7 and Table 4.1 show that the RVE simulation model of the CNRP proposed in the present work is a good option for predicting the mechanical behavior of the polymer matrix material reinforced with a SWCN.

Table 4.1. The RMSE and Chi-square error for the simulation model of the CNRP.

Volume fraction	RMSE	Chi-square error
1% - (16, 0) SWCN	0.4385	0.3256
2% - (16, 0) SWCN	0.3268	0.4287
5% - (16, 0) SWCN	0.4235	0.3682
10% - (16, 0) SWCN	0.2791	0.4395
1% - (9, 9) SWCN	0.3521	0.4135
2% - (9, 9) SWCN	0.2943	0.3916
5% - (9, 9) SWCN	0.3275	0.3785
10% - (9, 9) SWCN	0.3472	0.4861

4.6.3 Natural frequencies of CNRP

Effect on natural frequencies of the matrix material by addition of 4% volume fraction of SWCN is studied in this section. A modal analysis is performed on the CNRP material constructed and the polymer: PEEK, to investigate the influence of SWCN on the natural frequencies of the polymer matrix. Block Lanczos method [143] is used to perform the modal analysis on the model, which is often utilized in analyses where high accuracy is required. Clamped-Free (CF) boundary conditions are applied to the 3D multiscale finite-element model and the polymer material.

The natural frequencies of the first 15 modes of CNRP with 4% of SWCN volume fraction are compared in Table 4.2 to the natural frequencies of PEEK. It is observed from Table 4.2 that the addition of nanotubes significantly increases the natural frequencies of the polymer matrix, especially for the first mode number, which is the first bending mode frequency. This is explained by the high stiffness of the carbon nanotube reinforced polymer. The natural frequencies increase in a range of 21.05-63.35% with a (20, 0) SWCN as reinforcement. It can be noticed that for CNRP, the first bending mode frequency increases by 63.35% (first row in Table 4.2), while the first axial mode frequency increases by 21.05 % (fourth row in Table 4.2). Figure 4.8 shows the mode shapes for the first bending and the first axial mode frequencies of CNRP.

Table 4.2. Comparison of natural frequencies of the polymer matrix and CNRP in GHz for CF boundary condition.

Mode	PEEK	CNRP	(%) Increase
1	0.161	0.263	63.35
2	0.169	0.274	62.13
3	0.222	0.309	39.18
4	0.380	0.460	21.05
5	0.389	0.577	48.32
6	0.390	0.580	48.71
7	0.391	0.582	48.84
8	0.394	0.588	49.23
9	0.394	0.592	50.25
10	0.397	0.597	50.37
11	0.397	0.602	51.63
12	0.399	0.624	56.39
13	0.399	0.624	56.39
14	0.405	0.635	56.79
15	0.418	0.637	52.39

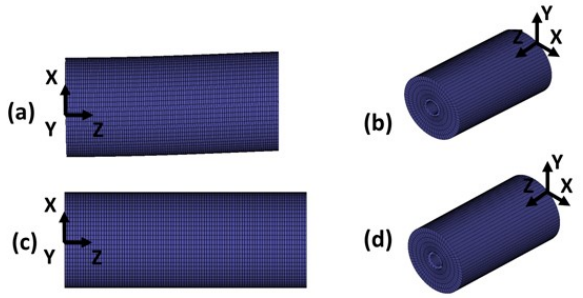

Figure 4.8. Mode shapes, first bending and first axial, of CNRP-PEEK for Clamped-Free boundary conditions: (a)-(b) first bending shape mode and (c)-(d) first axial shape mode.

4.6.4 Rate-dependent behavior of CNRP

The rate-dependent stress-strain curve of CNRP was determined using computations performed in commercial software ANSYS® based on the nonlinear stress-strain curve and the material parameters of Perzyna model [148], which is a widely-used viscoplastic formulation for this type of material. The Perzyna model parameters for the polymer matrix material are the material strain hardening parameter m and viscosity γ, which are taken as 0.25 and 0.5 [150], respectively, from the literature. The nonlinear stress-strain behavior of the polymer matrix is taken from Figure 4.6(a), and the same design of CNRP with 4% volume fraction is used in this study, as discussed in Section 4.3. Clamped-Free boundary conditions are applied on the RVE of CNRP to obtain the rate-dependent behavior of the composite material, where one end of the RVE is constrained, and a strain rate is applied at the free end. The strain rate used in this analysis is 10% strain (in nm/nm unit) per second, which is utilized in other applications for viscoplastic behavior of polymers [148]. Figure 4.9 shows a comparison between the rate-dependent stress-strain curve of CNRP and the static stress-strain behavior of the same composite material. It can be observed that the CNRP shows higher stress carrying capacity when it is pulled at a strain rate of 10% strain/sec compared to the static behavior, while there is a considerable decrease in the failure strain of the composite material. The ultimate strength at a strain rate of 10% strain/sec is 5.16 GPa, while in the static behavior, the ultimate strength is 4.29 GPa. In other words, the ultimate strength at a strain rate of 10% strain/sec is 20% higher than that of the static behavior. Regarding the failure strain, in the static behavior, this strain is 0.1601, while at a strain rate of

10% strain/sec, the failure strain is 0.0533. In other words, the failure strain at static behavior is 66% higher than that at a strain rate of 10% strain/sec.

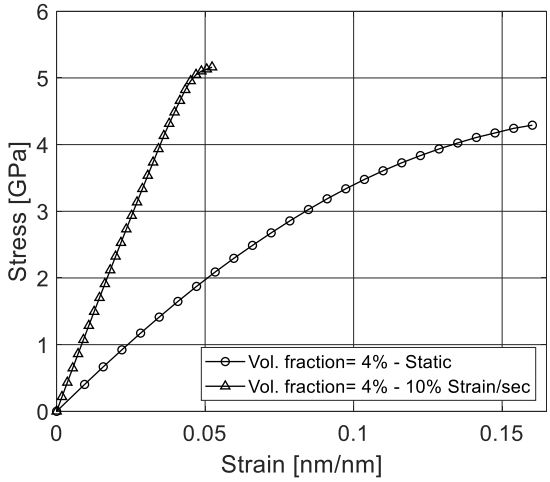

Figure 4.9. Stress-strain curves of CNRP at 10% strain rate and static loading conditions.

4.6.5 Viscous damping properties of CNRP

In viscous damping, when mechanical systems vibrate in a fluid medium such as air, gas, water, or oil, the resistance offered by the fluid to the moving body causes energy to be dissipated. In this case, the amount of dissipated energy depends on many factors, such as the size and shape of the vibrating body, the viscosity of the fluid, the frequency of vibration, and the velocity of the vibrating body. In viscous damping, the damping force is proportional to the velocity of the vibrating body. On the other hand, in structural damping, when a material is deformed, energy is absorbed and dissipated by the material. The effect is due to friction between the internal planes, which slip or slide as the deformations take place. Hence, the viscous damping of the Carbon-Nanotube-Reinforced-Polymer (CNRP) material is then sensitive to its natural frequencies, while the structural damping is sensitive to strain rate.

To investigate the damping of composite material, the same design and material properties of the RVE of the CNRP material are used as mentioned in the last sub-section. CF boundary conditions are applied, in which one end of CNRP is constrained and an axial harmonic strain $sin[2 \times \pi \times \omega \times t]$ is applied at the other end at 0.161 GHz and 0.38 GHz, which are the first bending mode frequency and first axial mode frequency, respectively. The ω and t are the

frequency and period, respectively. The stress and strain responses corresponding to the free end of CNRP at the first bending and first axial mode frequencies are shown in Figure 4.10, where the phase lag between the stress and strain is used to calculate the damping properties of the nanocomposite. The viscous damping material model can be calculated from Figure 4.10 by using the equations given in sub-section 4.4.2. It can be noticed from Figure 4.10 that the phase shift, between the cyclic stress and strain, for the first bending mode frequency is higher than the phase shift for the first axial mode frequency. In addition, it can be observed, in Figure 4.10(b), that the value of cyclic stress is higher in the first axial mode frequency than that in the first bending mode frequency in Figure 4.10(a).

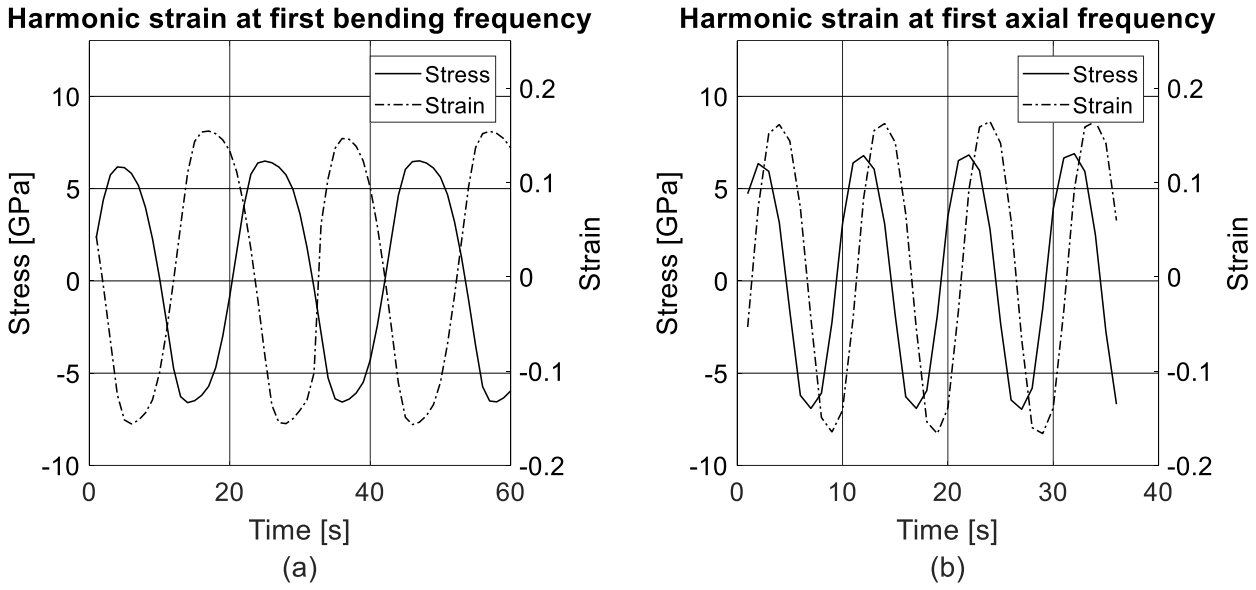

Figure 4.10. Stress and strain histories of CNRP subjected to an axial harmonic strain at first bending and first axial frequencies.

The viscous damping ratio is sensitive to the values of frequency of CNRP material, while the structural damping coefficient is associated to the contact between the structure of carbon nanotube and the polymer matrix material. The computed values of viscous damping ratio for each natural frequency are shown in Figure 4.11, where their numerical values are within a range of 0.0333-0.0860. it can be appreciated that the viscous damping ratio decreases considerably within a range between 0.263 - 0.577 GHz, while for natural frequencies higher than 0.577 GHz, the values of viscous damping ratios are similar. In Figure 4.12, the values of the viscous damping

ratio (corresponding to the 5th to 15th natural frequencies) are compared to the experimental results for an epoxy reinforced with Multi-Walled Carbon Nanotubes (MWCNs), which were presented in Ref. [152]. Diglycidyl ether of Bisphenol A (DGEBA) is used as epoxy in the experimental tests. For the experimental data, the weight percentage of the Carbon Nanotubes (CNs) for each sample are 0.25%, 0.5%, and 0.75%. The total number of samples is 3 for each case, but each sample has a different length. Hence, the three samples of Ref. [152] are defined in the present work as: CN-1, CN-2, and CN-3. From Figure 4.12, it can be appreciated that the values of the viscous damping ratio are 3.5 times higher than that of the damping ratio reported in Ref. [152]. In the next section, the structural damping properties are calculated.

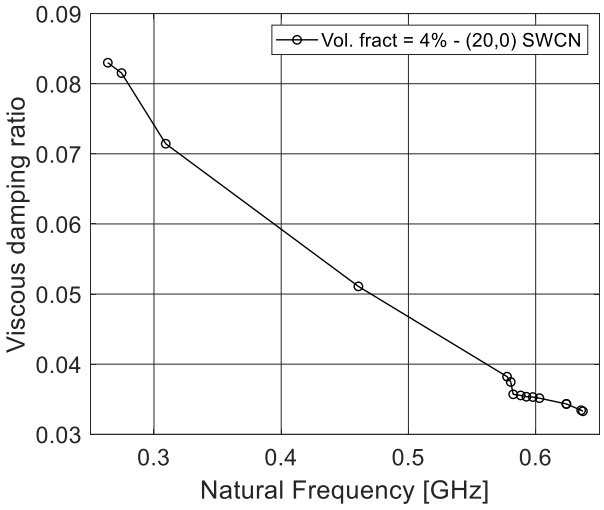

Figure 4.11. Viscous damping ratio for CNRP with Clamped-Free boundary condition.

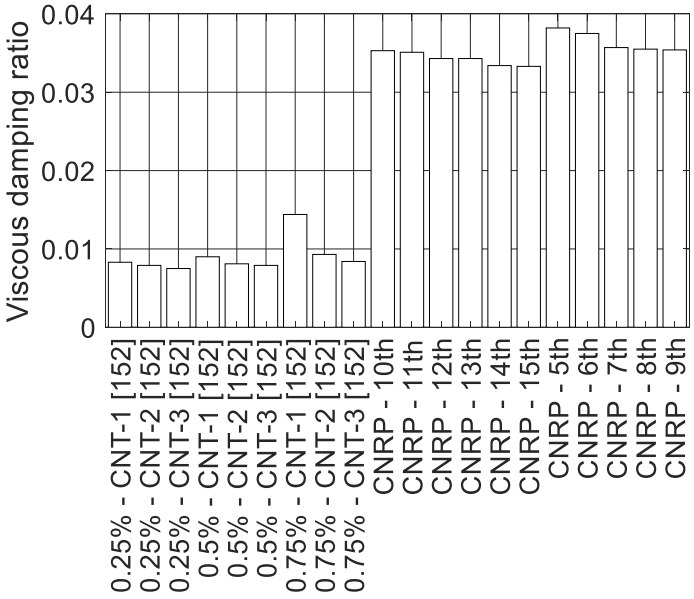

Figure 4.12. Comparison of the viscous damping ratio of CNRP with the experimental results for an epoxy-based nanocomposite material with MWCN given in Ref. [152].

4.6.6 Structural damping properties of CNRP

Structural damping properties are determined following the same design that was mentioned in section 4.3, but not considering the properties of Perzyna model in the polymer matrix material. By considering the stick-slip concept, which is introduced in sub-section 4.5.1, between the SWCN and the polymer matrix, one side of the RVE is clamped, and the other side is pulled by applying a displacement in the axial direction. It can be obtained that, up to a specific strain, the nodes of nanotube and corresponded nodes of the matrix, have similar displacement, and by increasing the strain, at the interface of matrix and nanotube slip occurs. Because of this, the displacement of matrix nodes will be larger than that of the corresponded nodes of the nanotube.

Damping properties can be obtained, if the RVE behaves exactly as per the mechanism of stick-slip motion and follows the equations that govern this mechanism. From the results of finite element simulations, the critical shear stress τ_{cr} and dissipation energy U_{diss} are determined and used with the model properties such as radius, area, and Young's modulus to calculate the structural damping properties from the equations given in sub-section 4.5.2. The dissipation energy and loss factor are investigated, and the results are shown in Figure 4.13 for the CNRP with 4%

volume fraction of SWCN. It can be noticed that for the CNRP, the dissipation energy increases due to nanocomposite's strain, and the loss factor decreases due to nanocomposite's strain. In Figure 4.13(a), the dissipation energy presents a similar value for strains lower than 0.03, while for strain values higher than 0.03, the dissipation energy values increase considerably. In Figure 4.13(b), the values of loss factor decrease considerably for strain values in a range between 0.03 and 0.135, however for strain values higher than 0.135, the loss factor takes on similar values. In Figure 4.13(b), the results of the loss factor are also compared to that of experimental results for 5% SWCN – Epoxy beam obtained from Ref. [140]. The epoxy is made of Epon 9405 (75 parts by weight), Epodil 749 for lowering viscosity (25 parts) and Ancamine 9470 hardener (41.4 parts). It can be appreciated that the values of the loss factor associated with the 5% SWCN – Epoxy beam decrease considerably for strain values in a range between 0.005 and 0.05. The loss factor of the CNRP also exhibits a similar behavior but in the range of strain values between 0.03 and 0.135.

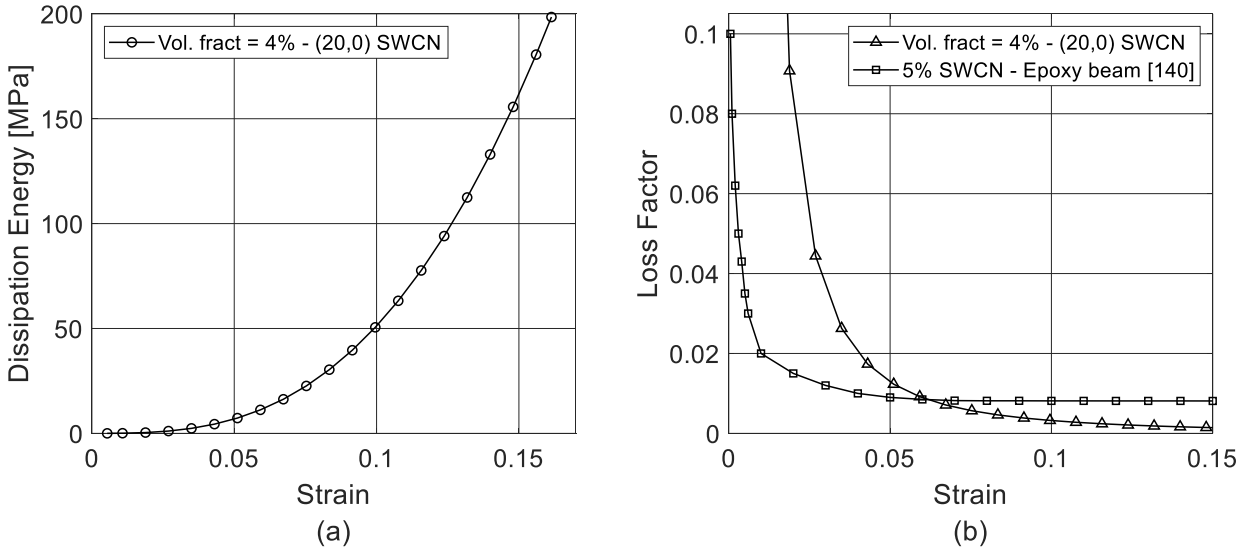

Figure 4.13. (a) Dissipation energy and (b) loss factor for CNRP and experimental results for 5% SWCN – Epoxy beam given in Ref. [140].

Regarding the structural damping, Figure 4.14(a) shows the structural damping coefficient for CNRP as a function of natural frequencies. The values for the structural damping coefficient are within a range of 0.0661 - 0.1597, and it can be appreciated that their numerical values decrease considerably within a range of natural frequencies of 0.263 - 0.577 GHz. The values of the

structural damping coefficient are similar for natural frequencies within a range of 0.577 - 0.637 GHz. In Figure 4.14(b), the values of the structural damping coefficient are compared to the experimental results for SWCN – Epoxy beam and MWCN – Epoxy beam given in Ref. [153] for different volume fractions. The epoxy is made of an epoxy resin and an amine hardener. It can be noticed that the values of the structural damping are seven times higher than that of MWCN – Epoxy beam and 16 times higher than that of the SWCN- Epoxy beam. In the next sub-section, a comparison between viscous and structural damping mechanisms is provided.

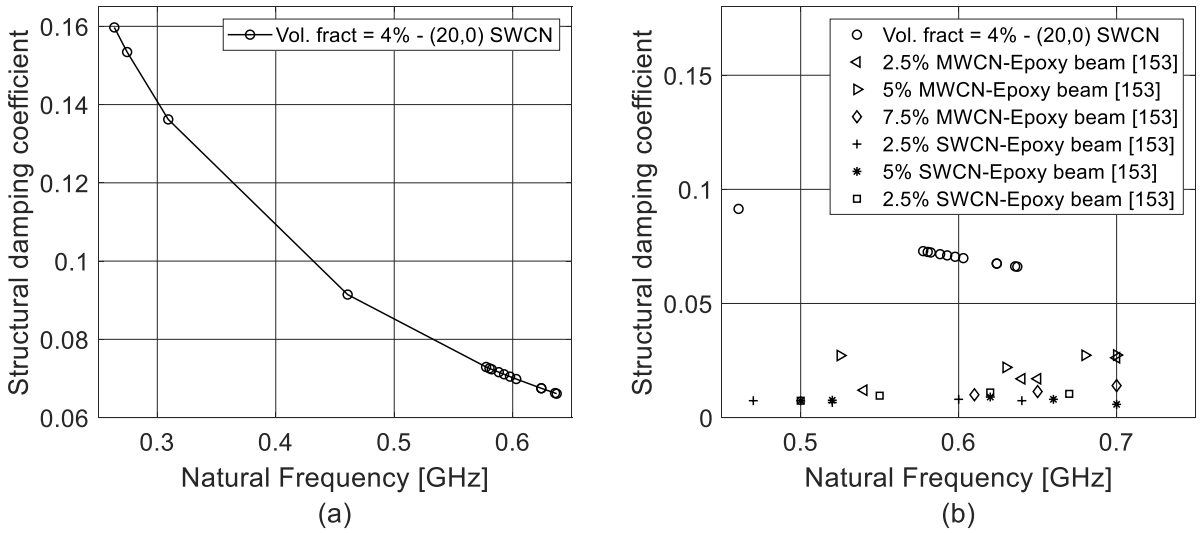

Figure 4.14. (a) Structural damping coefficient for CNRP with Clamped-Free boundary condition and, (b) structural damping coefficient for CNRP and experimental results for SWCN – Epoxy beam and MWCN – Epoxy beam given in Ref. [153].

4.6.7 Comparison between viscous and structural damping mechanisms

In this section, a comparison between viscous and structural mechanisms is provided to analyze the dynamic properties of CNRP. Table 4.3 shows the numerical values of both types of damping properties. In the case of viscous damping ratio, the numerical values are within a range of 0.0343 - 0.0830, while for structural damping coefficient, the numerical values are within a range of 0.0675 - 0.1597. According to Ref. [154], an approximate relationship between viscous damping ratio ζ and structural damping coefficient λ is given by $\lambda \approx 2\zeta$. It can be appreciated from Table 4.3 that λ is approximately 2 times higher than ζ. For example, in the case of the first

bending mode frequency (of 0.161) GHz, ζ is 0.0830 and λ is 0.1597 which means that the structural damping coefficient λ is 1.92 times higher than the viscous damping ratio ζ. For the case of the first axial mode frequency, ζ is 0.0511 and λ is 0.0914, which means that the structural damping coefficient λ is 1.78 times higher than the viscous damping ratio ζ.

Table 4.3. Comparison between viscous and structural damping mechanisms for CNRP (Vol. fract. = 4% - (20 0) SWCN).

Viscous damping ratio ζ	Structural damping coefficient λ
0.0830	0.1597
0.0815	0.1534
0.0714	0.1362
0.0511	0.0914
0.0382	0.0729
0.0375	0.0726
0.0357	0.0723
0.0355	0.0716
0.0354	0.0711
0.0353	0.0705
0.0351	0.0699
0.0343	0.0675
0.0343	0.0675
0.0334	0.0663
0.0333	0.0661

4.7 Conclusion

Regarding the mechanical behavior of the Carbon-Nanotube-Reinforced-Polymer (CNRP) material, static analysis was performed on the CNRP material with 4% volume fraction of (20, 0) SWCN as reinforcement to obtain its stiffness response in terms of its stress-strain behavior. The

Young's modulus of the nanocomposite E_c was 42.78 GPa, while for the unreinforced PEEK material, the Young's modulus E_m was 4.9 GPa. Hence, the Young's modulus E_c is eight times higher than that of PEEK, and this shows the influence of SWCN in the polymer matrix. The ultimate strength of the nanocomposite was higher than that of the plain polymer, where the ultimate strengths of the nanocomposite and the polymer were 4.29 GPa and 0.18 GPa, respectively. Also, the natural frequencies of the CNRP material with 4% volume fraction of (20, 0) SWCN as reinforcement were compared to that of PEEK. An increase in these frequencies, as much as 63.35%, especially for the first bending mode frequency, has been observed, due to the reinforcement with the SWCN.

Regarding the damping properties of CNRP, the viscoplastic behavior of the polymer matrix material was considered, and the rate-dependent characteristics of CNRP were studied, while the viscous damping ratio was calculated based on the loss factor obtained by applying an axial harmonic strain at free end in CF boundary conditions. The computed values of viscous damping ratio for each natural frequency were within a range of 0.0333-0.0860. On the other hand, the concept of stick-slip motion behavior was used to obtain the critical shear stress, dissipation energy, and loss factor to calculate the structural damping coefficient of CNRP. The values of the structural damping coefficient were within a range of 0.0661 - 0.1597. Both damping mechanisms were compared and analyzed to obtain a close relationship between both properties. From this analysis, it was determined that the structural damping coefficient is approximately two times higher than the viscous damping ratio. For example, in the case of first bending mode frequency, the viscous damping ratio was 0.0830, and the structural damping coefficient was 0.1597, which means that the structural damping coefficient is 1.92 times higher than the viscous damping ratio. For the case of the first axial mode frequency, the viscous damping ratio was 0.0511, and the structural damping coefficient was 0.0914, which means that the structural damping coefficient is 1.78 times higher than the viscous damping ratio.

Chapter 5. Reliability Evaluation of Carbon-Nanotube-Reinforced-Polymer Composites based on Multiscale Finite Element Model

Foreword

This chapter contains the journal paper: J. A. Palacios and R. Ganesan, "Reliability evaluation of Carbon-Nanotube-Reinforced-Polymer composites based on multiscale finite element model," Composite Structures, vol. 229, p. 111381, 2019.

In this chapter, a 3D multiscale finite element of the Representative Volume Element of the Carbon-Nanotube-Reinforced-Polymer-Composite (CNRPC) material is developed considering 5% of volume fraction and structural vacancies in the SWCN and the interface region based on Monte-Carlo Simulation technique. The structural vacancies are represented by missing carbon atoms and covalent bonds in the SWCN and van der Waals links in the interface region. The stress-strength (challenge-capacity) model prediction is utilized to perform the reliability evaluation of the stiffness response of the RVE of CNRPC material by using the Maximum Entropy Method.

5 Reliability Evaluation of Carbon-Nanotube-Reinforced-Polymer Composites based on Multiscale Finite Element Model

5.1 Abstract

Experimental investigations to study the material behavior of nanocomposites have limitations. Hence, computational modeling and simulation encompassing multiscale material behavior provide an alternate approach to study the mechanical properties of such materials. The objective of the present chapter is to develop a computational framework for performing a probabilistic analysis of a Carbon-Nanotube-Reinforced-Polymer (CNRP) material by using the stress-strength model to determine the reliability and hazard associated with its mechanical properties, in terms of its longitudinal elastic modulus and ultimate longitudinal strength. A 3D multiscale finite element model of the Representative Volume Element of the nanocomposite consisting of a polymer matrix, an imperfect Single-Walled-Carbon-Nanotube (SWCN) and an imperfect interface region has been constructed for this purpose. The polymer matrix is modeled with the Mooney-Rivlin strain energy, the imperfect SWCN is modeled as a space frame structure using the Morse potential, and the interface region is modeled via van der Waals (vdW) links. In practical applications, the SWCN is not perfect, and it possesses structural defects, and moreover, the vdW links are not perfect. Such imperfections are characterized using the Monte Carlo simulation technique. The reliability and hazard functions of the CNRP material are calculated using the Maximum Entropy Method.

5.2 Introduction

Composite materials have been increasingly used in not only aeronautical and aerospace applications but also in many other engineering applications due to their many unique advantages, such as higher stiffness and strength to weight ratios, corrosion resistance, long fatigue life, and durability, compared to metals. Hence, the use of carbon nanotubes as reinforcement in polymer materials is common in several engineering applications. Single-Walled-Carbon-Nanotubes (SWCNs) incorporated into polymers because of their exceptional and multipurpose properties create a new generation of nanocomposite materials [51]. Since experimentation at the nanoscale

is still a developing field, the most effective way of quantifying the effects of such parameters is predominantly through computational modeling techniques.

It is a standard practice to use a Representative Volume Element (RVE) in the simulation and modeling of any type of composites (that are metal-based, ceramic-based and polymer-based) [53]. For studying the mechanical properties of a polymer matrix with Single-Walled-Carbon-Nanotubes (SWCNs) as reinforcement, Li and Chou [91] constructed the RVE using a space frame structure for a SWCN, solid elements for the polymer, and truss rods to represent the interfacial region. However, some studies included non-linearities in the SWCN by using the Morse potential, such as Georgantzinos et al. [79], and in the interface region by using van der Vaals links, such as Wernik and Meguid [76]. In the case of the dynamic response of this type of nanocomposite, Latibari et al. [104] extended the model of [91] to calculate the damping ratio of the nanocomposite by evaluating its dissipation energy. Later, Jamal-Omidi et al. [105] analyzed a SWCN embedded in a volume element using 3D finite-element and analytical models to compute its natural frequencies considering different aspect ratios. Shokrieh et al. [106] predicted the viscoelastic properties for an embedded SWCN in a polymer matrix by using a time-dependent formulation of the interface region. The SWCN was modeled using a space frame beam, the interface region was modeled using non-linear springs based on van der Waals interactions and the polymer matrix using solid continuum elements. Later, Papadopoulos and Impraimakis [101] proposed a hierarchical multiscale approach to evaluate the nonlinear constitutive behavior of concrete reinforced with SWCNs. Other authors, such as Sun et al. [102], presented a multiscale computational analysis based on RVE modeling and molecular dynamics simulations to investigate the microscopic failure mechanisms of unidirectional carbon fiber reinforced polymer composites, while Chevalier et al. [103] proposed a multiscale approach to characterize and to model the transverse compression response of a unidirectional carbon fiber reinforced epoxy.

In the case of nano-reinforced polymer systems with structural imperfections, such as vacancy defects, Davoudabadi and Farahani [108] investigated the impact of different vacancy defects on Young's modulus of a SWCN – a reinforcement polymer composite in the axial direction by using a structural model in commercial software ANSYS®. Joshi et al. [110] proposed a multiscale 3D RVE approach for modeling the elastic behavior of carbon nanotube reinforced composites with vacancy defects. Later, Chawla et al. [111] explored the influence of vacancy defects on SWCN reinforced polypropylene composites using molecular dynamics simulation and

comparing the influence of a perfect SWCN and an imperfect SWCN as reinforcement. Other effects in polymer matrix composites, such as those due to the arrangement of carbon nanotubes, were studied by other authors. For instance, Zhu et al. [113] presented a probabilistic multiscale approach to model the random spatial distribution of local elastic properties arising from the heterogeneous waviness and orientation of SWCN fillers within a 3D microscale continuum RVE of a SWCN-reinforced polymer matrix. Recently, Jeong et al. [114] proposed a 3D stochastic computational homogenization model for SWCN-epoxy matrix composites. They found that stochastic waviness, agglomeration, and orientation of SWCN fillers caused random spatial variations of the elasticity tensor of the SWCN-epoxy matrix within a microscale RVE, resulting in probabilistic changes of the homogenized stiffness of the RVE. The effects of the random arrangement of carbon nanotubes in a polymer matrix, the entanglement of fillers and kinking, are probably dominant in polymer matrix composites. However, to the extent that the mechanical properties of the nanotube reinforcement influence the properties of the nanocomposite, there would be a corresponding sensitivity of the nanocomposite property to the variations in the properties of the nanotube reinforcement and interface properties. This source of randomness can be compared to the other sources mentioned before. Hence, considering the randomness due to defects in a carbon nanotube or interphase, while assuming that the carbon nanotubes are correctly aligned is duly justified in the references from the literature. Moreover, the use of stochastic modeling to analyze the effects of structural vacancies in the SWCN is also of interest in manufacturing, due to the fact that vacancies are randomly distributed in the SWCN and are unavoidable in engineering applications [39-42].

Another essential aspect of composites is their structural reliability. As for the reliability analysis of this type of materials, there are studies on laminated composite structures [155-157], including multiscale modeling [158]. However, there are no works that consider SWCN- polymer composites. Despite the work done on polymer composites with SWCNs as reinforcement, studies that characterize and analyze the structural vacancy problems using a stochastic modeling technique and the reliability of nanocomposite systems still need to be carried out. Hence, the objective of the present chapter is to perform probabilistic modeling and analysis of a Carbon-Nanotube-Reinforced-Polymer (CNRP) material to determine the reliability of its mechanical properties by using the stress-strength (challenge-capacity) modeling and prediction method [159]. The mechanical properties of the CNRP material analyzed in the present chapter are carried out in

terms of its longitudinal elastic modulus and ultimate longitudinal strength, which are considered as random variables. For modeling the CNRP material, a 3D multiscale finite-element model of the RVE of the nanocomposite material is developed. The CNRP material consists of a polymer matrix material, an imperfect SWCN, and an imperfect interface region. The multiscale modeling is performed in terms of using different theories and corresponding strain energies to model individual parts of the Representative Volume Element of the CNRP material. The macroscale continuum mechanics for the polymer matrix, the mesoscale mechanics for the imperfect interface region, and nanoscale-level atomistic mechanics for the imperfect SWCN. The polymer matrix is modeled with the Mooney-Rivlin strain energy function [82]. The imperfect SWCN is modeled as a space frame structure by using the Morse potential [79], while the imperfect interface region is modeled via van der Waals (vdW) links [83]. The structural vacancies of the imperfect SWCN and the interface region are modeled by using the Monte Carlo Simulation (MCS) technique [85]. The stress-strength (challenge-capacity) model is used to study the reliability of the CNRP material based on its longitudinal elastic modulus and ultimate longitudinal strength random variables. The probability distributions of the random variables are calculated using the Maximum Entropy Method [88] along with Gaussian and two-parameter Weibull distributions [87]. Finally, a reliability function is obtained for each distribution calculated, and a comparison is provided, as well as the hazard function as a measure of safety and risk [86]. To demonstrate and highlight the sensitivity of the material properties of the CNRP material to the imperfections in the SWCN and the vdW links, a comparative study is conducted. The values of the longitudinal elastic modulus of the CNRP material that has the SWCN as reinforcement of a perfect structure and perfect vdW links in the nanostructure, and that of the CNRP material that has the SWCN of an imperfect structure and imperfect vdW links, are determined. They are compared with the longitudinal elastic modulus of two SWCN-reinforced polymer systems, one with perfectly aligned SWCNs and another with randomly aligned SWCNs, using the material property data obtained from the literature. In this comparison, a (16, 0) SWCN-reinforced Polyetheretherketone (PEEK) is considered as the CNRP material.

5.3 Finite Element Modeling and Analysis of Representative Volume Element (RVE)

The Representative Volume Element (RVE) investigated in the present chapter consists of a Single-Walled-Carbon-Nanotube (SWCN) embedded in a polymer matrix and an interface region

between the SWCN and the polymer material (Figure 5.1). The interactions between the SWCN and the polymer matrix are treated as nonbonded van der Waals interactions. The volume fraction of the SWCN in the composite material denoted as V_n, with respect to the RVE, can be calculated as follows [79]:

$$V_n = \frac{8r_n t_n}{4r_m^2 - (2r_n - t_n)^2} \tag{5.1}$$

where r_n is the mean radius of the nanotube, r_m is the radius of the matrix material and t_n is the thickness of the nanotube. The matrix is regarded as a continuum medium since the matrix volume is far higher than that of the SWCN for the volume fraction considered.

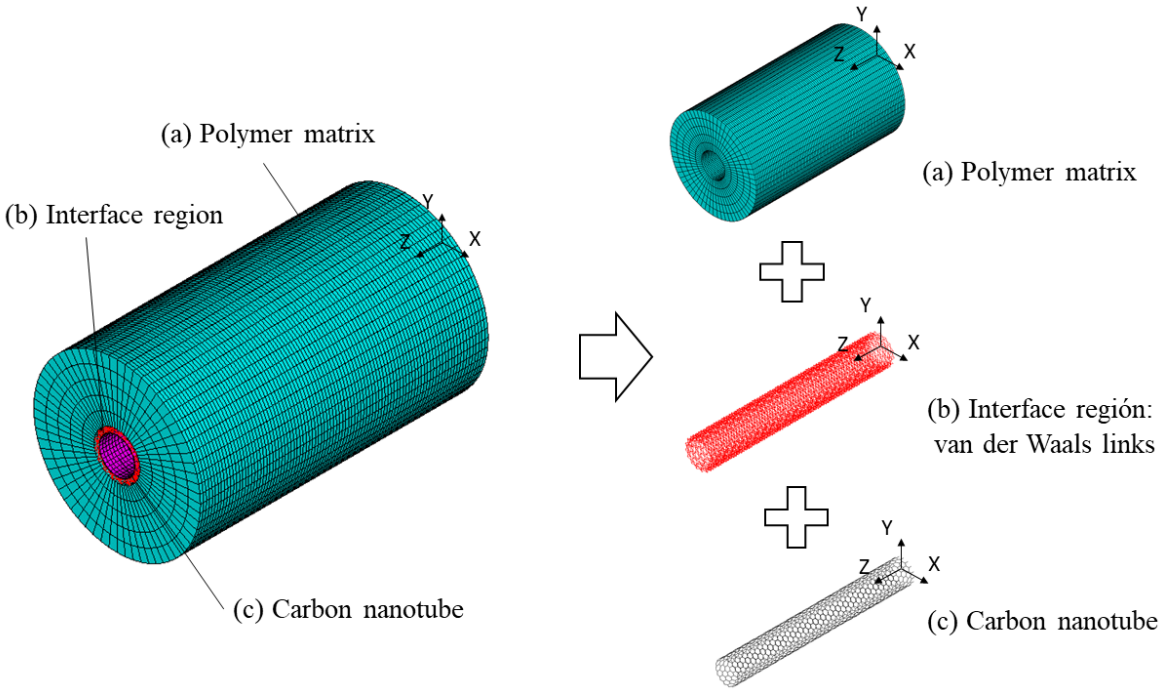

Figure 5.1. Representative Volume Element (RVE) of the nanocomposite.

5.3.1 Space frame model of Single-Walled-Carbon-Nanotube (SWCN)

The mechanical behavior of a Single-Walled-Carbon-Nanotube (SWCN) depends on its atomistic nanostructure. For computational modeling, the SWCN is modeled as a space frame structure wherein the carbon atoms are represented by the so-called nodes of the frame finite-

element. Their positions in three-dimensional space for a particular (n, m) SWCN are defined with the following transformation equation [124]:

$$(x, y, z) = \left(r_n cos\left(\frac{x'}{r_n}\right), r_n sin\left(\frac{x'}{r_n}\right), y'\right) \tag{5.2}$$

where (x', y') are the graphene atomic coordinates which are converted to the nodes in the (x, y, z) coordinates. The nodes, with coordinates defined by the Equation (5.2), are connected by non-linear frame finite elements to represent the potential energy of the interatomic interactions. This potential energy is expressed by using the Morse potential. The effect of the angle-bending potential is negligible, so that the bond stretching potential, denoted by $U_{stretch}$, alone can adequately describe the nanotube behavior. $U_{stretch}$ can be calculated as follows [79]:

$$U_{stretch} = D_e\left(\left[1 - e^{-\beta\Delta r}\right]^2 - 1\right) \tag{5.3}$$

where $U_{stretch}$ represents the energy corresponding to bond stretching, $\Delta r = r - r_0$ is the bond length variation, and D_e and β are the force parameters in the potential energy. The stretching force $F_{stretch}$ of the non-linear behavior of the frame finite-element can be obtained by differentiating $U_{stretch}$ potential with respect to Δr. Hence, $F_{stretch}$ is obtained to be:

$$F_{stretch}(\Delta r) = 2\beta D_e\left(1 - e^{-\beta\Delta r}\right)e^{-\beta\Delta r} \tag{5.4}$$

It is considered that the C-C bond breaks at 19% bond strain, according to Ref. [79], and correspondingly, the force parameters are: D_e = 6.03105 x 10^{-19} Nm, β = 2.625 x 10^{10} m^{-1} and r_0 = 1.421 x 10^{-10} m. BEAM188 element, which is available in commercial software ANSYS®, is used to model the non-linear frame finite-element. This element is capable of uniaxial tension or compression along with torsional and bending deformations, and it has six degrees of freedom at each of its end nodes, which include the translations in the x, y, and z directions and rotations about the x, y, and z-axes. The density ρ_b = 2.3 x 10^3 kg/m^3 is used for the frame element, following Ref. [125], and the mass of the carbon atom m_c= 2.0 x 10^{-26} kg, following Ref. [125]. The mass

m_c is used at the nodes, representing the mass of the carbon atoms. The number of elements of the SWCN is 4512.

5.3.2 Polymer matrix

The polymer matrix is modeled by using linear three-dimensional hexahedral isoparametric finite-element SOLID185, which is available in commercial software ANSYS®. SOLID185 element is capable of simulating both material and geometrical nonlinearities of the hyperelastic material. This element is defined by eight nodes having three degrees of freedom at each node: translations in the nodal x, y, and z directions. In order to describe the mechanical behavior of the polymer matrix, the following Mooney–Rivlin strain energy density function is utilized in conjunction with the SOLID185 element [82]:

$$W(I_1, I_2, I_3, v_m) = c_{1m}(I_1 - 3) + c_{2m}(I_2 - 3) + c_{3m}(I_1 - 3)(I_2 - 3) + \frac{1}{2}k_m(I_3 - 3)^2 \tag{5.5}$$

where I_1, I_2, and I_3 define the invariants of the strain tensor, v_m is the Poisson's ratio, c_{1m}, c_{2m} and c_{3m} are material parameters and k_m is the bulk modulus of the material. Polyetheretherketone (PEEK) is considered as the polymer matrix material. Tension experiments were carried out by El-Qoubaa et al. [147] to determine the mechanical properties of PEEK. The fitting of the experimental stress-strain behavior of this material with the specific Mooney-Rivlin parameters is carried out in the present chapter by using the method of least squares, which is a standard approach in regression analysis to the approximate solution of the overdetermined system. Thus, the stress-strain curve determined is depicted in Figure 5.2 with the Mooney-Rivlin parameters c_{1m}= -3.75 GPa, c_{2m}= 4.82 GPa, c_{3m}= 1.5 GPa, and k_m= 4.083 GPa.

The model parameters for the polymer material consist of an inner radius, an outer radius and 10.0 nm length. The Young's modulus E_m of the polymer material is obtained from the stress-strain curve to perform the vibration analysis. Hence, the mechanical properties of PEEK used in the vibration analysis are the following: E_m= 4.9 x 10^9 Pa, density ρ_m = 1.3 x 10^3 kg/m^3 and Poisson's ratio v_m= 0.3. The number of elements of the polymer matrix material is 36480.

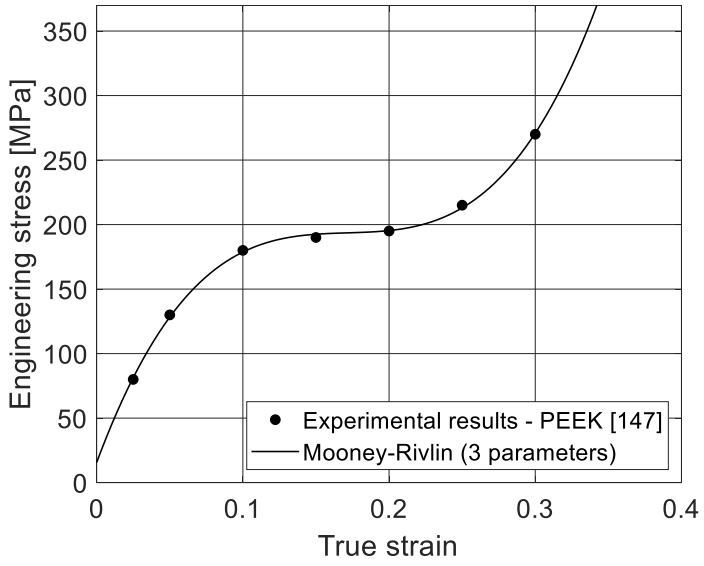

Figure 5.2. Stress-strain behavior of PEEK under uniaxial loading.

5.3.3 Interface modeling

The interface can be simulated either as a continuum or as a discrete region. For convenience in the calculations, only the van der Waals (vdW) interactions between the nanotube and the inner surface of the polymer matrix are considered. Hence, in this chapter the interface region is represented with the use of truss elements, also called LINK elements in commercial software ANSYS®, connecting carbon atoms of the discrete structure of the SWCN to nodes of the internal surface of the matrix elements. The COMBIN39 element is used to model trusses, link, and springs and it is a uniaxial tension-compression element with three degrees of freedom at each node: translations in the nodal x, y, and z directions. For simulations of van der Waals interactions at the nanotube-polymer interface, a truss element model, which was introduced in Ref. [76], is adopted. The properties of the LINK elements are obtained by using the corresponding van der Waals forces based on the Lennard-Jones potential, which is expressed as [83]:

$$U(r) = 4\tilde{\varepsilon}\left[\left(\frac{\tilde{\sigma}}{r}\right)^{12} - \left(\frac{\tilde{\sigma}}{r}\right)^{6}\right] \tag{5.6}$$

where r is the distance between interacting atoms of the nanotube and the polymer matrix, and $\tilde{\varepsilon}$ and $\tilde{\sigma}$ are the Lennard–Jones parameters. For carbon atoms, the Lennard–Jones parameters are $\tilde{\varepsilon}$ = 0.0556 kcal/mole and $\tilde{\sigma}$ = 3.4 Angstroms. Based on the Lennard-Jones potential, the van der Waals force F_{vdW} between interacting atoms is written as follows:

$$F_{vdW}(r) = -\frac{dU(r)}{dr} = 24\frac{\tilde{\varepsilon}}{\tilde{\sigma}}\left[2\left(\frac{\tilde{\sigma}}{r}\right)^{13} - \left(\frac{\tilde{\sigma}}{r}\right)^{7}\right] \tag{5.7}$$

The activation of the truss element in the computational simulation is determined by the distance between an atom (a node) in the nanotube and a node in the internal surface of the polymer matrix, so that if this distance is less than $2.5\tilde{\sigma}$ (0.85 nm), the truss element is activated. The number of elements of the interface region is 7560.

5.4 Probabilistic Modeling and Analysis

5.4.1 Monte Carlo Simulation (MCS) of structural vacancy defects in Single-Walled-Carbon-Nanotube (SWCN) and the interface region

A Macro file is written and developed in MATLAB and run in commercial software ANSYS ® to investigate the effect of structural vacancy defects in the Single-Walled-Carbon-Nanotube (SWCN) and the interface region on the mechanical behavior of the nanocomposite. To represent their structural vacancy defects the Macro file contains the geometry of the perfect SWCN and perfect interface region along with a computer code based on the Monte Carlo Simulation (MCS) technique [85]. This computer code randomly removes C-C bonds and van der Waals (vdW) links in the nanostructure and the interface region, following a specific statistical distribution. The parameters of the distribution and the positions of C-C bonds and vdW links removed (belonging to the missing atoms) along the axial and circumferential directions of the SWCN and the interface region are pre-selected. The total number of simulations of this computational algorithm is 10,000 to achieve good accuracy in the results due to the stochastic implementation of the MCS technique [85]. It should be noted that if there is an element removed at any of the ends of the Representative Volume Element (RVE) of Carbon-Nanotube-Reinforced-Polymer (CNRP) material, the code will generate a new specific statistical distribution to remove C-C bond and vdW links. Thus, the model

is checked carefully prohibiting this specific local effect. The flowchart of the code simulating the stochastic SWCN and the stochastic interface region with vacancy defects is described in Figure 5.3.

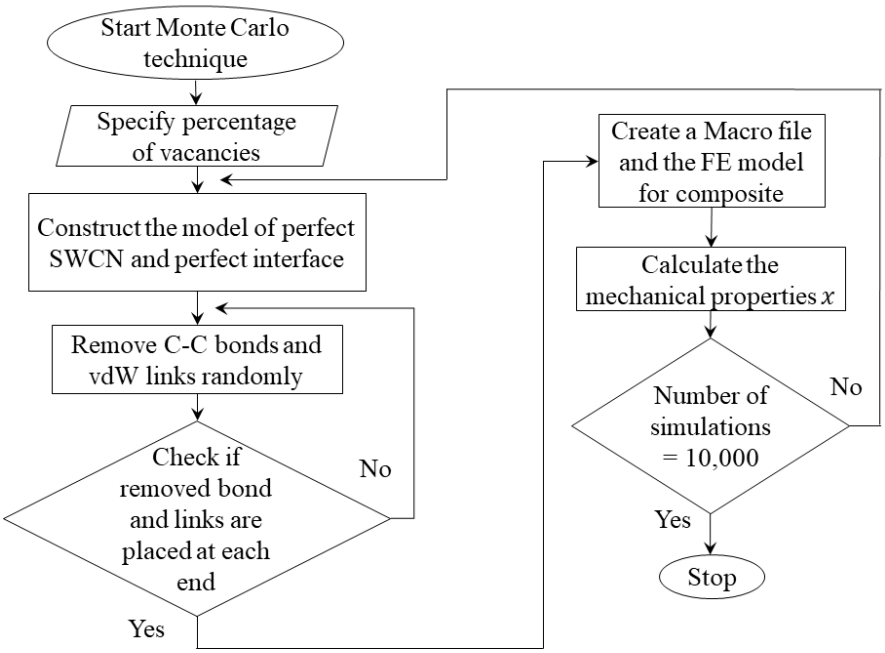

Figure 5.3. Flowchart of modeling and analysis process for imperfect SWCN and imperfect interface region based on Monte Carlo simulation technique.

Regarding the MCS technique, the mechanical properties of the SWCN are determined for every simulation of the nanostructure. Therefore, these mechanical properties depend on the configuration of the SWCN (carbon atoms and C-C bonds) and change for every simulation of the MCS technique. The MCS technique starts with an input uniform distribution to select the position and the distribution of the missing carbon atoms. Then, the C-C bonds and vdW links, which belong to the missing carbon atoms, along the axial and circumferential directions of the SWCN and the interface region are selected and removed following the input distribution. In the present chapter, a (16, 0) SWCN is used as reinforcement material and is modeled through in each simulation, with different vacancy defects (missing atoms and C-C bonds), until reaching 10000 simulations. Figure 5.4 shows the MCS process of the (16, 0) SWCN for a percentage of atomic vacancies of 5% for different simulations of its ultimate longitudinal strength. It can be noticed

that in every iteration, the SWCN shows different vacancy defects in its structure. Hence, the mechanical properties of the (16, 0) SWCN change in every simulation as is depicted in Figure 5.4, so that a specific statistical distribution is determined for each mechanical property. It should be mentioned that for each atomic vacancy, the vdW links in the interface surface of the nanocomposite are also removed along with each iteration of the MCS technique.

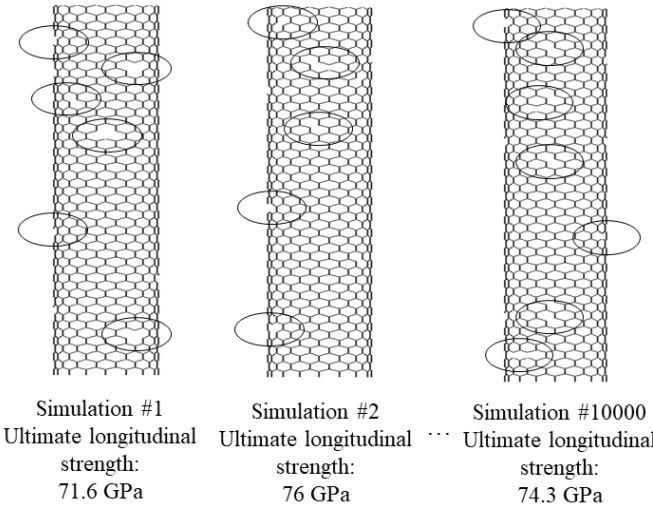

Figure 5.4. Monte Carlo Simulation process for a (16, 0) SWCN.

5.4.2 Maximum Entropy Method

The principle of Maximum Entropy (ME) [88] can represent stochastic information in data using a probability density function (pdf) that depends on its moment constraints. This principle states that any stochastic data can be described, among all the probability distributions compatible with the information available in data, by the pdf with the highest entropy, in other words, the pdf that best represents the information in data. According to the principle of ME, all likelihoods are to be considered based on the information available in data, which in this case is the set of truncated moments related to the distribution of interest. For a random variable x, whereby its realization x takes on all values over an integral of real numbers with unique pdf $f(x)$, the Entropy SE can be defined as [86]:

$$SE(x) = -\int_{\mathbb{R}} f(x) \ln f(x) dx \tag{5.8}$$

In the moment-based ME method, the Entropy SE is maximized subject to:

$$\int_{\mathbb{R}} x^i f(x)\, dx = m_i \tag{5.9}$$

where m_i are the constrained moments, $(i = 0, \dots, n)$ and n is the number of moments. Using the method of Lagrange multipliers [90], the optimization problem with n+1 constraints is then reduced to the optimization of the unconstrained function:

$$\mathcal{L}(\boldsymbol{\lambda}) = \int_{\mathbb{R}} exp\left(\sum_{i=0}^{n} \lambda_i x^i\right) dx - \sum_{i=0}^{n} \lambda_i x^i \tag{5.10}$$

where $\boldsymbol{\lambda} = \{\lambda_i\}$ for $i = \{0, \dots, n\}$ are the Lagrange multipliers for its corresponding $\boldsymbol{x} = \{x^i\}$. Equation (5.10) has a solution for $f(x)$ as follows [88]:

$$f(x) = exp\left(\sum_{i=0}^{n} \lambda_i x^i\right) \tag{5.11}$$

All the ME distributions are achieved when $\partial\mathcal{L}/\partial\boldsymbol{\lambda} = 0$, which satisfies the moment constraints in Equation (5.9) and takes the general form of $f(x)$ in Equation (5.11). Note that since $x^0 = 1$ (for $i = 0$) in Equation (5.11), λ_0 can be determined by using the following expression:

$$\lambda_0 = -ln \int_{\mathbb{R}} exp\left(\sum_{i=0}^{n} \lambda_i x^i\right) dx \tag{5.12}$$

The gradient $\partial\mathcal{L}/\partial\boldsymbol{\lambda}$ and the elements H_{ij} of Hessian matrix $[H]$ of the Lagrangian function in Equation (5.10) are given, respectively, as follows:

$$(\nabla\mathcal{L})_i = \frac{\partial\mathcal{L}}{\partial\lambda_i} = \int_{\mathbb{R}} x^i f(x)\, dx - x^i \tag{5.13}$$

$$H_{ij} = \int_{\mathbb{R}} x^{i+j} f(x)\, dx \tag{5.14}$$

The Lagrange multipliers $\boldsymbol{\lambda}$ in Equation (5.11) can be found by using the methodology proposed in Ref. [88], which involves the Newton method [90].

5.4.3 Reliability Evaluation based on the stress-strength (challenge-capacity) model

A mechanical system fails when the strength S (the capacity of the system) is less than the applied stress s (the challenge of the system), where both strength and stress are random variables. The strength is considered as the capacity of the system to tolerate damage, while the stress is regarded as the challenge that the system must tolerate [159]. The probability density function for the stress is denoted by $f_s(s)$ and that for strength by $f_S(S)$. If the probability density function curves for both strength and stress interfere, as shown in Figure 5.5(a), then the shaded area where the curves interfere is an indication that the component will fail, because the stress exceeds its strength. The failure probability of the system P_f, which is the probability that the stress exceeds the strength, is expressed as follows:

$$P_f = P(Stress \geq Strength) \tag{5.15}$$

also, the reliability R, which is the probability that the stress is less than the strength, is expressed as follows:

$$R = P(Strength \geq Stress) \tag{5.16}$$

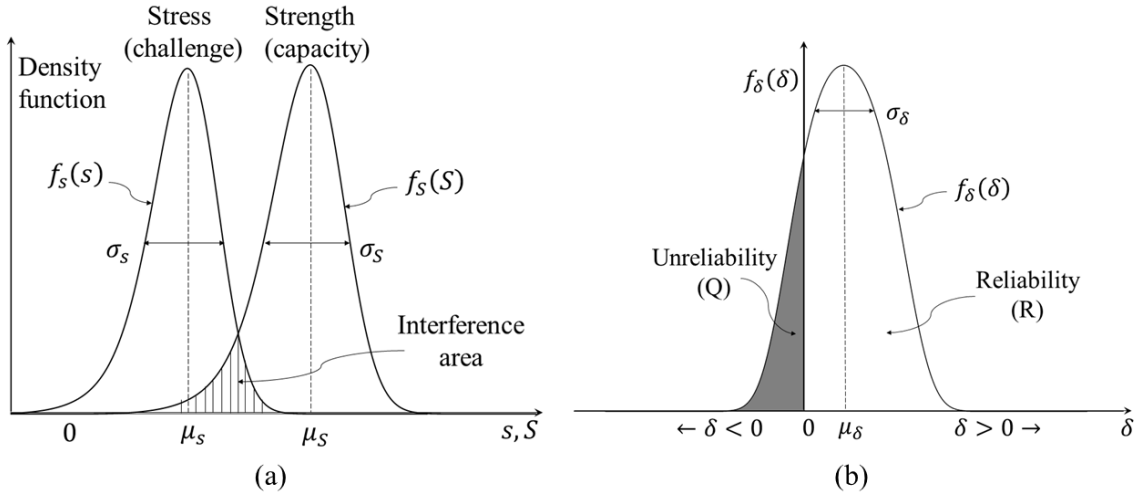

Figure 5.5. (a) Probability of failure from stress-strength distributions and (b) Reliability from interference variable.

The reliability of a mechanical system can be calculated if the density functions for the strength $f_S(S)$ and the stress $f_s(s)$ are known. However, if a variable is defined as $\delta \equiv S - s$, where S and s are independent random variables and both are greater than or equal to zero, the reliability can be then obtained based on this variable [159]. The variable δ would also be considered as a random variable, which is called interference random variable. Therefore, the reliability R can be defined as follows:

$$R = P(\delta \geq 0) \tag{5.17}$$

Thus, the reliability can be calculated by the expression given by:

$$R = \int_0^{\infty} f_\delta(\delta) d\delta \tag{5.18}$$

This probability in terms of the area under the density function of the interference random variable δ is shown in Figure 5.5(b), where $\mu_\delta = \mu_S - \mu_s$ is the mean value of δ, μ_S is the mean value of strength S, μ_s is the mean value of stress s, and σ_δ represents the standard deviation of δ. Similarly, the unreliability Q is given by:

$$Q = \int_{-\infty}^{0} f_\delta(\delta) d\delta \tag{5.19}$$

The areas corresponding to R and Q are shown in Figure 5.5(b). It is possible to evaluate the reliability or unreliability of a mechanical system considering various density functions of stress and strength.

5.5 Results and discussion

5.5.1 Comparison of results with data from the literature

The effects of random arrangement of carbon nanotubes in a polymer matrix, the entanglement of fillers and kinking are probably dominant in polymer matrix composites, as it was mentioned before. However, the use of stochastic modeling to analyze the effects of structural vacancies in the Single-Walled-Carbon-Nanotube (SWCN) is also of interest in manufacturing,

because such vacancies are randomly distributed in the SWCN and are unavoidable in engineering applications [39-42]. To the extent that the mechanical properties of the nanotube reinforcement influence the properties of the nanocomposite, there would be a corresponding sensitivity of the nanocomposite property to the variations in the properties of the nanotube reinforcement and interface properties. Hence, a comparison of the results between a Poly {(m-phenylenevinylene)-co-[(2,5-dioctoxy-p-phenylene)vinylene]} matrix [100], known as PmPV, with perfectly aligned SWCNs, and the Carbon-Nanotube-Reinforced-Polymer (CNRP) material is provided. The results of the SWCN-reinforced PmPV were calculated for its longitudinal elastic modulus considering different chiralities of zigzag SWCNs. The CNRP material used for this comparison is a (16, 0) SWCN-reinforced PEEK, considering a perfect structure for the SWCN and the van der Waals (vdW) links. The volume fractions of SWCN used for the longitudinal elastic modulus were 0.035, 0.070, 0.105, 0.140, and 0.175. Figure 5.6 shows the comparison of the longitudinal elastic modulus of the SWCN-reinforced PmPV and the (16, 0) SWCN-reinforced PEEK. It can be appreciated from Figure 5.6 that the longitudinal elastic modulus of the (16, 0) SWCN-reinforced PEEK shows a similar tendency as the results of the SWCN-reinforced PmPV.

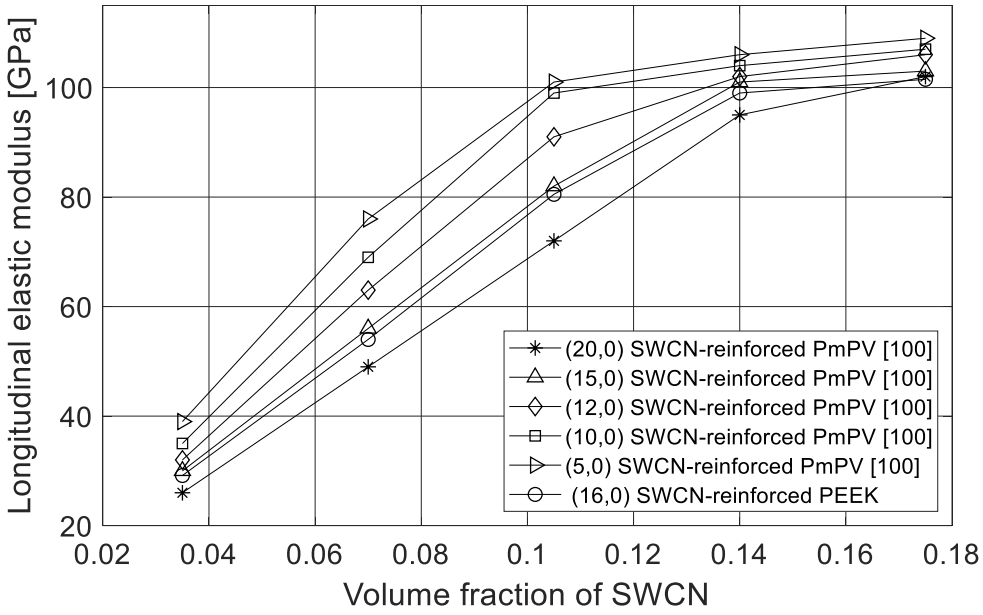

Figure 5.6. Comparison of the longitudinal elastic modulus of the (16, 0) SWCN-reinforced PEEK and the SWCN-reinforced PmPV [100], considering perfectly aligned SWCNs.

In the case of structural vacancies in the SWCN and the vdW links, the longitudinal elastic modulus of the CNRP material is determined for an imperfect (16, 0) SWCN-reinforced PEEK, considering a perfectly aligned SWCN. The imperfect (16, 0) SWCN-reinforced PEEK presents 5% atomic vacancies in the nanotube. The results of the imperfect (16, 0) SWCN-reinforced PEEK are compared to that of the perfect SWCN-reinforced PmPV with randomly aligned SWCNs. In Figure 5.7, the longitudinal elastic modulus of the imperfect (16, 0) SWCN-reinforced PEEK is approximately two times higher than that of the perfect SWCN-reinforced PmPV with randomly aligned SWCNs. The results of the imperfect (16, 0) SWCN-reinforced PEEK also show a similar tendency as the results of the perfect SWCN-reinforced PmPV. These results indicate an increase of the longitudinal elastic modulus considering higher values of SWCN volume fraction.

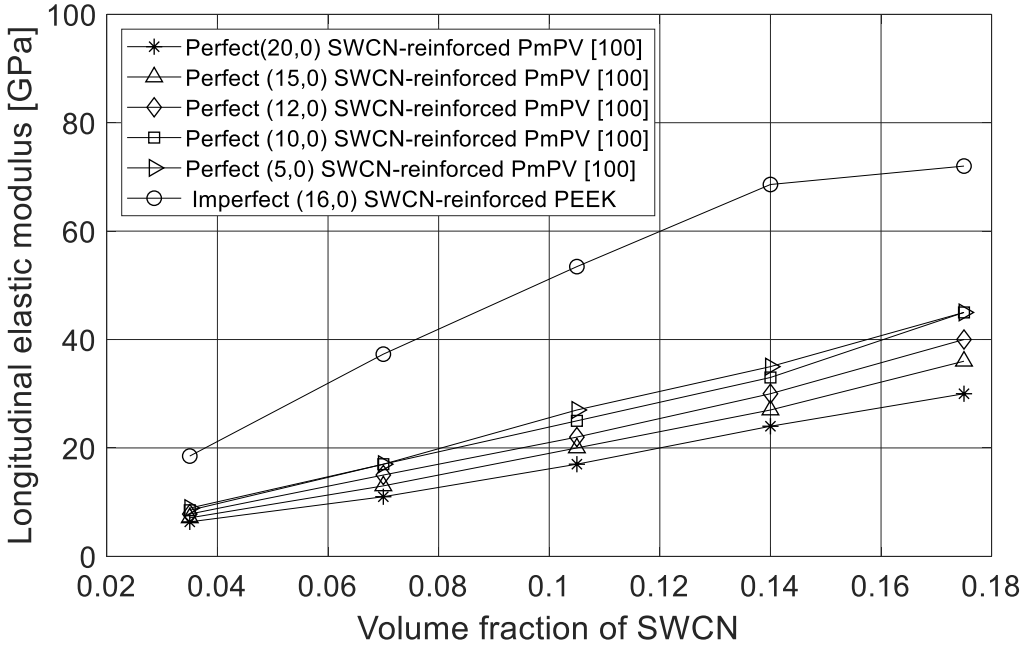

Figure 5.7. Comparison of the longitudinal elastic modulus of the imperfect (16, 0) SWCN-reinforced PEEK and the SWCN-reinforced PmPV [100] with randomly aligned SWCNs.

Regarding the CNRP material reinforced with a perfect or an imperfect SWCN, Figure 5.8 shows the comparison of the longitudinal elastic modulus of the (16, 0) SWCN-reinforced PEEK considering a perfect SWCN and an imperfect SWCN. The longitudinal elastic modulus decreases if there are structural vacancies in the nanostructure. For example, in the case of 3.5% volume fraction, the longitudinal elastic modulus decreases by about 37%, while in the case of 17% volume

fraction, the longitudinal modulus decreases by about 29%. Hence, in sub-section 4.2, a probabilistic analysis is performed on the CNRP material with structural vacancies to determine its reliability and hazard associated with its ultimate longitudinal strength and an applied external stress. Such vacancy defects are essential randomness to be considered in a conservative and safe design of the nanocomposite.

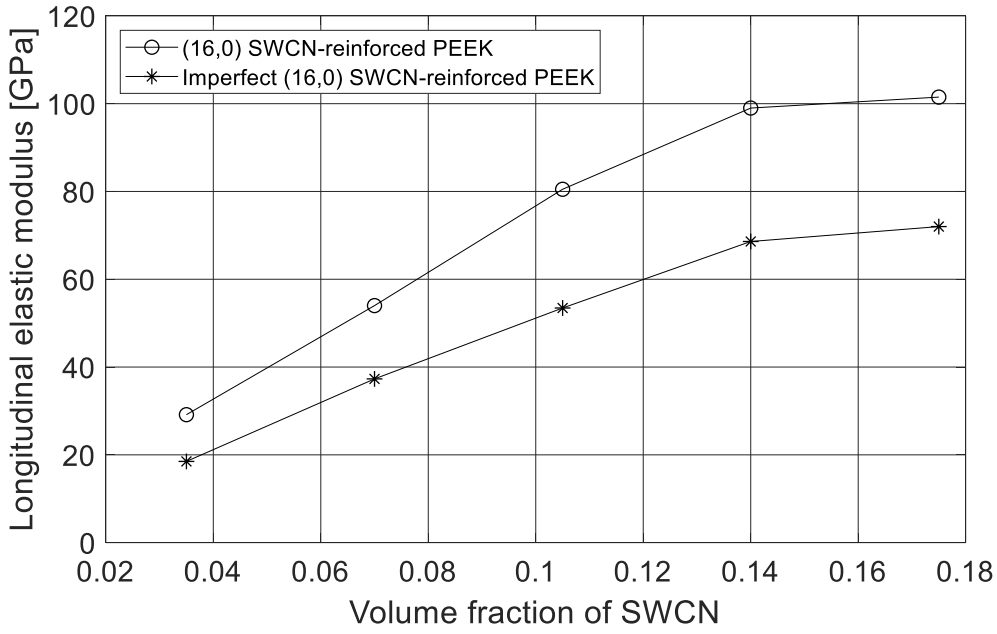

Figure 5.8. Comparison of the longitudinal elastic modulus of the (16, 0) SWCN-reinforced PEEK, considering a perfect and an imperfect SWCN.

5.5.2 Probabilistic analysis of mechanical properties of Carbon-Nanotube-Reinforced-Polymer (CNRP) material

Probabilistic analysis of the mechanical properties of the Carbon-Nanotube-Reinforced-Polymer (CNRP) material is discussed in this section. The case study is performed on a CNRP material with 5% volume fraction of Single-Walled-Carbon-Nanotube (SWCN), considering an imperfect (16, 0) SWCN along with an imperfect interface region. The percentage of atomic vacancies in the imperfect (16, 0) SWCN is 5%, which implies having C-C bonds and van der Waals (vdW) links correspondingly removed in the structure for the SWCN and the interface region, respectively. The vacancy defects in the imperfect SWCN are characterized based on the Monte Carlo Simulation (MCS) technique. Therefore, several iterations are required to meet the

mentioned convergence criterion (10,000 simulations) [85]. The length L_n of the CNRP material is 10 nm and the thickness t_n of the SWCN is 0.34 nm. The diameter of the (16, 0) SWCN is 1.2535 nm. Hence, the aspect ratio (length /diameter) of the (16, 0) SWCN is 7.977. The boundary conditions for this analysis are Clamped-Free (CF), where one end of the polymer matrix material is fully constrained, and an axial displacement is applied at the other (free) end.

The statistical distributions for the longitudinal elastic modulus and the ultimate longitudinal strength of the CNRP material are obtained based on the MCS technique, as well as the applied stress of the stress-strength model. For each distribution, the skewness, the median, the mean and the mode are calculated to determine if the statistical distributions are symmetric or asymmetric. The skewness for the longitudinal elastic modulus is -0.5623, which means that it is a left-skewed distribution with its median higher than its mean. The median of the longitudinal elastic modulus is 25.585 GPa, the mean is 25.536 GPa, and the mode is 25.539 GPa. For the ultimate longitudinal strength, the skewness is -0.5605, which means that this distribution is also a left-skewed distribution with its median higher than its mean. The median of the ultimate longitudinal strength is 3.572 GPa, the mean is 3.565, and the mode is 3.566 GPa. In the case of the applied stress for the stress-strength model, the skewness is -0.5612, which means that this distribution is also a left-skewed distribution. The median of the applied stress is 3.247 GPa, the mean is 3.240 GPa, and the mode is 3.242 GPa. Hence, from the analysis of the skewness of the statistical distributions, it can be noticed that the distributions are asymmetric. Thus, an entropy distribution can show a more realistic probability density function (pdf) for each random variable.

The pdfs studied in the present chapter are the Maximum-Entropy distribution with four-moments (ME4) and the Maximum-Entropy distribution with five-moments (ME5), along with Gaussian and two-parameter Weibull distributions [87]. Table 5.1 lists the moment constraints in calculating the maximum entropy distributions for the material properties mentioned before and the applied stress. In Table 5.1, there are available four-moment constraints for the ME4 distribution and five-moment constraints for the ME5 distribution for each random variable.

Table 5.1. Moment constraints used in calculating maximum entropy distributions

Material properties	First order (GPa)	Second order (GPa^2)	Third order (GPa^3)	Fourth order (GPa^4)	Fifth order (GPa^5)
Longitudinal elastic modulus	25.536	6527.137	16698.243	427562.727	109572808.624
Ultimate longitudinal strength	3.564	12.720	45.430	162.395	580.990
Applied stress	3.240	10.512	34.132	110.918	360.749

Figure 5.9 shows the longitudinal elastic modulus frequency histogram along with ME4, ME5, Gaussian and Weibull pdfs in a range of 22-28 GPa and a Relative Uncertainty (RU) of 3.021 x 10^{-13} Pa, which is obtained as RU $= \sigma_{RU}/\mu_{RU}\sqrt{n_{RU}}$, where σ_{RU} is the standard deviation, μ_{RU} is the mean value, and n_{RU} is the number of simulations. Their corresponding cumulative distribution functions (cdfs) are also plotted along with the Empirical Frequency cdf of Longitudinal Elastic Modulus (EFLEM cdf). EFLEM cdf is determined by calculating first the area of each frequency bar in the histogram (of the longitudinal elastic modulus). Then, each of these areas (of each frequency bar) is added to the area of the previous one until all of these areas (of all frequency bars) are included. The initial value of the cumulative sum of the areas is zero, and the final value is 1. The frequency histogram of the ultimate longitudinal strength of the CNRP material is illustrated in Figure 5.10 along with ME4, ME5, Gaussian, and Weibull pdfs in a range of 3-4 GPa and an RU of 3.023 x 10^{-13} Pa. Their corresponding cdfs are also plotted along with the Empirical Frequency cdf of Ultimate Longitudinal Strength (EFULS cdf). EFULS cdf is calculated using the same procedure as that of EFLEM cdf but considering the frequency histogram of the ultimate longitudinal strength. Regarding the applied stress, Figure 5.11 shows its frequency histogram along with ME4, ME5, Gaussian, and Weibull pdfs in a range of 2.8-3.6 GPa and an RU of 3.022 x 10^{-13} Pa. Their corresponding cdfs are also plotted along with the Empirical Frequency cdf of Applied Stress (EFAS cdf). EFAS cdf is calculated using the same

procedure as that of EFLEM cdf and EFULS cdf but considering the frequency histogram of the applied stress.

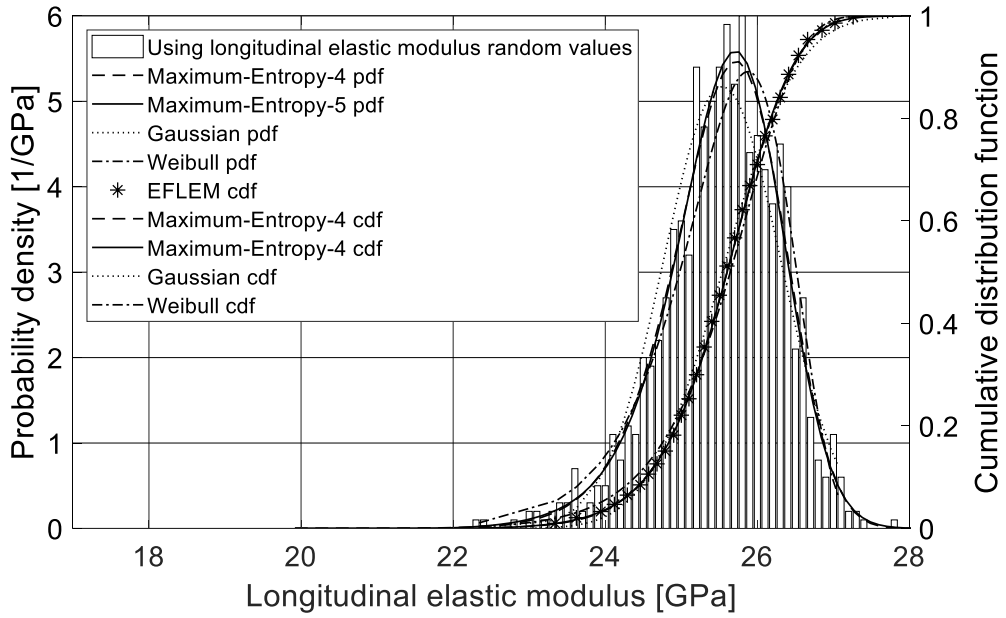

Figure 5.9. Frequency histogram and probability density and distribution functions of the longitudinal elastic modulus.

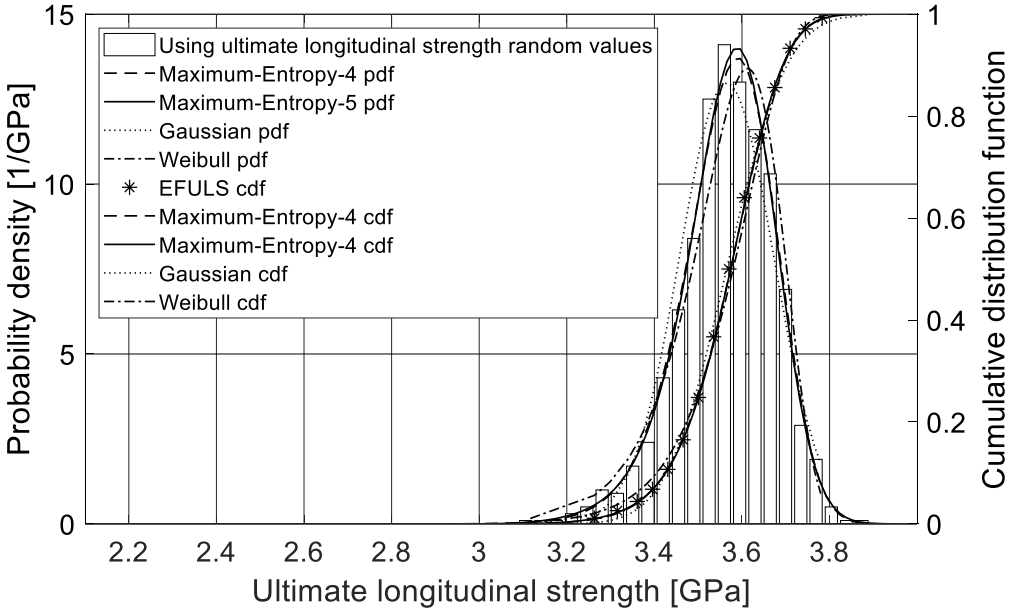

Figure 5.10. Frequency histogram and probability density and distribution functions of the ultimate longitudinal strength.

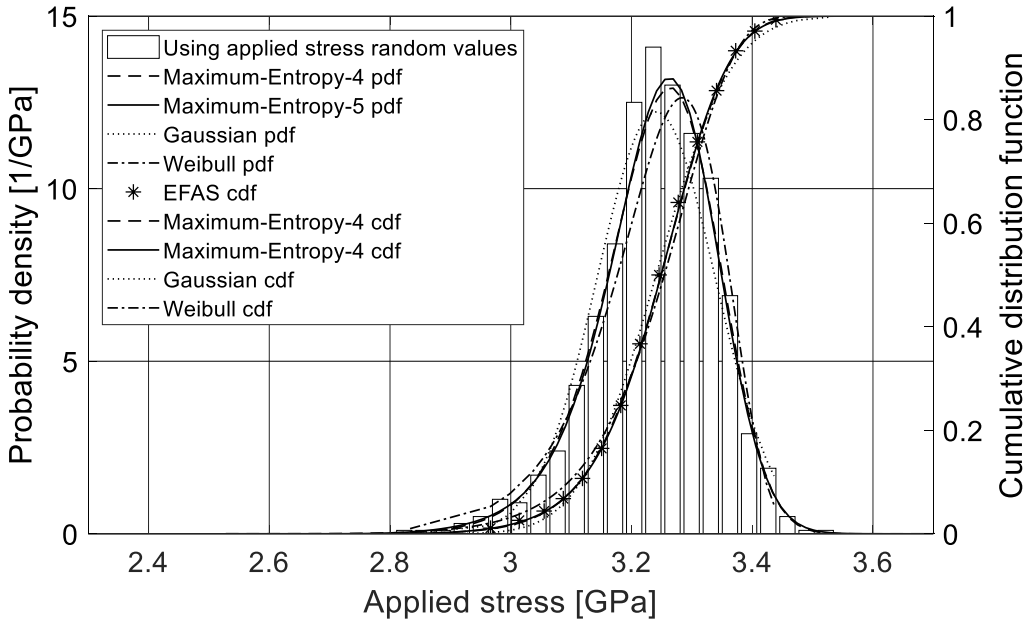

Figure 5.11. Frequency histogram and probability density and distribution functions of applied stress.

Table 5.A-1 in Appendix A summarizes the computed Lagrange multipliers for the mechanical properties mentioned before and the applied stress. Each Lagrange multiplier has been considered with three-digits after the decimal, which is required to guarantee the accuracy of computation since their small changes may cause an extreme variation in the exponential probability function. The maximum iteration numbers in searching acceptable Lagrange multipliers never exceed 20 for the random variables in the present chapter. The entropy quantity has the lowest numerical value for the ME5 distribution, regardless of the random variable considered.

Table 5.2 summarizes the computed Gaussian and Weibull parameters for each mechanical property of the CNRP material and the applied stress. The Weibull parameters for the longitudinal elastic modulus are: scale-parameter $\beta = 25.894$ GPa and shape-parameter $\alpha = 37.628$, while the Gaussian parameters are: mean value $\mu = 25.536$ GPa and standard deviation $\sigma = 0.771$ GPa. In the case of the ultimate longitudinal strength, the Weibull parameters are: scale-parameter $\beta = 3.614$ GPa and shape-parameter $\alpha = 37.608$, while the Gaussian parameters are: mean value $\mu = 3.564$ GPa and standard deviation $\sigma = 0.107$ GPa. Regarding the applied stress, the Weibull

parameters are: scale-parameter $\beta = 3.286$ GPa and shape-parameter $\alpha = 37.608$, while the Gaussian parameters are: mean value $\mu = 3.240$ GPa and standard deviation $\sigma = 0.097$ GPa.

Table 5.2. Weibull and Gaussian parameters computed for different material properties.

Material properties	Weibull parameters		Gaussian parameters	
	β (GPa)	α	μ (GPa)	σ (GPa)
Longitudinal elastic modulus	25.894	37.628	25.536	0.771
Ultimate longitudinal strength	3.614	37.608	3.564	0.107
Applied stress	3.286	37.608	3.240	0.097

Regarding the reliability analysis based on the stress-strength model, an interference random variable δ is calculated to obtain the reliability of the CNRP material involving its ultimate longitudinal strength and an applied stress. The reliability is obtained based on the probability density function of δ for values of δ higher than or equal to zero. Therefore, the distribution of δ is computed by using the MCS technique with the ultimate longitudinal strength and the applied stress, considering the definition $\delta \equiv$ strength - stress. Calculating the skewness of variable δ is possible to define if its statistical distribution is symmetric or asymmetric. The skewness of variable δ is 0.3645, which means that this distribution is a right-skewed distribution with its median lower than its mean. The median of the variable δ is 0.38 GPa, the mean is 0.4 GPa, and the mode is 0.28 GPa. Hence, it can be observed that this distribution is asymmetric. Thus, an entropy distribution can show a realistic pdf for this variable, as well as the distributions of the mechanical properties of the CNRP material and the applied stress already calculated.

Figure 5.12 shows the frequency histogram of variable δ along with ME4, ME5, Gaussian, and Weibull pdfs when $\delta > 0$ with an RU of 5.95 x 10^{-12} Pa. Their corresponding cumulative distribution functions (cdf) are also plotted along with the Empirical Frequency cdf of Interference Random Variable (EFIRV cdf). EFIRV cdf is determined by calculating first the area of each frequency bar in the histogram (of variable δ). Then, each of these areas (of each frequency bar) is added to the area of the previous one until all of these areas (of all frequency bars) are included. The initial value of the cumulative sum of the areas is zero, and the final value is 1. Table 5.A-2 in Appendix A summarizes the moment constraints in calculating ME4 and ME5 distributions for

the interference random variable δ, as well as the corresponding Lagrange multipliers, and the Weibull and Gaussian parameters for their pdfs shown in Figure 5.12.

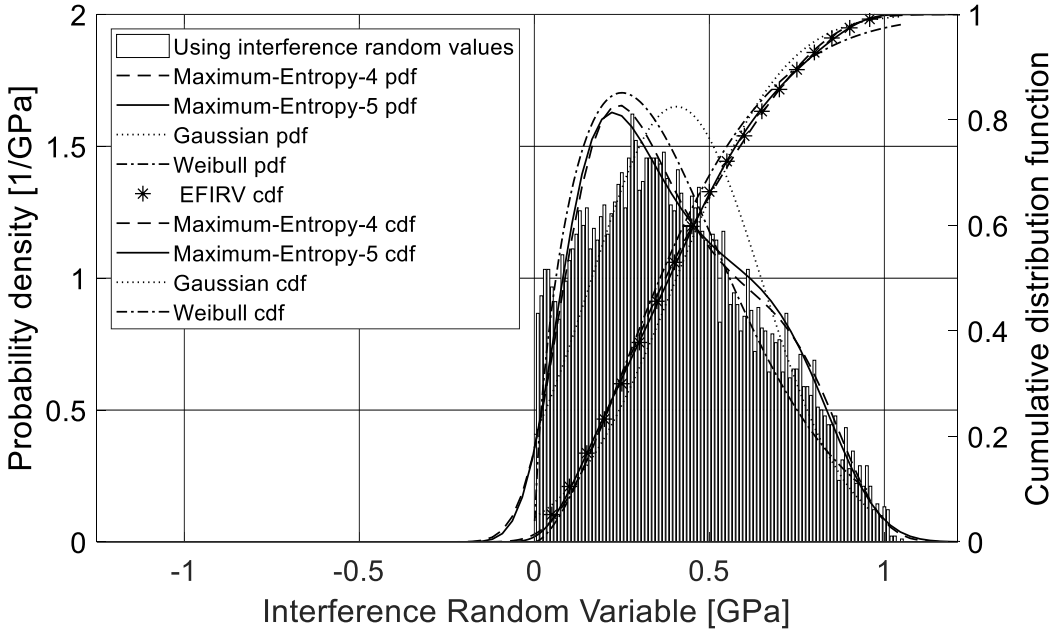

Figure 5.12. Frequency histogram and probability density functions of interference random variable δ and its cumulative distribution functions.

Figure 5.13 shows the reliability of the CNRP material for values of the operational stress obtained from the random variable δ for different distributions: ME4, ME5, Weibull, and Gaussian. It can be appreciated from Figure 5.13 that the operational stress is in a range of 3.11-4.16 GPa. It can also be observed that the reliabilities based on ME4 and ME5 distributions fit better the Empirical Frequency of Operational Stress (EFOS) reliability than that of the Weibull and Gaussian distributions. EFOS is obtained by using the values of EFIRV cdf associated to the frequency histogram of variable δ. However, the comparison between the reliability values based on the different distributions plotted in Figure 5.13, and that of the EFOS reliability is provided based on the Root-Mean-Square-Error (RMSE) and Chi-Square Error. Table 5.3 shows the RMSE and Chi-Square Error for the reliabilities based on the different distributions with respect to EFOS reliability, corresponding to the operational stress in the CNRP material. From Table 5.3, it can be appreciated that the ME4 reliability presents a RMSE of 0.0075604 and a Chi-square error of 0.0002294, while the ME5 reliability presents a RMSE of 0.0071344 and a Chi-square error of

0.0001659. Regarding the Weibull reliability, this distribution presents a RMSE of 0.1119983 and a Chi-square error of 0.0013706, while The Gaussian reliability presents a RMSE of 0.1485945 and a Chi-square error of 0.0021110. The errors calculated in Table 5.3 show that Weibull and Gaussian reliabilities give a RMSE that is 15 times higher than that of ME4 and ME5 reliabilities. In the case of the Chi-square error, the Weibull reliability is six times higher than that of the ME4 reliability and eight times higher than that of the ME5 reliability, while the Gaussian reliability is nine times higher than that of the ME4 reliability and 12 times higher than that of the ME5 reliability. Therefore, it can be observed that ME4 and ME5 distributions are closer to EFOS than Weibull and Gaussian distributions, which lead to a better calculation and characterization of the reliability and performance of the CNRP material.

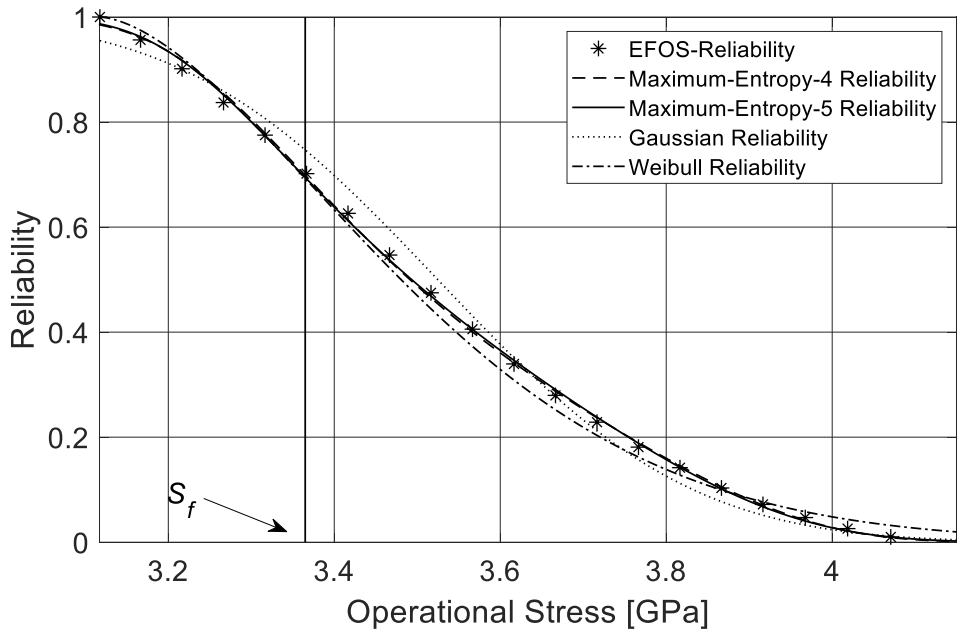

Figure 5.13. Reliability of the CNRP material for different distributions of δ.

Table 5.3. RMSE and Chi-square error for variable δ

Distribution	RMSE	Chi-square error
ME4	0.0075604	0.0002294
ME5	0.0071344	0.0001659
Weibull	0.1119983	0.0013706
Gaussian	0.1485945	0.0021110

The reliability analysis is a needed component of design. Therefore, it is possible to determine, from the reliability results, the Mean-Stress-To-Failure (MSTF) [160] and the Mean-Residual-Strength (MRS) [160]. As the name indicates, the MSTF denotes the expected stress to failure for a non-repairable system. On the other hand, the MRS is defined as the expected value of the remaining strength of the system after a fixed stress point, which can be determined when the reliability value decreases until reaching values close to zero. The fixed stress point to calculate the MRS is determined from Figure 5.13 when the reliability value presents a considerable change in its behavior towards an area with low-reliability values close to zero, and from the MSTF results. This fixed stress point is denoted as S_f and it can be appreciated in Figure 5.13. The reliability zone after S_f can be considered as a failure zone, which can be further characterized by the hazard function. The value of S_f is calculated by using the values of MSTF shown in Table 5.4, which shows the MSTF and the MRS for each distribution and EFOS. The MSTF of EFOS is 3.5283 GPa, and the MRS of EFOS is 4.6965 GPa. It can be appreciated in Table 5.4 that the maximum value of the MSTF based on the distributions is 3.6502 GPa, so the value of S_f should be lower than the maximum value of the MSTF. In this analysis S_f has a numerical value of 3.365 GPa.

Regarding the analysis of the MSTF based on the distributions, the ME4 distribution presents a percent error of 0.00031 with respect to EFOS, the ME5 distribution presents a percent error of 0.00028 with respect to EFOS, the Weibull distribution presents a percent error of 0.00277 with respect to EFOS and the Gaussian distribution shows a percent error of 0.00345 with respect to EFOS. It can be noticed for the MSTF that the error percentage of the Weibull distribution is eight times higher than that of the ME4 distribution and nine times higher than that of the ME5 distribution, while for the Gaussian distribution, the error percentage is 11 times higher than that of the ME4 distribution and 12 times higher than that of the ME5 distribution. Hence, it can be observed that the results obtained from ME4 and ME5 distributions are more suitable and appropriate for a high-performance design of the CNRP material than that of Weibull and Gaussian distributions concerning EFOS. Regarding the analysis of the MRS based on the distributions, the error percentage of the Weibull distribution is five times higher than that of the ME4 distribution and 20 times higher than that of the ME5 distribution, while for the Gaussian distribution, the error percentage is 10 times higher than that of the ME4 distribution and 40 times higher than that of the ME5 distribution. Therefore, it can be appreciated, as in the results of MSTF, that the results

of ME4 and ME5 distributions lead to a better conservative design than that of Weibull and Gaussian distributions concerning EFOS.

Table 5.4. MSTF and MRS for each distribution.

Distribution	MSTF (GPa)	Error* (%)	MRS (GPa)	Error* (%)
EFOS	3.5283	-	4.6965	-
ME4	3.5294	0.00031	4.6585	0.00809
ME5	3.5293	0.00028	4.6869	0.00204
Weibull	3.6262	0.00277	4.4995	0.04190
Gaussian	3.6502	0.00345	4.3155	0.08112

*with respect to EFOS

Regarding the hazard analysis, the hazard function is more physically meaningful as a measure of performance, safety and risk than is the reliability function itself [86]. Therefore, from the reliability results, the cumulative hazard function H can be calculated with the following expression: $H = ln(1/R)$, where R is the reliability function [86]. Figure 5.14 shows the cumulative hazard function corresponding to the different distributions and EFOS, where it can be appreciated that with the increase of the operational stress, the CNRP material can fail more catastrophically because of its structural problems. If the fixed stress point S_f is observed in Figure 5.14, it is possible to identify two zones for the hazard function, the zone for values lower than S_f, which is considered as the useful strength for the CNRP material, and the region for values higher than S_f, which is considered as the failure zone of the CNRP material. Hence, the MSTF and S_f can be used to determine a safety factor SFc for the CNRP material by using the most repetitive value (the mode) of the applied stress, which is 3.242 GPa. The safety factor SFc can be calculated as: SFc = strength/applied stress [161]. Table 5.5 shows different values of SFc based on the MSTF for the probability distributions and S_f. The SFc obtained from the MSTF of EFOS is 1.0883, while from the ME4 and ME5 distributions it is 1.0886. The SFc obtained from the Weibull distribution is 1.1185 and from the Gaussian distribution is 1.1265, while the SFc obtained from S_f is 1.0379. Therefore, it is observed that ME4 and ME5 distributions give safety factor values

lower than that of Weibull and Gaussian distributions. Thus, these distributions and S_f lead to a conservative, safe, and reliable design of the CNRP material, as in the reliability analysis.

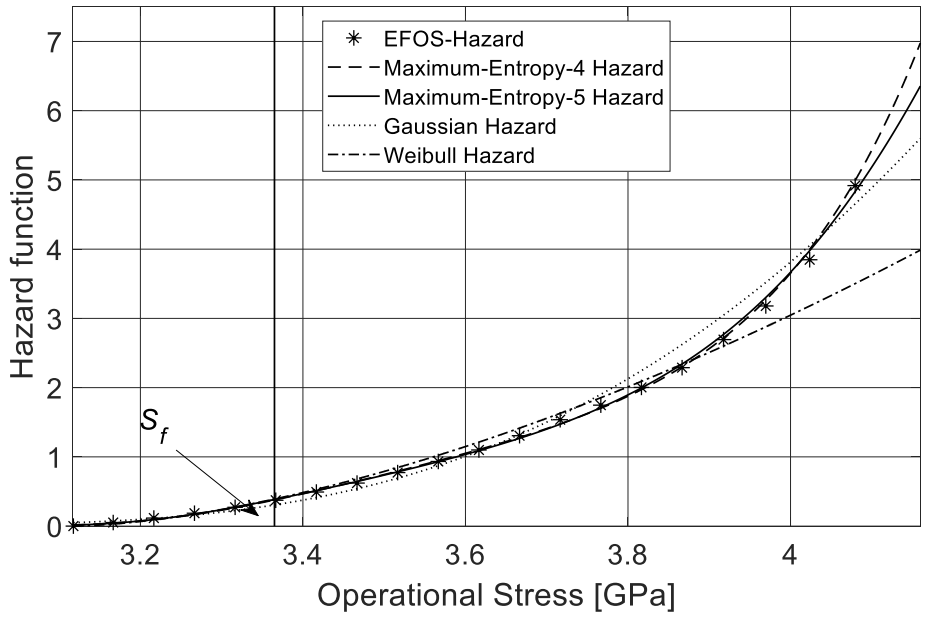

Figure 5.14. Cumulative hazard function of the CNRP material for different distributions of δ.

Table 5.5. Safety Factor (SFc) based on various distributions and S_f .

Distribution	MSTF (GPa)	SFc
EFOS	3.5283	1.0883
ME4	3.5294	1.0886
ME5	3.5293	1.0886
Weibull	3.6262	1.1185
Gaussian	3.6502	1.1265
	S_f	SFc
	3.365	1.0379

5.6 Conclusion

In the present chapter, a comparison of the longitudinal elastic modulus of the Representative Volume Element (RVE) of the Carbon-Nanotube-Reinforced-Polymer (CNRP) material with results from the literature was performed. The results showed that structural vacancies constitute an essential randomness to be considered in the design of a nanocomposite. In the present chapter, a perfect (16, 0) Single-Walled-Carbon-Nanotube (SWCN) and an imperfect (16, 0) SWCN were considered during the analysis. Atomic vacancies of 5% were considered in the imperfect (16, 0) SWCN. Hence, the longitudinal elastic modulus decreased with the presence of structural vacancies in the CNRP material. For instance, the longitudinal elastic modulus decreased by about 37% with 3.5% volume fraction of SWCN, while in the case of 17% volume fraction of SWCN, the longitudinal modulus decreased by about 29%.

Reliability analysis was also performed on the RVE of the CNRP material, considering an imperfect (16, 0) SWCN as reinforcement and an imperfect interface region between the SWCN and the polymer matrix material. The imperfect (16, 0) SWCN was simulated with 5% of atomic vacancies by using the Monte Carlo Simulation (MCS) technique. The distributions based on the the MCS technique were obtained for the longitudinal elastic modulus and the ultimate longitudinal strength of the CNRP material, and the applied stress of the stress-strength model. The distributions obtained for each random variable were based on the Maximum Entropy Method, along with two-parameter Weibull and Gaussian distributions. The Maximum Entropy (ME) distributions used in the present chapter were determined with four-moment constraints (ME4) and with five-moment constraints (ME5).

During the reliability analysis based on the stress-strength model, the reliability distributions were compared to the empirical distribution obtained using the data collected from the interference random variable δ. The results showed that ME4 and ME5 distributions were more appropriate and accurate than Weibull and Gaussian distributions. The errors calculated in this analysis showed that Weibull and Gaussian reliabilities presented a Root-Mean-Square-Error (RMSE) that was 15 times higher than that of ME4 and ME5 distributions. In the case of the Chi-square error, the Weibull reliability was six times higher than that of the ME4 distribution and eight times higher than that of the ME5 distribution, while the Gaussian reliability was nine times higher than that of the ME4 distribution and 12 times higher than that of the ME5 distribution. Although the RMSE

and Chi-square error were higher in Weibull and Gaussian distributions, these distributions are also appropriate to obtain the reliability function using the analysis presented in this chapter.

In addition to the reliability functions, the Mean-Stress-To-Failure (MSTF) and the Mean-Residual-Strength (MRS) were determined. Also, a fixed stress point S_f was established based on the results of the reliability analysis. The results showed that the MRS was higher than the MSTF. The error percentage of MSTF for the Weibull distribution was eight times higher than that of the ME4 distribution and nine times higher than that of the ME5 distribution, while for the Gaussian distribution, the error percentage was 11 times higher than that of the ME4 distribution and 12 times higher than that of the ME5 distribution. The error percentage of MRS for the Weibull distribution was five times higher than that of the ME4 distribution and 20 times higher than that of the ME5 distribution, while for the Gaussian distribution, the error percentage was ten times higher than that of the ME4 distribution and 40 times higher than that of the ME5 distribution. Hence, ME4 and ME5 distributions were more suitable and precise to calculate the reliability of the CNRP material than Weibull and Gaussian distributions.

The hazard function was also computed based on the results of the reliability analysis for each distribution as a measure of safety and risk. From the hazard analysis, it was possible to identify two zones for the hazard function, the zone for values lower than S_f, which was considered as the useful strength for the CNRP material and the region for values higher than S_f, which was regarded as the failure zone of the CNRP material. Different values of the safety factor SFc were determined for the CNRP material in a range of 1.0379-1.1265 based on the results obtained from the MSTF for the different distributions and S_f. Hence, ME4 and ME5 distributions gave the lowest values of the safety factor, which indicates that these distributions lead to a high-performance, safe, conservative, and reliable design of the CNRP material. By combining the finite-element modeling and analysis of the RVE with the probabilistic analysis and modeling (based on the MCS technique and the stress-strength model), it was possible to provide an alternative solution to study and to characterize the material behavior of the nanocomposite with structural problems (i.e. missing carbon atoms and C-C bonds in the SWCN).

5.7 Appendix A

Tables 5.A-1 and 5.A-2 are presented in this section.

Table 5.A-1. Lagrange multipliers computed for different material properties.

Material properties		Lagrange multipliers						Entropy
		λ_0	λ_1	λ_2	λ_3	λ_4	λ_5	
Longitudinal elastic modulus	ME4	4973.7	-863.97	56.600	-1.65	0.018		1050.67
	ME5	92714	-18588.3	1487.069	-59.30	1.17	-0.0093	1050.05
Ultimate longitudinal strength	ME4	4838.2	-6032.51	2839.426	-596.04	46.96		-5516.48
	ME5	91931	-132071	75708.31	-21634.3	3080.2	-174.73	-5520.99
Applied stress	ME4	4838.1	-6635.75	3435.700	-793.33	68.75		-6762.56
	ME5	91925	-145271	91602.06	-28793.7	4509.6	-281.38	-6767.52

Table 5.A-2. Moment constraints, Lagrange multipliers and, Weibull and Gaussian parameter for variable δ.

	First order (GPa)	Second order (GPa^2)	Third order (GPa^3)	Fourth order (GPa^4)	Fifth order (GPa^5)
Random variable δ based on ultimate longitudinal strength and applied stress	0.4063	0.2227	0.1421	0.0997	0.0747

	Lagrange multipliers						Entropy
	λ_0	λ_1	λ_2	λ_3	λ_4	λ_5	
ME4	1.0706	-16.769	60.2701	-84.0182	42.0924		-224.488
ME5	1.0869	-19.058	81.0124	-146.407	117.3528	-31.4214	-231.239

Weibull parameters		Gaussian parameters	
β (GPa)	α	μ (GPa)	σ (GPa)
0.4519	1.6474	0.4063	0.2401

Chapter 6. Reliability Evaluation based on Modal Parameters of Carbon-Nanotube-Reinforced-Polymer-Composite Material using Multiscale Finite Element Model

Foreword

This chapter is a journal paper in preparation.

In this chapter, a 3D multiscale finite element of the Representative Volume Element of the Carbon-Nanotube-Reinforced-Polymer-Composite (CNRPC) material is developed considering 5% of volume fraction and structural vacancies in the SWCN and the interface region to study its dynamic reliability and dynamic hazard. The structural vacancies are represented by missing carbon atoms and covalent bonds in the SWCN and van der Waals links in the interface region. The imperfections in the SWCN are characterized using the Monte-Carlo Simulation technique. The evaluation of dynamic reliability and dynamic hazard is performed by using the challenge-capacity model for on the modal parameters of CNRPC material to determine if an external excitation frequency is close to any of those frequency. Hence, it considers the frequency sweep of the excitation and the nearness to resonance of the material system as a characterization approach.

6 Reliability Evaluation based on Modal Parameters of Carbon-Nanotube-Reinforced-Polymer-Composite Material using Multiscale Finite Element Model

6.1 Abstract

Nanocomposite materials exhibit a much more extensive range of scatter in material properties than that of conventional materials. The objective of the present chapter is to develop a computational framework to perform a probabilistic analysis of Carbon-Nanotube-Reinforced-Polymer-Composite (CNRPC) material by using a 3D multiscale finite element model of the Representative Volume Element (RVE) of the nanocomposite material to determine the dynamic reliability and dynamic hazard based on its modal parameters. The consideration of the frequency sweep of the excitation and the nearness to resonance of the material system is used as a basis for the evaluation of dynamic reliability and dynamic hazard. A computational model consisting of a polymer matrix, an imperfect Single-Walled-Carbon-Nanotube (SWCN) and an imperfect interface region has been constructed for this purpose. The polymer matrix is modeled with the Mooney-Rivlin strain energy function, while the imperfect interface region is modeled via van der Waals (vdW) links. The imperfect SWCN possesses structural vacancies, which are characterized by using the Monte Carlo simulation technique, and is modeled using the Morse potential. The challenge-capacity model is used to calculate the dynamic reliability and dynamic hazard of the CNRPC material for its natural frequencies associated with bending and axial modes. The dynamic reliability and dynamic hazard functions of the CNRPC material are determined as a measure of safety and risk using the Maximum Entropy Method.

6.2 Introduction

Single-Walled-Carbon-Nanotubes (SWCNs) incorporated into polymers because of their exceptional and multipurpose properties create a new generation of nanocomposite materials [51]. However, the main problem in their structural design is to properly account for the uncertainties in their material properties [52]. The structural analysis under uncertainty is the main task of the stochastic or probabilistic analysis, which has developed fast in the last decades mainly focused on the use of finite element approaches in connection with stochastic or probabilistic methods [162].

It is a standard practice to use a Representative Volume Element (RVE) in the simulation and modeling of any type of composites (that are metal-based, ceramic-based and polymer-based) [53]. Hence, there are a few studies that analyze the structural aspects, such as vacancy defects, in a polymer matrix reinforced with a SWCN. For example, Shokrieh & Rafiee [41] developed a full stochastic multiscale modeling technique to estimate mechanical properties of carbon-nanotube-reinforced-polymers considering valid parameters at nano, micro, meso, and macro-scales. Later, Davoudabadi and Farahani [108] investigated the influence of different vacancy defects on the Young's modulus of a SWCN - reinforcement polymer composite in the axial direction by using a structural model in commercial software ANSYS®. In other work, Ghasemi et al. [39] studied the uncertainties propagation and their effects on the reliability of polymeric nanocomposite continuum structures considering material, structural, and modeling uncertainties. They considered the length, waviness, agglomeration, orientation, and dispersion of the SWCNs as random variables. Yuan & Lu [109] proposed a geometric generation algorithm to produce a 3D finite element model of a polymeric composite with randomly dispersed and wavy SWCNs to analyze its elastic-plastic properties, as well as Joshi et al. [110], who proposed a multiscale 3D RVE approach for modeling the elastic behavior of carbon nanotubes reinforced composites with vacancy defects. Other authors, such as Ju et al. [42], investigated the interfacial strengths between polypropylene-carbon fiber composites through experimental observation as well as using molecular dynamics simulation to determine its optimal chemical functionalization groups, while Rafiee & Mahdavi [40] presented a theoretical characterization of the interaction between a SWCN and a surrounding polymer using molecular dynamics simulation. They conducted a stochastic analysis treating numbers of established covalent bonds between the SWCN and the polymer material, and their positions as random parameters. Moreover, Rafiee et al. [163] investigated experimentally the vibration and damping characteristics of epoxy composites reinforced by pristine and functionalized multiwalled carbon nanotubes for potential use as integral passive damping elements in structural composite applications.

Later, Chawla et al. [111] explored the effect of vacancy defects on SWCN reinforced polypropylene composites using molecular dynamics simulation and comparing the influence of a perfect and an imperfect SWCN as reinforcement. Ozden-Yenigun et al. [112] studied the crosslinking route and interfacial interactions for achieving superior properties in a SWCN-reinforced epoxy by using multiscale modeling. Other authors, such as Zhu et al. [113], presented

a probabilistic multiscale approach to model the random spatial distribution of local elastic properties arising from the heterogeneous waviness and orientation of SWCN fillers within a 3D microscale continuum RVE of a SWCN-reinforced polymer matrix. Recently, Jeong et al. [114] proposed a 3D stochastic computational homogenization model for SWCN-epoxy matrix composites. They found that stochastic waviness, agglomeration, and orientation of SWCN fillers caused random spatial variations of the elasticity tensor of the SWCN-epoxy matrix within a microscale RVE, resulting in probabilistic variations of the sufficient homogenized stiffness of the RVE.

The consideration of the randomness due to defects in a carbon nanotube or interphase while assuming that the carbon nanotubes are correctly aligned is duly justified in the references from the literature. Moreover, the use of stochastic modeling to analyze the effects of structural vacancies in the SWCN is also of interest in manufacturing, due to the fact that vacancies are randomly distributed in the SWCN and are unavoidable in engineering applications [39-42]. Another essential aspect of composites is the study of their structural reliability.

In the analysis of reliability, there are studies of laminated composites [156, 157], including multiscale modeling [158]. However, there are no works considering SWCN polymer composites. Despite the work done on this type of composites, studies to characterize and to analyze its structural reliability considering a stochastic modeling technique still need to be carried out. Hence, the objective of the present chapter is to perform probabilistic modeling and analysis of a Carbon-Nanotube-Reinforced-Polymer-Composite (CNRPC) material to determine the dynamic reliability and dynamic hazard of its modal response by using the challenge-capacity modeling and reliability prediction method [159]. The modal response of the CNRPC material analyzed in the present chapter is carried out in terms of its bending and axial mode natural frequencies, which are considered as random variables. For modeling the CNRPC material, a 3D multiscale finite-element model of the RVE of the composite material is developed. The CNRPC material consists of a polymer matrix material, an imperfect SWCN, and an imperfect interface region. The multiscale modeling is performed in terms of using different theories and corresponding strain energies to model individual parts of the Representative Volume Element of the CNRPC material. The macroscale continuum mechanics for the polymer matrix, the mesoscale mechanics for the imperfect interface region, and nanoscale-level atomistic mechanics for the imperfect SWCN. The polymer matrix is modeled with the Mooney-Rivlin strain energy [82]. The imperfect SWCN, with

structural vacancies, is modeled as a space frame structure by using the Morse potential [79], while the imperfect interface region is modeled via van der Waals (vdW) links [83]. The structural vacancies of the imperfect SWCN and the imperfect interface region are modeled by using the Monte-Carlo Simulation (MCS) technique [82]. The probability distributions of the random variables are calculated using the Maximum Entropy Method [88]. The challenge-capacity model for the natural frequencies and the excitation frequency is used to study the dynamic reliability [164] and dynamic hazard [86] functions of the CNRPC material in bending and axial modes as a measure of safety and risk.

6.3 Finite Element Modeling and Analysis of Representative Volume Element (RVE)

The Representative Volume Element (RVE) investigated in the present chapter consists of a Single-Walled Carbon Nanotube (SWCN) embedded in a polymer matrix and an interface region between the SWCN and the polymer material (Figure 6.1). The interactions between the SWCN and the polymer matrix are treated as nonbonded van der Waals interactions. The volume fraction of SWCN in the composite material denoted as V_n, with respect to the RVE, can be calculated as follows [79]:

$$V_n = \frac{8 r_n t_n}{4 r_m^2 - (2 r_n - t_n)^2} \tag{6.1}$$

where r_n is the mean radius of the nanotube, r_m is the radius of the matrix material and t_n is the thickness of the nanotube. The matrix is regarded as a continuum medium since the matrix volume is far higher than that of the SWCN for the volume fractions considered.

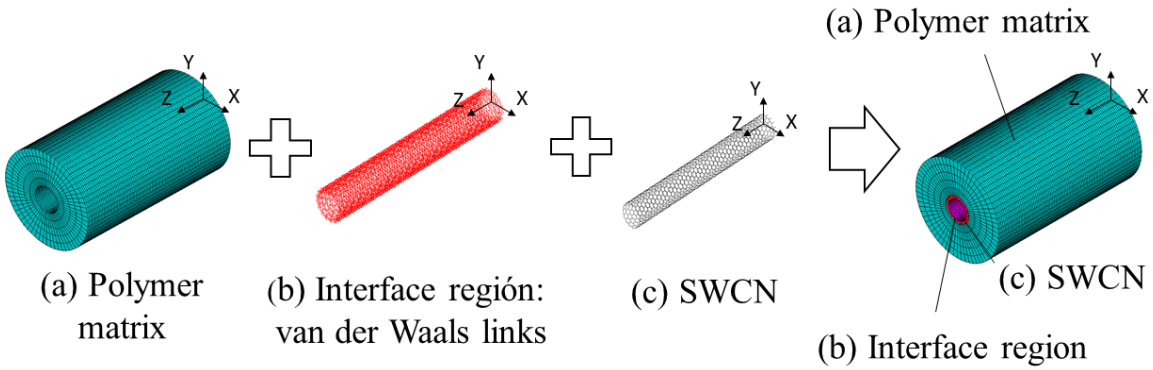

Figure 6.1. Representative Volume Element (RVE) of the nanocomposite.

6.3.1 Space frame model of Single-Walled-Carbon-Nanotubes (SWCN)

The mechanical behavior of a Single-Walled-Carbon-Nanotube (SWCN) depends on its atomistic nanostructure. For computational modeling, the SWCN is modeled as a space frame structure wherein the carbon atoms are represented by the so-called nodes of the frame finite-element. Their positions in three-dimensional space for a particular (n, m) SWCN are defined with the following transformation equation [124]:

$$(x, y, z) = \left(r_n cos\left(\frac{x'}{r_n}\right), r_n sin\left(\frac{x'}{r_n}\right), y'\right) \tag{6.2}$$

where (x', y') are the graphene atomic coordinates which are converted to the nodes in the (x, y, z) coordinates. The nodes, with coordinates defined by the Equation (6.2), are connected by non-linear frame finite elements in order to represent the potential energy of the interatomic interactions. This potential energy is expressed by using the Morse potential. The effect of the angle-bending potential is negligible, so that the bond stretching potential, denoted by $U_{stretch}$, alone can adequately describe the nanotube behavior. $U_{stretch}$ can be calculated as follows [79]:

$$U_{stretch} = D_e\left(\left[1 - e^{-\beta\Delta r}\right]^2 - 1\right) \tag{6.3}$$

where $U_{stretch}$ represents the energy corresponding to bond stretching, $\Delta r = r - r_0$ is the bond length variation, and D_e and β are the force parameters in the potential energy. The stretching force $F_{stretch}$ of the non-linear behavior of the frame finite-element can be obtained by differentiating U_{streth} potential with respect to Δr. Hence, $F_{stretch}$ is obtained to be:

$$F_{stretch}(\Delta r) = 2\beta D_e\left(1 - e^{-\beta\Delta r}\right)e^{-\beta\Delta r} \tag{6.4}$$

It is considered that the C-C bond breaks at 19% bond strain, according to Ref. [79], and correspondingly the force parameters are: D_e = 6.03105 x 10^{-19} Nm, β = 2.625 x 10^{10} m^{-1} and r_0 = 1.421 x 10^{-10} m. BEAM188 element, which is available in commercial software ANSYS®, is used to model the non-linear frame finite element. This element is capable of uniaxial tension or

compression along with torsional and bending deformations, and it has six degrees of freedom at each of its end nodes, which include the translations in the x, y, and z directions and rotations about the x, y, and z-axes. The density ρ_b = 2.3 x 10^3 kg/m^3 is used for the frame element, in accordance to Ref. [125], and the mass of the carbon atom m_c = 2.0 x 10^{-26} kg, following Ref. [125]. The mass m_c is used at the nodes, representing the mass of the carbon atoms. The number of elements of the SWCN is 4512.

6.3.2 Polymer matrix

The polymer matrix is modeled by using linear three-dimensional hexahedral isoparametric finite-element SOLID185, which is available in commercial software ANSYS®. SOLID185 element is capable of simulating both material and geometrical nonlinearities of hyperelastic material. This element is defined by eight nodes having three degrees of freedom at each node: translations in the nodal x, y, and z directions. In order to describe the mechanical behavior of the polymer matrix, the following Mooney–Rivlin strain energy density function is utilized in conjunction with the SOLID185 element [82]:

$$W(I_1, I_2, I_3, v_m) = c_{1m}(I_1 - 3) + c_{2m}(I_2 - 3) + c_{3m}(I_1 - 3)(I_2 - 3) + \frac{1}{2}k_m(I_3 - 3)^2 \tag{6.5}$$

where I_1, I_2, and I_3 define the invariants of the strain tensor, v_m is the Poisson's ratio, c_{1m}, c_{2m} and c_{3m} are material parameters and k_m is the bulk modulus of the material. Polyetheretherketone (PEEK) is considered as the polymer matrix material. Tension experiments were carried out by El-Qoubaa et al. [147] to determine the mechanical properties of PEEK. The fitting of the experimental stress-strain behavior of this material with the specific Mooney-Rivlin parameters is carried out in the present chapter by using the method of least squares, which is a standard approach in regression analysis to the approximate solution of the overdetermined system. Thus, the stress-strain curve determined is depicted in Figure 6.2 with the Mooney-Rivlin parameters c_{1m}= -3.75 GPa, c_{2m}= 4.82 GPa, c_{3m}= 1.5 GPa, and k_m= 4.083 GPa.

The model parameters for the polymer material consist of an inner radius, an outer radius, and 10.0 nm length. The Young's modulus E_m of the polymer material is obtained from the stress-

strain curve in order to perform the vibration analysis. Hence, the mechanical properties of PEEK used in the vibration analysis are as follows: E_m= 4.9 x 10^9 Pa, density ρ_m = 1.3 x 10^3 kg/m^3 and Poisson's ratio v_m= 0.3. The number of elements of the polymer matrix material is 36480.

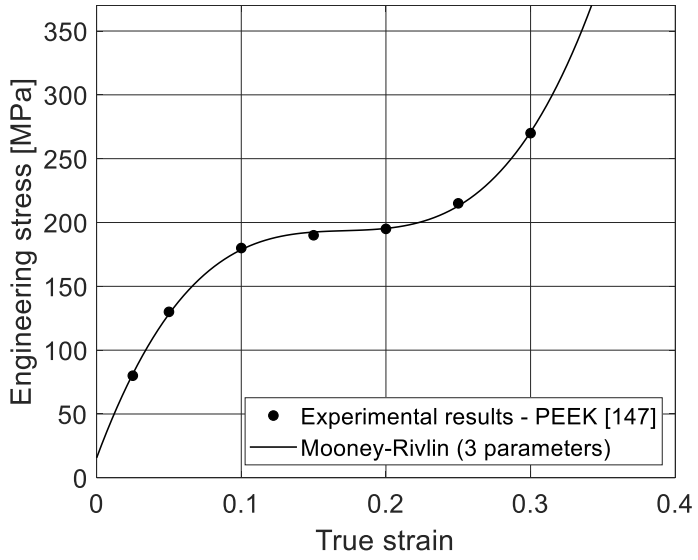

Figure 6.2. Stress-strain behavior of PEEK under uniaxial loading.

6.3.3 Interface modeling

The interface can be simulated either as a continuum or as a discrete region. For convenience in the calculations, only the van der Waals (vdW) interactions between the nanotube and the inner surface of the polymer matrix are considered. Hence, in this chapter the interface region is represented with the use of truss finite elements, also called LINK elements in commercial software ANSYS®, connecting carbon atoms of the discrete structure of Single-Walled-Carbon-Nanotube (SWCN) to nodes of the internal surface of matrix elements. The COMBIN39 element is used to model trusses, links, and springs, and it is a uniaxial tension-compression element with three degrees of freedom at each node: translations in the nodal x, y, and z directions. For simulations of van der Waals interactions at the nanotube-polymer interface, a truss element model, which was introduced in Ref. [76], is adopted. The properties of the LINK elements are obtained by using the corresponding van der Waals forces based on the Lennard-Jones potential, which is expressed as [83]:

$$U(r) = 4\tilde{\varepsilon}\left[\left(\frac{\tilde{\sigma}}{r}\right)^{12} - \left(\frac{\tilde{\sigma}}{r}\right)^{6}\right] \tag{6.6}$$

where r is the distance between interacting atoms of the nanotube and the polymer, $\tilde{\varepsilon}$ and $\tilde{\sigma}$ are the Lennard–Jones parameters. For carbon atoms, the Lennard–Jones parameters are $\tilde{\varepsilon}$ = 0.0556 kcal/mole and $\tilde{\sigma}$ = 3.4 Angstroms. Based on the Lennard-Jones potential, the van der Waals force F_{vdW} between interacting atoms is written as follows:

$$F_{vdW}(r) = -\frac{dU(r)}{dr} = 24\frac{\tilde{\varepsilon}}{\tilde{\sigma}}\left[2\left(\frac{\tilde{\sigma}}{r}\right)^{13} - \left(\frac{\tilde{\sigma}}{r}\right)^{7}\right] \tag{6.7}$$

The activation of the truss element in the computational simulation is determined by the distance between an atom (a node) in the nanotube and a node in the internal surface of the polymer matrix, so that if this distance is less than $2.5\tilde{\sigma}$ (0.85 nm), the truss element is activated. The number of elements of the interface region is 7560.

6.4 Probabilistic Modeling and Analysis

6.4.1 Monte Carlo Simulation (MCS) of structural vacancy defects in Single-Walled-Carbon-Nanotube and the interface region

In order to investigate the effect of structural vacancy defects in the Single-Walled-Carbon-Nanotube (SWCN) and the interface region on the mechanical behavior of the nanocomposite, a Macro file is written and developed in MATLAB and run in commercial software ANSYS®. To represent their structural vacancy defects the Macro file contains the geometry of the perfect SWCN and perfect interface region along with a computer code based on the Monte Carlo Simulation (MCS) technique [85]. This computer code randomly removes C-C bonds and van der Waals (vdW) links in the nanostructure and the interface region following a specific statistical distribution. The parameters of the distribution and the positions of C-C bonds and vdW links removed (belonging to the missing atoms) along the axial and circumferential directions of the SWCN and the interface region are pre-selected. The total number of simulations of this

computational algorithm is 10,000 to achieve good accuracy in the results due to the stochastic implementation of the MCS technique [85]. It should be noted that if an element is removed at any of the ends of the Representative Volume Element (RVE) of the Carbon-Nanotube-Reinforced-Polymer-Composite (CNRPC) material, the code will generate a new specific statistical distribution to remove the C-C bonds and the vdW links. Thus, the model is checked carefully prohibiting this specific local effect. The flowchart of the code simulating the stochastic SWCN and the stochastic interface region with vacancy defects is described in Figure 6.3.

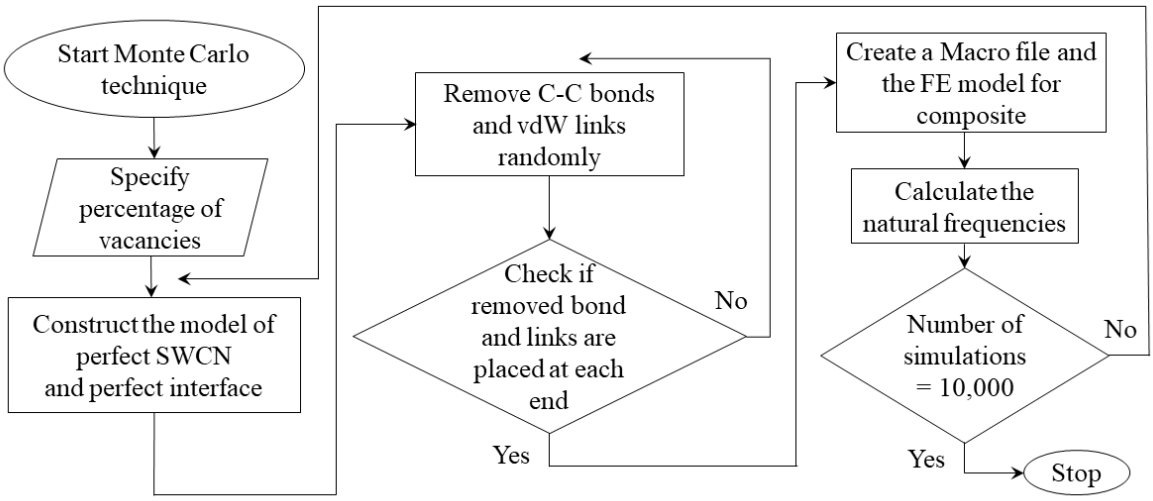

Figure 6.3. Flowchart of modeling and analysis process for imperfect SWCN and imperfect interface region based on Monte Carlo simulation technique.

Regarding the MCS technique, the natural frequencies of the SWCN are determined for every simulation of the nanostructure. Therefore, these natural frequencies depend on the configuration of the SWCN (carbon atoms and C-C bonds) and change for every simulation of the MCS technique. The MCS technique starts with an input uniform distribution to select the position and the distribution of the missing carbon atoms. Then, the C-C bonds and vdW links, which belong to the missing carbon atoms, along the axial and circumferential directions of the SWCN and the interface region are selected and removed following the input distribution. In the present chapter, a (16, 0) SWCN is used as reinforcement material and is modeled through in each simulation, with different vacancy defects, until reaching 10000 simulations. Figure 6.4 shows the

MCS process of the (16, 0) SWCN with a percentage of atomic vacancies of 5% for different simulations of its first bending mode frequency. It can be noticed that in every iteration, the SWCN shows different vacancy defects in its structure. The natural frequencies of the (16, 0) SWCN change in every simulation as is depicted in Figure 6.4, so that a specific statistical distribution is determined for each natural frequency. It should be mentioned that for each atomic vacancy, vdW links in the interface surface of the nanocomposite are also removed with each iteration of the MCS technique.

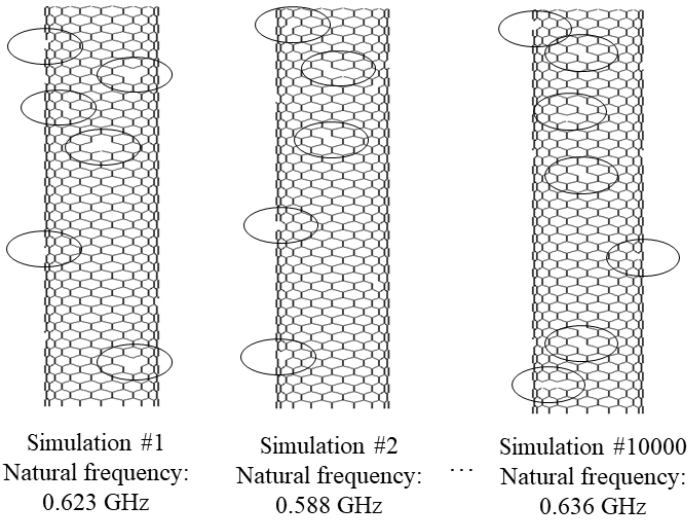

Figure 6.4. Monte Carlo Simulation process for a (16, 0) SWCN.

6.4.2 Maximum Entropy Method

The principle of Maximum Entropy (ME) [88] can represent stochastic information in data using a probability density function (pdf) that depends on its moment constraints. According to the principle of ME, all likelihoods are to be considered based on the information available in data, which in this case is the set of truncated moments related to the distribution of interest. For a random variable x, whereby its realization x takes on all values over an integral of real numbers with unique pdf $f(x)$, the Entropy SE can be defined as [86]:

$$SE(x) = -\int_{\mathbb{R}} f(x) \ln f(x) dx \tag{6.8}$$

In the moment-based ME method, the Entropy SE is maximized subject to:

$$\int_{\mathbb{R}} x^i f(x)\, dx = m_i \tag{6.9}$$

where m_i are the constrained moments, $(i = 0, \dots, n)$ and n is the number of moments. Using the method of Lagrange multipliers [90], the optimization problem with n+1 constraints is then reduced to the optimization of the unconstrained function:

$$\mathcal{L}(\boldsymbol{\lambda}) = \int_{\mathbb{R}} exp\left(\sum_{i=0}^{n} \lambda_i x^i\right) dx - \sum_{i=0}^{n} \lambda_i x^i \tag{6.10}$$

where $\boldsymbol{\lambda} = \{\lambda_i\}$ for $i = \{0, \dots, n\}$ are the Lagrange multipliers for its corresponding $\boldsymbol{x} = \{x^i\}$. Equation (6.10) has a solution for $f(x)$ as follows [88]:

$$f(x) = exp\left(\sum_{i=0}^{n} \lambda_i x^i\right) \tag{6.11}$$

All the ME distributions are achieved when $\partial\mathcal{L}/\partial\boldsymbol{\lambda} = 0$, which satisfies the moment constraints in Equation (6.9) and takes the general form of $f(x)$ in Equation (6.11). Note that since $x^0 = 1$ (for $i = 0$) in Equation (6.11), λ_0 can be determined by using the following expression:

$$\lambda_0 = -ln \int_{\mathbb{R}} exp\left(\sum_{i=0}^{n} \lambda_i x^i\right) dx \tag{6.12}$$

The gradient $\partial\mathcal{L}/\partial\boldsymbol{\lambda}$ and the elements H_{ij} of Hessian matrix $[H]$ of the Lagrangian function in Equation (6.10) are given, respectively, as follows:

$$(\nabla\mathcal{L})_i = \frac{\partial\mathcal{L}}{\partial\lambda_i} = \int_{\mathbb{R}} x^i f(x)\, dx - x^i \tag{6.13}$$

$$H_{ij} = \int_{\mathbb{R}} x^{i+j} f(x)\, dx \tag{6.14}$$

The Lagrange multipliers $\boldsymbol{\lambda}$ in Equation (6.11) can be found by using the methodology proposed in Ref. [88], which involves the Newton method [90].

6.4.3 Dynamic reliability evaluation based on the challenge-capacity model for natural frequencies

A mechanical system fails when the capacity of the system is less than the challenge that the system must face, where both capacity and challenge are random variables [159]. In the present chapter, the capacity is represented by the natural frequencies of the Carbon-Nanotube-Reinforced-Polymer-Composite (CNRPC) material, and the challenge is represented by the excitation frequency of the dynamic force that is applied on the CNRPC material. The natural frequencies are the frequencies at which the CNRPC material tends to oscillate in the absence of any applied force and when subjected to initial conditions. The motion patterns of the nanocomposite oscillating at its natural frequencies are called the normal modes (if all parts of the nanocomposite move sinusoidally with that same frequencies). The excitation frequency at which the amplitude of the motion of the nanocomposite is highest is known as the resonant frequency. Hence, the n-th natural frequency ω_n is the capacity of the CNRPC material to oscillate in the absence of any applied force and the excitation frequency Ω is the challenge that the CNRPC material must tolerate to keep itself away from resonant frequencies. The probability density function of the excitation frequency is denoted by $f_{\Omega}(\Omega)$ and that of the n-th natural frequency by $f_{\omega_n}(\omega_n)$. If the probability density function curves for both natural frequency and excitation frequency interfere, as shown in Figure 6.5(a) and 6.5(b), then the shaded area where the curves interfere is an indication that the component will be in resonance condition, because the excitation frequency is very close to the natural frequency. The failure probability of the system (P_f) is defined as the probability that the excitation frequency is very close to any one of the natural frequencies of the system. P_f can be expressed as follows:

$$P_f = P(Excitation\ frequency = Natural\ frequency) \tag{6.15}$$

Moreover, the dynamic reliability R_D is the probability that the excitation frequency is far away (represented by $<$ or $>$ symbol) from any one natural frequency of the system, which is expressed as follows:

$$R_D = P(Natural\ frequency < \text{or} > Excitation\ frequency) \tag{6.16}$$

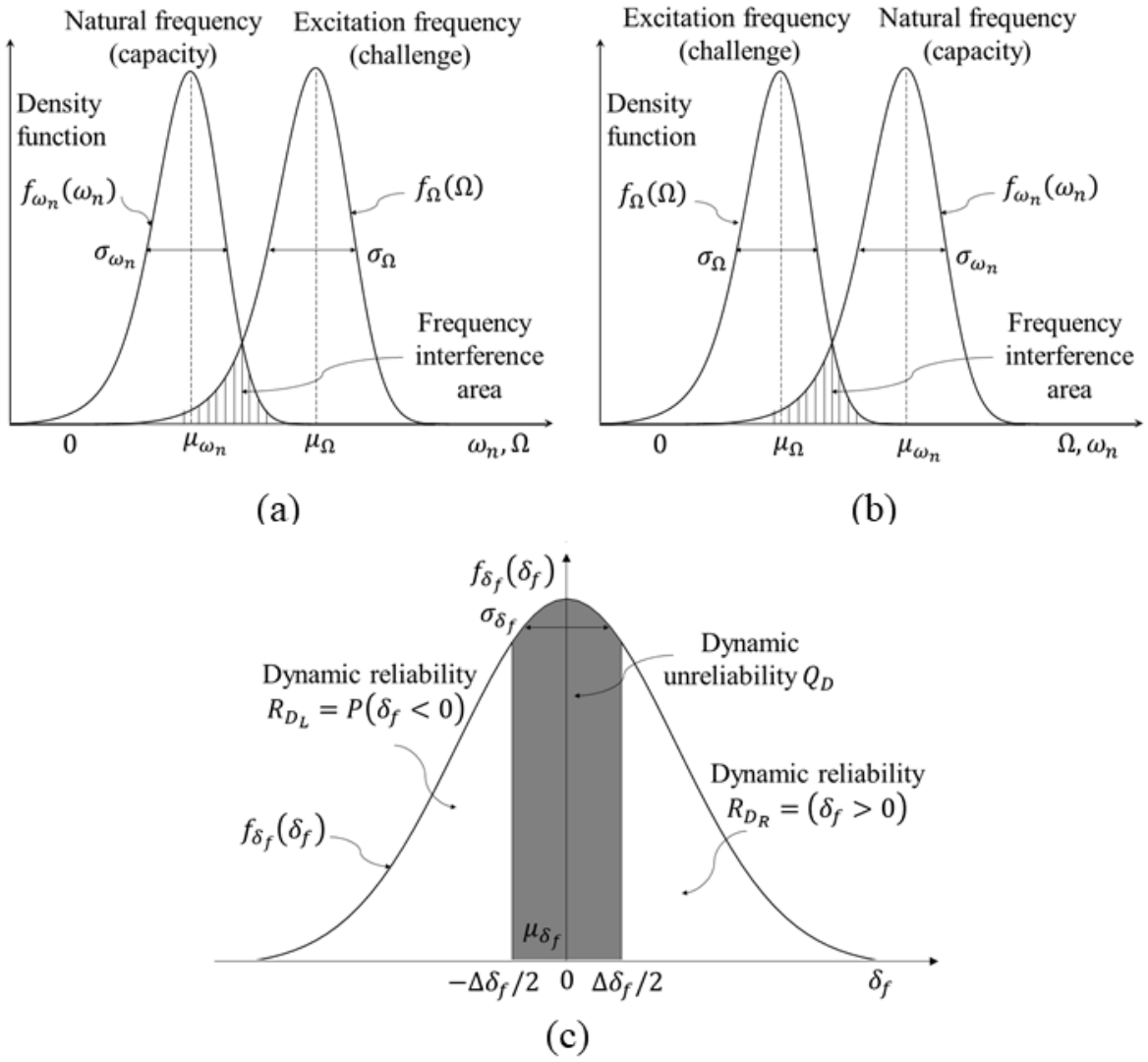

Figure 6.5. (a) Probability of failure based on excitation frequency (challenge) and natural frequency (capacity) distributions when $\mu_{\omega_n} < \mu_\Omega$, (b) probability of failure based on natural frequency (challenge) and excitation frequency (capacity) distributions when $\mu_\Omega < \mu_{\omega_n}$, and (c) Dynamic reliability based on frequency interference variable.

The dynamic reliability of the CNRPC material can be calculated if the density functions for the natural frequency $f_{\omega_n}(\omega_n)$ and the excitation frequency $f_\Omega(\Omega)$ are known. If a variable is defined as $\delta_f \equiv \omega_n - \Omega$, where ω_n and Ω are independent random variables and both are greater

than or equal to zero, then the dynamic reliability can be obtained based on this variable. The variable δ_f would also be considered as a random variable, which is called herein as "frequency interference random variable". The random variable δ_f represents the nearness to the resonance condition for the considered natural frequency, with $\delta_f = 0$ representing the resonance condition. Since ω_n, Ω and hence δ_f are continuous random variables, $P(\delta_f = 0)$ is undefined. To circumvent the resulting problem in reliability calculation, a very narrow band for δ_f with bandwidth $\Delta\delta_f$ is defined as shown in Figure 6.5(c). This band characterizes the nearness to resonance of the nanocomposite material system.

Correspondingly, according to Figure 6.5(c), the dynamic reliability R_D can be ideally defined as:

$$R_D = P(\delta_f < 0 \text{ or } \delta_f > 0) \tag{6.17a}$$

However, this definition can be redefined as:

$$R_D \simeq P\left(\delta_f > \frac{\Delta\delta_f}{2} \text{ or } -\delta_f > -\frac{\Delta\delta_f}{2}\right) \tag{6.17b}$$

Thus, the dynamic reliability can be calculated by the expressions given by:

$$R_{D_L} = P(\delta_f < 0) \simeq \int_{-\infty}^{-\Delta\delta_f/2} f_{\delta_f}(\delta_f)d\delta_f \tag{6.18a}$$

$$R_{D_R} = P(\delta_f > 0) \simeq \int_{\Delta\delta_f/2}^{\infty} f_{\delta_f}(\delta_f)d\delta_f \tag{6.18b}$$

This probability in terms of the area under the density function of the frequency interference random variable δ_f is shown in Figure 6.5(c), where $\mu_{\delta_f} = \mu_{\omega_n} - \mu_\Omega$ is the mean value of δ_f, μ_{ω_n} is the mean value of the natural frequency ω_n and μ_Ω is the mean value of the excitation frequency Ω, and σ_{δ_f} represents the standard deviation of δ_f. Correspondingly, the dynamic unreliability Q_D is given by:

$$Q_D = \int_{-\Delta\delta_f/2}^{\Delta\delta_f/2} f_{\delta_f}(\delta_f) d\delta_f \tag{6.19}$$

The areas under the $f_{\delta_f}(\delta_f)$ curve corresponding to R_D and Q_D are shown in Figure 6.5(c).

6.5 Results and discussion

6.5.1 Comparison of results with data from the literature

The effects of the random arrangement of carbon nanotubes in a polymer matrix, the entanglement of fillers and kinking, are probably dominant in polymer matrix composites. However, the use of stochastic modeling to analyze the effects of structural vacancies in the Single-Walled-Carbon-Nanotube (SWCN) is also of interest in manufacturing, because such vacancies are randomly distributed in the SWCN and are unavoidable in engineering applications [39-42]. To the extent that the mechanical properties of the nanotube reinforcement influence the properties of the nanocomposite, there would be a corresponding sensitivity of the nanocomposite property to the variations in the properties of the nanotube reinforcement and interface properties. Hence, a comparison of the results of the longitudinal elastic modulus of the Carbon-Nanotube-Reinforced-Polymer-Composite (CNRPC) material and a SWCN-reinforced polymer [41] is provided. The SWCN-reinforced polymer was represented as an elastic and isotropic resin with Young's modulus of 10 GPa and 0.3 as Poisson's ratio, reinforced with randomly aligned zigzag SWCNs (which are not specified in Ref. [41]). The CNRPC material used for this comparison is a (16, 0) SWCN-reinforced PEEK, considering an imperfect structure for the SWCN and the van der Waals (vdW) links, and considering a perfect structure for the SWCN and the vdW links. The perfect and imperfect structures for the SWCNs of the CNRPC material are perfectly aligned. The imperfect SWCN of the CNRPC material considers 5% of atomic vacancies. The volume fractions of SWCN used for the longitudinal elastic modulus were 0.050, 0.055, 0.060, 0.065, 0.070, and 0.075.

Figure 6.6 shows the comparison of the longitudinal elastic modulus of the (16, 0) SWCN-reinforced PEEK with a perfect structure and an imperfect structure for the SWCN and the vdW links, and the SWCN-reinforced polymer with randomly aligned zigzag SWCNs [41]. The results display that the longitudinal elastic modulus of the imperfect (16, 0) SWCN-reinforced PEEK is two times higher than that of the SWCN-reinforced polymer with randomly SWCNs. The results

also show that the longitudinal elastic modulus of the perfect (16, 0) SWCN-reinforced PEEK is three times higher than that of the SWCN-reinforced polymer with randomly aligned zigzag SWCNs.

Figure 6.6 also shows the comparison of the longitudinal elastic modulus of the (16, 0) SWCN-reinforced PEEK considering a perfect SWCN and an imperfect SWCN. The longitudinal elastic modulus decreases by about 37% because of the structural vacancies in the nanostructure. Hence, in sub-section 6.5.2, dynamic reliability evaluation is performed on the CNRPC material with structural vacancies to determine if an excitation frequency is close to any of its resonant frequencies. Such vacancy defects are essential randomness to be considered in a conservative and safe characterization of the nanocomposite.

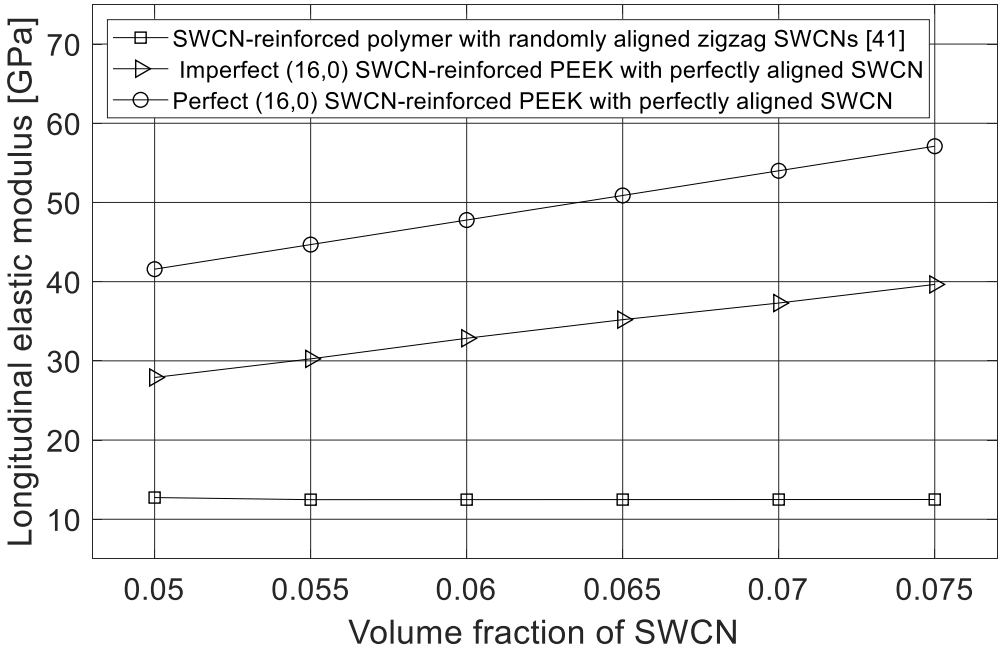

Figure 6.6. Comparison of the longitudinal elastic modulus of the perfect and imperfect (16, 0) SWCN-reinforced PEEK, and the SWCN-reinforced polymer with randomly aligned zigzag SWCNs [41].

6.5.2 Dynamic reliability evaluation of CNRPC based on natural frequencies and excitation frequency

The dynamic reliability of the Carbon-Nanotube-Reinforced-Polymer-Composite (CNRPC) material is obtained based on the challenge-capacity model prediction, where the bending and axial mode natural frequencies are defined as the capacity of the system and an external excitation frequency is defined as the challenge that the system must tolerate. The CNRPC material analyzed in this section is considered to possess structural defects and it consists of an imperfect (16, 0) Single-Walled-Carbon-Nanotube (SWCN) and an imperfect interface surface. The structural defects of the imperfect (16, 0) SWCN are modeled based on the Monte-Carlo Simulation (MCS) technique considering a percentage of atomic vacancies of 5%. The CNRPC material considers 5% volume fraction of SWCN, a length L_n of 10 nm and a thickness t_n for the SWCN of 0.34 nm. The diameter of the (16, 0) SWCN is 1.2535 nm. Hence, the aspect ratio (length /diameter) of the (16, 0) SWCN is 7.977. The boundary conditions considered for this analysis are Clamped-Free (CF), where one end of the polymer matrix material is fully constrained, and the other end is free to move.

In sub-section 6.5.2.1, the dynamic reliability analysis based on the first bending mode natural frequency of the CNRPC material and an external excitation frequency is performed, based on the challenge-capacity model prediction, to determine if the CNRPC material system is close to the first bending resonance condition. In sub-section 6.5.2.2, the dynamic reliability analysis of the CNRP material system is continued, following the results obtained in sub-section 6.5.2.1, but considering the second and third bending mode frequencies of the nanocomposite. Finally, in sub-section 6.5.2.3, the dynamic reliability analysis is performed on the CNRPC material system by applying an excitation frequency in axial mode.

6.5.2.1 Dynamic reliability analysis for the first bending mode resonance

The statistical distribution of the first bending mode natural frequency ω_{b_1} of the Carbon-Nanotube-Reinforced-Polymer-Composite (CNRPC) material is obtained based on the Monte Carlo Simulation (MCS) technique, while the excitation frequency Ω is represented by a small uniform distribution $(\Omega - \Delta\Omega/2) < \Omega < (\Omega + \Delta\Omega/2)$, where $\Delta\Omega \to 0$. Both distributions are used for the application of the challenge-capacity model to determine the dynamic reliability associated

with the first bending resonance condition of the CNRPC material. For the distribution of the first bending mode natural frequency, the skewness, the median, the mean and the mode are calculated. The skewness for the first bending mode natural frequency (Figure 6.7) is -0.7311, which means that it is a left-skewed distribution with its median higher than its mean. The median of the first bending mode natural frequency is 0.2290 GHz, the mean is 0.2282 GHz, and the mode is 0.2290 GHz. Hence, from the analysis of the skewness, it can be noticed that this distribution is asymmetric. Therefore, a more efficient and accurate approach such as the Maximum Entropy Method [88] should be used for estimating the probability density function (pdf) of this random variable.

The pdfs studied in the present analysis are the Maximum-Entropy distribution with four-moments (ME4) and the Maximum-Entropy distribution with five-moments (ME5), along with Gaussian and two-parameter Weibull distributions [87]. Table 6.1 lists the moment constraints in calculating the maximum entropy distributions for the first bending mode natural frequency.

Table 6.1. Moment constraints used in calculating the maximum entropy distributions for the first bending mode natural frequency.

Frequency	First order (GHz)	Second order (GHz^2)	Third order (GHz^3)	Fourth order (GHz^4)	Fifth order (GHz^5)
First bending	0.2282	0.0520	0.0118	0.0027	0.0006

Figure 6.7 shows the frequency histogram of the First Bending mode Natural Frequency (FBNF) along with ME4, ME5, Gaussian, and Weibull pdfs in a range of 0.205-0.240 GHz. Their corresponding cumulative distribution functions (cdfs) are also plotted along with the Empirical Frequency cdf of First Bending mode Natural Frequency (EFFBNF cdf). EFFBNF cdf is determined by calculating the area of each frequency bar in the histogram (of the first bending mode natural frequency). Then, each of these areas (of each frequency bar) is accumulated with the previous one until completing all of these areas (of all frequency bars). The initial value of the cumulative sum of the areas is zero, and the final value is 1. Table 6.A-1 in Appendix 6.A summarizes the computed Lagrange multipliers and Gaussian and Weibull parameters for the first bending mode natural frequency. The maximum iteration numbers in searching acceptable Lagrange multipliers never exceed 20 for the natural frequencies in the present chapter.

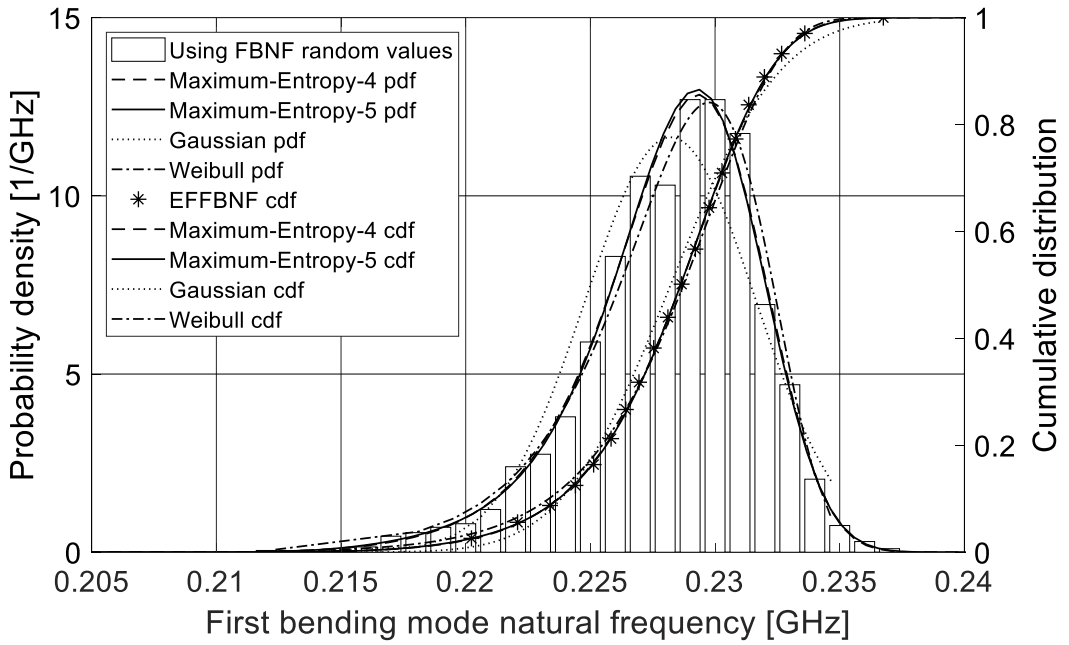

Figure 6.7. Frequency histogram and probability density and distribution functions of first bending mode natural frequency.

Regarding the excitation frequency Ω, an uniform distribution over a very small range of excitation frequency is used to represent the values of this frequency. In this analysis, the central value of this uniform distribution Ω is defined by using the value of the mode of the first bending mode natural frequency (which is 0.2290 GHz), while ΔΩ is defined as 0.002 GHz. Hence, the uniform distribution is determined over: $\Omega - \Delta\Omega/2$ = 0.228 GHz and $\Omega + \Delta\Omega/2$ = 0.230 GHz. Figure 6.8 shows the uniform band that represents the excitation frequency in bending mode.

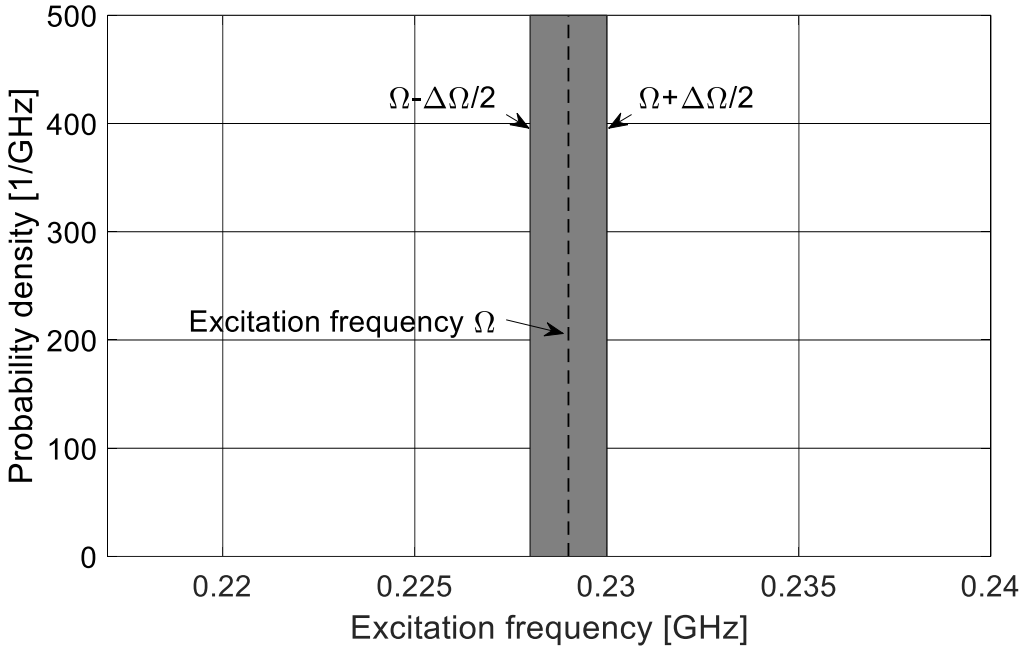

Figure 6.8. Uniform distribution that represents the excitation frequency Ω in bending mode, considering $\Omega - \Delta\Omega/2$ and $\Omega + \Delta\Omega/2$.

Regarding the dynamic reliability analysis based on the challenge-capacity model, a frequency interference random variable δ_f (for bending mode) is calculated to obtain the dynamic reliability of CNRPC material based on the first bending natural mode frequency ω_{b_1} and the excitation frequency Ω. The dynamic reliability is obtained based on the probability density function of δ_f for values of δ_f higher or lower than zero, considering the definition $\delta_f \equiv \omega_{b_1} - \Omega$. Hence, the random variable δ_f represents the nearness to the first resonance condition for bending mode, with $\delta_f = 0$ representing the first resonance condition. First, considering the condition that the first bending mode natural frequency $\omega_{b_1} <$ excitation frequency Ω, it is possible to calculate the dynamic reliability $\left(R_{D_L} = P(\delta_f < 0)\right)$ function before reaching the resonance condition ($\delta_f = 0$).

By calculating the skewness of variable δ_f, it is possible to define if its statistical distribution is symmetric or asymmetric. The skewness of variable δ_f is -0.0222, which means that it is a left-skewed distribution with its median higher than its mean. The median of the variable δ_f is -0.0090 GHz, the mean is -0.0092 GHz, and the mode is -0.0040 GHz. From the analysis of the skewness,

it can be observed that this distribution is asymmetric. Thus, an entropy distribution can show a realistic pdf for this variable. Figure 6.9 shows the frequency histogram of the variable δ_f along with ME4, ME5, Gaussian, and Weibull pdfs when $\delta_f < 0$. Their corresponding cumulative distributions functions (cdf) are also plotted along with the Empirical Frequency cdf of Frequency Interference Random Variable in bending mode (EFFIRV cdf – bending mode). EFFIRV cdf – bending mode is determined by calculating the area of each frequency bar in the histogram (of variable δ_f). Then, each of these areas (of each frequency bar) is accumulated with the previous one until completing all of these areas (of all frequency bars). The initial value of the cumulative sum of the areas is zero, and the final value is 1. Table 6.A-2 in Appendix A summarizes the moment constraints in calculating maximum entropy distributions, ME4 and ME5, for the interference variable δ_f for bending mode when $\delta_f < 0$, as well as the corresponding Lagrange multipliers, and the Weibull and Gaussian parameters for their pdfs shown in Figure 6.9.

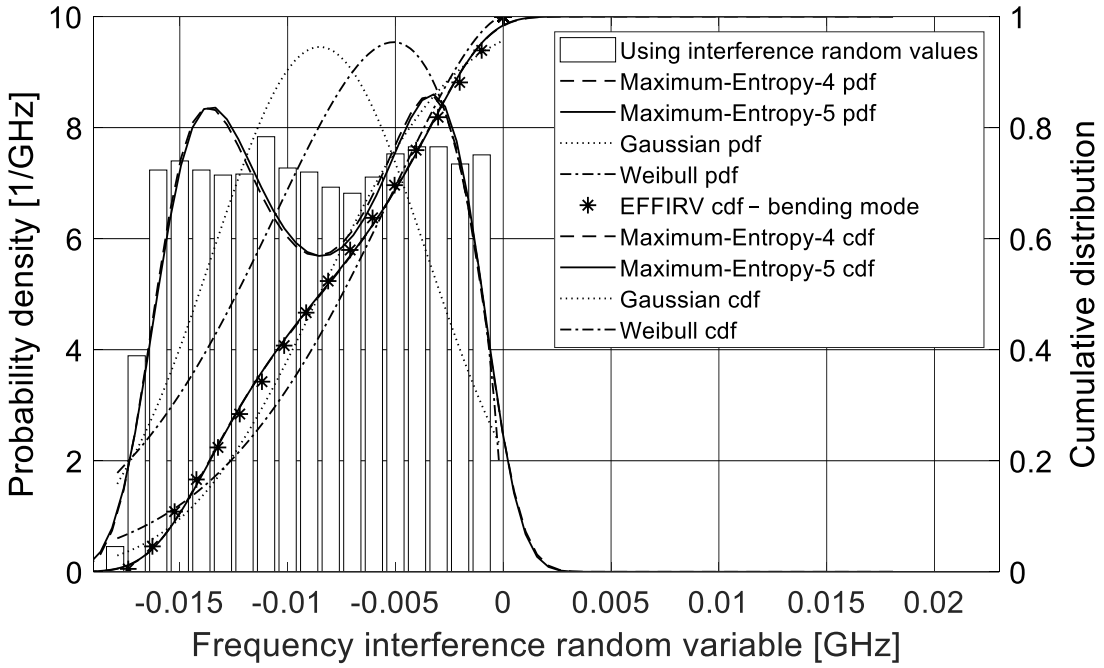

Figure 6.9. Frequency histogram and probability density and distribution functions of the frequency interference random variable δ_f (for bending mode) and its cumulative distribution functions when: first bending mode frequency $\omega_{b_1} <$ excitation frequency Ω.

Figure 6.10 shows the dynamic reliability of the CNRPC material for various values of the operational frequency obtained from the random variable δ_f (for bending mode) for different distributions: ME4, ME5, Weibull, and Gaussian. It can be appreciated from Figure 6.10 that the operational frequency obtained from the challenge-capacity model is in a range of 0.212-0.229 GHz. It can also be observed that the dynamic reliability functions present a considerable change in their behavior towards an area with low-reliability values close to zero before reaching the resonance condition. The Empirical Frequency of Operational Frequency in bending mode (EFOF – bending mode) reliability is obtained by using the values of EFFIRV cdf – bending mode associated with the frequency histogram of the variable δ_f. The comparison between the reliabilities based on the different distributions plotted in Figure 6.10 and that of the EFOF – bending mode is provided based on the Root-Mean-Square-Error (RMSE) and Chi-Square Error. Hence, Table 6.2 shows the RMSE and Chi-Square Error for the reliabilities based on the different distributions with respect to EFOF – bending mode reliability

From Table 6.2, it can be appreciated that ME4 reliability presents a RMSE of 0.0117212 and a Chi-square error of 0.0005302, while ME5 reliability presents a RMSE of 0.0099296 and a Chi-square error of 0.0003785. Regarding the Weibull reliability, this distribution presents a RMSE of 0.1464053 and a Chi-square error of 0.0022561, while the Gaussian reliability presents a RMSE of 0.1920637 and a Chi-square error of 0.0047490. The errors calculated in Table 6.2 show that the Weibull reliability presents a RMSE that is 12 times higher than that of the ME4 reliability and 14 times higher than that of the ME5 reliability, while the Gaussian reliability presents a RMSE that is 16 times higher than that of the ME4 reliability and 19 times higher than that of the ME5 reliability. In the case of the Chi-square error, the Weibull reliability is four times higher than that of the ME4 reliability and six times higher than that of the ME5 reliability, while the Gaussian reliability is eight times higher than that of the ME4 reliability and 12 times higher than that of the ME5 reliability. Therefore, it can be observed that ME4 and ME5 distributions are closer to EFOF – bending mode than Weibull and Gaussian distributions, which lead to a better calculation and characterization of the CNRPC material behavior.

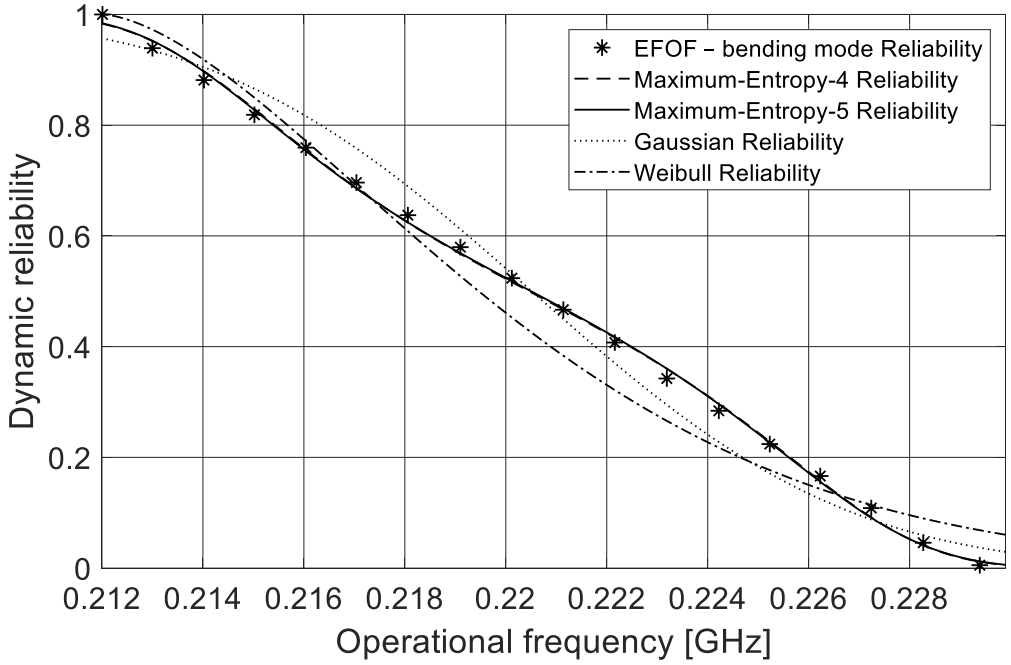

Figure 6.10. Dynamic reliability of the CNRPC material system for different distributions of δ_f for bending mode when the first bending mode natural frequency $\omega_{b_1} <$ excitation frequency Ω $(\delta_f < 0)$.

Table 6.2. RMSE and Chi-square error for dynamic reliability in bending mode when $\delta_f < 0$.

Distribution	RMSE	Chi-square error
ME4	0.0117212	0.0005302
ME5	0.0099296	0.0003785
Weibull	0.1464053	0.0022561
Gaussian	0.1920637	0.0047490

In a similar manner, the condition that the first bending mode natural frequency $\omega_{b_1} >$ excitation frequency Ω is considered. Figure 6.11 shows the dynamic reliability $\left(R_{D_R} = P(\delta_f > 0)\right)$ of the CNRPC material for different distributions of the frequency interference random variable for bending mode when $\omega_{b_1} > \Omega$ in a range of 0.230-0.238 GHz. It can be noticed that the dynamic reliability functions present a considerable change in their behavior towards an

area with high-reliability values close to one after passing through the resonance condition. If the dynamic reliability functions of both conditions (i.e. $\omega_{b_1} > \Omega$ and $\omega_{b_1} < \Omega$) are considered together, it is possible to determine the dynamic reliability function for a conservative, safe, and reliable characterization of the CNRPC material.

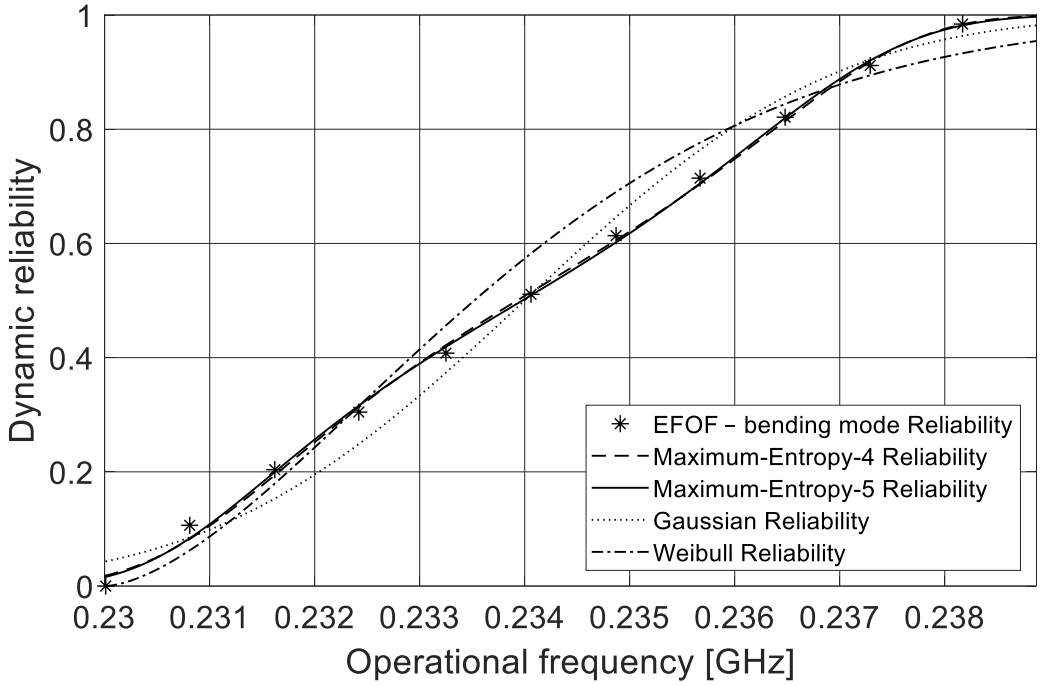

Figure 6.11. Dynamic reliability of the CNRP system for different distributions of δ_f for bending mode when the first bending mode natural frequency ω_{b_1} > excitation frequency Ω $(\delta_f > 0)$.

6.5.2.2 Dynamic reliability analysis for the first, second and third bending mode resonances

Dynamic reliability analysis is performed now on the Carbon-Nanotube-Reinforced-Polymer-Composite (CNRPC) material following the results obtained in sub-section 6.5.2.1 and considering the second and third bending mode natural frequencies of the CNRPC material, and considering different values of the excitation frequency Ω through frequency sweep, corresponding to startup and shutdown service conditions. The statistical distributions of the second and third bending mode natural frequencies are obtained based on the Monte Carlo Simulation (MCS) technique. In the case of the second bending mode natural frequency ω_{b_2}, the skewness is -0.7311, which means that this distribution is a left-skewed distribution with its median higher than its

mean. The median of ω_{b_2} is 0.4580 GHz, the mean is 0.4564 GHz, and the mode is 0.4580 GHz. Regarding the third bending mode natural frequency ω_{b_3}, the skewness is -0.7312, which represents a left-skewed distribution with its median higher than its mean. The median of ω_{b_3} is 0.6870 GHz, the mean is 0.6846 GHz, and the mode is 0.6870 GHz. Both bending natural frequencies are asymmetric. Thus, the Maximum Entropy Method (MEM) [88] should be used for estimating their probability density functions (pdfs). The Maximum-Entropy distribution with five-moments (ME5) is used to represent the values of the second and third bending mode natural frequencies, according to the results calculated in Table 6.2.

In the previous analysis, the dynamic reliability function of the CNRPC material corresponding to the first bending resonance condition was determined. By considering now the uniform distribution of the excitation frequency Ω shown in Figure 6.8, it is possible to determine the dynamic reliability and dynamic hazard associated with the first, second and third bending mode natural frequencies of the CNRPC material. Figure 6.12(a) shows the frequency histograms of the first, second and third bending mode natural frequencies along with their ME5 distributions. In Figure 6.12(a), it can be observed that the first bending mode natural frequency ω_{b_1} has the same statistical distribution as in the previous analysis. Table 6.A-3 in Appendix A summarizes the moment constraints used in calculating the ME5 distributions for ω_{b_2} and ω_{b_3}, as well as the corresponding Lagrange multipliers for their pdfs shown in Figure 6.12(a).

The challenge-capacity model prediction is used to determine the frequency interference random variable δ_f, in order to obtain the dynamic reliability and dynamic hazard functions by using the ME5 distribution. The conditions corresponding to the first bending mode natural frequencies (i.e. $\omega_{b_1} > \Omega$ and $\omega_{b_1} < \Omega$) are now considered along with the conditions corresponding to the second and third bending mode natural frequencies, which are: $\omega_{b_2} < \Omega$ and $\omega_{b_2} > \Omega$, and $\omega_{b_3} < \Omega$ and $\omega_{b_3} > \Omega$, respectively.

Figure 6.12(b) shows the dynamic reliability function for the bending mode natural frequencies obtained from the challenge-capacity model in a range of 0.100-0.750 GHz, considering the excitation frequency Ω shown in Figure 6.8. It can be observed that the dynamic reliability function remains stable at a value equal to one during the passage through the first bending mode natural frequency ω_{b_1}, when $\omega_{b_1} > \Omega$. However, the dynamic reliability values present a considerable change in their behavior towards an area with low-reliability values close

to zero before reaching the resonance condition corresponding to ω_{b_1}. This resonance condition occurs when $\omega_{b_1} = \Omega$. After this condition, the dynamic reliability function presents a considerable change towards an area with high-reliability values close to one after leaving the resonance condition, when $\omega_{b_1} < \Omega$. When the excitation frequency Ω goes through the second bending mode natural frequency ω_{b_2} and the third bending mode natural frequency ω_{b_3}, the dynamic reliability values remain equal to one because of the conditions: $\omega_{b_2} < \Omega$ and $\omega_{b_2} > \Omega$, and $\omega_{b_3} < \Omega$ and $\omega_{b_3} > \Omega$, respectively.

If the probability of failure or dynamic unreliability Q_D is determined, it is possible to define the values of the dynamic reliability R_D for the bending mode natural frequencies, which are shown in Table 6.3. Regarding the first bending mode natural frequency, the probability of failure Q_D is represented as $P(\Omega = \omega_{b_1}) = 1$. Thus, the dynamic reliability is defined as $R_D = 1 - Q = 0$, which means that the CNRPC system is in a resonance condition. For the second bending mode natural frequency, the probability of failure Q_D is represented as $P(\Omega = \omega_{b_2}) = 0$. Thus, the dynamic reliability is defined as $R_D = 1$, which means that ω_{b_2} is far from Ω. In the case of the third bending mode natural frequency, the probability of failure Q_D is represented as $P(\Omega = \omega_{b_3}) = 0$. Thus, the dynamic reliability is defined as $R_D = 1$, which means that ω_{b_3} is far from Ω.

Table 6.3. Dynamic reliability and dynamic unreliability of the bending mode natural frequencies considering the excitation frequency Ω in Figure 6.8.

Condition	Dynamic reliability (R_D)	Dynamic unreliability (Q_D)
$P(\Omega = \omega_{b_1})$.	0	1
$P(\Omega = \omega_{b_2})$	1	0
$P(\Omega = \omega_{b_3})$	1	0

From the dynamic reliability results, it is possible to calculate the dynamic hazard function of the CNRPC material for the bending mode natural frequencies. The dynamic hazard function is more physically meaningful as a measure of performance, safety and risk than is the reliability function itself [86]. Hence, the cumulative dynamic hazard function H_D can be calculated with the following expression: $H_D = ln(1/R_D)$, where R_D is the dynamic reliability function [86]. Figure

6.12(c) shows the cumulative dynamic hazard function corresponding to the ME5 distributions of the bending mode natural frequencies. It can be appreciated that the dynamic hazard function increases in its magnitude in the zone where $\omega_{b_1} \cong \Omega$, which is considered as the failure zone of the CNRPC material because of the resonance condition. For the zones representing the conditions: $\omega_{b_1} < \Omega$, $\omega_{b_1} > \Omega$, $\omega_{b_2} < \Omega$, $\omega_{b_2} > \Omega$, $\omega_{b_3} < \Omega$ and $\omega_{b_3} > \Omega$, the dynamic hazard function remains with low-magnitude values. Therefore, these areas are considered as the safe zones for the CNRPC material. Hence, the dynamic reliability and dynamic hazard analyses lead to a better conservative and safe characterization of the CNRPC material, considering different bending mode natural frequencies.

Vibration data collected through the frequency sweep of Ω, corresponding to startup and shutdown service conditions and the nearness to resonance of the material system, provides a wealth of information on the dynamic response of the CNRPC material that is not available from steady-state data. Most importantly, it provides the ability to study the vibration amplitude throughout the entire frequency range considering any small fluctuation of the excitation frequency. This small fluctuation can cause that the material system is in a resonance condition, and thus, it can cause violent swaying motions and even catastrophic failures in the structure of the nanocomposite. Resonance is characterized by a large increase in vibration at the resonant frequencies, but generally lower amplitudes at all other frequencies. Moreover, this type of vibration analysis generates overall information on the natural frequencies of the CNRPC material.

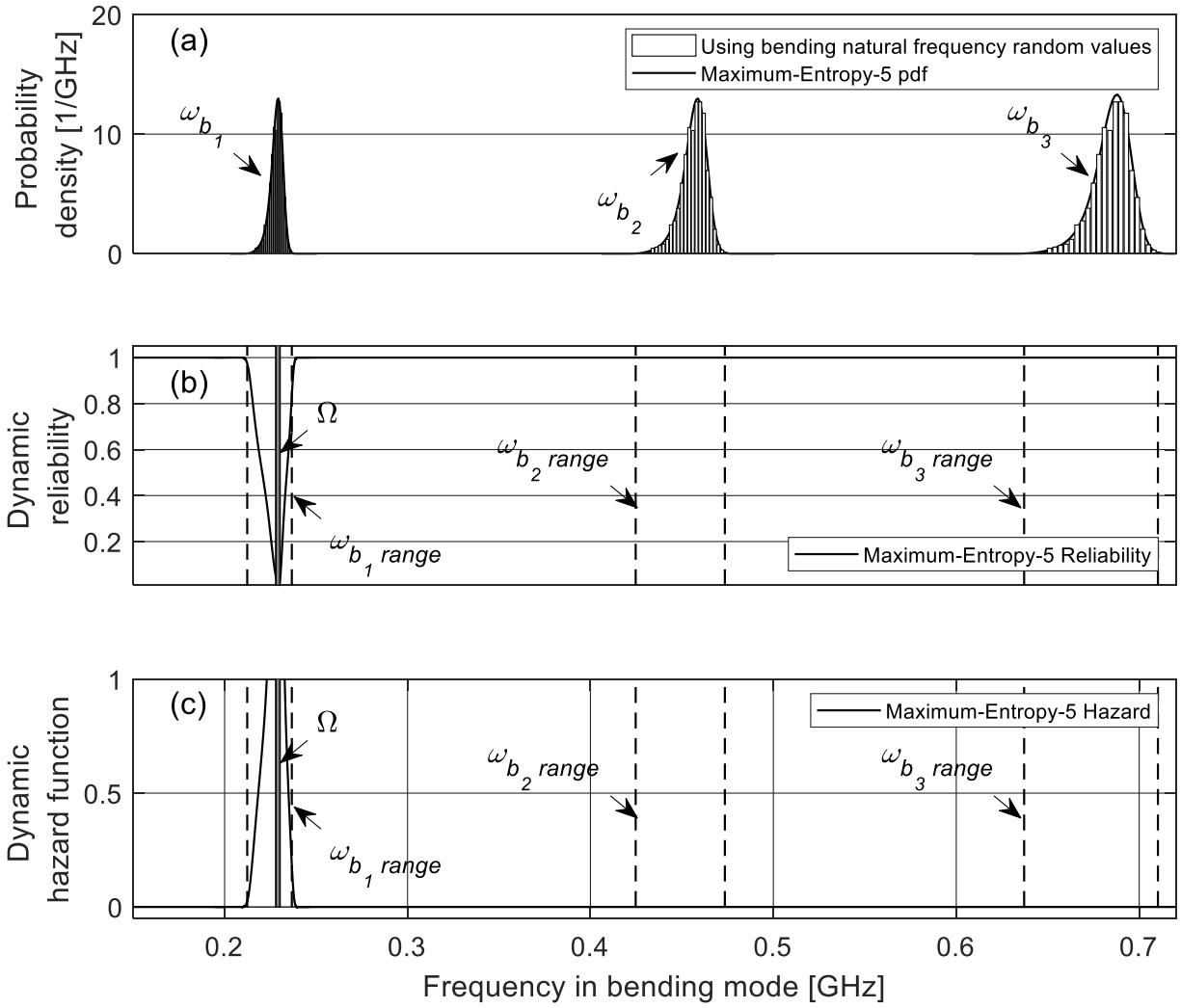

Figure 6.12. (a) Frequency histogram and probability density and distribution functions of the bending mode natural frequencies of the CNRPC material, (b) dynamic reliability function for the CNRPC material with an excitation frequency in the first bending resonance condition and (c) dynamic hazard function for the CNRPC material with an excitation frequency in the first bending resonance condition.

If an excitation force is now applied on the CNRPC material, considering an uniform distribution for the excitation frequency Ω as before, as is shown in Figure 6.13(a), the dynamic reliability and dynamic hazard functions are then different compared to that of the previous analysis corresponding to Figure 6.12. In Figure 6.13(a), the frequency histograms and ME5 distributions of the bending mode natural frequencies of the CNRPC material can be observed

along with the new excitation frequency Ω. The dynamic reliability function can be calculated based on the frequency interference random variable δ_f, which is obtained from the challenge-capacity model. In Figure 6.13(b), it can be appreciated that the reliability remains constant and at a value equal to one during the passage through the bending mode natural frequencies (ω_{b_1}, ω_{b_2} and ω_{b_3}) because the excitation frequency Ω is far from these natural frequencies. Thus, the CNRPC material is not close to or at any resonance condition. Table 6.4 shows different values for the dynamic reliability R_D and dynamic unreliability Q_D corresponding to the bending mode natural frequencies. It can be noticed that the dynamic unreliability Q_D is represented as: $P(\Omega = \omega_{b_1}) = 0, P(\Omega = \omega_{b_2}) = 0$ and $P(\Omega = \omega_{b_3}) = 0$. Thus, the dynamic reliability is defined as $R_D = 1 - Q_D = 1$ for all the bending mode natural frequencies.

Table 6.4. Dynamic reliability and dynamic unreliability of the bending mode natural frequencies considering the excitation frequency Ω in Figure 6.13(a)

Condition	Dynamic reliability (R_D)	Dynamic unreliability (Q_D)
$P(\Omega = \omega_{b_1})$.	1	0
$P(\Omega = \omega_{b_2})$	1	0
$P(\Omega = \omega_{b_3})$	1	0

Regarding the dynamic hazard analysis, Figure 6.13(c) shows the cumulative dynamic hazard function of the bending mode natural frequencies. It can be noticed that during the passage of the excitation frequency Ω through the bending mode natural frequencies, the magnitude of the dynamic hazard function remains at low-magnitude values because Ω is far from any of these natural frequencies. Hence, these areas are considered as safe zones for the CNRPC material.

If a comparison between Figures 6.12(b) and 6.13(b) is provided, the influence of the excitation frequency Ω on the dynamic reliability function can be appreciated. If Ω is close to any bending mode natural frequency as is shown in Figure 6.12(b), the dynamic unreliability Q_D is represented as $P(\Omega = \omega_b) = 1$, and thus, the dynamic reliability is defined as $R_D = 1 - Q_D = 0$. On the other hand, if Ω is far from any bending mode natural frequency as is shown in Figure 6.13(b), the dynamic unreliability Q_D is represented as $P(\Omega = \omega_b) = 0$, and thus, the dynamic reliability is defined as $R_D = 1 - Q_D = 1$. In Figures 6.12(c) and 13(c), similar behavior is

presented in the dynamic hazard function. In Figure 6.12(c), the magnitude of the dynamic hazard function increases considerably during the passage of Ω through the first bending resonance condition, which means that this area is considered as a failure zone for the CNRPC material. In Figure 6.13(c), the hazard function remains constant at low-magnitude values during the passage of Ω through the bending mode natural frequencies, which means that these areas are represented as safe zones for the CNRPC material.

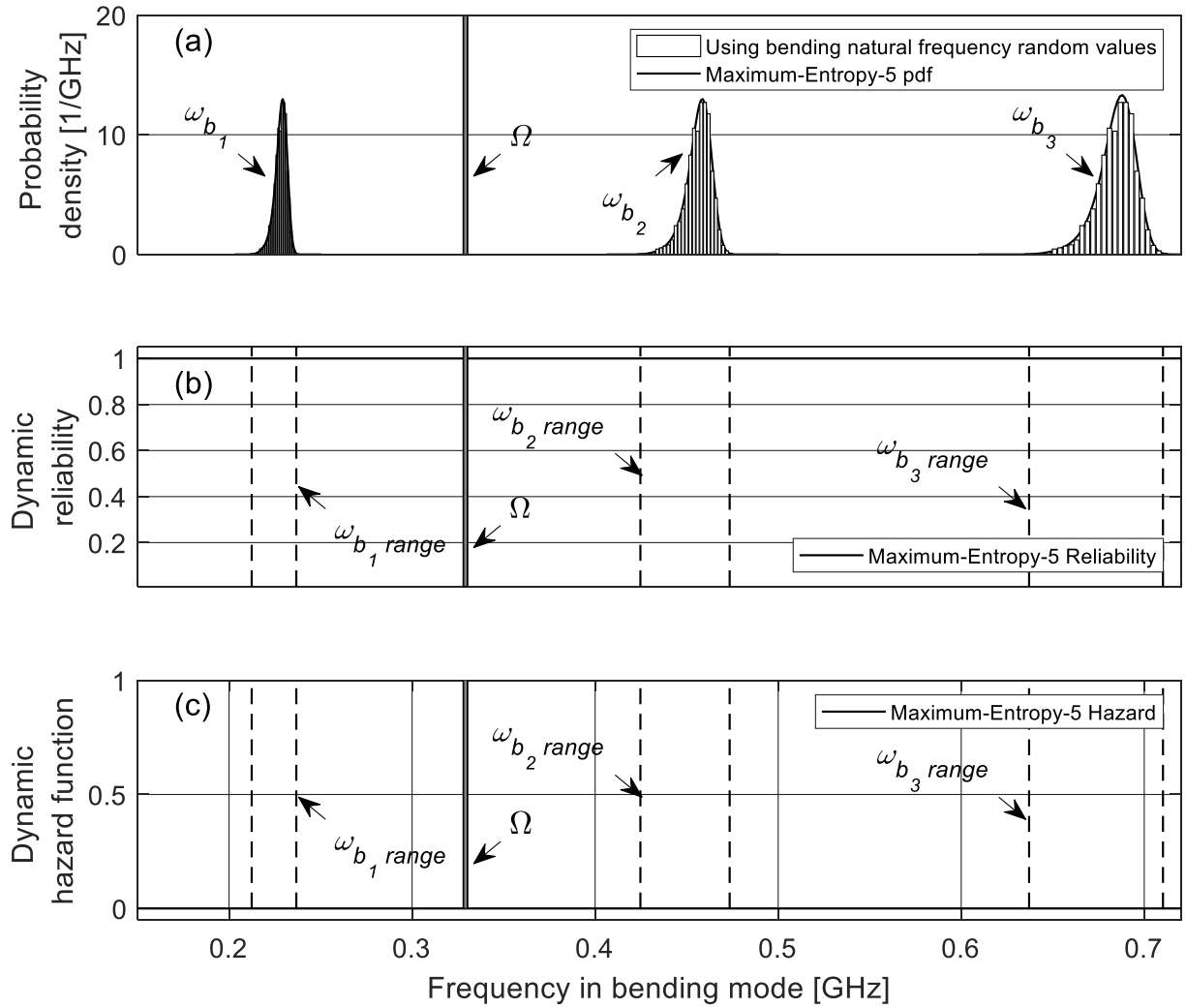

Figure 6.13. (a) Frequency histogram and probability density and distribution functions of the bending mode natural frequencies of the CNRPC material, (b) dynamic reliability function for the CNRPC material with an excitation frequency far from any bending resonance condition and (c) dynamic hazard function for the CNRPC material with an excitation frequency far from any bending resonance condition.

The operational frequency of the CNRPC material system can be calculated from the frequency interference random variable δ_f based on the challenge-capacity model. Figure 6.14(a) shows the dynamic reliability function for different values of the operational frequency of the CNRPC material. The operational frequencies used in this analysis are the following: 0.229 GHz, 0.458 GHz and 0.687 GHz. These values of operational frequency correspond to the first, second and third bending mode natural frequencies, respectively. It can be noticed that for each bending mode resonance, the dynamic reliability reaches low values close to zero. Hence, Table 6.5 shows different values for the dynamic reliability R_D and dynamic unreliability Q_D corresponding to each bending mode resonance. It can be noticed that the dynamic unreliability Q_D is represented as: $P(\Omega = \omega_{b_1}) = 1, P(\Omega = \omega_{b_2}) = 1$ and $P(\Omega = \omega_{b_3}) = 1$. Thus, the dynamic reliability is defined as $R_D = 1 - Q_D = 0$ for all the bending mode resonances.

Table 6.5. Dynamic reliability and dynamic unreliability of the bending mode resonances considering the operational frequency of the CNRPC material in Figure 6.14(a).

Condition	Dynamic reliability (R_D)	Dynamic unreliability (Q_D)
$P(\Omega = \omega_{b_1})$.	0	1
$P(\Omega = \omega_{b_2})$	0	1
$P(\Omega = \omega_{b_3})$	0	1

Regarding the hazard function, Figure 6.14(c) shows the cumulative dynamic hazard function of the bending mode resonances based on the operational frequency of the CNRPC material. It can be observed that the dynamic hazard function increases considerably in its magnitude during the passage through each bending mode resonance, which means that these areas are failure zones for the CNRPC material. On the other hand, the areas where the dynamic hazard function remains constant at low-magnitude values are considered as safe zones for the operational frequency of the CNRPC material. The dynamic reliability and dynamic hazard analyses also allow exploring the characterization of the CNRPC material by using frequencies of other types of excitation. Hence, in the next sub-section, a dynamic reliability analysis is now performed on the CNRPC material by considering different values of an excitation frequency in axial mode through a frequency sweep.

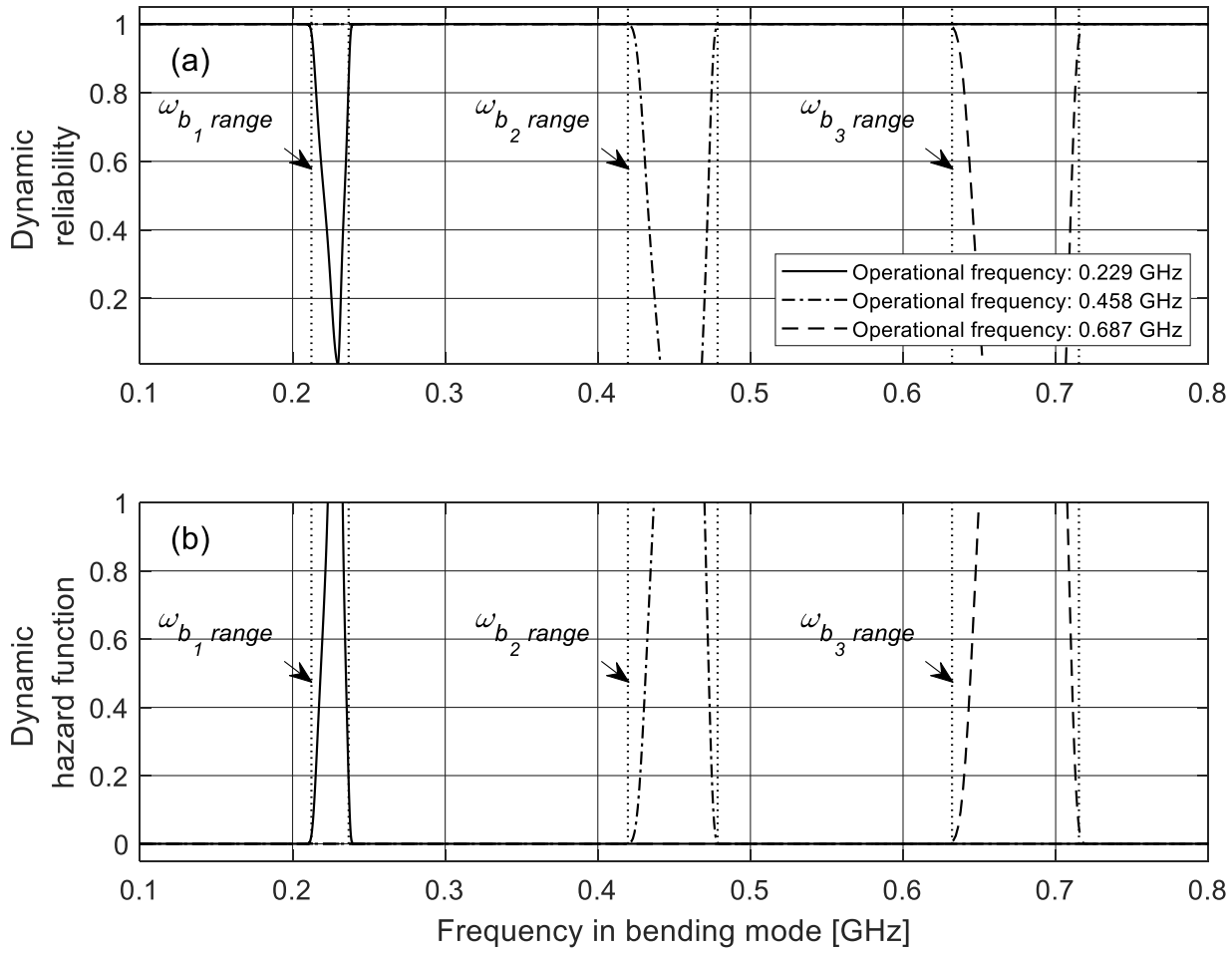

Figure 6.14. (a) Dynamic reliability function of the operational frequency of the CNRPC material in bending mode and (b) dynamic hazard function of the operational frequency of the CNRPC material in bending mode.

6.5.2.3 Dynamic reliability analysis for the first, second and third axial mode resonances

A dynamic reliability analysis is now performed on the Carbon-Nanotube-Reinforced-Polymer-Composite (CNRPC) material, considering different values of the excitation frequency Ω in axial mode, through frequency sweep, corresponding to start up and shut down service conditions. The challenge-capacity model is used to determine if the excitation frequency is close to any axial mode natural frequency. Regarding the excitation frequency Ω, a small uniform distribution is used to represent the values of this frequency. In the first analysis of this sub-section, the central value of this uniform distribution Ω is defined by using the value of the mode of the

second axial mode natural frequency (which is 0.7807 GHz), while $\Delta\Omega$ is defined as 0.002 GHz. Hence, the uniform distribution is determined over: $\Omega - \Delta\Omega/2$ = 0.7797 GHz and $\Omega + \Delta\Omega/2$ = 0.7817 GHz. Figure 6.15 shows the uniform distribution that represents the excitation frequency in axial mode.

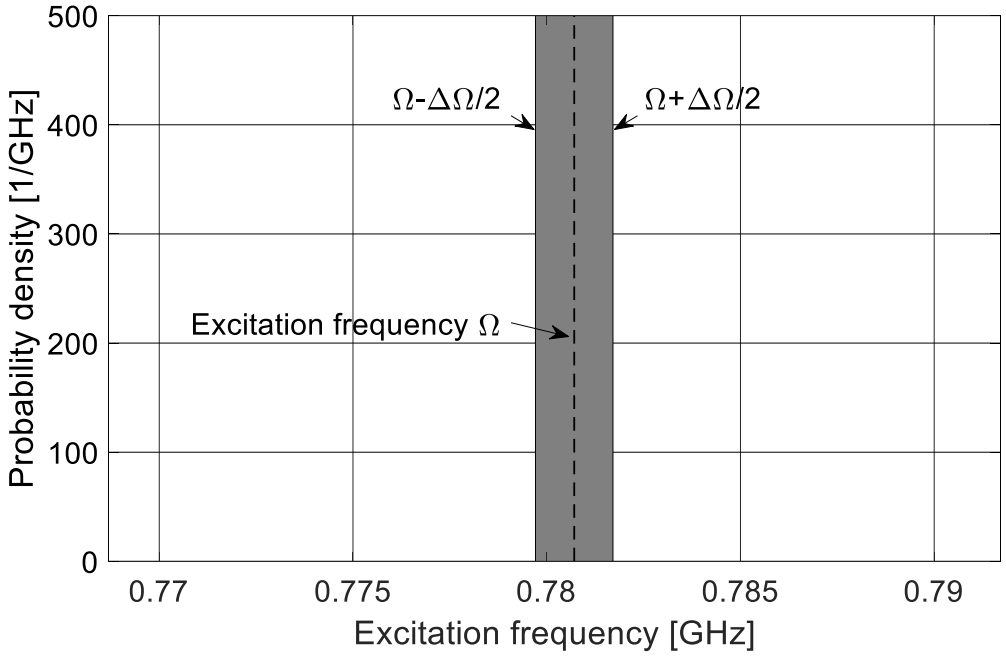

Figure 6.15. Uniform distribution that represents the excitation frequency Ω in axial mode, considering $\Omega - \Delta\Omega/2$ and $\Omega + \Delta\Omega/2$.

The statistical distributions of the first, second and third axial mode natural frequencies of CNRPC material are obtained based on the Monte Carlo Simulation (MCS) technique. The skewness of the first axial mode natural frequency ω_{a_1} is -1.0840, which represents a left-skewed distribution with its median higher than its mean. The median of ω_{a_1} is 0.5860 GHz, the mean is 0.5858 GHz, and the mode is 0.5870 GHz. In the case of the second axial mode natural frequency ω_{a_2}, the skewness is -1.085, which means that this distribution is a left-skewed distribution with its median higher than its mean. The median of ω_{a_2} is 0.7793 GHz, the mean is 0.7791 GHz, and the mode is 0.7807 GHz. Regarding the third axial mode natural frequency ω_{a_3}, the skewness is -1.086, which represents a left-skewed distribution with its median higher than its mean. The median of ω_{a_3} is 0.9727 GHz, the mean is 0.9725 GHz, and the mode is 0.9744 GHz.

From the analysis of the skewness of the statistical distributions of the first, second and third axial mode natural frequencies, it can be noticed that the distributions are asymmetric. Thus, the Maximum Entropy Method [88] should be used for estimating their probability density functions (pdfs). The Maximum-Entropy distribution with five-moments (ME5) is used according to the results calculated in Table 6.2. By considering now the uniform distribution of the excitation frequency Ω shown in Figure 6.15, it is possible to determine the dynamic reliability and dynamic hazard based on the axial mode natural frequencies of the CNRPC material. Figure 6.16(a) shows the distributions obtained from the ME5 distributions and the frequency histograms of the first, second, and third axial mode natural frequencies. Table 6.A-4 in Appendix 6.A summarizes the moment constraints used in calculating the ME5 distributions for ω_{a_1}, ω_{a_2} and ω_{a_3}, as well as the corresponding Lagrange multipliers for their pdfs.

The challenge-capacity model is used to determine the frequency interference random variable δ_f, in order to obtain the dynamic reliability and dynamic hazard functions by using the ME5 distribution. The conditions corresponding to the second axial mode natural frequency: $\omega_{a_2} > \Omega$ and $\omega_{a_2} < \Omega$ are considered along with the conditions corresponding to the first and third axial mode natural frequencies, which are: $\omega_{a_1} < \Omega$ and $\omega_{a_1} > \Omega$, and $\omega_{a_3} < \Omega$ and $\omega_{a_3} > \Omega$, respectively.

Figure 6.16(b) shows the dynamic reliability function for the axial mode natural frequencies obtained from the challenge-capacity model in a range of 0.550-1.000 GHz, considering the excitation frequency Ω shown in Figure 6.15. It can be observed that the dynamic reliability function remains constant at a value equal to one during the passage through the first axial mode natural frequency ω_{a_1}, when $\omega_{a_1} < \Omega$ and $\omega_{a_1} > \Omega$, and during the passage through the second axial mode natural frequency ω_{a_2}, when $\omega_{a_2} < \Omega$. However, the dynamic reliability values present a considerable change in their behavior towards an area with low-reliability values close to zero before reaching the resonance condition corresponding to ω_{a_2}. This resonance condition occurs when $\omega_{a_2} = \Omega$. After this condition, the dynamic reliability function presents a considerable change towards an area with high-reliability values close to one after leaving the resonance condition, when $\omega_{a_2} > \Omega$. When the excitation frequency goes through the third axial mode frequency ω_{a_3}, the reliability values remain constant at a value equal to one because of the conditions: $\omega_{a_3} < \Omega$ and $\omega_{a_3} > \Omega$.

If the probability of failure or dynamic unreliability Q_D is analyzed, it is possible to define the value of the dynamic reliability R_D. Hence, Table 6.6 shows different values for the dynamic reliability and dynamic unreliability corresponding to the axial mode natural frequencies. Regarding the second axial mode natural frequency, the probability of failure Q_D is represented as $P(\Omega = \omega_{a_2}) = 1$. Thus, the dynamic reliability is defined as $R_D = 1 - Q_D = 0$, which means that the CNRPC material system is in a resonance condition. For the first axial mode natural frequency, the probability of failure Q_D is represented as $P(\Omega = \omega_{a_1}) = 0$. Thus, the dynamic reliability is defined as $R_D = 1$, which means that ω_{a_1} is far from Ω. In the case of the third axial mode natural frequency, the probability of failure Q_D is represented as $P(\Omega = \omega_{a_3}) = 0$. Thus, the dynamic reliability is defined as $R_D = 1$, which means that ω_{a_3} is far from Ω.

Table 6.6. Dynamic reliability and dynamic unreliability of the axial mode natural frequencies considering the excitation frequency Ω in Figure 6.15.

Condition	Dynamic reliability (R_D)	Dynamic unreliability (Q_D)
$P(\Omega = \omega_{a_1})$.	1	0
$P(\Omega = \omega_{a_2})$	0	1
$P(\Omega = \omega_{a_3})$	1	0

From the dynamic reliability results, it is possible to calculate the dynamic hazard function of the CNRPC material for the axial modes. Figure 6.16(c) shows the cumulative dynamic hazard function corresponding to the ME5 distributions of the axial mode natural frequencies of the CNRPC material. It can be appreciated that the dynamic hazard function increases in its magnitude in the zone where $\omega_{a_2} \cong \Omega$, which is considered as the failure zone of the CNRPC material because of the resonance condition. For the zones representing the conditions: $\omega_{a_1} < \Omega$, $\omega_{a_1} > \Omega$, $\omega_{a_2} < \Omega$, $\omega_{a_2} > \Omega$, $\omega_{a_3} < \Omega$ and $\omega_{a_3} > \Omega$, the dynamic hazard function remains with low-magnitude values. Therefore, these areas are considered as safe zones for the CNRPC material. The dynamic reliability and dynamic hazard analyses lead to a better conservative and safe characterization of the CNRPC material, considering different axial mode natural frequencies.

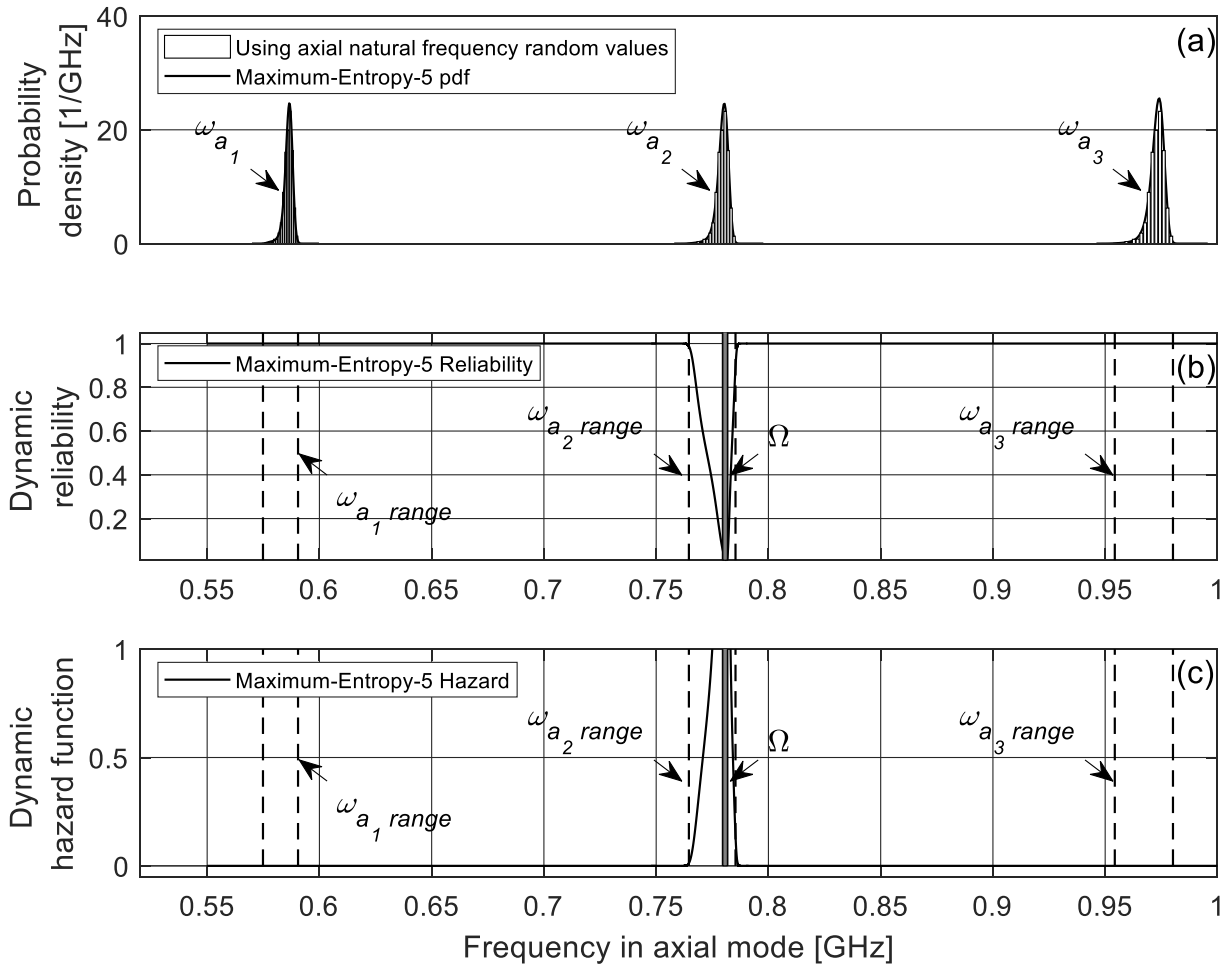

Figure 6.16. (a) Frequency histogram and probability density and distribution functions of the axial mode natural frequencies of the CNRPC material, (b) dynamic reliability function for the CNRPC material with an excitation frequency in the second axial resonance condition and (c) dynamic hazard function for the CNRPC material with an excitation frequency in the second axial resonance condition.

If an excitation force is now applied on the CNRPC material, considering an uniform distribution for the excitation frequency Ω as before, as is shown in Figure 6.17(a), the dynamic reliability and dynamic hazard functions are then different compared to that of the previous analysis corresponding to Figure 6.16. In Figure 6.17(a), the frequency histograms and ME5 distributions of the axial mode natural frequencies of the CNCPC material can be observed along with the new excitation frequency Ω. The dynamic reliability function can be calculated based on

the frequency interference random variable δ_f, which is obtained from the challenge-capacity model.

In Figure 6.17(b), it can be appreciated that the dynamic reliability remains constant and at a value equal to one during the passage through the axial mode natural frequencies (ω_{a_1}, ω_{a_2} and ω_{a_3}) because the excitation frequency Ω is far from these natural frequencies. Thus, the CNRPC material is not close to or at any resonance condition. Table 6.7 shows different values for the dynamic reliability R_D and dynamic unreliability Q_D corresponding to the axial mode natural frequencies. It can be noticed that the dynamic unreliability Q_D is represented as: $P(\Omega = \omega_{a_1}) = 0, P(\Omega = \omega_{a_2}) = 0$ and $P(\Omega = \omega_{a_3}) = 0$. Thus, the dynamic reliability is defined as $R_D = 1 - Q_D = 1$ for all the axial mode natural frequencies.

Table 6.7. Dynamic reliability and dynamic unreliability of the axial mode natural frequencies considering the excitation frequency Ω in Figure 6.17(a)

Condition	Dynamic reliability (R_D)	Dynamic unreliability (Q_D)
$P(\Omega = \omega_{a_1})$.	1	0
$P(\Omega = \omega_{a_2})$	1	0
$P(\Omega = \omega_{a_3})$	1	0

Regarding the dynamic hazard analysis, Figure 6.17(c) shows the cumulative dynamic hazard function of the axial mode natural frequencies. It can be noticed that during the passage of the excitation frequency Ω through the axial mode natural frequencies, the magnitude of the dynamic hazard function remains at low-magnitude values because Ω is far from any of these natural frequencies. Hence, these areas are considered as safe zones for the CNRPC material.

If a comparison between Figures 6.16(b) and 6.17(b) is provided, the influence of the excitation frequency on the dynamic reliability function can be appreciated. If Ω is close to any axial mode natural frequency as is shown in Figure 6.16(b), the dynamic unreliability Q_D is represented as $P(\Omega = \omega_a) = 1$, and thus, the dynamic reliability is defined as $R_D = 1 - Q_D = 0$. On the other hand, if Ω is far from any axial mode natural frequency as is shown in Figure 6.17(b), the dynamic unreliability Q_D is represented as $P(\Omega = \omega_a) = 0$, and thus, the dynamic reliability is defined as $R_D = 1 - Q_D = 1$. In Figures 6.16(c) and 6.17(c), similar behavior is presented in

the dynamic hazard function. In Figure 6.16(c), the magnitude of the dynamic hazard function increases considerably during the passage of Ω through the second axial resonance condition, which means that this area is considered as a failure zone for the CNRPC material. In Figure 6.17(c), the dynamic hazard function remains constant at low-magnitude values during the passage of Ω through the axial mode natural frequencies, which means that these areas are represented as safe zones for the CNRPC material.

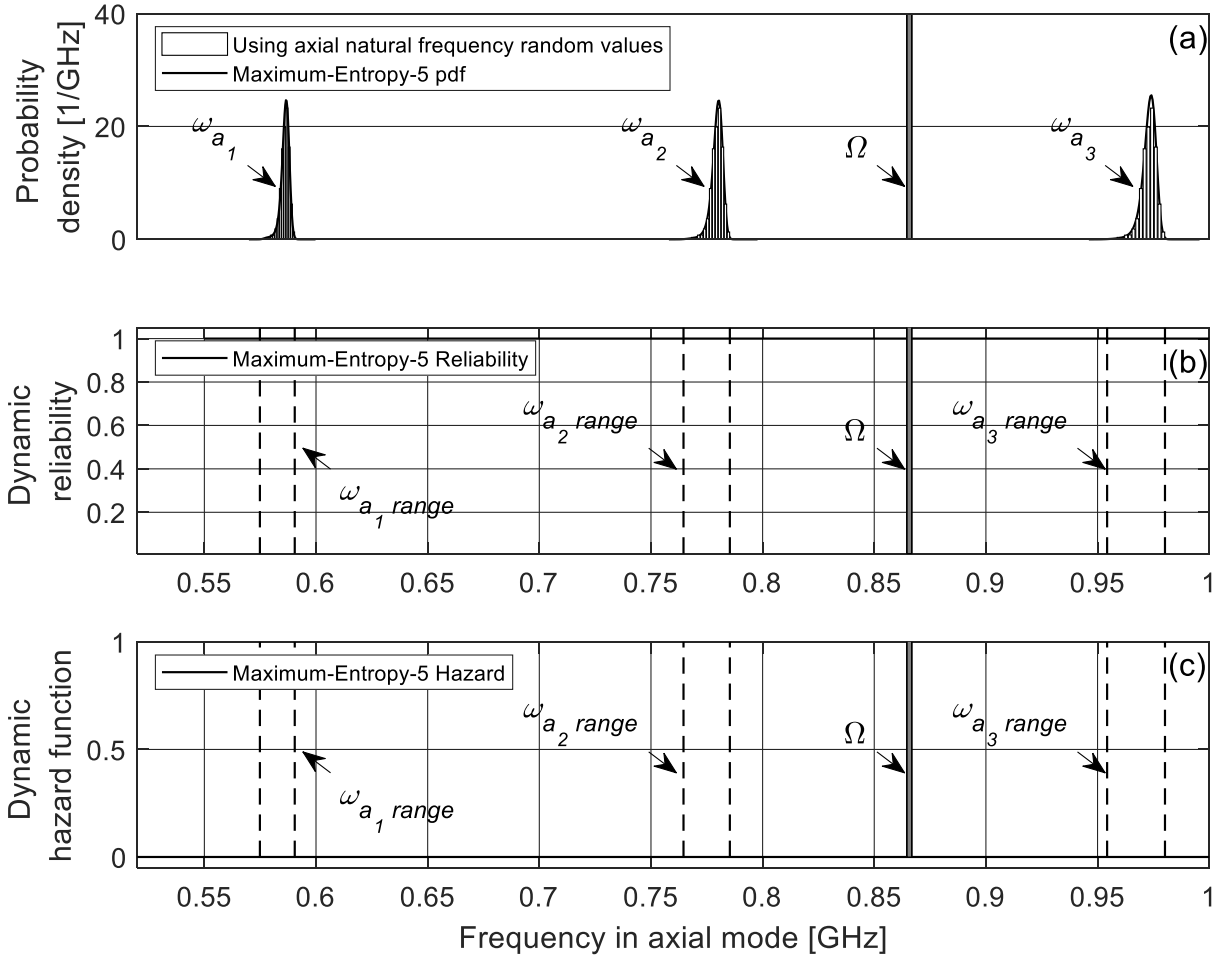

Figure 6.17. (a) Frequency histogram and probability density and distribution functions of the axial mode natural frequencies of the CNRPC material, (b) dynamic reliability function for the CNRPC material with an excitation frequency far from any axial resonance condition and (c) dynamic hazard function for the CNRPC material with an excitation frequency far from any axial resonance condition.

The operational frequency of the CNRPC material system in axial mode can be calculated from the frequency interference random variable δ_f based on the challenge-capacity model prediction. Figure 6.18(a) shows the dynamic reliability function for different values of the operational frequency of the CNRPC material in axial mode. The operational frequencies used in this analysis are the following: 0.587 GHz, 0.780 GHz and 0.974 GHz. These values of operational frequency correspond to the first, second and third axial mode natural frequencies, respectively. It can be noticed that for each axial mode resonance, the dynamic reliability reaches low values close to zero. Hence, Table 6.8 shows different values for the dynamic reliability R_D and dynamic unreliability Q_D corresponding to each axial mode resonance. It can be noticed that the dynamic unreliability Q_D is represented as: $P(\Omega = \omega_{a_1}) = 1, P(\Omega = \omega_{a_2}) = 1$ and $P(\Omega = \omega_{a_3}) = 1$. Thus, the dynamic reliability is defined as $R_D = 1 - Q_D = 0$ for all the axial mode resonances.

Table 6.8. Dynamic reliability and dynamic unreliability of the axial mode resonances considering the operational frequency of the CNRPC material in Figure 6.18(a).

Condition	Dynamic reliability (R_D)	Dynamic unreliability (Q_D)
$P(\Omega = \omega_{a_1})$.	0	1
$P(\Omega = \omega_{a_2})$	0	1
$P(\Omega = \omega_{a_3})$	0	1

Regarding the dynamic hazard function, Figure 6.18(c) shows the cumulative dynamic hazard function of the axial mode resonances based on the operational frequency of the CNRPC material. It can be observed that the dynamic hazard function increases considerably in its magnitude during the passage through each axial mode resonance, which means that these areas are considered as failure zones for the CNRPC material. On the other hand, the areas where the dynamic hazard function remains constant at low-magnitude values are considered as safe zones for the operational frequency of the CNRPC material. Therefore, the dynamic reliability and dynamic hazard analyses allow exploring different types of failure, considering frequencies of several types of excitation.

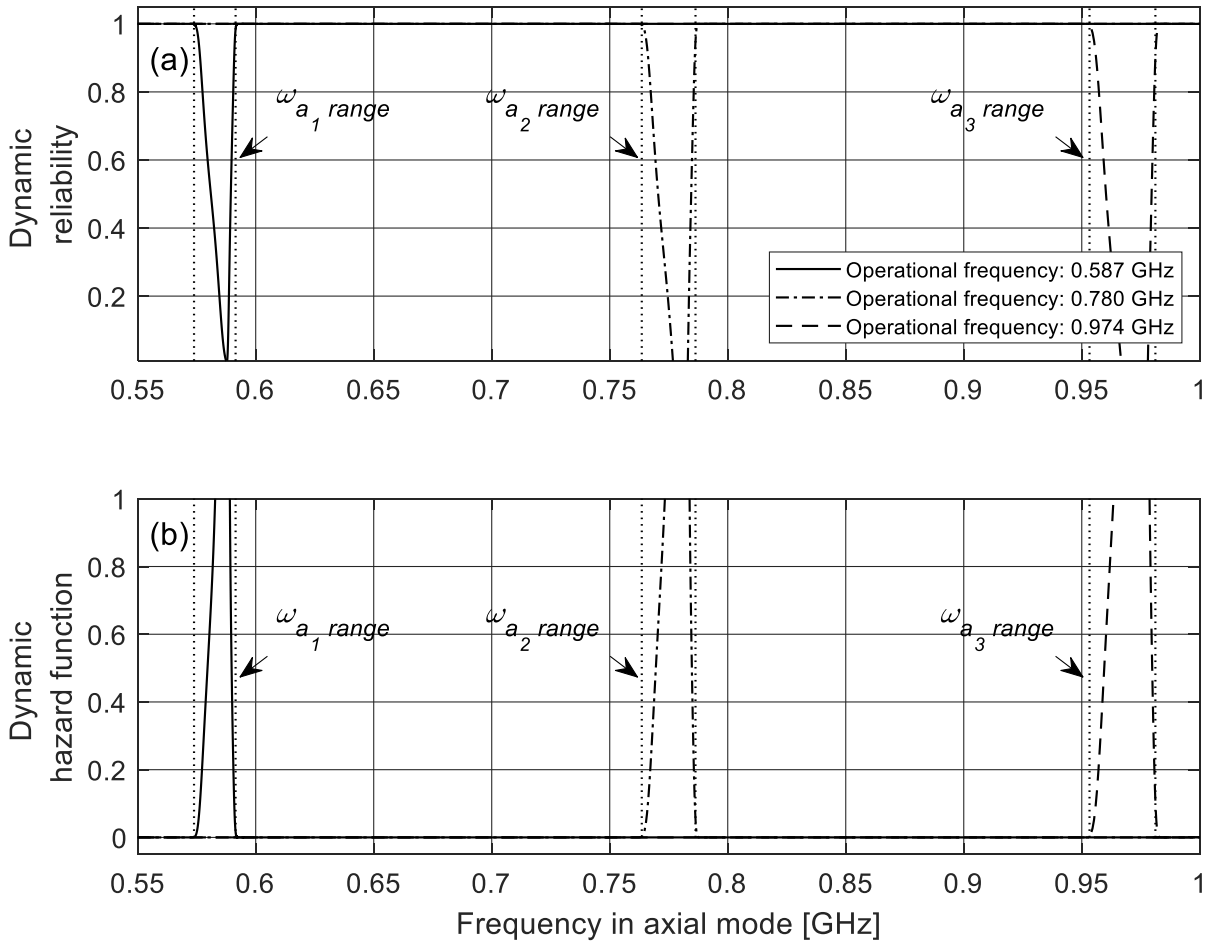

Figure 6.18. (a) Dynamic reliability function of the operational frequency of the CNRPC material in axial mode and (b) dynamic hazard function of the operational frequency of the CNRPC material in axial mode.

6.6 Conclusion

The dynamic reliability analysis of the material system was performed on the Representative Volume Element (RVE) of the Carbon-Nanotube-Reinforced-Polymer-Composite (CNRPC) material, based on the challenge-capacity model, to determine the dynamic reliability and dynamic hazard associated with its modal parameters. The modal parameters were based on the bending and axial mode natural frequencies, which were considered as random variables. The distributions based on the MCS technique were obtained by using the Maximum Entropy Method. In the dynamic reliability and dynamic hazard analyses, the challenge-capacity model was used to

determine the frequency interference random variable δ_f considering different distribution values for the excitation frequency Ω in bending and axial modes. The distributions of the excitation frequency Ω were placed close to or far from any natural frequency to determine the corresponding different behaviors of the dynamic reliability and dynamic hazard functions.

In the case of the bending mode natural frequencies, the distribution of the excitation frequency Ω was first placed close to the first bending mode natural frequency ω_{b_1} of the CNRPC material to study its behavior corresponding to this resonance condition. Later, the second and third bending mode natural frequencies were included in the analysis to calculate their dynamic unreliability Q_D and dynamic reliability R_D. As Ω was close to ω_{b_1}, the dynamic unreliability Q_D was determined as $P(\Omega = \omega_{b_1}) = 1$, and thus, the dynamic reliability as $R_D = 0$, which means that the CNRPC system was in a resonance condition when $\Omega = \omega_{b_1}$. On the other hand, as Ω was far from the second and third bending mode natural frequencies, ω_{b_2} and ω_{b_3}, respectively, the dynamic unreliability was calculated as $Q_D = 0$ and the dynamic reliability as $R_D = 1$. In the case of a distribution of Ω far from any of the bending mode natural frequencies, the dynamic unreliability Q_D was represented as $P(\Omega = \omega_b) = 0$ and the dynamic reliability as $R_D = 1$. For the operational frequency, the dynamic unreliability Q_D was represented as $P(\Omega = \omega_b) = 1$ and the dynamic reliability as $R_D = 0$. The dynamic hazard function was utilized to determine the failure and safe zones corresponding to the bending mode frequencies of the CNRPC material, considering the failure zones as resonance conditions.

Corresponding, in the case of the axial mode natural frequencies, the distribution of the excitation frequency Ω was first placed close to the second axial mode natural frequency ω_{a_2} of the CNRPC material to study its behavior associated with this resonance condition, including the first and third axial mode natural frequencies, ω_{a_1} and ω_{a_3}, respectively. As Ω was close to ω_{a_2}, the dynamic unreliability Q_D was determined as $P(\Omega = \omega_{\mathrm{a}_2}) = 1$, and thus, the dynamic reliability as $R_D = 0$, which means that the CNRPC system was in a resonance condition. On the other hand, as Ω was far from ω_{a_1} and ω_{a_3}, the dynamic unreliability was calculated as $Q_D = 0$ and the dynamic reliability as $R_D = 1$. In the case of a distribution of Ω far from any of the axial mode natural frequencies, the dynamic unreliability Q_D was represented as $P(\Omega = \omega_a) = 0$ and the dynamic reliability as $R_D = 1$. For the operational frequency, the dynamic unreliability Q_D was

represented as $P(\Omega = \omega_a) = 1$ and the dynamic reliability as $R_D = 0$. The dynamic hazard function was used to determine the failure zones corresponding to the axial mode frequencies of the CNRPC material. These zones are considered as resonance conditions of the CNRPC material.

The dynamic reliability and dynamic hazard analyses, based on the challenge-capacity model, led to a high-performance, conservative, and reliable characterization of the CNRPC material system associated with its dynamic response. By combining the finite-element modeling and analysis of the RVE with the probabilistic analysis and modeling (based on the MCS technique and the challenge-capacity model), it was possible to provide an alternative solution to study the dynamic material behavior of the nanocomposite with structural problems (i.e. missing carbon atoms and C-C bonds in the SWCN). Moreover, vibration data collected through frequency sweep of Ω, corresponding to startup and shutdown service conditions and the nearness to resonance of the material system, provides a wealth of information on the dynamic response of the CNRPC material that is not available from steady-state data. Most importantly, it provides the ability to study the vibration amplitude throughout the entire frequency range considering small fluctuations of the excitation frequency.

Appendix 6.A

Tables 6.A-1, 6.A-2, 6.A-3 and 6.A-4 are presented in this section.

Table 6.A-1. Lagrange multipliers and Weibull and Gaussian parameters computed for the first bending mode natural frequency.

Lagrange multipliers						
	λ_0	λ_1	λ_2	λ_3	λ_4	λ_5
ME4	$2.89\text{x}10^5$	$-5.23\text{x}10^6$	$3.56\text{x}10^7$	$-1.07\text{x}10^8$	$1.21\text{x}10^8$	
ME5	$2.74\text{x}10^6$	$-5.98\text{x}10^7$	$5.20\text{x}10^8$	$-2.26\text{x}10^9$	$4.91\text{x}10^9$	$-4.25\text{x}10^9$

Weibull parameters		Gaussian parameters	
β (GHz)	α	μ (GHz)	σ (GHz)
0.2298	78.82	0.2282	0.0034

Table 6.A-2. Moment constraints, Lagrange multipliers and, Weibull and Gaussian parameters for the variable δ_f in bending mode $(\delta_f < 0)$.

Random variable δ_f based on first bending and excitation frequency	First order (GHz)	Second order (GHz^2)	Third order (GHz^3)	Fourth order (GHz^4)	Fifth order (GHz^5)
	0.0085	$9.74x10^{-5}$	$1.25x10^{-6}$	$1.71x10^{-8}$	$2.45x10^{-10}$
	Lagrange multipliers				
		λ_0	λ_1	λ_2	λ_3	λ_4	λ_5
	ME4	-3.02	-915.3	$2.20x10^5$	$-1.95x10^7$	$5.70x10^8$	
	ME5	-3.02	-982.8	$2.55x10^5$	$-2.50x10^7$	$9.66x10^8$	$-9.18x10^9$
	Weibull parameters			Gaussian parameters			
	β (GPa)		α	μ (GHz)		σ (GHz)	
	0.0094		1.6100	0.0085		0.0050	

Table 6.A-3. Moment constraints and Lagrange multipliers for the second and third bending mode natural frequencies.

Second bending mode frequency	First order (GHz)	Second order (GHz^2)	Third order (GHz^3)	Fourth order (GHz^4)	Fifth order (GHz^5)
	0.4564	0.2083	0.0951	0.0434	0.0198
	Lagrange multipliers				
		λ_0	λ_1	λ_2	λ_3	λ_4	λ_5
	ME5	$2.0x10^6$	$-2.27x10^7$	$9.83x10^7$	$-2.12x10^8$	$2.29x10^8$	$-9.86x10^7$
Third bending mode frequency	First order (GHz)	Second order (GHz^2)	Third order (GHz^3)	Fourth order (GHz^4)	Fifth order (GHz^5)
	0.6846	0.4688	0.3211	0.2200	0.1507

	Lagrange multipliers					
	λ_0	λ_1	λ_2	λ_3	λ_4	λ_5
ME5	$2.0\text{x}10^{6}$	$-1.48\text{x}10^{7}$	$4.29\text{x}10^{7}$	$-6.18\text{x}10^{7}$	$4.44\text{x}10^{7}$	$-1.27\text{x}10^{7}$

Table 6.A-4. Moment constraints and Lagrange multipliers for the first, second and third axial mode natural frequencies.

First axial mode frequency	First order (GHz)	Second order (GHz^2)	Third order (GHz^3)	Fourth order (GHz^4)	Fifth order (GHz^5)
	0.5861	0.3435	0.2013	0.1180	0.0691
	Lagrange multipliers				
	λ_0	λ_1	λ_2	λ_3	λ_4	λ_5
ME5	$8.08\text{x}10^{9}$	$-6.90\text{x}10^{10}$	$2.36\text{x}10^{11}$	$-4.03\text{x}10^{11}$	$3.44\text{x}10^{11}$	$-1.17\text{x}10^{11}$
Second axial mode frequency	First order (GHz)	Second order (GHz^2)	Third order (GHz^3)	Fourth order (GHz^4)	Fifth order (GHz^5)
	0.7795	0.6076	0.4737	0.3693	0.2878
	Lagrange multipliers				
	λ_0	λ_1	λ_2	λ_3	λ_4	λ_5
ME5	$2.23\text{x}10^{9}$	$-1.45\text{x}10^{10}$	$3.78\text{x}10^{10}$	$-4.93\text{x}10^{10}$	$3.21\text{x}10^{10}$	$-8.38\text{x}10^{9}$
Third axial mode frequency	First order (GHz)	Second order (GHz^2)	Third order (GHz^3)	Fourth order (GHz^4)	Fifth order (GHz^5)
	0.9729	0.9466	0.9210	0.8962	0.8720
	Lagrange multipliers				
	λ_0	λ_1	λ_2	λ_3	λ_4	λ_5
ME5	$1.88\text{x}10^{9}$	$-9.60\text{x}10^{9}$	$1.96\text{x}10^{10}$	$-2.00\text{x}10^{10}$	$1.02\text{x}10^{10}$	$-2.08\text{x}10^{9}$

Chapter 7. Conclusions, contributions and future work

7.1 Conclusions

The main objective of this thesis was to study the static (stiffness and strength) and dynamic responses of polymer matrix materials reinforced with a perfectly aligned Single-Walled-Carbon-Nanotube (SWCN). The different analyses were carried out on the Representative Volume Element (RVE) of a Carbon-Nanotube-Reinforced-Polymer-Composite (CNRPC) material. A 3D multiscale finite element model consisting of a polymer matrix material, a Single-Walled-Carbon-Nanotube (SWCN) and an interface region between the polymer material and the SWCN was constructed for this purpose. The polymer matrix was modeled by using the Mooney-Rivlin strain energy function to calculate its non-linear response and the interface region was modeled via van der Waals (vdW) links. The SWCN was modeled as a space frame by using the Morse potential and then as a thin shell by using a suitable shell theory. However, in practical applications, the SWCN is not perfect, and it possesses structural defects and further, the vdW links are not perfect. Such imperfections were characterized in this thesis by using the Monte Carlo simulation technique. The challenge-capacity modeling and prediction approach was used for the reliability and hazard characterization of the stiffness response and natural frequencies of the CNRPC material. The overall conclusions of this thesis are explained in the following paragraphs.

The Single-Walled-Carbon-Nanotube (SWCN) modeled as a thin shell model based on Donnell's Shell Theory is suitable for the physical properties of SWCNs for different values of aspect ratio (that was defined as length of nanotube/diameter of nanotube) lower than 8.28 for Clamped-Free (CF) boundary conditions and lower than 13.89 for Clamped-Clamped (CC) boundary conditions. For aspect ratios higher than the previous ones, Flugge's and Sanders' Shell Theories are more suitable, except for an aspect ratio of 31.64 in CF boundary conditions and an aspect ratio of 21.06 in CC boundary conditions. Hence, the thin shell model presented enough accuracy of SWCN modeling and allowed to study other mechanical properties, such as bending, buckling, and torsion response.

The RVE of the CNRPC material showed an increase in its natural frequencies for all volume fractions of SWCN compared to that of the plain polymers, such as Polyamide-imide (PAI) and

Polyetheretherketone (PEEK). Regarding the damping properties of the CNRPC material, the concept of the stick-slip motion behavior was used to obtain the critical shear stress, dissipation energy, and loss factor in order to calculate the structural damping ratio of the CNRPC material for different volume fractions. The values of damping ratios of the CNRPC material decreased with higher values of the natural frequencies of the CNRPC material for all volume fractions of SWCN, considering PAI as a polymer matrix material. Correspondingly, in the case of PEEK as a polymer matrix material, the values of the structural damping coefficient were within a range of 0.0661-0.1597 for 4% SWCN volume fraction. The structural damping coefficient values decreased with higher values of the natural frequencies of the CNRPC material.

In the case of the viscous damping ratio of the CNRPC material, which considered PEEK as polymer matrix material and 4% SWCN volume fraction, the viscoplastic behavior of the polymer matrix material was considered, and the rate-dependent characteristics of the CNRPC material were studied, while the viscous damping ratio was calculated based on the loss factor obtained by applying an axial harmonic strain at free end in CF boundary conditions. The computed values of the viscous damping ratio for each natural frequency were within a range of 0.0333-0.0860. A comparison between structural damping mechanisms was provided, and it was determined that the structural damping coefficient was approximately two times higher than the viscous damping ratio. In the harmonic analysis, the results expose that the amplitude of the vibration for the CNRPC material decreased considerably due to the reinforcement with the SWCN, while for the polymer material the amplitude of the vibration was a lot higher. The RVE of the CNRPC material considered PAI polymer matrix.

In the static characterization, the results showed that the Maximum Entropy (ME) distributions for the reliability function were more appropriate and accurate than Weibull and Gaussian distributions. The errors calculated in this analysis showed that Weibull and Gaussian distributions presented a Root-Mean-Square-Error (RMSE) that was 15 times higher than that of ME distributions, while for the Chi-square error, the Weibull and Gaussian distributions were between 6-12 times higher than that of the ME distributions. In addition to the reliability functions, the Mean-Stress-To-Failure (MSTF) and the Mean-Residual-Strength (MRS) were determined. Also, a fixed stress point S_f was established based on the results of the reliability analysis to differentiate two zones in the reliability plot: a zone for reliability values close to one and a zone for reliability values close to zero. In the static hazard analysis, it was possible to identify two

zones for the hazard function, the zone with low-magnitude values, which was considered as the useful strength for the CNRPC material and the region for high-magnitude values, which was regarded as the failure zone of the CNRPC material. From the hazard analysis, it was possible to define a safety factor SFc, which was defined as SFc = strength/applied stress. The values of SFc were determined for the CNRPC material in a range of 1.0379-1.1265 for the different distributions. The SFc values for the ME distributions were 1.0386, while for the Weibull and Gaussian distribution were 1.1185 and 1.1265, respectively.

In the dynamic characterization, when the excitation frequency Ω was close to a natural frequency ω_n, the dynamic unreliability Q_D was determined as $P(\Omega = \omega_{\mathrm{n}}) = 1$, and thus, the dynamic reliability as $R_D = 0$, which means that the CNRPC system was in a resonance condition when $\Omega = \omega_{\mathrm{n}}$. On the other hand, as Ω was far from the other natural frequencies, the dynamic unreliability was calculated as $Q_D = 0$ and the dynamic reliability as $R_D = 1$. In the case of a distribution of Ω far from any of the natural frequencies, the dynamic unreliability Q_D was represented as $P(\Omega = \omega_n) = 0$ and the dynamic reliability as $R_D = 1$. For the operational frequency, the dynamic unreliability Q_D was represented as $P(\Omega = \omega_n) = 1$ and the dynamic reliability as $R_D = 0$. The dynamic hazard function was utilized to determine the failure and safe zones corresponding to the natural frequencies of the CNRPC material, considering near-resonance conditions as the failure zones. By combining the finite element modeling and analysis of the RVE with the probabilistic analysis and modeling (based on the MCS technique and the challenge-capacity model), it was possible to provide an alternative solution to study the dynamic behavior of the nanocomposite material with structural defects (i.e. missing carbon atoms and C-C bonds in the SWCN).

7.2 Contributions

In this section, the major contributions of this thesis are presented as follows:

1- Development of a 3D finite element model of the Single-Walled-Carbon-Nanotube (SWCN) to determine its mechanical and dynamic properties. The SWCN was first modeled as a space frame structure by using the Morse Potential and then as a thin shell based on shell theory. The non-linear behavior obtained from Morse potential was used to model the SWCN as a thin circular

shell. Then, a comparison between various shell theories was provided to determine which shell theory was more suitable for modeling the SWCN.

2- Development of a 3D multiscale finite element model of the Representative Volume Element of Carbon-Nanotube-Reinforced-Polymer-Composite (CNRPC) material to conduct a parametric study to determine its dynamic response, in terms of its modal and steady-state responses and damping properties, for different volume fractions of SWCNs. A model consisting of an SWCN, an interface region, and the polymer matrix was constructed for this purpose.

3- Development of a parametric study of the RVE of the CNRPC material with 4% volume fraction of SWCN to compare its viscous and structural damping mechanisms with the experimental data available from the literature.

4- Development of a 3D multiscale finite element model of the RVE of the CNRPC material with 5% of volume fraction, that considers the structural vacancies in the SWCN and the interface region based on Monte Carlo Simulation (MCS) technique. The structural vacancies were represented by missing carbon atoms and covalent bonds in the SWCN and van der Waals links in the interface region.

5- Development of an advanced probabilistic analysis to determine the probability density functions (pdfs) of the material properties and natural frequencies of the RVE of the CNRPC material based on the results of the MCS technique by using the Maximum Entropy Method (MEM).

6- Using the stress-strength (challenge-capacity) model prediction to obtain the static reliability and static hazard characterization of the stiffness response of the RVE of CNRPC material based on the results of the MCS technique and the pdfs obtained from MEM along with Gaussian and Weibull distributions. The ultimate longitudinal strength of CNRPC was considered as the capacity of the material system and the applied stress as the challenge that the CNRPC material must tolerate.

7- Using the challenge-capacity model prediction to obtain the dynamic reliability and dynamic hazard characterization of the modal response of the RVE of CNRPC based on the results of the MCS technique and the pdfs obtained from MEM. The reliability and hazard characterization were performed by using the challenge-capacity model for the natural frequencies of CNRPC to

determine if an external excitation frequency was close to or far from any of its natural frequencies. The consideration of the frequency sweep of the excitation and the nearness to resonance of the material system was used as a basis for the characterization of dynamic reliability and dynamic hazard. The dynamic reliability and dynamic hazard functions were obtained using the MEM.

7.3 Future work

In this section, a few avenues for future work regarding nano-reinforced polymer systems are proposed as follows:

7.3.1 Different types of structural defects in the nanocomposite material

The mechanical behavior of the Representative Volume Element (RVE) of the Carbon-Nanotube-Reinforced-Polymer-Composite (CNRPC) material can be determined using different types of structural defects. The Single-Walled-Carbon-Nanotube (SWCN) can present an imperfect structure considering defects, such as Stone-Wales (SW) defects. In a SW defect, four adjacent hexagons are converted into two pentagons and two heptagons with a 90° rotation of the horizontal bond of the hexagonal structure. In the analysis, the nanocomposite structure can be analyzed including SW and vacancy defects in the imperfect SWCN. A comparison of the results between these types of defects in the SWCN can be provided as well.

7.3.2 Random vibration analysis

Random vibration analysis can be performed on the RVE of the CNRPC material to determine its mean square response. Random vibrations can be measured with a technique called spectrum analysis that is a method in which the results of the modal analysis are used with a known spectrum (which is a graph of spectral value versus frequency that captures the intensity and frequency content of time-history loads) to calculate displacements and stresses in the RVE of the CNRPC material. It is mainly used in place of a time-history analysis to determine the response of structures to random or time-dependent loading conditions.

For non-deterministic random vibration analysis, a Power Spectral Density (PSD) spectrum, which is a statistical measure defined as the limiting mean-square value of a random variable, can be used to study the behavior of a structure or mechanical system under random loads (such as white-noise, broad-band, and narrow-band loads). In a PSD spectrum, the instantaneous

magnitudes of the response can be specified only by probability distributions that show the probability of the magnitude taking a particular value. Besides, a PSD spectrum can be represented as a graph of the PSD value versus frequency, where the PSD may be a displacement PSD, velocity PSD, acceleration PSD, or force PSD. Mathematically, the area under a PSD-versus-frequency curve is equal to the variance (square of the standard deviation of the response). This method can be utilized in a FEM software to get the response to the PSD, which may be used to determine a safety factor for random loading conditions for stationary systems.

7.3.3 Random vibration and reliability

The results of the random vibration analysis of the CNRPC material can be used to obtain its reliability. In this case, the reliability concept is the probability of the nanocomposite material not failing within a specified time interval. Furthermore, it is necessary to define a failure criterion. It is assumed that the CNRPC material fails if its deformations exceed some specific value η (a threshold). This problem in the literature is referred to as the "first passage problem" [165-167].

References

[1] P. Anand, D. Rajesh, M. Senthil Kumar and I. Saran Raj, "Investigations on the performances of treated jute/Kenaf hybrid natural fiber reinforced epoxy composite," *Journal of Polymer Research,* vol. 25, no. 94, pp. 1-9, 2018.

[2] X. Wang, L. Wang, W. Lian, A. Zhou, X. Cao and Q. Hu, "The influence of carbon spheres on thermal and mechanical properties of epoxy composites," *Journal of Polymer Research ,* vol. 25, no. 223, pp. 1-7, 2018.

[3] R. Yuan, H. Liu, P. Yu, H. Wang and J. Liu, "Enhancement of adhesion, mechanical strength and anti-corrosion by multilayer superhydrophobic coating embedded electroactive PANI/CNF nanocomposite," *Journal of Polymer Research,* vol. 25, no. 151, pp. 1-14, 2018.

[4] S. Kostromin, N. Saprykina, E. Vlasova , D. Ţîmpu, V. Cozan and S. Bronnikov, "Nanocomposite polyazomethine/reduced graphene oxide with enhanced conductivity," *Journal of polymer research,* vol. 24, no. 211, pp. 1-12, 2017.

[5] S. Iijima, "Helical microtubules of graphitic carbon," *Nature,* vol. 354, no. 568, pp. 56-58, 1991.

[6] Y. Saito, K. Hamaguchi, K. Hata, K. Uchida, Y. Tasaka, F. Ikazaki, M. Yumura, . A. Kasuya and Y. Nishina, "Conical beams from open nanotubes," *Nature,* vol. 389, p. 554–555, 1997.

[7] A. K.-T. Lau and D. Hui, "The revolutionary creation of new advanced materials—carbon nanotube composites," *Composites Part B: Engineering,* vol. 33, no. 4, pp. 263-277, 2002.

[8] E. T. Thostenson, Z. Ren and T.-W. Chou, "Advances in the science and technology of carbon nanotubes and their composites: a review," *Composites Science and Technology,* vol. 61, no. 13, pp. 1899-1912, 2001.

[9] L. S. Schadler, S. C. Giannaris and P. M. Ajayan, "Load transfer in carbon nanotube epoxy composites," *Applied Physics Letters,* vol. 73, pp. 3842-3844, 1998.

[10] L. Vaccarini, C. Goze, L. Henrard, E. Hernández, P. Bernier and A. Rubio, "Mechanical and electronic properties of carbon and boron–nitride nanotubes," *Carbon,* vol. 38, no. 11–12, pp. 1681-1690, 2000.

[11] Z. Hu and X. Hu, "Chapter 8 - Mechanical Properties of Carbon Nanotubes and Graphene," in *Carbon Nanotubes and Graphene (Second Edition)*, Amsterdam, Elsevier Ltd. , 2014, pp. 165-200.

[12] S. I. Yengejeh, . M. Akbarzade and A. Öchsner, "Numerical Charaterization of the Shear Behavior of Hetero-Junction Carbon Nanotubes," *Journal of Nano Research,* vol. 26, no. 9, pp. 143-151, 2014.

[13] S. I. Yengejeh, M. A. Zadeh and A. Öchsner, "On the buckling behavior of connected carbon nanotubes with parallel longitudinal axes," *Applied Physics A,* vol. 115, no. 4, p. 1335–1344, 2014.

[14] S. I. Yengejeh, M. A. Zadeh and A. Öchsner, "On the tensile behavior of hetero-junction carbon nanotubes," *Composites Part B: Engineering,* vol. 75, pp. 274-280, 2015.

[15] S. I. Yengejeh, S. A. Kazemi and A. Öchsner, "Advances in mechanical analysis of structurally and atomically modified carbon nanotubes and degenerated nanostructures: A review," *Composites Part B: Engineering,* vol. 86, pp. 95-107, 2016.

[16] S. O'Donnell, . K. Sprong and . B. Haltli, "Potential impact of carbon nanotube reinforced polymer composite on commercial aircraft performance and economic," in *AIAA 4th Aviation Technology, Integration and Operations (ATIO) Forum*, Chicago, 2004.

[17] P. Saini, V. Choudhary, B. P. Singh, R. B. Mathur and S. K. Dhawan, "Polyaniline–MWCNT nanocomposites for microwave absorption and EMI shielding," *Materials Chemistry and Physics,* vol. 113, no. 2-3, pp. 919-926, 2009.

[18] D. Janas and K. K. Kozio, "Rapid electrothermal response of high-temperature carbon nanotube film heaters," *Carbon,* vol. 59, pp. 457-463, 2013.

[19] H. Chu, Z. Zhang, Y. Liu and J. Leng, "Self-heating fiber reinforced polymer composite using meso/macropore carbon nanotube paper and its application in deicing," *Carbon,* vol. 66, pp. 154-163, 2014.

[20] K. Molnár, G. Szebényi, B. Szolnoki, G. Marosi, L. M. Vas and . A. Toldy, "Enhanced conductivity composites for aircraft applications: carbon nanotube inclusion both in epoxy matrix and in carbonized electrospun nanofibers," *Polymer for advanced technologies,* vol. 25, no. 9, p. 981–988, 2014.

[21] M. H. Al-Saleh and U. Sundarara, "Electromagnetic interference shielding mechanisms of CNT/polymer composites," *Carbon,* vol. 47, no. 7, pp. 1738-1746, 2009.

[22] Q.-M. Gong, Z. Li, Z. Zhang, B. Wu, X. Zhou, Q.-Z. Huang and J. Liang, "Tribological properties of carbon nanotube-doped carbon/carbon composites," *Tribology International,* vol. 39, no. 9, pp. 937-944, 2006.

[23] W. Zhao, M. Li and H. Peng, "Functionalized MWNT-Doped Thermoplastic Polyurethane Nanocomposites for Aerospace Coating Applications," *Macromolecular Materials and Engineering,* vol. 295, no. 9, pp. 838-845, 2010.

[24] M. J. Biercuk, M. C. Llaguno, M. Radosavljevic, J. K. Hyun and A. T. Johnson, "Carbon nanotube composites for thermal management," *Applied Physics Letters,* vol. 80, no. 15, pp. 2767-2769, 2002.

[25] H. Huang , C. H. Liu, Y. Wu and S. Fan, "Aligned Carbon Nanotube Composite Films for Thermal Management," *Advanced Materials,* vol. 17, no. 13, pp. 1652-1656, 2005.

[26] P. B. Kaul, M. F. Bifano and V. Prakash, "Multifunctional carbon nanotube–epoxy composites for thermal energy management," *Journal of Composite Materials,* vol. 47, no. 1, pp. 77-95, 2013.

[27] A. Yu, P. Ramesh, X. Sun, . E. Bekyarova, M. E. Itkis and R. C. Haddon, "Enhanced Thermal Conductivity in a Hybrid Graphite Nanoplatelet – Carbon Nanotube Filler for Epoxy Composites," *Advanced Materials,* vol. 20, no. 24, pp. 4740-4744, 2008.

[28] C. H. Liu, H. Huang, Y. Wu and S. S. Fan, "Thermal conductivity improvement of silicone elastomer with carbon nanotube loading," *Applied Physics Letters,* vol. 84, no. 21, pp. 4248-4250, 2004.

[29] T. Zhou, X. Wang, X. Liu and D. Xiong, "Improved thermal conductivity of epoxy composites using a hybrid multi-walled carbon nanotube/micro-SiC filler," *Carbon,* vol. 48, no. 4, pp. 1171-1176, 2010.

[30] K. I. Tserpes, P. Papanikos, G. Labeas and S. G. Pantelakis, "Multi-scale modeling of tensile behavior of carbon nanotube-reinforced composites," *Theoretical and Applied Fracture Mechanics,* vol. 49, p. 51–60, 2008.

[31] K. I. Tserpes, P. Papanikos and S. A. Tsirkas, "A Progressive Fracture Model for Carbon Nanotubes," *Composites Part B: Engineering,* vol. 37, pp. 662-669, 2006.

[32] N. Hu, H. Fukunaga, C. Lu, M. Kameyama and B. Yan, "Prediction of elastic properties of carbon nanotube reinforced composites," *Proceedings of the Royal Society A,* vol. 461, pp. 1685-1710, 2005.

[33] K. I. Tserpes and P. Papanikos, "Finite Element Modeling of Single-Walled Carbon Nanotubes," *Composites Part B: Engineering,* vol. 36, no. 5, pp. 468-477, 2005.

[34] M. S. Dresselhaus, G. Dresselhaus and R. Saito, "Physics of carbon nanotubes," *Carbon,* vol. 33, no. 7, pp. 883-891, 1995.

[35] T. Natsuki, K. Tantrakarn and M. Endo, "Prediction of elastic properties for single-walled carbon nanotubes," *Carbon,* vol. 42, no. 1, pp. 39-45, 2004.

[36] M. T. Ahmadi, J. F. Webb, R. Ismail and M. Rahmandoust, "Carbon-Based Materials Concepts and Basic Physics," in *Advanced Nanoelectronics*, Boca Raton, Francis & Taylor Group, 2013, pp. 49-82.

[37] C. W. To, "Bending and Shear Moduli of Single-Walled Carbon Nanotubes," *Finite Elements in Analysis and Design,* vol. 42, p. 404 – 413, 2006.

[38] C. Li and T.-W. Chou, "A structural mechanics approach for the analysis of carbon nanotubes," *International Journal of Solids and Structures,* vol. 40, no. 10, pp. 2487-2499, 2003.

[39] H. Ghasemi, R. Rafiee, X. Zhuang, J. Muthu and T. Rabczuk, "Uncertainties propagation in metamodel-based probabilistic optimization of CNT/polymer composite structure using stochastic multiscale modeling," *Computational Materials Science,* vol. 85, p. 295–305, 2014.

[40] R. Rafiee and M. Mahdavi, "Characterizing nanotube–polymer interaction using molecular dynamics simulation," *Computational Materials Science,* vol. 112, p. 356–363, 2016.

[41] M. M. Shokrieh and R. Rafiee, "Stochastic multi-scale modeling of CNT/polymer composites," *Computational Materials Science,* vol. 50, p. 437–446, 2010.

[42] S.-P. Ju, C.-C. Chen, T.-J. Huang, C.-H. Liao, H.-L. Chen, Y.-C. Chuang, Y.-C. Wu and H.-T. Chen, "Investigation of the structural and mechanical properties of polypropylene-based carbon fiber nanocomposites by experimental measurement and molecular dynamics simulation," *Computational Materials Science,* vol. 115, p. 1–10, 2016.

[43] G. P. Tandon and G. J. Weng, "Average stress in the matrix and effective moduli of randomly oriented composites," *Composites Science and Technology,* vol. 27, no. 2, pp. 111-132, 1986.

[44] Y. Benveniste, "A new approach to the application of Mori-Tanaka's theory in composite materials," *Mechanics of Materials,* vol. 6, no. 2, pp. 147-157, 1987.

[45] M. Ferrari and G. C. Johnson, "The effective elasticities of short-fiber composites with arbitrary orientation," *Mechanics of Materials,* vol. 8, no. 1, pp. 67-73, 1989.

[46] R. Makvandi and A. Öchsner, "On a numerical strategy to simulate nanotube-reinforced composite materials," *Materials Science and Engineering Technology,* vol. 45, no. 5, p. 429–435, 2014.

[47] I. E. Afrooz, A. Öchsner and M. Rahmandoust, "Effects of the carbon nanotube distribution on the the macroscopic stiffness of composite materials," *Computational Materials Science,* vol. 51, no. 1, pp. 422-429, 2012.

[48] M. Rahmandoust and M. R. Ayatollahi, Characterization of Carbon Nanotube-Based Composites Under Consideration of Defects, London: Springer International Publishing AG Switzerland, 2016.

[49] P. G. Collins, "Defects and disorder in carbon nanotubes," in *Oxford Handbook of Nanoscience and Technology: Volume 2: Materials: Structures, Properties and Characterization Techniques*, Oxford, Oxford University Press, 2009.

[50] P. Ehrhart, Properties and Interactions of Atomic Defects in Metals and Alloys, Berlin: Springer-Verlag, 1992.

[51] S. I. Yengejeh, S. A. Kazemi and A. Öchsner, "Carbon nanotubes as reinforcement in composites: a review of the analytical, numerical and experimental approaches," *Computational Materials Science,* vol. 136, pp. 85-101, 2017.

[52] G. Pal and S. Kumar, "Modeling of carbon nanotubes and carbon nanotube–polymer composites," *Progress in Aerospace Sciences,* vol. 80, pp. 33-58, 2016.

[53] Z. Shan and A. M. Gokhale, "Representative volume element for non-uniform micro-structure,," *Computational Materials Science,* vol. 24, p. 361–379, 2002.

[54] E. Weinan, Principles of multiscale modeling, New York: Cambridge University Press, 2011.

[55] E. Weinan and B. Engquist, "The Heterogeneous Multiscale Methods," *Communications in Mathematical Sciences,* vol. 1, no. 1, pp. 87-132, 2003.

[56] Y. Efendiev, J. Galvis and T. Y. Hou, "Generalized multiscale finite element methods (GMsFEM)," *Journal of Computational Physics,* vol. 251, p. 116–135, 2013.

[57] W. K. Liu, E. G. Karpov and H. S. Park, Nano Mechanics and Materials: Theory, Multiscale Methods and Applications, Chichester: John Wiley & Sons Ltd, 2006.

[58] C. R. Weinberger and . G. J. Tucker, Multiscale Materials Modeling for Nanomechanics, Philadelphia: Springer International Publishing, 2016.

[59] S. Schmauder and . I. Schäfer, Multiscale Materials Modeling: Approaches to Full Multiscaling, Berlin: Walter de Gruyter GmbH, 2016.

[60] T. Y. Hou and X.-H. Wu, "A Multiscale Finite Element Method for Elliptic Problems in Composite Materials and Porous Media," *JOURNAL OF COMPUTATIONAL PHYSICS,* vol. 134, p. 169–189, 1997.

[61] Y. Efendiev, J. Galvis, R. Lazarov, M. Moon and M. Sarkis, "Generalized multiscale finite element method. Symmetric interior penalty coupling," *Journal of Computational Physics,* vol. 255, p. 1–15, 2013.

[62] Y. Efendiev, J. Galvis and X.-H. Wu, "Multiscale finite element methods for high-contrast problems using local spectral basis functions," *Journal of Computational Physics,* vol. 230, no. 4, p. 937–955, 2011.

[63] Y. Efendiev, J. Galvis, G. Li and M. Presho, "Generalized Multiscale Finite Element Methods. Oversampling Strategies," *International Journal for Multiscale Computational Engineering,* vol. 12, no. 6, pp. 465-484, 2014.

[64] Y. Efendiev, T. Y. Hou and X.-H. Wu, "Convergence of a nonconforming multiscale finite element method," *SIAM Journal on Numerical Analysis,* vol. 37, no. 3, p. 888–910, 2000.

[65] E. T. Chung, Y. Efendiev and S. Fu, "Generalized multiscale finite element method for elasticity equations," *International Journal on Geomathematics,* vol. 5, no. 2, p. 225–254, 2014.

[66] H. Waisman and J. Fish, "Space-time multigrid method for molecular dynamics simulations," *Computer Methods in Applied Mechanics and Engineering ,* vol. 195, no. 44-47, pp. 6542-6559, 2006.

[67] J. Fish, T. Jiang and Z. Yuan, "A staggered nonlocal multiscale model for a heterogeneous medium," *International Journal for Numerical Methods in Engineering,* vol. 91, no. 2, p. 142–157, 2012.

[68] M. Fermeglia and S. Pricl, "Multiscale molecular modeling in nanostructured material design and process system engineering," *Computers and Chemical Engineering,* vol. 33, no. 10, p. 1701–1710, 2009.

[69] S. B. Ramisetti, G. Anciaux and J. F. Molinari, "Spatial filters for bridging molecular dynamics with finite elements at finite temperatures," *Computer Methods in Applied Mechanics and Engineering,* vol. 253, p. 28–38, 2013.

[70] A. Tabarraei, X. Wang, A. Sadeghirad and J. H. Song, "An enhanced bridging domain method for linking atomistic and continuum domains," *Finite Elements in Analysis and Design,* vol. 92, p. 36–49, 2014.

[71] P. Ladevéze, L. Blanc, P. Rouch and C. Blanzé, "A multiscale computational method for medium-frequency vibrations of assemblies of heterogeneous plates," *Computers and Structures,* vol. 81, no. 12, p. 1267–1276, 2003.

[72] M. V. Kireitseu and L. V. Bochkareva, "Modelling and Optimization of Vibration Damping (Dynamic) Properties in Nanoscale-Reinforced Materials," in *38th International Symposium on Microelectronics, IMAPS 2005*, Philadelphia, 2005.

[73] P. Xiang and K. M. Liew, "Free vibration analysis of microtubules based on an atomistic-continuum model," *Journal ofSound and Vibration,* vol. 331, no. 1, p. 213–230, 2012.

[74] J. M. Sanz-Serna, "Modulated Fourier expansions and heterogeneous multiscale methods," *IMA Journal of Numerical Analysis,* vol. 29, p. 595–605, 2009.

[75] M. A. Köbis and M. Arnold, "Numerical solution of penalty formulations for constrained mechanical systems using heterogeneous multiscale methods," *Journal of Computational and Applied,* vol. 262, p. 193–204, 2014.

[76] J. M. Wernik and S. A. Meguid, "Multiscale modeling of the nonlinear response of nano-reinforced polymers," *Acta Mechanica,* vol. 217, no. 1-2, p. 1–16, 2011.

[77] Y. J. Liu and X. L. Chen, "Evaluations of the effective material properties of carbon nanotube-based composites using a nanoscale," *Mechanics of Materials,* vol. 35, p. 69–81, 2003.

[78] M. M. Shokrieh and R. Rafiee, "On the Tensile Behavior of an Embedded Carbon Nanotube in Polymer Matrix with Non-Bonded Interphase Region," *Composite Structures,* vol. 92, no. 3, pp. 647-652, 2010.

[79] S. Georgantzinos, G. Giannopoulos and N. Anifantis, "Investigation of stress–strain behavior of single walled carbon nanotube/rubber composites by a multi-scale finite element method," *Theoretical and Applied Fracture Mechanics,* vol. 52, no. 3, p. 158–164, 2009.

[80] L. H. Donnell, Beams, Plates and Shells, New York: McGraw-Hill Book Company, 1976.

[81] A. W. Leissa, Vibration of Shells, Washington : NASA, 1973.

[82] R. W. Ogden, Non-Linear Elastic Deformations, New York: Dover Publications, 1997.

[83] C. Li and T. W. Chou, "Elastic Moduli of Multi-Walled Carbon Nanotubes and the Effect of Van der Waals Forces," *Composites Science and Technology,* vol. 63, no. 11, pp. 1517-1524, 2003.

[84] A. Haldar and S. Mahadevan, Probability, Reliability, and Statistical Methods in Engineering Design, New York: Wiley, 1999.

[85] D. B. Kececioglu, Robust engineering design-by-reliability-with emphasis on mechanical components & structural reliability, Lancaster: DEStech Publications, 2003.

[86] J. N. Siddall, Probabilistic engineering design: principles and applications, New York: Marcel Dekker, 1983.

[87] F. J. Liu and T. P. Chang, "Validity analysis of maximum entropy distribution based on different moment constraints for wind energy assessment," *Energy,* vol. 36, pp. 1820-1826, 2011.

[88] A. Rajan, Y. C. Kuang, M. Po-Leen, S. N. Demidenko and H. Carstens, "Moment-constrained maximum entropy method for expanded uncertainty evaluation," *IEEE Access,* vol. 6, pp. 4072 - 4082, 2018.

[89] E. T. Jaynes, "Information theory and statistical mechanics," *Physical Review Journals Archive,* vol. 106, no. 620, 1957.

[90] D. P. Bertsekas, Nonlinear programming: 3rd edition, Belmont: Athena Scientic, 1999.

[91] C. Li and T. Chou, "Multiscale modeling of compressive behavior of carbon nanotube/polymer composites," *Composites Science and Technology,* vol. 66, no. 14, p. 2409–2414, 2006.

[92] S. K. Georgantzinos, G. I. Giannopoulos and N. K. Anifantis, "Effective Young's Modulus of Carbon Nanotube Composites From Multi-Scale Finite Element Predictions to an Analytical Rule," *Journal of Computational and Theoretical Nanoscience,* vol. 7, no. 8, p. 436–1442, 2010.

[93] K. N. Spanos, S. K. Georgantzinos and N. K. Anifantis, "Investigation of stress transfer in carbon nanotube reinforced composites using a multi-scale finite element approach," *Composites: Part B Engineering,* vol. 63, p. 85–93, 2014.

[94] E. Mohammadpour, M. Awang, S. Kakooei and H. M. Akilb, "Modeling the Tensile Stress-Strain Response of Carbon nanotube/polypropylene Nanocomposites using Nonlinear Representative Volume Element," *Materials and Design ,* vol. 58, no. 1, pp. 36-42, 2014.

[95] M. Ionita, "Multiscale molecular modeling of SWCNTs/epoxy resin composites mechanical behaviour," *Composites Part B: Engineering,* vol. 2012, p. 3491–3496, 2012.

[96] A. Ghorbanpour Arani, E. Haghparast, Z. Khoddami Maraghi and S. Amir, "Static stress analysis of carbon nano-tube reinforced composite (CNTRC) cylinder under non-

axisymmetric thermo-mechanical loads and uniform electro-magnetic fields," *Composites Part B: Engineering,* vol. 68, p. 136–145, 2015.

[97] A. R. Ghasemi, M. M. Mohammadi and M. Mohandes, "The role of carbon nanofibers on thermo-mechanical properties of polymer matrix composites and their effect on reduction of residual stresses," *Composites Part B: Engineering,* vol. 77, pp. 519-527, 2015.

[98] Z. Jia, H.-l. Ma, L.-K. Cheng, L. Kin-tak, D. Hui and G. Yuan, "Stress transfer properties of carbon nanotube reinforced polymer composites at low temperature environments," *Composites Part B: Engineering,* vol. 106, pp. 356-365, 2016.

[99] B. Kyu Choi, G. Ho Yoon and S. Lee, "Molecular dynamics studies of CNT-reinforced aluminum composites under uniaxial tensile loading," *Composites Part B: Engineering,* vol. 91, pp. 119-125, 2016.

[100] E. García-Macías, C. Felipe Guzmán, E. I. Saavedra Flores and R. Castro-Triguero, "Multiscale modeling of the elastic moduli of CNT-reinforced polymers and fitting of efficiency parameters for the use of the extended rule-of-mixtures," *Composites Part B: Engineering,* vol. 159, p. 114–131, 2019.

[101] V. Papadopoulos and M. Impraimakis, "Multiscale modeling of carbon nanotube reinforced concrete," *Composite Structures,* vol. 182, p. 251–260, 2017.

[102] Q. Sun, Z. Meng, G. Zhou, S.-P. Lin, H. Kang, S. Keten, H. Guo and X. Su, "Multi-Scale Computational Analysis of Unidirectional Carbon Fiber Reinforced Polymer Composites under Various Loading Conditions," *Composite Structures,* vol. 196, pp. 30-43, 2018.

[103] J. Chevalier, P. P. Camanho, F. Lani and T. Pardoen, "Multi-scale characterization and modelling of the transverse compression response of unidirectional carbon fiber reinforced epoxy," *Composite Structures,* vol. 209, pp. 160-176, 2019.

[104] S. T. Latibari, M. Mehrali, L. Mottahedin, A. Fereidoon and H. S. Cornelis Metselaar, "Investigation of interfacial damping nanotube-based composite," *Composites Part B: Engineering,* vol. 50, pp. 354-361, 2013.

[105] M. Jamal-Omidi, M. ShayanMehr and R. Mosalmani, "Investigating the effect of interphase and surrounding resin on carbon nanotube free vibration behavior," *Physica E: Low-dimensional Systems and Nanostructures,* vol. 68, pp. 42-52, 2015.

[106] M. M. Shokrieh, R. Ghajar and A. R. Shajari, "The effect of time-dependent slightly weaken interface on the viscoelastic properties of CNT/polymer nanocomposites," *Composite Structures,* vol. 146, pp. 122-131, 2016.

[107] S. O. Gajbhiye and S. P. Singh, "Multiscale Modeling of Dynamic Characteristics of Carbon Nanotube Reinforced Nanocomposites," *NANO: Brief Reports and Reviews,* vol. 11, no. 7, pp. 1-12, 2016.

[108] M. R. Davoudabadi and S. D. Farahani, "Investigation of vacancy defects on the Young's modulus of carbon nanotube reinforced composites in axial direction via a multiscale modeling approach," *Journal of Solid Mechanics,* vol. 2, no. 3, pp. 248-256, 2010.

[109] Z. Yuan and Z. Lu, "Numerical analysis of elastic–plastic properties of polymer composite reinforced by wavy and random CNTs," *Computational Materials Science,* vol. 95, p. 610–619, 2014.

[110] U. A. Joshi, S. C. Sharma and S. P. Harsha, "Characterizing the strength and elasticity deviation in defective CNT reinforced composites," *Composites Communications,* vol. 2, pp. 9-14, 2016.

[111] R. Chawla, S. Sharma, A. Bansal and M. Dhawan, "Effect of vacancy defects on the mechanical properties of carbon nanotube reinforced polypropylene," *International Journal of Mechanical Engineering and Technology,* vol. 8, no. 7, p. 1370–1375, 2017.

[112] E. Ozden-Yenigun, C. Atilgan and J. A. Elliott, "Multi-scale modelling of carbon nanotube reinforced crosslinked interfaces," *Computational Materials Science,* vol. 129, p. 279–289, 2017.

[113] F.-Y. Zhu, S. Jeong, H. J. Lim and G. J. Yun, "Probabilistic multiscale modeling of 3D randomly oriented and aligned wavy CNT nanocomposites and RVE size determination," *Composite Structures,* vol. 195, p. 265–275, 2018.

[114] S. Jeong, F. Zhu, H. Lim, Y. Kim and G. J. Yun, "3D stochastic computational homogenization model for carbon fiber reinforced CNT/epoxy composites with spatially random properties," *Composite Structures,* vol. 207, p. 858–870, 2019.

[115] M. Endo, T. Hayashi, Y. A. Kim, M. Terrones and M. S. Dresselhaus, "Applications of carbon nanotubes in the twenty-first century," *Philosophical Transactions of the The Royal Society A,* vol. 362, p. 2223–2238, 2004.

[116] S. Kirtania and D. Chakraborty, "Finite Element Based Characterization of Carbon Nanotubes," *Journal of Reinforced Plastics and Composites,* vol. 26, no. 15, pp. 1557-1570, 2007.

[117] S. Kirtania and D. Chakraborty, "Failure analysis of carbon nanotube/epoxy composites having a broken carbon nanotube," *Journal of Reinforced Plastics and Composites,* vol. 34, no. 19, pp. 1639-1647, 2015.

[118] X. Y. Wang and X. Wang, "Torsional Buckling of Multi-walled Carbon Nanotubes Subjected to Torsional Loads," *Journal of Reinforced Plastics and Composites,* vol. 26, no. 5, pp. 479-494, 2007.

[119] T. Belytschko, S. P. Xiao, G. C. Schatz and R. S. Ruoff, "Atomistic simulations of nanotube fracture," *PHYSICAL REVIEW B,* vol. 65, no. 235430, pp. 1-8, 2002.

[120] B. I. Yakobson, C. J. Brabec and J. Bernholc, "Nanomechanics of Carbon Tubes: Instabilities Beyond Linear Response," *Physical Review Letters,* vol. 76, no. 14, pp. 2511-2514, 1996.

[121] A. N. R. Chowdhury, C. M. Wang and S. J. Adrian Koh, "Continuum Shell Model for Buckling of Single-Walled Carbon Nanotubes with Different Chiral Angles," *International Journal of Structural Stability and Dynamics,* vol. 14, no. 2, pp. 1-12, 2014.

[122] C. M. Wang, Z. Y. Tay and A. N. R. Chowdhury, "Examination of Cylindrical Shell Theories for Buckling of Carbon Nanotubes," *International Journal of Structural Stability and Dynamics,* vol. 11, no. 6, pp. 1035-1058, 2011.

[123] M. Hussain, M. N. Naeem, A. Shahzad and M. He, "Vibrational behavior of single-walled carbon nanotubes based on cylindrical shell model using wave propagation approach," *AIP ADVANCES,* vol. 7, no. 045114, pp. 1-17, 2017.

[124] J. Kołoczek, Y.-K. Kwon and A. Burian, "Characterization of Spatial Correlations in Carbon Nanotubes-Modelling Studies," *Journal of Alloys and Compounds,* vol. 328, no. 1-2, pp. 222-225, 2001.

[125] J. H. Lee and B. S. Lee, "Modal Analysis of Carbon Nanotubes and Nanocones using FEM," *Computational Materials Science,* vol. 51, no. 1, pp. 30-42, 2012.

[126] S. S. Gupta, F. G. Bosco and B. C. Batra, "Wall thickness and elastic moduli of single-walled carbon nanotubes from frequencies of axial, torsional and inextensional modes of vibration," *Computational Materials Science,* vol. 47, no. 4, pp. 1049-1059, 2014.

[127] S. Sun, D. Cao and S. Chu, "Free vibration analysis of thin rotating cylindrical shells using wave propagation approach," *Archive of Applied Mechanics,* vol. 83, p. 521–531, 2013.

[128] C. Wang and J. C. S. Lai, "Prediction of natural frequencies of finite length circular cylindrical shells," *Applied Acoustics,* vol. 59, pp. 385-400, 2000.

[129] X. M. Zhang, G. R. Liu and K. Y. Lam, "Vibration analysis of thin cylindrical shells using wave propagation approach," *Journal of Sound and Vibration,* vol. 239, p. 397–403, 2001.

[130] X. M. Zhang, G. R. Liu and K. Y. Lam, "Coupled vibration analysis of fluid-filled cylindrical shells using the wave propagation," *Applied Acoustics,* vol. 62, p. 229–243, 2001.

[131] M. Meo and M. Rossi, "A molecular-mechanics based finite element model for strength prediction of single wall carbon nanotubes," *Materials Science and Engineering: A,* vol. 454–455, p. 170–177, 2007.

[132] S. Sihn, V. Varshney, A. K. Roy and B. L. Farmer, "Modeling for predicting strength of carbon nanostructures," *Carbon,* vol. 95, pp. 181-189, 2015.

[133] Y. Y. Zhang, C. M. Wang and V. B. C. Tan, "Assessment of Timoshenko Beam Models for Vibrational Behavior of Single-Walled Carbon Nanotubes using Molecular Dynamics," *Advances in Applied Mathematics and Mechanics,* vol. 1, no. 1, pp. 89-106, 2009.

[134] T. Chang, J. Geng and X. Guo, "Prediction of chirality- and size-dependent elastic properties of single-walled carbon nanotubes," *Proceeding of the Royal Society A,* vol. 462, pp. 2523-2540, 2006.

[135] X. Xu, C. Koomson, M. Doddamani, R. Kumar Beheraa and N. Gupta, "Extracting elastic modulus at different strain rates and temperatures from dynamic mechanical analysis data: A study on nanocomposites," *Composites Part B: Engineering,* vol. 159, p. 346–354, 2019.

[136] J. Richeton, S. Ahzi, K. S. Vecchio, F. C. Jiang and R. R. Adharapurapu, "Influence of temperature and strain rate on the mechanical behavior of three amorphous polymers: Characterization and modeling of the compressive yield stress," *International Journal of Solids and Structures,* vol. 43, p. 2318–2335, 2006.

[137] S. B. Sinnott, "Chemical functionalization of carbon nanotubes," *Journal of Nanoscience and Nanotechnology,* vol. 2, no. 2, p. 113–123, 2002.

[138] F. Buffa, G. A. Abraham, B. P. Grady and D. Resasco, "Effect of nanotube functionalization on the properties of single-walled carbon nanotube/polyurethane composites," *Journal of Polymer Science Part B: Polymer Physics,* vol. 45, no. 1, pp. 490-501, 2007.

[139] M. Kireitseu, D. Hui and G. Tomlinson, "Advanced shock-resistant and vibration damping of nanoparticle-reinforced composite material," *Composites Part B: Engineering,* vol. 39, no. 1, pp. 128-138, 2008.

[140] X. Zhou, E. Shin, K. W. Wang and C. E. Bakis, "Interfacial damping characteristics of carbon nanotube-based composites," *Composites Science and Technology,* vol. 64, no. 15, pp. 2425-2437, 2004.

[141] M. Carfagni, E. Lenzi and M. Pierini, "The loss factor as a measure of mechanical damping," in *Proceedings of the 16th International Modal Analysis Conference*, Santa Barbara, 1998.

[142] S. S. Rao, Mechanical Vibrations, Upper Saddle River: Prentice Hall, 2011.

[143] G. H. Golub and R. Underwood, "The Block Lanczos Method for Computing Eigenvalues," in *Proceedings of a Symposium Conducted by the Mathematics Research Center, the University of Wisconsin–Madison,* , Wisconsin–Madison, 1977.

[144] L. M. Gil-Martín, J. F. Carbonell-Márquez, E. Hernández-Montes, M. Aschheim and M. Pasadas-Fernández, "Dynamic magnification factors of SDOF oscillators under harmonic loading," *Applied Mathematics Letters,* vol. 25, pp. 38-42, 2012.

[145] E. M. Sadek, D. E. El-Nashar, A. A. Ward and S. M. Ahmed, "Study on the properties of multi-walled carbon nanotubes reinforced poly (vinyl alcohol) composites," *Journal of Polymer Research,* vol. 25, no. 249, pp. 1-13, 2018.

[146] X. Qi-lin and T. Xin, "Effect of polymer matrix and nanofiller on non-bonding interfacial properties of nanocomposites," *Journal of Polymer Research,* vol. 24, no. 15, pp. 1-9, 2017.

[147] Z. El-Qoubaa and R. Othman, "Characterization and modeling of the strain rate sensitivity of polyetheretherketone's compressive yield stress," *Materials and Design,* vol. 66, pp. 336-345, 2015.

[148] A. Arriaga, R. Pagaldai, A. M. Zaldua, A. Chrysostomou and M. O'Brien, "Impact testing and simulation of a polypropylene component. Correlation with strain rate sensitive constitutive models in ANSYS and LS-DYNA," *Polymer Testing,* vol. 29, p. 170–180, 2010.

[149] P. Perzyna, "Fundamental Problems in Viscoplasticity," *Advances in Applied Mechanics,* vol. 10, no. 2, pp. 243-377, 1966.

[150] C. Galliot and R. H. Luchsinger, "Uniaxial and biaxial mechanical properties of ETFE foils," *Polymer Testing,* vol. 30, no. 4, pp. 356-365, 2011.

[151] D. Vasiukov, S. Panier and A. Hachemi, "Non-linear material modeling of fiber-reinforced polymers based on coupled viscoelasticity–viscoplasticity with anisotropic continuous damage mechanics," *Composite Structures,* vol. 132, pp. 527-535, 2015.

[152] A. Alva and S. Raja, "Damping Characteristics of Epoxy-Reinforced Composite with Multiwall Carbon Nanotubes," *Mechanics of Advanced Materials and Structures,* vol. 21, no. 3, pp. 197-206, 2014.

[153] H. Rajoria and N. Jalili, "Passive vibration damping enhancement using carbon nanotube-epoxy reinforced composites," *Composites Science and Technology,* vol. 65, p. 2079–2093, 2005.

[154] W. W. Soroka, "Note on the Relations Between Viscous and Structural Damping Coefficients," *Journal of the Aeronautical Sciences ,* vol. 16, no. 7, pp. 409-410, 1949.

[155] A. Haeri and M. J. Fadaee, "Efficient reliability analysis of laminated composites using advanced Kriging surrogate model," *Composite Structures,* vol. 149, pp. 26-32, 2016.

[156] X. Chen and Z. Qiu, "Reliability assessment of fiber-reinforced composite laminates with correlated elastic mechanical parameters," *Composite Structures,* vol. 203, pp. 396-403, 2018.

[157] S. L. Omairey, P. D. Dunning and S. Sriramula, "Influence of micro-scale uncertainties on the reliability of fibre-matrix composites," *Composite Structures,* vol. 203, pp. 204-216, 2018.

[158] X.-Y. Zhou, P. D. Gosling, Z. Ullah, L. Kaczmarczyk and C. J. Pearce, "Exploiting the benefits of multi-scale analysis in reliability analysis for composite structures," *Composite Structures,* vol. 155, p. 197–212, 2016.

[159] K. B. Misra, Reliability analysis and prediction, Amsterdam: Elsevier, 1992.

[160] R. Billinton and R. N. Allan, Reliability evaluation of engineering systems: concepts and techniques, New York: Springer Science+Business Media, 1992.

[161] M. Hyer, Stress analysis of fiber-reinforced composite materials, Lancaster: DEStech Publications, 2009.

[162] H. G. Matthies, C. E. Brenner, C. G. Bucher and C. Guedes Soares, "Uncertainties in probabilistic numerical analysis of structures and solids-Stochastic finite elements," *Structural Safety,* vol. 19, no. 3, pp. 283-336, 1997.

[163] M. Rafiee, F. Nitzsche and M. R. Labrosse, "Effect of functionalization of carbon nanotubes on vibration and damping characteristics of epoxy nanocomposites," *Polymer Testing,* vol. 69, pp. 385-395, 2018.

[164] R. E. Melchers and . A. T. Beck, Structural Reliability Analysis and Prediction, Chichester: John Wiley & Sons Ltd, 2017.

[165] G. Cederbaum , I. Elishakoff, J. Aboudi and L. Librescu, Random Vibration and Reliability of Composite Structures, Pennsylvania: Technomic Publishing Company, 1992.

[166] R. S. Langley, "First Passage Approximation for Normal Stationary Random Processes," *Journal of Sound and Vibration,* vol. 122, no. 2, pp. 261-275, 1988.

[167] A. B. Mason Jr and W. D. Iwan, "Approach to the First Passage Problem in Random Vibration," *Journal of Applied Mechanics, Transactions ASME,* vol. 50, no. 3, pp. 641-646, 1983.